Photodynamic therapies of high-grade gliomas : from theory to clinical perspectives

Clément Dupont

LILLE UNIVERSITY, LAW AND HEALTH

DOCTORAL SCHOOL BIOLOGY AND HEALTH

DOCTORAL THESIS

Subject: Physics

Specialty: Elementary constituents

Photodynamic therapies of high-grade gliomas: from theory to clinical perspectives

Clément DUPONT

Thesis supervised by Dr. Maximilien VERMANDEL

Presented and defended publicly on November 24th, 2017

Reviewers:

Pr. Thierry BASTOGNE

Dr. Stéphanie BONNEAU

Examiners:

Pr. Florence LEFRANC

Dr. Emilie LERHUN

Pr. Nicolas REYNS

Dr. Gord VON CAMPE

UNIVERSITÉ DE LILLE, DROIT ET SANTÉ

ÉCOLE DOCTORALE BIOLOGIE SANTÉ DE LILLE

THÈSE DE DOCTORAT

Discipline : Physique

Spécialité : Constituants élémentaires

Thérapies photodynamiques appliquées aux gliomes de haut grade : de la théorie à la réalité clinique

Clément DUPONT

Thèse supervisée par Dr. Maximilien VERMANDEL

Présentée et soutenue publiquement le 24 novembre 2017

Rapporteurs.rices :

Pr. Thierry BASTOGNE

Dr. Stéphanie BONNEAU

Examinateurs.rices :

Pr. Florence LEFRANC

Dr. Emilie LERHUN

Pr. Nicolas REYNS

Dr. Gord VON CAMPE

Photodynamic therapies of high-grade gliomas: from theory to clinical perspectives

Gliomas are the most common primary brain tumors in adults. Among them, glioblastoma (GBM) represents the most frequent primary brain tumor and have the most dismal prognosis. Its annual incidence is about 3 to 5 cases for 100,000 persons (about 3000 news cases each year in France). Median survival varies between 14 to 15 months according to the extent of tumor resection.

The standard of care includes surgery and is followed by radiation therapy and chemotherapy. Maximal resection is expected to delay recurrence. Despite of using intraoperative photodynamic diagnosis, or fluorescence guided resection (FGR), which improves the extent of resection, relapse still occurs in these resection margins in 85% of cases.

Alternatives therapies have to be developed to enhance patients' overall survival. In this context, Photodynamic Therapy (PDT) seems relevant. PDT is based on the synergy of three parameters: a photosensitizing molecule, the photosensitizer (PS) that concentrates preferentially into the tumor cells, laser light and oxygen. Laser light induces a reaction between the PS and the oxygen of the cell. This reaction produces highly cytotoxic molecules (including singlet oxygen) and leads to death of tumor cells. Two treatment modalities are investigated: interstitial PDT (iPDT) or intraoperative PDT.

The main goal of this thesis is to provide technological tools to develop the PDT for GBM treatment. Thus, the two treatment modalities have been investigated.

When tumor resection is non-achievable (approximately 20% to 30% of cases), iPDT may be preferred. This modality aims to insert optical fibers directly into the target to illuminate tumor tissues. Thus, simulation of light propagation in brain tissues is required to plan the location of optical fibers. Considered as reference method, a Monte-Carlo model accelerated by graphics processing unit was developed. This model computes the light propagation emitted by a cylindrical diffusor inside heterogeneous media. Accuracy of the model was evaluated with experimental measurements. The acceleration provided by the parallelization allows its use in clinical routine.

The iPDT has to be planned using a Treatment Planning System (TPS). A proof of concept of a TPS dedicated to the stereotactic iPDT treatment of GBM was developed. This software provides basic tools to plan the stereotactic insertion of cylindrical diffusors in patient's brain

and to compute the associated dosimetry. The stereotactic registration and the dosimetry computation's accuracy were evaluated with specific methodologies.

When tumor resection is achievable, the intraoperative PDT may be applied early after the FGR. It takes advantage of the presence of the PS (protoporphyrin IX) used for FGR purpose and that is already concentrates into the tumor cells. Thus, the proposed treatment strategy fits into the current standard of care. A medical device was designed into fit to the resection cavity and illuminate homogeneously the cavity's margins. The device is constituted of two parts: a trocar coupled to an inflatable balloon and a fiber guide developed in the ONCO-THAI laboratory allowing to insert the light source. Specific methodologies were developed to calibrate and assess the device in terms of mechanical properties and dosimetry. The calibration process leaded to a transfer function that provides fast, robust and easy treatment duration prescription to induce a PDT response in cavity margins. Furthermore, a comprehensive experimental design has been worked out prior to the clinical trial that evaluate the safety of the procedure.

Keywords: photodynamic therapy, glioblastoma, dosimetry, Monte-Carlo simulation, GPU computing, medical device, clinical trial.

Thérapies photodynamiques appliquées aux gliomes de haut grade : de la théorie à la réalité clinique

Les gliomes sont les tumeurs cérébrales primaires les plus communes chez l'adulte. Parmi eux, le glioblastome (GBM) représente la tumeur cérébrale la plus fréquente avec le pronostic le plus sombre. Son incidence annuelle est d'environ 3 à 5 cas pour 100 000 personnes (environ 3000 nouvelles chaque année en France). La survie médiane varie entre 14 et 15 mois selon la qualité de la résection tumorale.

Le standard de soins inclut une résection chirurgicale suivie d'une radiothérapie et d'une chimiothérapie. Une résection maximale est souhaitée afin de diminuer les risques de récidive. Bien que l'utilisation de la technique de diagnostic photodynamique peropératoire, appelée résection fluoroguidée (FGR), améliore la qualité de résection, une récidive survient dans ces berges de la cavité opératoire dans 85% des cas.

Des thérapies alternatives doivent être développées pour améliorer la survie globale des patients. Dans ce contexte, la thérapie photodynamique (PDT) semble pertinente. La PDT est basée sur la synergie de trois paramètres : une molécule, le photosensibilisateur (PS) qui se concentre préférentiellement dans les cellules tumorales, la lumière laser et l'oxygène. La lumière laser induit une réaction entre le PS et l'oxygène de la cellule. Cette réaction produit des molécules cytotoxiques (dont l'oxygène singulet) et conduit à la mort de cellules tumorales. Deux modalités de traitement sont étudiées : la PDT interstitielle (iPDT) ou la PDT peropératoire.

L'objectif principal de cette thèse est de fournir des outils technologiques afin développer la PDT pour le traitement du GBM. Ainsi, les deux modalités de traitement ont été étudiées.

Lorsque la résection n'est pas réalisable (environ 20% à 30% des cas), l'iPDT peut être privilégiée. Cette modalité vise à insérer des fibres optiques dans la cible thérapeutique pour éclairer les tissus tumoraux. Ainsi, la simulation de la propagation de la lumière dans les tissus est nécessaire pour planifier la localisation des fibres optiques. Considéré comme méthode de référence, un modèle Monte-Carlo accéléré par processeurs graphiques a été développé. Ce modèle calcule la propagation de la lumière émise par un diffuseur cylindrique dans des milieux hétérogènes. La précision du modèle a été évaluée avec des mesures expérimentales. L'accélération fournie par la parallélisation permet son utilisation dans la routine clinique.

L'iPDT doit être planifiée à l'aide d'un système de planification de traitement (TPS). Une preuve de concept d'un TPS dédié au traitement stéréotaxique iPDT du GBM a été développée. Ce logiciel fournit des outils de base pour planifier l'insertion stéréotaxique de diffuseurs cylindriques et calculer la dosimétrie associée. Le recalage stéréotaxique et la précision du calcul dosimétrique ont été évalués avec des méthodologies spécifiques.

Lorsque la résection est réalisable, la PDT peropératoire peut être appliquée juste après la FGR. Celle-ci profite de la présence du PS (la protoporphyrine IX) utilisé pour la FGR et qui s'est déjà concentrée dans les cellules tumorales. Ainsi, la stratégie de traitement proposée peut s'inclure facilement au standard de soin. Un dispositif médical a été conçu pour s'adapter à la cavité et éclairer de façon homogène les berges de la cavité opératoire. Le dispositif est constitué de deux parties : un trocart couplé à un ballon gonflable et un guide de fibre optique développé au sein du laboratoire ONCO-THAI permettant d'insérer la source lumineuse. Des méthodologies spécifiques ont été développées pour étalonner et évaluer l'appareil en termes de contraintes mécaniques et dosimétrique. L'étalonnage a permis la création d'une fonction de transfert permettant une prescription de durée de traitement rapide, robuste et facile. De plus, de nombreux tests ont été réalisés en amont de l'essai clinique qui évalue la sécurité de la procédure.

Mots clés : thérapie photodynamique, glioblastome, dosimétrie, simulation Monte-Carlo, calcul parallèle par processeur graphique, dispositif médical, étude clinique

Acknowledgments

I would like to express my sincere gratitude to the members of the jury for giving me the honor of reviewing my work.

I reserve special thanks to my thesis supervisor, Dr. Maximilien VERMANDEL, for his constant and unfailing scientific support, and also for his friendship.

I thank my laboratory director, Pr. Serge MORDON for giving me the opportunity to work in a fulfilling environment.

At the end of this experience, I would like my colleagues to know how much their support and enthusiasm have been dear cornerstones:
Elise, Jean-Baptiste and Laura for their precious friendship;
Anne-Sophie and Gregory for their respective considerable mathematical and computing assistance in this work in addition to their exceptional goodwill and friendship;
Bertrand, Fabienne, José, Nacim, Pascal and Wael for making each day in the laboratory living and friendly;
Isabelle and Marjorie who succeeded in the most complex files and who made this doctorate a unique experience;
All the "master's degree": Camille and Henri-Arthur for their good mood, Claire for her kindness, Dris and Mathilde and their tremendous "rats", Périne and Yohan and their weird anecdotes, Henry and Julie for their respective burst of laughter;
Among all interns, Florent and Tanguy who saved me precious time.

I would also like to thank Pr. Nicolas REYNS and all the people involved in the INDYGO clinical trial.

My gratitude is also extended to all I met during these years in all different projects.

Finally, I fully dedicate this manuscript and its essence to the person who "reminded me of what true happiness is".

This work has been funded by the Hospital of Lille and the Photobrain project.

“I want to believe so badly; in a truth beyond our own hidden and obscured from all but the most sensitive eyes.”

Fox Mulder, The X-files.

“J’ai voulu que les moments de ma vie se suivent et s’ordonnent comme ceux d’une vie qu’on se rappelle. Autant vaudrait tenter d’attraper le temps par la queue.”

La Nausée, Jean-Paul Sartre

This thesis has been prepared within the laboratory INSERM Unité 1189 OncoThAI

1, avenue Oscar Lambret

59037 LILLE Cedex

France

Contents

General introduction

1. Context

Gliomas are the most common primary brain tumors in adults. Among them, glioblastoma (GBM) has the most dismal prognosis. It represents the most frequent primary brain tumor in adults [1-3] with an annual incidence of about 3 to 5 cases for 100,000 persons [4-6]. Even if no environmental risks factor has been identified except in radiation therapies [7, 8], the population growth and aging, the diagnostic improvement and the dismal prognosis of this tumor are expected to challenge the research community to find relevant answers to this medical emergency [9].

The first-line treatment is usually surgery, either to confirm the diagnosis with a biopsy or to remove as much of the tumor as possible. Once the surgery or biopsy has been realized, adjuvant treatments, such as radio and/or chemotherapy, are administered according to the grade and the genetic profile of the tumor. Unfortunately, this standard of care has a modest result regarding the patient's survival. Thus, alternative therapies using different ways of treatment are expected to bring effective solutions to GBM treatment.

Among the recent alternatives, the photodynamic therapy (PDT) may be a promising treatment in oncology and particularly in the treatment of brain cancers, including GBM. PDT is a non-thermal energy-based therapy relying on light exposure after photosensitization of tumor cells. A PDT effect is the result of the synergy of three elements: a photosensitizing molecule, the energy delivered through laser light exposure in order to excite the molecule, and the oxygen. The combination of these three components leads to the formation of reactive oxygen species, including singlet oxygen, which are cytotoxic molecules that damage the tumor cells.

PDT was firstly used in the Antiquity to treat skin disease [10] and was reconsidered in 1972 [11]. The first clinical trial using PDT on GBM was realized in 1980 by Perria et al. [12]. The advent of this therapy is largely related to the improvement of laser systems, particularly in medicine. Currently, two clinical PDT modalities for neurosurgery are investigated. When the surgical resection cannot be achieved because of surgical constraints, the PDT is delivered interstitially. This treatment modality plans to insert optical fibers under stereotactic conditions and to vehicle light directly into the tumor. When the patient can undergo to surgery, PDT is delivered intraoperatively, i.e., early after the resection. This

lighting modality aims at illuminating the cavity created by the surgical resection in order to treat the remaining tumor tissue that cannot be removed.

Although there are few studies demonstrating proofs of concepts, this therapy is not adapted to current clinical therapeutic modalities for several issues yet. No consensus has been defined on the use of a photosensitizer and there is a lack of reliable and reproducible therapy delivery systems (medical devices and treatment planning software). All these disparities lead to the absence of randomized, controlled multicenter clinical trials on the treatment of GBM by PDT.

2. Contributions

This work has been achieved in the ONCO-ThAI laboratory (Inserm, University of Lille, Hospital of Lille), which develops therapies based on laser light, mostly in oncology. An interdisciplinary research is led in order to reach the clinic evaluation of the technologies developed in the laboratory.

The main objective of this thesis was to develop technological tools adapted to clinical routine, both software and hardware, dedicated to the treatment of GBM by PDT. Several axis of research have been investigated in which the dosimetry was the guideline: planning the PDT in both lighting modalities (interstitial and intraoperative) and designing the device to deliver the treatment.

The main contributions of this thesis can be summarized as follows:

- A GPU-accelerated Monte-Carlo method is proposed to compute the light distribution emitted from cylindrical diffusers in heterogeneous biological tissues.
- A proof of concept of a treatment planning system dedicated to stereotactic interstitial photodynamic treatment is introduced. The workflow of this software is similar to the one used in neuro-radiosurgery. It proposed to plan the stereotactic insertion of several cylindrical diffusers and compute the light propagation during the treatment procedure.
- A new medical device dedicated to intraoperative photodynamic therapy has been designed and characterized using ex vivo experimentations. Results have been compared to Monte-Carlo simulations.
- A transfer function has been created in order to easily obtain the treatment duration according to the size of the cavity to obtain a therapeutic effect at 5 mm inside margins resection.

- A clinical trial has been set up to evaluate the safety of the procedure using this medical device. This phase one clinical trial is currently under evaluation.

3. Roadmap

This dissertation is organized as follows.

Chapter I introduces laser technologies and their application in medicine including the PDT. A focus is made on the photosensitizer and the biological mechanisms involved. Then, a description of the glioblastoma, its standard of care and alternative treatments are presented. Among them, previous photodynamic treatments of GBM, including interstitial and intraoperative modalities treatment, are listed.

In order to plan PDT treatments, a dosimetry modelling is needed. Since light is one of the three major components of PDT, Chapter II details the physics interactions of light propagation in biological tissues used in the predictive dosimetry. Among all dosimetric features, models of light delivery computing are presented. Also, some monitoring methods used to evaluate the PDT dosimetry are described.

The Monte-Carlo method used to model the light propagation in tissue is still the reference model. Chapter III presents this model and techniques to reduce the computing time. Among them, a Monte-Carlo model based on acceleration by GPU parallel computing is proposed. Its implementation and the evaluation methodology are presented. Also, optimization of algorithm's performances is described.

A proof of concept of a treatment planning system dedicated to stereotactic interstitial photodynamic treatment is detailed in chapter IV. Methodologies to validate the stereotactic registration and evaluate the dosimetry part are described. Future improvements including the integration of the GPU Monte-Carlo model presented in chapter III are discussed.

Finally, Chapter V is dedicated to the intraoperative PDT treatment. The design of a new lighting applicator is described. Methodologies to characterize the device is detailed, including its dosimetry, a mechanical assessment and other safety tests. Thus, the method proposed enables to obtain the treatment duration according to the cavity size in order to obtain a therapeutic effect in resection margins. The clinical investigation of the device within the clinical trial INDYGO is described. Further improvements and future technologies to substitute this medical device are discussed.

Chapter I

Introduction and research context

This chapter presents the concept of photodynamic therapy (PDT) dedicated to the treatment of High-Grade Gliomas (HGG). An overview on laser is firstly given which includes a brief history of laser technology, the physics principles, the main technological components and its current applications in medicine. Then, photosensitizers are presented with a specific focus on the precursor, 5-aminolevulinic acid (5-ALA). Direct and indirect processes of tumor cells destruction resulting from PDT are highlighted. In the context of this study, primary brain tumors, especially glioblastoma (GBM) and their standard of care are described before a systematic review of PDT technics dedicated to treat HGG.

I. Photodynamic therapy

1. LASER: History

> "This property of elementary processes as expressed by equation (12) makes a quantum theory of radiation almost unavoidable. The weakness of the theory lies, on the one hand, in its not bringing us closer to a union with the wave theory, and, on the other hand, that it leaves the time and direction of the elementary processes to chance; in spite of this, I have full confidence in the trustworthiness of this approach." [13]

This quote comes from a paper published by Albert Einstein in 1917. In this paper, the scientist confirms his interest in the Planck's theory according to which light radiation is composed of several "quanta" (namely photons) that can be absorbed or emitted discontinuously. Furthermore, he carries on the corpuscular theory of light and its duality with the wave theory and describes for the first time the stimulated emission of radiation process [14]. Later, this physical principle will be used in the MASER technology (Microwave Amplification by Stimulated Emission of Radiation), the ancestor of the well-known LASER (Light Amplification by Stimulated Emission of Radiation) described by Gould in 1959 [15] and firstly designed by Maiman in 1960 [16, 17].

a. Physics principles

The laser is based on two main physic processes: the stimulated emission of radiation and the population inversion.

The stimulated emission of radiation occurs when a photon with a particular energy encounters an excited atom (see figure 1.1). If the energy level *hv* of the incident photon is equal to the difference between levels of the electrons E_1 and E_0, the incident photon then stimulates the electron return to the ground state E_0. This relaxation leads to the creation of a second photon bearing the same properties of the incident photon.

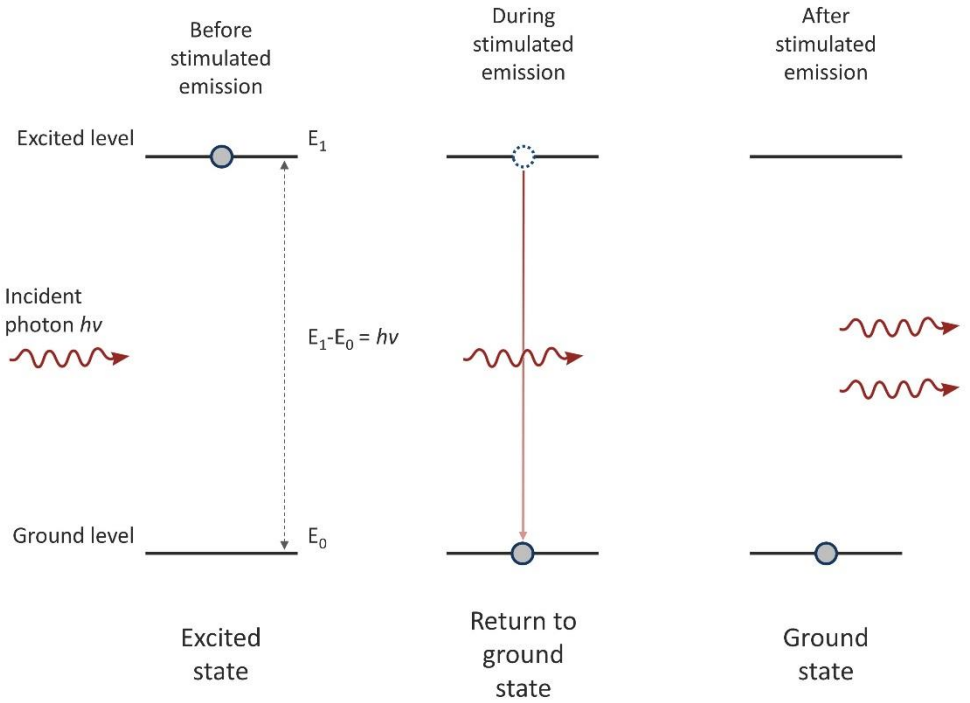

Figure 1.1: Illustration of the stimulated emission of radiation.

Regarding laser, light beam of 1J at a wavelength of 630nm requires about 3.10^{19} photons using stimulated emission process. If the two photons resulting from this stimulated emission process do not meet other excited atoms, then, they have a strong probability to be absorbed. It appears thus necessary to have a majority of excited atoms to produce a large number of photons and because atoms are mostly naturally at the ground state, another energy source is expected to excite atoms.

A second issue occurs if we consider only two states atoms constituting the irradiated media. To create enough photons from stimulated emission process, photons must have a higher probability to meet an excited atom than to meet a stable one. However, if a photon is emitted in a media composed of 50% of excited atoms at an energy level E_1 and 50% of ground state atoms E_0, statistically, only absorption and spontaneous emission processes is obtained (independently from the initial conditions of the atoms population). Thus, a third state must be considered to perform a "population inversion" (see figure 1.2). This term defines the process during which a media owns more excited atoms than natural ground state atoms. This inversion can occur only with at least a triple states system.

Let us consider a media with triple states atoms: at the Boltzmann equilibrium, there are more atoms at the ground state E_0 than excited state E_1, and there are more atoms at the excited state E_1 than excited state E_2. However, if an external source of energy E_{ext} equal to $E_2 - E_0$ is applied to this system, several E_0 atoms are promoted to the E_2 energy level. The number of E_2 atoms tends towards the same number of E_0 atoms but cannot exceed this number. Nonetheless, the population of E_2 atoms can be larger than the population of E_1 atoms. In this case, the inversion population between E_2 and E_1 is reached. An incident photon owns therefore more chances to encounter an excited atom and to provoke a stimulated emission corresponding to a relaxation of E_2 - E_1. The stimulated emission of two excited atoms by photons from a first stimulated emission induces four photons and consequently leads to a cascade of photons. If the excited atoms proportion is maintained higher than the proportion of ground state atoms and if the photons created by stimulated emission remain with a sufficient number for them to induce stimulated emission processes, a laser light is created.

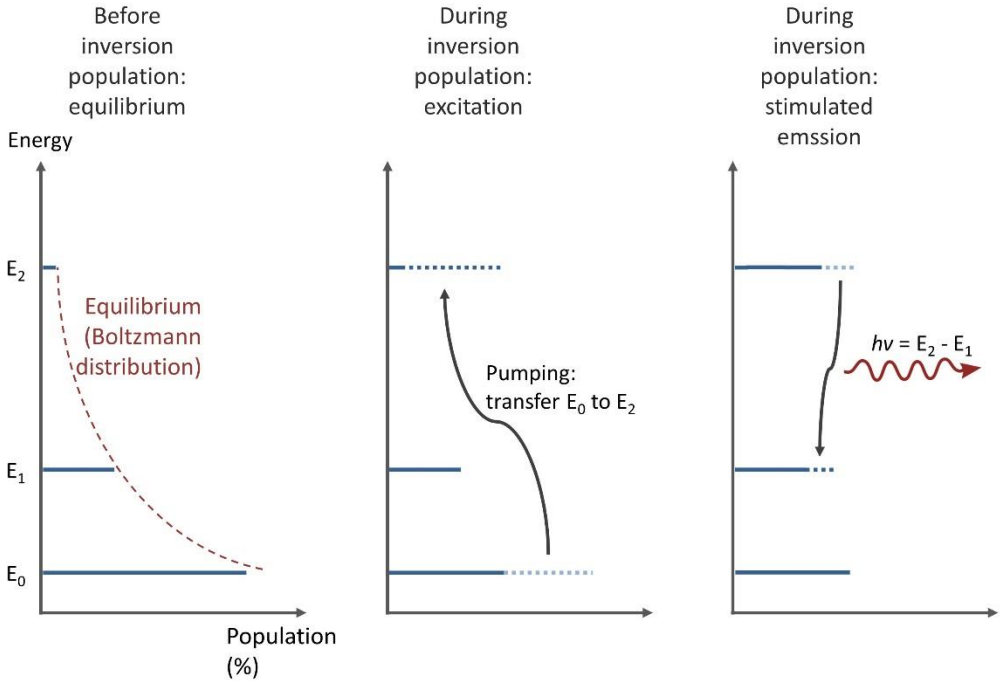

Figure 1.2: Jablonski diagram of triple state inversion population.

Mainly due to the conservation of photon's properties during the stimulated emission process, each photon composing the light beam owns the same features.

Thus, laser light is:

- Monochromatic: each photon has the same wavelength. However, due to several mechanisms of spectral emission broadening, a laser light cannot be a pure monochromatic light beam.
- Directional: the light beam produced by a laser has a very small divergence in space. This strong directionality allows to obtain a highly focal beam.
- Temporally coherent: because all photons produced by a laser are almost with the same wavelength, each photon's phase is synchronized and is the same for all of them.
- Spatially coherent: additionally, in a perpendicular plan to the light propagation, all photons have the same electromagnetic field (value and direction).

Using these particular properties, laser light has quickly found several applications in many different fields.

b. Technological setting

To produce stimulated emission and population inversion, all lasers are composed of three different parts: active gain medium, pumping and resonating cavity.

Active gain medium is the core of a laser, where the stimulated emissions happen. It is composed of atoms with determined energy levels that define the wavelength of the laser light. Changing the composition of this part can modify the wavelength of the laser light. Several active gain media are employed and allow the classification of the laser type according to the material composition:

- Solid state: crystal (ruby, Nd-YAG) and optical fiber (silicate or phosphate glasses)
- Semi-conductor material
- Liquids: dyes
- Gases (CO^2, He-Ne, argon)

Amplifier or laser pumping is dedicated to the realization of the inversion population. It transfers an external energy to the active gain medium in order to excite atoms and to produce in return stimulated emission of radiation. Several types of pumping have been developed including:

- Optical pumping using flash lamp, arc lamp or the use of an additional laser
- Electrical pumping: application of an external electric current or electron beam, glow discharge
- Other types such as thermic pumping (adiabatic cooling), chemical reaction and even using nuclear reaction products.

Resonating cavity is composed of two face-to-face mirrors and one is partially transparent. The proportion of transparency must be highly controlled. If too many photons leave the resonator, the percentage of stimulated emission decreases and tends toward zero. Furthermore, the distance between those two mirrors represents one of the main filters to obtain an output light beam with a narrow waist of the spectral emission peak. The distance is computed in order to attenuate most of non-desired wavelengths using resonance phenomenon.

c. Applications

Decades ago, laser device was highly unstable, expensive, cumbersome, with a very bad efficiency and was mostly dedicated to research applications. With the advent and the development of the semi-conductor technology, laser technology has been strongly democratized in many applications, including medicine. Nowadays, laser systems in medicine are more efficient, portable and can be highly powerful (see figure 1.3). Most of lasers currently manufactured are based on laser diode technology. Its three parts (active gain medium, pumping and resonating cavity) are contained in an electronic component of only few millimeters. Output power can easily reach several watts. Additionally, with the improvement in the electronic doping and recent semi-conductor compositions, a large range of wavelength is possible (from 405nm with Indium-Gallium-Nitride compound to 980nm with Indium-Gallium-Arsenide compound). All these improvements have led to a larger use of the laser in the medical field.

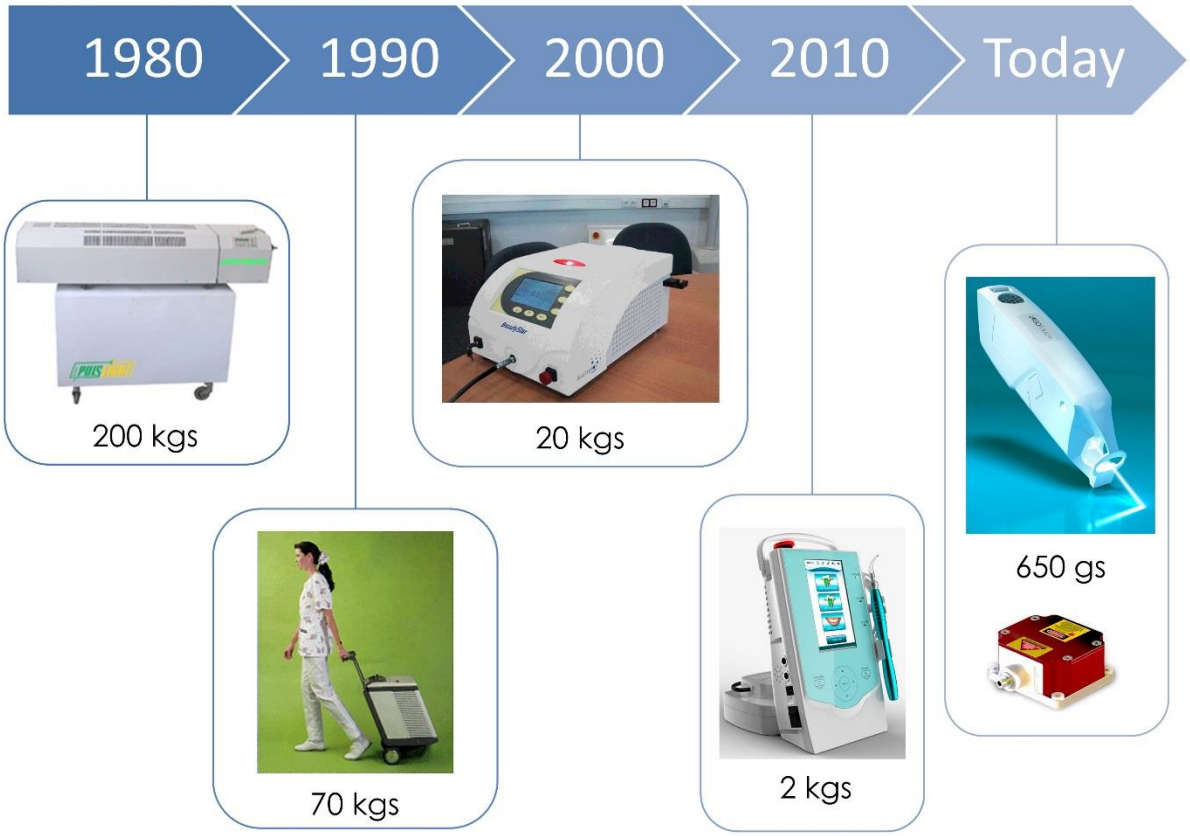

Figure 1.3: Laser evolution from 80's to current device.

2. Photosensitizer

The use of molecules for which the cytotoxic effect can be activated by laser light

emerged in medicine. Photosensitization is the process of initiating a reaction using a molecule called photosensitizer (PS) able to absorb a radiation and transfer this energy to reagents. Using this absorption property, numerous natural or synthetic molecules can be used as therapeutic agents from chemical reactions occurring after their activation by radiations.

a. Photophysical mechanism

Photodynamic activity of a PS is based on the interaction between energy delivered by the light and its absorption by the molecule (see figure 1.4). The absorption of this energy by an electron excites the PS, moving an electron to an upper level of energy. This absorption can only occur if the incident energy is exactly the same required to make this transition. Consequently, only allowed electronic transitions can be used to activate the PS. Using the Planck's relation between energy and wavelength, these electronic transitions follow a specific absorption spectrum. Each absorption peak matches with an allowed electronic transition of each atom constituting the PS. Thus, in order to excite the PS, it is required to use the correct wavelength. There are two different processes to return to the ground state: radiative and non-radiative transitions.

On each relaxation process, dissipation of energy is required. Non-radiative transitions do not involve the light radiation emission but rather a heat emission for example. Conversely, radiative transition emits a photon with an energy that corresponds to the gap between the two allowed energy levels. In the case of a radiative process, the emitted photon has a lower energy than the incident one due to vibrational relaxation and internal conversion. Two different types of relaxation lead to light emission: fluorescence or phosphorescence (depending on the initial singlet or triplet state).

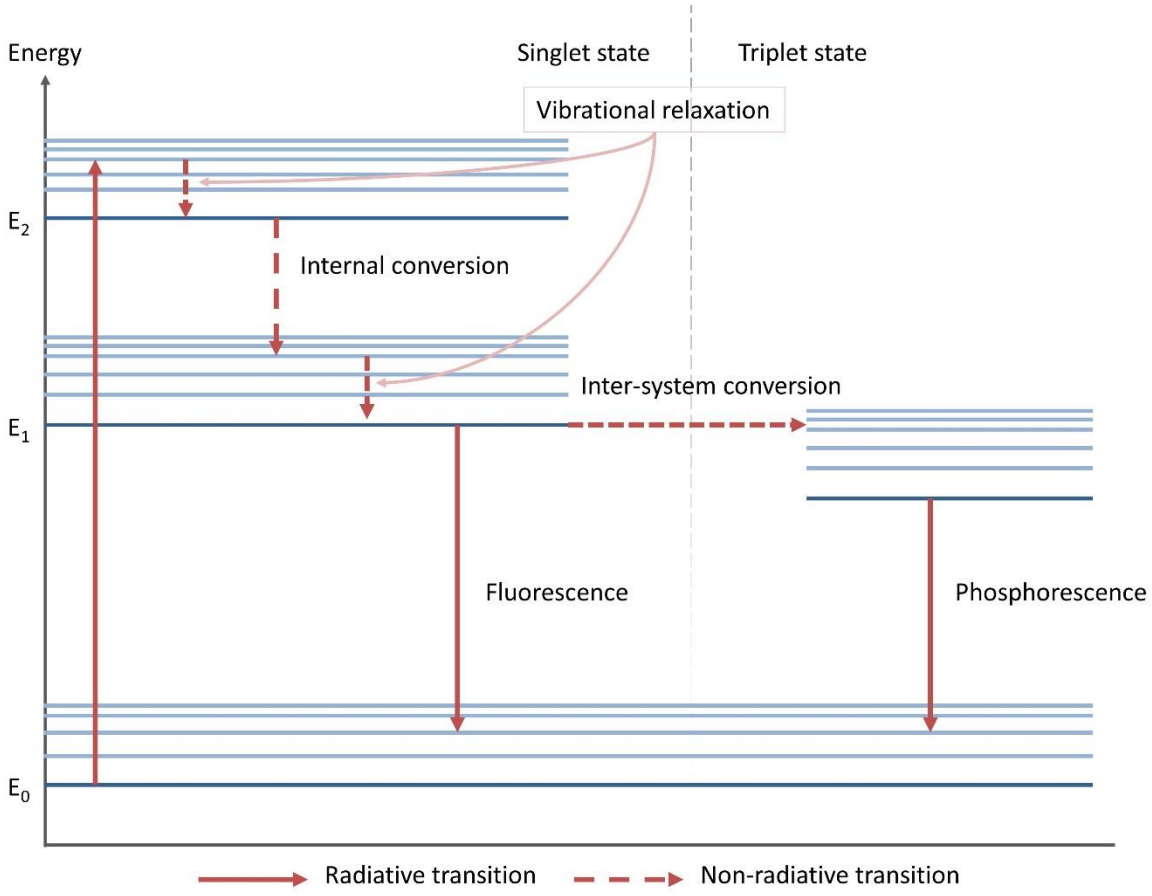

Figure 1.4: Jablonski diagram of photophysical processes.

The PS, initially at the ground and singlet state, absorbs a photon and goes straight to an excited singlet state. Using vibrational relaxation, the PS energy decreases slightly to reach the lower allowed transition of its excited state. At this stage, this singlet state can move to a triplet state. Fluorescence occurs with the singlet state relaxation, phosphorescence with the triplet one. In the case of the triplet state, photo-oxidation mechanisms produce reactive oxygen species (ROS) (such as hydrogen peroxide, hydroxyl and Superoxide radicals, singlet oxygen) and free radicals. These species lead to the degradation of several cell components and induce the cell death.

Limitation appears when ROS, which is produced by the PS activation, damages the PS. This gradual degradation of the activated PS during illumination is called photobleaching [18]. This reaction induces a reduction in PS absorption and fluorescence [19-22]. Photobleaching results from PS photodegradation, which is the modification of the molecule structure (i.e., fragmentation of the sensitizer, relocalization and photomodification without rupture of the porphyrin rings) leading to the creation of non-absorbent photoproducts [23, 24].

b. First and other PS generations

One of the first PS, called first generation PS, is mainly composed of hematoporphyrin and hematoporphyrin derivative (HpD). Photofrin®, the commercial name of the HpD, was one of the main PS used in several studies and clinical trials using photodynamic mechanisms [25-28].

An ideal PS should have at the same time a strong selectivity for tumor tissues and the ability to generate ROS efficiently. It should also have a stable composition and be easily produced. In addition, the PS spectrum absorption should display several high absorption coefficients in the red or near-infrared part in order to be activated as far as possible in biological tissues. Regarding the pharmacokinetics parameters, an ideal PS should have a favorable absorption, distribution, metabolism, excretion and the lowest post-treatment photosensitivity [29].

In the light of this description, this first generation of PS had several drawbacks such as a very poor selectivity and a very long duration of photosensitivity (about 30 days). In order to circumvent those issues, two generations of PS have been developed. The porphyrins group development (aminolevulinic acid, texaphyrin, or phthalocyanine) was the main interest of the second generation. Those molecules have good tissue selectivity and a modest absorption on the range 600-700nm that allows them to be activated until several millimeters in biological tissue. They own a fluorescence property (light emission around 450nm) and a correct ROS production. Some molecules are already commercialized such as the temoporfin, (commercial name Foscan®), verteporfin (commercial name Visudyne®) and the 5-aminolevulinic acid (5-ALA) (commercial name Gliolan®).

Although the second PS generation shows correct results and is deeply involved in many clinical trials, the third PS generation is currently under investigation mainly in order to increase the tissue selectivity. Several technics are under development to graft other molecules on second PS generation to better target tumor molecules. Nano-particles are also highly attractive to improve the PS selectivity using encapsulation process or being used as contrast agent for imaging [30-33].

c. Case of the 5-aminolevulinic acid

Because of its growing interest in oncology field using its photophysical properties, it appears essential to highlight the 5-ALA molecule. 5-ALA is a precursor drug that is converted into the actual PS, protoporphyrin IX (PpIX), by using the heme-synthesis [34] (see

figure 1.5). 5-ALA administration leads to high tumor-selective PpIX accumulation in the tumor cells and its strong ability to penetrate the blood brain barrier (BBB) also contributes to the high PpIX uptake. PpIX is a photoactive substance endogenously synthesized in the metabolic pathway for heme. In a healthy cell, the maximum rate of ALA synthesis is always lower than the maximum rate of the heme synthesis. If heme is less consumed than synthesized, the ALA synthesis is naturally inhibited. Thus, neither the intermediate products nor heme is accumulated in a normal cell. In the case of tumor cells, individual steps of the heme synthesis process are altered and might cause accumulation of various intermediate products leading to a PpIX accumulation in tumor cells only. Then, an exogenous exposure to 5-ALA leads to a strong escalation of PpIX concentration in tumors cells up to 6-8 h before saturation.

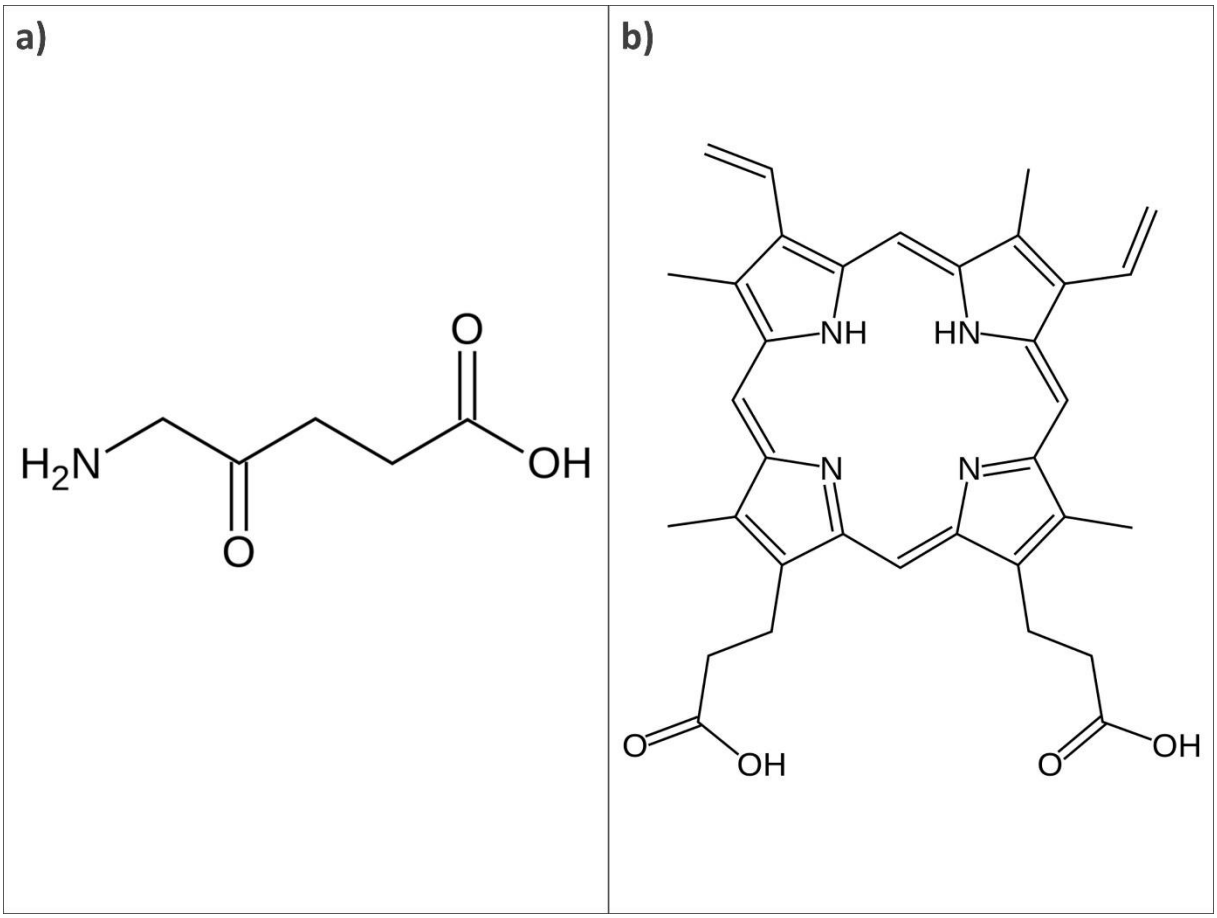

Figure 1.5: a) 5-ALA molecular structure, precursor of the photosensitize b) Protoporphyrin IX molecular structure.

As said previously, PS are molecules that use their photophysical properties to induce chemical reactions. For some decades, researchers and clinicians have tried to put this

photosensitization to good use in clinical applications and particularly in oncology.

3. Photodynamic therapy

a. History

The very first applications of a treatment using daylight (named "heliotherapy") appeared during the antiquity with Egypt, Chinese, Indian and Greek civilizations to treat skin diseases mostly [10]. However, a therapy using an exogenous substance (extern from the metabolism) reacting with photons' sun was only observed in India during the XVth century BC. Psoralen, a natural chemical compound originating from *Psoralea Corylifolia* stems that is a common plant in India, allowed a repigmentation of the skin (auto-immune disease leading to large white plate on body skin). At the beginning of the XXth century, Oscar Raab was the first to introduce a scientific consideration about the interaction between light and a molecule (a dye called "acridine") in order to obtain a medical treatment [10]. The term "photodynamic therapy" (PDT) appeared for the first time in 1907 in a book written by Van Tappeiner to describe the necessity of the presence of the oxygen to obtain a chemical reaction [35]. Following this publication, Van Tappeiner leaded the first clinical trial on three patients with skin cancer using PDT. An eosin solution had first been applied on treated areas and then been irradiated using sun light or an arc lamp during several weeks. He observed an improvement of patients' condition.

b. Definition

PDT is a non-thermal energy based therapy relying on light exposure after PS accumulation in the tumor cells. A PDT effect is the result of the synergy of three elements: a PS, the energy delivered through light exposure at a specific wavelength to excite the PS and the presence of oxygen. Combination of these three components leads to the formation of ROS, including singlet oxygen, which are cytotoxic molecules that damage the PS-targeted cells.

The sequence of a PDT treatment begins with the PS administration to the patient topically, orally or by intravenous injection. Once the PS goes through the blood circulation's patient, it spreads into the organism using several proteins according to its physical and chemical characteristics. It concentrates selectively using different processes (depending on whether the drug is a precursor or the PS itself) into the neoplastic tissues. In this way, a higher PS concentration (that can vary according to the tumor-selective PS uptake) is

observed in the tumor cell than in the healthy one.

Under irradiation, several reactions occur between PS and the oxygen inside the cell. In order to excite the PS, the light wavelength used must fit into one peak absorption of the PS. In most cases, a LASER light is applied (use of the monochromaticity property) as closely as possible to the therapeutic target. Light depth penetration depends on two factors: the wavelength and the size of the light source.

The higher wavelength, the deeper the light penetrates tissues (see figure 1.6a). A compromise must be found between a minimal light absorption by tissues and a maximal light absorption by the PS.

Light penetration depends also on the size of the light source (see figure 1.6b). The larger the light source, the deeper light penetrates tissues, independently from the wavelength. However, a limit of depth penetration is reached even if the light source continues to grow.

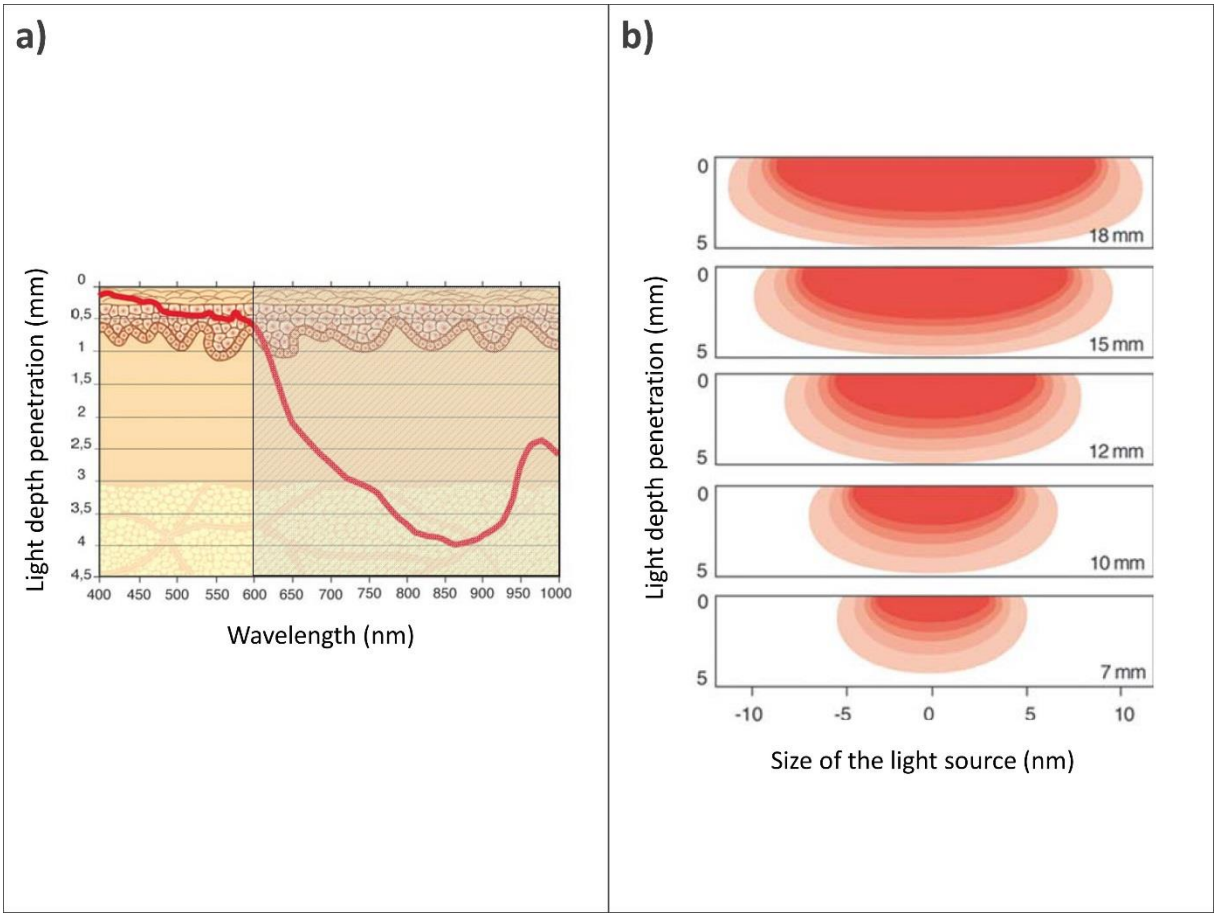

Figure 1.6: Illustration of the light depth penetration in biological tissue: a) dependency of the wavelength and b) dependency of the size of the light source (taken from [36]).

When using a PS with a poor selectivity, light must be applied only on areas to be

treated (e.g., hematoporphyrin, Photofrin® [26, 27]) and organs at risk must be defined to avoid side effects. Conversely, regarding PS with a higher selectivity (e.g the temoporfin, Foscan® or protoporphyrin IX, Gliolan® [37-40]), defining safety margins to achieve a selective treatment is not needed. Indeed, if the PS uptake is low, cells will not be killed.

Several lighting modalities are available and can vary according to the topology of the target zone (see figure 1.7):

- Optical fibers, called “frontal diffusers”, emit a lighting cone that can vary according the numerical aperture of the fiber. They are mostly used in topical illumination or interstitially but remain little used in clinic,
- Optical fibers, called “cylindrical diffusers”, allow to illuminate a larger volume than a frontal diffuser. They are used for interstitial or cavity treatments,
- Lighting devices with a shape of one or several balloons (e.g., the Freiburg flap) can be used to illuminate cavity with a more homogeneous light distribution than fibers,
- LED panels are often used in dermatology applications to illuminate large surfaces,
- Lighting fabrics are constituted by optical fibers braided or knitted. This modality allows to obtain a more homogeneous light distribution on non-plane surfaces compared to LED panels,
- The “daylight PDT” uses the light produced by the sun to bring a low power light for dermatology treatments.

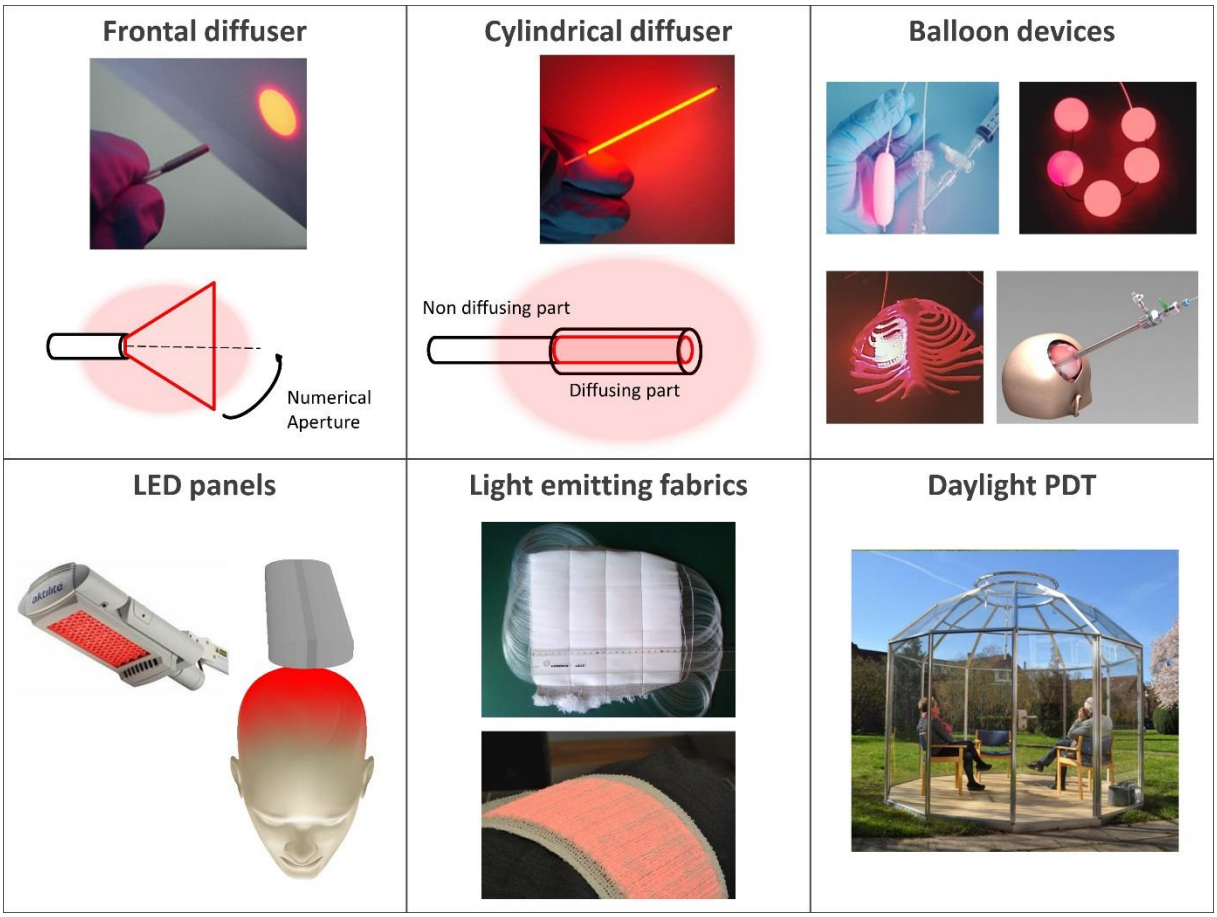

Figure 1.7: Illustration of lighting modalities available for PDT treatments (illustrations taken from [41]).

c. Direct mechanisms: apoptosis and necrosis

The tumor microenvironment can be divided into three parts:

- The tumor core is essentially composed of tumor cells
- The tumor vascularization is composed of endothelial cells
- The interstitial space is composed of stromal and immune cells

The creation of singlet oxygen, main cytotoxic product of a PDT reaction, induces tough modifications inside the intracellular media: lipids oxidation, spreading of amino acid and cross-linkage of protein components of cell membranes [42]. These modifications can impair permeability of cell's membrane, provoke a loss of fluidity and inhibit enzyme receptors on cell membrane, which leads to the cell death. Lifetime of the singlet oxygen is very short (approximately 50 nanoseconds). Its distance of diffusion is very short (approximately 20 nm), which restricts the PDT reaction inside cell's organelles only. Several organelles concentrate PS: mitochondria, lysosome, endoplasmic reticulum, Golgi apparatus and inside cell membrane [43, 44].

Two mechanisms of cell death can occur during a PDT treatment: apoptosis and necrosis (see figure 1.8).

Apoptosis defines the programmed cell death. This type of cell death occurs naturally inside the organism and allows to evacuate damaged cells. Multiplication of damaged cells could lead to the tumor creation and development. Thus, apoptosis is one of the filters that can stop the tumor emergence and progression.

Necrosis defines the non-programmed cell death. This destruction is not determined by internal cell actions but by external cell factors leading to the cell's membrane breach. Because necrosis produces a strong inflammatory response, apoptosis is generally preferred to decrease clinical complications.

d. Indirect mechanisms: Vascular and immune

Currently under investigation, other mechanisms with delayed actions appear also after a PDT treatment.

During a PDT treatment, a large proportion of oxygen inside tissues is consumed by the chemical reaction. The weak oxygen concentration can lead to an oxidative stress and provoke an ischemia of the treated tumor. To overcome this lack of oxygen supply and to continue its development, the tumor creates new vessels (neo-angiogenesis). Vascular endothelial growth factor (VEGF) are spread into the extracellular media during hypoxia, which can amplify the angiogenesis process [45]. An anti-angiogenesis treatment is often coupled to a PDT treatment to annihilate the process and to decrease the tumor recurrence risk. However, recent studies measure a decrease of VEGF secretion post-PDT on some cell lines [46-50]. These results demonstrate the significance of choosing a PS that best fits the targeted cells by PDT [42].

A growing number of studies about the long-term effect of the PDT using the activation of the immune system is observed. During the inflammatory response induced by the destruction of cells by reactive species, Damage-Associated Molecular Patterns (DAMPs) are secreted and can be recognized by Pattern Recognition Receptors (PRR). These PRR are receptors of the innate immune system. Cytokines (interleukine IL-4, IL-10 et IL-12 mainly) and chemokynes are created and differentiate immune cells to provoke an immune response to inflammation [51, 52]. Also, DAMPs activate the differentiation of T cells (CD4+ and CD8+) and B cells to initiate a response of the adaptive immune system [53]. Activation of the innate and adaptive immune system using inflammation due to reactive oxygen species (ROS) during PDT treatment might provoke a long-term destruction of the tumor and, consequently,

decreases the recurrence risk.

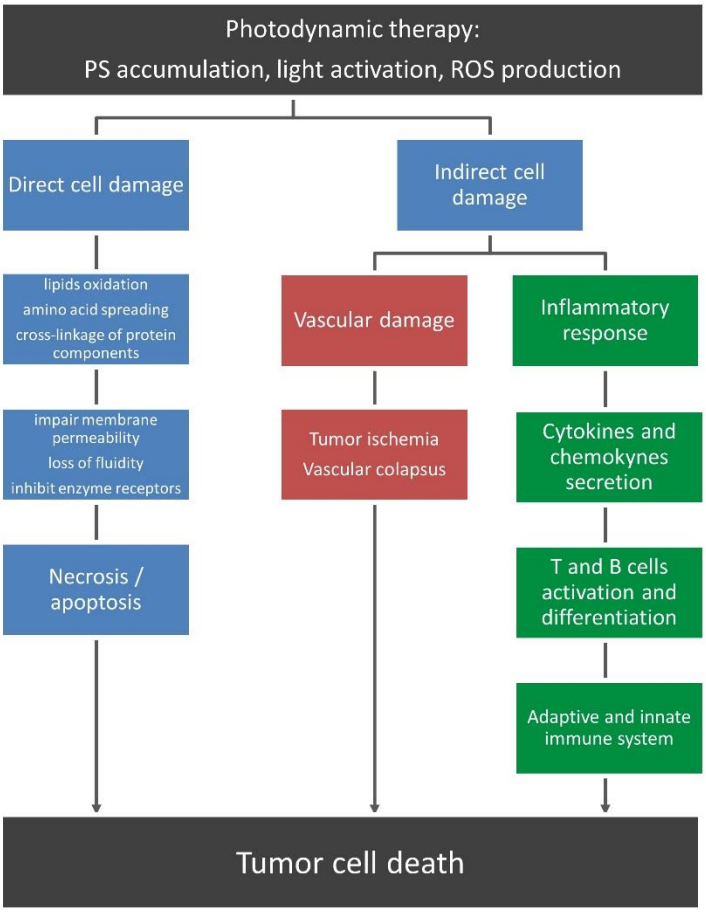

Figure 1.8: Illustration of cell death mechanism induced by PDT treatment (inspired by [54, 55]).

e. Applications

A growing number of scientific papers about PDT is observed: 443 results in 2000, 1425 results in 2015 (obtained with MEDLINE database (Medical Literature Analysis and Retrieval System Online) using the keywords “photodynamic therapy”). Applications are currently under investigation in the following fields:

- Oncology: head and neck cancer, pulmonology, urology, neurosurgery, gastroenterology, dermatology, gynecology [56]
- Antimicrobial agent: ulcer treatment, sinusitis, acne and skin burn.
- Ophthalmology: retinoblastoma treatment

II. Glioblastoma

Gliomas are the most common primary brain tumors in adults. They are malignant tumors based on histologic similarity to mature glial cells, including astrocytes and

oligodendrocytes or a mix of both cell types. According to the latest World Health Organization (WHO) classification [57], they are categorized from Grade I to grade IV depending on their malignancy (see figure 1.9). Low-grade gliomas (LGG) include pylocytic astrocytoma (WHO grade I) and astrocytoma, oligodendroglioma (WHO Grade II). High-grade gliomas (HGG) include anaplastic astrocytoma (WHO grade III), anaplastic oligodendroglioma (WHO grade III), and Glioblastoma (GBM, WHO Grade IV).

Grade I	Pilocytic astrocytoma Subependymal giant cell astrocytoma Angiocentric glioma
Grade II	Diffuse astrocytoma, IDH-mutant Oligodendroglioma, IDH-mutant and 1p/19q-codeleted Choroid glioma of third ventricle
Grade III	Anaplastic astrocytoma IDH-mutant Anaplastic oligodendroglioma, IDH-mutant and 1p/19q-codeleted Anaplastic pleomorphic xanthoastrocytoma Anaplastic ependymoma Choroid plexus carcinoma Anaplastic ganglioglioma Anaplastic meningioma
Grade IV	Glioblastoma, IDH-wildtype Glioblastoma, IDH-mutant Diffuse midline glioma, IDH-mutant and 1p/19q-codeleted Embryonal tumors
Addition of 3 new subtypes of tumors to the WHO 2016 classification	IDH mutated, 1p19q-codeleted (best response to treatment) IDH mutated, 1p19q-retained (intermediate response to treatment) No IDH mutation (worst response to treatment)

Figure 1.9: Gliomas classification according to the world health organization.

1. Description and latest classification

Among them, GBM have the most dismal prognosis. GBM is a malignant astrocytic tumor with the most common glioma histology. It represents the most frequent primary brain tumor in adults [1-3] with an annual incidence of about 3 to 5 cases for 100,000 persons [4-6]. Prevalence is estimated at about 3 cases for 100,000 persons each year [58-62]. Although it may occur at any age, 70% of patients are between 45 and 70 years of age [63]. GBM appears usually in the brain hemispheres, but can be found anywhere in the central nervous system. The disease often grows rapidly (over 2 to 3 months), except when the glioblastoma develops within a pre-existing low-grade astrocytoma (secondary glioblastoma). Approximately 90%

of GBM are primary tumors [64]. GBM is characterized by its diffuse property and its strong inter and intra-tissue heterogeneity. Regarding the etiology of the disease, no factor has been reported, except the exposition to ionizing radiations in the context of brain tumor radiotherapy [2, 65].

Prognosis is poor, especially in the absence of gross total resection, in elderly patients and in case of severe neurological impairments. Lacroix et al. published in 2001 [66] a study including 416 patients with GBM. A 53 ± 14 years mean age was reported, whom 63% of male and 37% female patients. Currently, median survival varied between 14 to 15 months according the extent of tumor resection percentage [4, 67-69].

a. Tumor development

The diagnosis is most often achieved with an MRI imaging following the manifestation of patient's symptoms. A strong contrast is often observed: a necrotic core surrounded by a hyper-intense signal showing the edema and tumor infiltration [70]. GBM distinction from the other grade III gliomas is realized using the histologic profile. Criteria include hypercellularity, nuclear atypia, and mitotic activity [71]. Furthermore, diagnosis requires either microvascular proliferation and/or tumor necrosis. However, many aspects of these histologic features remain poorly correlated with GBM genetic markers. Main primary brain tumor markers are the loss of 10q chromosome, amplification of the gene coding for the EFGR gene and the inactivation of the CDKN2A/P16 gene. However, a mutation on the IDH (Isocitrate DeHydrogenase) gene is observed on secondary GBM. In addition, among IDH wild type high-grade, the key molecular chromosomal changes are shared between histologic grade III (anaplastic astrocytoma) and GBM (histologic grade IV) tumors.

Histopathologically, several patterns exist, including giant cell GBM, small cell GBM, and gliosarcoma. Gliosarcoma cell can be observed at initial diagnosis or at recurrence, and appears to have some similar genetic aberrations as GBM. The term "GBM with oligodendroglioma component" (GBM-O) is sometimes specified where the tumor appears regionally similar to anaplastic oligodendroglioma. These tumors are easily distinguished from GBM by the presence or absence of 1p/19q co-deletion. GBM-O is distinguished from anaplastic oligodendroglioma by the absence of 1p/19q deletion, and the presence of IDH mutation and 1p/19q deletion effectively defines anaplastic oligodendroglioma and is therefore incompatible with the diagnosis of GBM-O.

b. Standard of care

The first-line treatment is usually surgery (advised by the European Society for Medical Oncology (ESMO) [72]), either to confirm the diagnosis with a biopsy (in order to assess the grade of the glioma) or to remove as much as possible of the tumor (see figure 1.10). Resection plays a crucial role in the improvement of patient's survival. Currently, aggressive resection is encouraged to realize a maximal extent of resection (EOR) using intraoperative neuro-navigation tools. This technic enables to preserve organs at risk and functional areas to provide the patient a better quality of life. A resection surgery considered as "complete" can improve the progression free survival (PFS) of about 3 to 5 months [66, 73, 74].

Increase of the EOR and prolonging of the progression-free survival (PFS) have been observed when resection is carried under blue light after administration of 5-ALA (Fluorescence Guided Resection, FGR). A PFS improvement of about 2 months was observed using FGR. Because PpIX is a highly selective photosensitizer, the PS emits a fluorescence light (635 nm) if the resection cavity is exposed to blue light (375 - 440 nm) [75, 76]. This light emission helps the surgeon detecting remaining tumor tissue at surface of the resection cavity and therefore, to improve the EOR. Unfortunately, improvement of overall survival cannot be currently statistically proved although there is a trend toward increase of survival [77].

Once the surgery or biopsy realized, adjuvant treatments are administered according to the grade and the genetic profile of the tumor with different treatment options (figure 1.10):

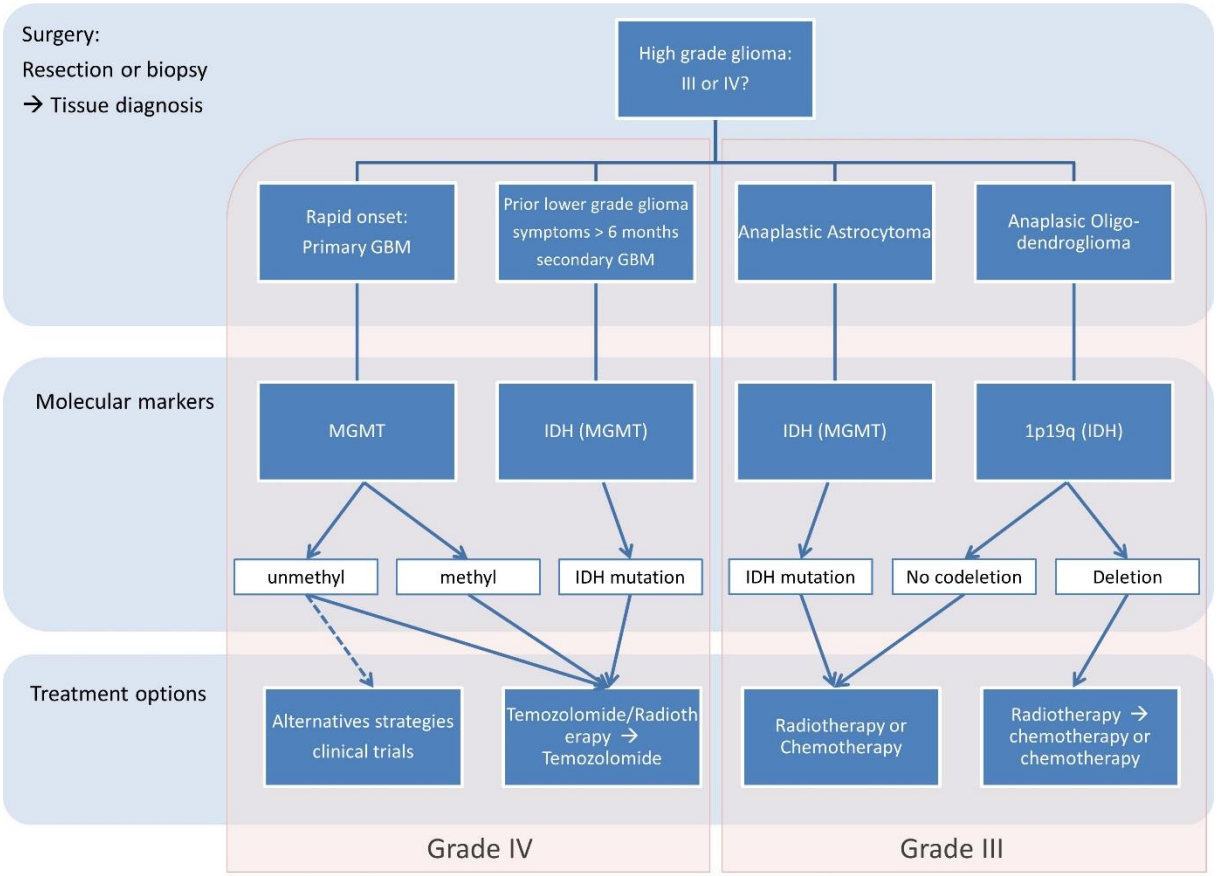

Figure 1.10: Decision algorithm of the HGG treatment plan.

The loss of heterozygosity of the 1p19q gene [78, 79], IDH mutation and methylguanine methyltransferase (MGMT) methylation enzyme (enzyme used in DNA reparation process) are the three major keys points occurring into the decision algorithm of adjuvant treatments.

In terms of survival, the benefits from adjuvant treatments after resection surgery are significant, although they remain modest. Because tumor cells infiltrate the whole brain, a full resection cannot be performed. Radiotherapy combined with chemotherapy help to complete the treatment.

In case of relapse, the WHO does not establish a standard of care. Generally, a second-line of chemotherapy or surgery is achieved.

c. Limits of the standard treatment and alternative treatments

Although standard treatment for patients with GBM, that includes surgical resection, radio and chemotherapy, allows to improve the patient's survival, patients cannot be cured of their disease. These modest results are in part due to the cellular composition and more

particularly, to the presence of self-renewing, tumorigenic stem cells that contribute to tumor initiation and recurrence [80, 81]. Furthermore, conventional chemotherapies fail to bring an effective response to GBM treatment due to a poor BBB penetration. In this context, several alternative therapies appear using different treatment ways [82]:

- Immunotherapy: this recent treatment modality is based on the immune system activation. In GBM treatment context, checkpoint molecules and monoclonal antibodies are targeted. Checkpoint molecules inhibition is aimed at enhancing immune activation. Monoclonal antibodies target tumor-specific antigens to cause tumor cell death [83, 84].
- Epigenetic: this therapy affects the genes expression. In GBM treatment context, Histone deacetylase (HDAC) inhibitors appear as a promising way to stop tumorigenesis [85]. HDAC expression is related directly to the patient's survival. HDAC inhibition can provoke both direct effects (apoptosis, enhanced ROS production) and indirect effects (angiogenesis, metastasis and glucose utilization inhibition).
- HIFU: the therapy named High-Intensity Focused Ultrasound is mostly combined with chemotherapy for the GBM treatment. This therapy is based on the emission of multiple ultrasound (approximately 1 Mhz) beams focused on the same spot in order to create a thermal and/or a mechanical effect [83, 86-89]. The main goal of this approach is to disrupt the BBB to allow drug used in chemotherapies to penetrate into tumor tissues.
- Proton therapy: currently, conventional radiotherapies do not deposit a precise enough dose, as brain tumors treatment requires. However, proton therapy brings a successful way to obtain a high dose in a very selective volume and to reduce radio-toxicities [90]. However, like photon radiotherapy, proton therapy can target only the visible part of the tumor with a small margin of macroscopic healthy brain tumor.

III. PDT treatment of HGG

1. History

To our knowledge, PDT to treat brain tumors was first studied in 1972 [11]. From the observation of Haematoporphyrin concentration in neoplasm tissues, the authors grafted 20 rats with GBM cells. Tumor-selective PS uptake along with the death of tumor cells after light

exposure was observed. However, the authors failed to obtain total tumor destruction. They emitted the hypothesis that the inhomogeneous PS or the light distribution could lead to this incomplete treatment.

In 1980, the first clinical trial using intraoperative PDT to treat HGG was realized by Perria et al. [12]. Nine patients were treated using a He-Ne laser (632.8 nm) to illuminate the resection cavity with hematoporphyrin derivative (HpD) PS. Each patient received a fluence of 9 J/cm² with an injection between 2.5 to 10.0 mg/kg of HpD. No adjuvant treatments (radio or chemotherapy) were delivered to the patients. However, survival remains very weak: between 6 to 44 weeks.

One year later, in 1981, a report on the first phase I clinical trial using interstitial PDT treatment was published by Laws et al.. Five patients were treated with 5 mg/kg of HpD and were protected from direct or indirect sunlight during at least 2 weeks [91]. A single optical fiber (400µm diameter with a numerical aperture of 0.35) was inserted at the center of the tumor using stereotactic localization. The argon-pumped laser provided red light (630 nm) with a power of 300 to 400mW delivered at the end of the fiber. Authors administered a 300mW red light during 45 minutes. Three grade III and two grade IV were treated. The authors concluded that a CT-guided needles insertion might be interesting during treatment planning to insert multiple fibers in order to reach an optimal tumor exposure to laser light. Reaction to PDT could be observed in CT post-treatment.

2. Interstitial PDT

When the surgical resection cannot be achieved because of surgical constraints (e.g., functional area, relapse), PDT delivered interstitially is investigated (approximately 15% of all cases [92-94]). This modality plans to insert optical fibers under stereotactic conditions and to vehicle light directly into the tumor (see figure 1.11a).

a. Instrumentation

In most studies, optical fibers are used to deliver laser light through brain tissues. Two types of medical devices are used: frontal and cylindrical diffusers as mentioned before (see figure 1.7). They are mainly made with silica core (0.4 to 0.6mm diameter) surrounded by a plastic casing. Frontal diffusers (or bare-end fibers) are characterized by their numerical aperture, which can vary from 0.2 to 0.4. This feature defines the size of the cone beam: the higher the numerical aperture, the higher the angle of the cone is. This type of diffuser is

mostly used in dermatology [95], urology [96], gastroenterology [97], pre-clinical trials on small animals [98] or in optical measurements [99]. Cylindrical diffusers produce an ellipsoid illumination around the extremity composed of a diffusing tip. Currently, this type of diffuser is more used in clinical applications because it maximizes the irradiated volume during the procedure and thus, minimizes both the number of fiber to insert and the treatment time [100].

With technological improvements (imaging and computing performance), a few treatment planning systems (TPS) have been developed in PDT field: pleural application [101], urology [102-104]. Some more advanced or commercial applications are available such as iDOSE developed by Spectracure [105]. It provides an optimization of the fiber position into the body's patient, generated from a 3D tissues model using ultrasound imaging. A second example is the TPS provided with the technical solution named Tookad developed to plan an interstitial PDT treatment of prostate cancer [106].

Improvement of accuracy of surgical gesture in neurosurgery is mainly due to the apparition of the stereotactic surgery method [107]. In 1908, Horsley and Clarke published a paper describing the first apparatus dedicated to a monkey head and allowing to localize a point in a 3D Cartesian coordinate system. The first trial of stereotactic devices on humans was realized by Speigel et al. in 1947 [108]. In 1951, Lars Leksell described an apparatus set-up on the patient's head, defining a 3D polar coordinate system much easier to use during surgical procedure [109]. At the same period, Jean Talairach and Pierre Tournoux developed also a stereotaxic frame [110, 111] to create a brain atlas [112]. Since their respective commercialization, several other systems have been proposed to improve the technic and adapt it to the advent of imaging system (CT and MRI). This tool could be a real advantage in interstitial PDT treatment for both planning step and surgical gesture and, furthermore, for computer-assisted which is on the rise. Robot-assisted stereotactic neurosurgery is an technology allowing high accuracy treatment on laser interstitial thermal therapy, responsive neuro-stimulation or stereo electroencephalography [113, 114]. Replacing conventional tools (e.g., electrodes, needles) by optical fibers, an accurate interstitial PDT treatment could be delivered by such robot-aided system.

b. Clinical trials

The following table represents the major clinical trials of interstitial PDT treatment of GBM.

Authors	Patients	Photosensitizer and posology	Follow up status	Illumination features
Laws et al.[91], 1981	5 patients including 2 GBM	hematoporphyrin derivative, 5 mg/kg 48-72hours prior surgery	One GBM and one grade III died	One frontal diffuser, 400µm, NA: 0.35 coupled with argon laser (630nm), 300mW during 45 minutes
Powers et al. [115], 1991	7 patients including 2 grade IV	2 mg/kg of Photofrin 24 hours prior to surgery	Recurrence at 2 and 27 weeks for GBM, and 6 and 8 weeks with 2 stable patients	One 5-25mm cylindrical diffusor for each patient, the light dose was about 1000J
Krishnamurthy et al. [116], 2000	18 gliomas including 12 GBM	2 mg/kg of Photofrin 24 hours prior to surgery	Enhancement of median survival of 116.5 days for GBM, 493 days for AA	Interstitial PDT (25 mm cylindrical diffuser, 6 insertions max) with three goups of different light dose : 1500J-3700J / 3700J-4400J / 4400J-5900J
Beck et al. [117, 118], 2007	10 patients	20 mg/kg body weight of 5-ALA	Median survival was 15 months	Insertion of 4-6 cylindrical diffuser per patient, Mean fluence was 4320-11520 J.
Johansson et al. [19], 2013	5 GBM	20 or 30 mg/kg body weight of 5-ALA	No progression at 29, 30 and 36 months, death at 3 and 9 months	Insertion of 4-6 cylindrical diffuser per patient

Table 1.1: Major clinical trials of interstitial PDT treatment of GBM.

3. Intraoperative PDT

Intraoperative PDT treatment has been the first PDT modality used to treat brain tumors (see figure 1.11b). This lighting modality aims at illuminating the cavity created by the surgical resection in order to treat the remaining tumor tissue that cannot be removed. It also aims at treating the healthy brain invaded by infiltrating tumor cells inevitably.

a. Instrumentation

The first clinical trial of brain tumors using PDT achieved by Perria et al. in 1980 had been performed during the surgical procedure [12]. A He-Ne Laser (632.8 nm) was used to illuminate the cavity. After a second intraoperative PDT trial conducted by McCulloch et al.

in 1984 [119], Muller and Wilson developed the first medical device dedicated to the intraoperative PDT [120] one year later. They designed an inflatable balloon to replace the volume of the removed tumor tissue after the surgical resection. This balloon was composed of a glove middle finger and a stainless steel tube. The balloon was then filled with a diffusing solution (lipid emulsion (Abbott Laboratories Ltd, Chicago, IL, USA) concentrated at 0.1%) in order to obtain the most homogeneous light distribution around the balloon. The device could dilate from a diameter of 3 to 5 cm. A frontal diffuser, with a nominal numerical aperture of 0.4 coupled to a 7.5 W argon laser, was inserted in the tube and the balloon. Since this rudimentary irradiator, several improvements were realized in order to provide a more straightforward and safer device. In 2000, Dwyer et al. proposed a laboratory-made balloon and a flexible nylon tube to handle the device during the surgery and carry the frontal diffuser [121]. In 2007, Moseley et al. published the latest paper dedicated to the development of a balloon device for intraoperative PDT brain tumors treatment [122].

Some clinical trials used a single optical fiber placed at the center of the cavity. Differences appear between frontal diffuser, cylindrical diffuser and spherical diffuser. In many cases, the resection cavity is filled with diffusing solution.

Another type of irradiator was proposed by Schmidt et al. in 1996 using properties of LED [123]. An inflatable balloon-shape device was designed to fit into the resection cavity to deliver light provided by a light source composed of 144 LED chips. These chips were arranged as a cylinder and placed at the center of the balloon. Three inputs were created in the tube fixed to the balloon: firstly to provide electricity for the LED tip, secondly to fill the balloon with diffusing liquid and thirdly, to cool the LED tips using sterile water. A total light power of 1.0W was measured with a peak emission at 677nm and with a wide bandwidth of about 20 – 25nm. This device was evaluated in clinical trial and compared to laser beam.

Recently, Akimoto et al. proposed a diode laser combined to the microscope from the operating room to enable surgeons to determine accurately target area during the surgery [124]. Once the target identified, the laser diode produces a $1cm^2$ beam at a wavelength of 664 nm and 150 mW power and an irradiation time of 180 seconds.

b. Clinical trials

The following table displays the major clinical trials of intraoperative PDT treatment of GBM.

Authors	Patients	Photosensitizer and posology	Follow up status	Illumination features
Perria et al.[12], 1980	9 patients	hematoporphyrin derivative, 2.5-10.0 mg/kg	Survival between 6 to 44 weeks	He-Ne laser (632.8 nm)
Kaye et al.[125], 1987	22 patients including 15 primary and 7 recurrent	hematoporphyrin derivative, 5 mg/kg 24hours prior surgery	Two recurrences at 2 and 13 months for primary GMB, 4 deaths for recurrent GBM	One frontal diffuser placed in resection cavity, mean illumination time was about 60 minutes with a fluence of 145 J/cm² at 630nm
Perria et al. [126], 1988	8 patients including 2GBM	hematoporphyrin derivative, 5 mg/kg 24hours prior surgery	6 deaths (30days, 3.5, 6, 6, 6, 13 months)	One frontal diffuser placed in resection cavity, illumination time varied between 33 to 225 minutes with a light dose of 2400J at 630nm
Kostron et al. [127], 1996	39 GBM including 25 first recurrences	hematoporphyrin derivative, 2.5 mg/kg 24-48 hours prior surgery	Median time of recurrence was 13 months, median survival was 10 months For primary GBM, median survival of 19 months	A spherical diffuser was placed in the cavity filled with Intralipid, the fluence was 15-260J/cm²
Rosental et al. [128], 2003	29 patients including 16 GBM (7 primary and 9 recurrent)	boronated porphyrin, 0.25 – 8 mg/kg 24h prior surgery	Median overall survival of 5 months for de novo GBM and 11 months for recurrent GBM	One optical fiber placed inside the resection cavity, the light dose was between 25 to 100J/cm² at 630nm
Schmidt et al. [129], 2004	20 patients including 4 GBM	Photofrin, 0.75-2 mg/kg 18-24 hours prior to surgery Compared to 0.25mg.kg of Benzoporphyrin derivative	15.8 months of PFS	Comparison between balloor or single 15mm cylindrical diffuser versus balloon composed of 144 LED chips, the light dose was 1 800J for both device used
Stylli et al. [130], 2005	145 gliomas (30 AA primary, 29 AA recurrent,	Haemetaporphyrin derivative (HpD), 5 mg/kg 24 hours prior to surgery	Median survival of 76.5 months for AA, 14.3	Intralipid in cavity and optical fiber, a total light dose of 240 J/cm² was

	31 GBM primary, 55 GBM recurrent)		for GBM	administered to most patients
Muller et al. [131], 2006	112 gliomas (including 49 GBM)	Photofrin, 2 mg/kg 12-36 hours prior to surgery	Median survival of 30 weeks for GBM, 67 weeks for non-GBM	Balloon device, the light dose was 58 ± 17 J/cm²
Kostron et al. [38], 2006	26 GBM	0.15 mg/kg body weight of FOSCAN®	Median survival of 8.5 months	Balloon device or interstitial 20 mm cylindrical diffuser, The light dose was 20 J/cm²
Eljamel et al. [132], 2007	13 GBM treated by PDT, 14 without	Photofrin (2 mg/kg body weight) ,48h prior to surgery and 5-ALA (20 mg/kg body weight) 3h prior anesthesia	Mean survival of 52.8 weeks with PDT, 24.2 weeks without PDT	Repetitive PDT (balloon catheter) inflated with 0.8% Intralipid solution), a dose of 100 J/cm², five PDT treatments were given on subsequent days
Akimoto et al. [124, 133], 2013	13 GBM	Talaporfin sodium, 40 mg/m² prior to surgery	24.8 months of median survival	Diode Laser coupled to the operating microscope, 27J/cm²

Table 1.2: Major clinical trials of intraoperative PDT treatment of GBM.

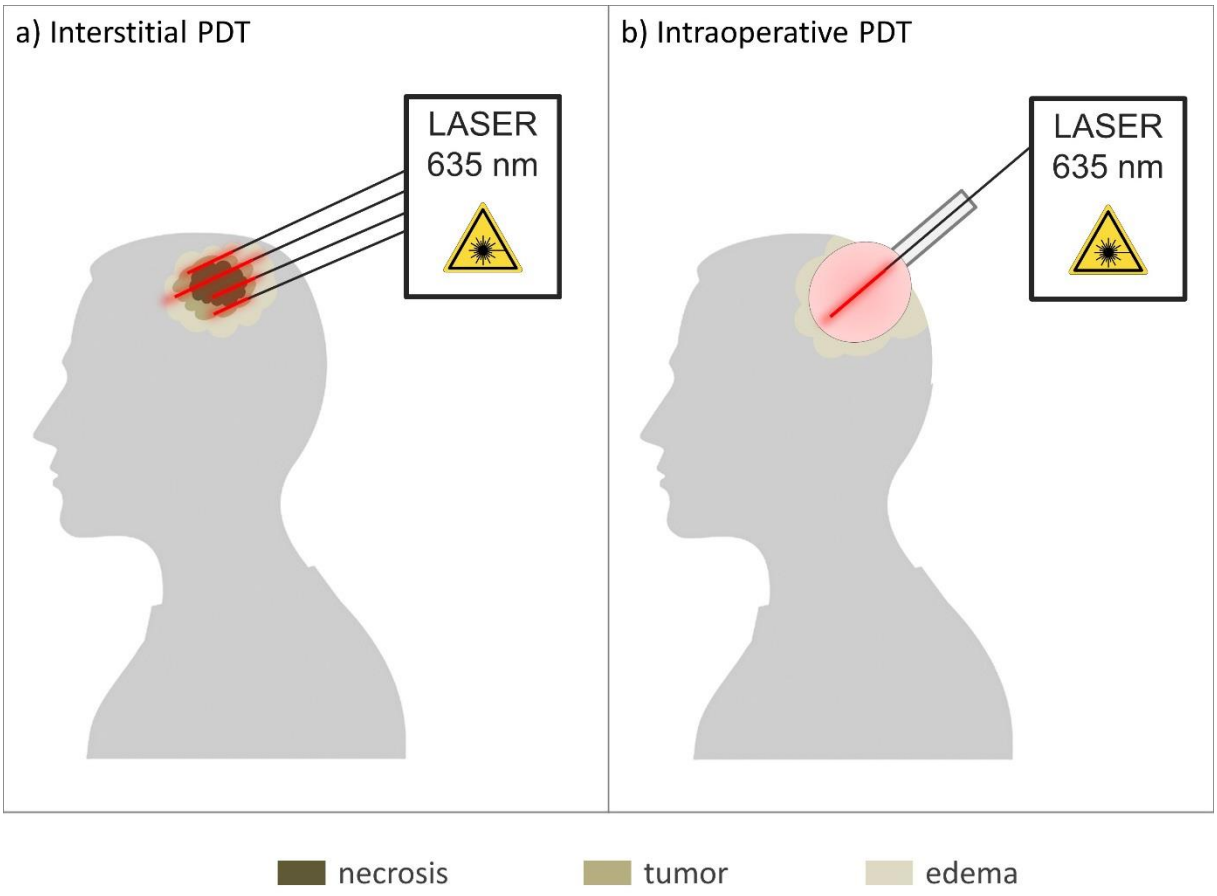

Figure 1.11 : The two main clinical PDT modalities for neurosurgery a) Interstitial PDT: optical fibers are inserted through the skull into the tumor core that contains heterogeneous tissues (necrosis, tumor, and edema). b) Intraoperative PDT: a balloon device is inserted into brain patient to treat borders of the resection cavity.

Chapter conclusion

With the improvement and miniaturization of LASER device, the use of this technology increases in the medical field whether it is in esthetic surgery, ophthalmology, dermatology than cancerology.

Despite strong efforts accomplished to improve GBM care, most of studies revealed that the current standard of care does not bring an effective solution for the recovery of the patient. Moreover, adjuvant treatments such as radio and chemotherapy have a modest impact on the extension of the PFS and even more on the overall survival.

Among recent therapies, the use of LASER with the PDT has shown an interest and significance for the management of GBM, even when the surgical resection cannot be achieved. Several studies have already been publishing with encouraging results. However,

PDT has not been adapted to clinical routine for several issues yet. No consensus has been defined on the use of a photosensitizer dedicated to GBM treatment. A lack of reliable and reproducible therapy schemes regarding the clinical devices, light delivery systems and TPSs is also observed between clinical studies. All of these disparities cause an absence of randomized and controlled multicentre clinical trials on the GBM 5-ALA PDT treatment. Thus, the main objective of this thesis work is to provide common tools (software and light delivery systems) for PDT in the GBM management.

Chapter II

Photodynamic therapy dosimetry

Predictive dosimetry models the three major features PDT components (light propagation, photosensitizer distribution and oxygen concentration) in order to plan the PDT treatment delivery. The monitoring of PDT treatment aims to evaluate the preoperative planning and if necessary, to optimize intraoperatively the PDT treatment.

To obtain a relevant dosimetry, a comprehensive understanding of light interaction within biological media is essential. Thus, physics interactions between light and matter are presented from microscopic to macroscopic scale. Since several models have been developed to compute these dosimetric parameters, a state of the art with a focus on light propagation computing through biological media is introduced. Additionally, with improvement of measuring systems, monitoring markers used in PDT monitoring are shortly described.

I. Light and matter

In this first part, only the particle theory of the wave-particle duality is considered to describe processes occurring during photons history. Throughout this manuscript, “light” and “photon” refer to theories applied in the range of non-ionizing radiations energies.

1. Optical properties

From a simplified point of view, light constituted of photons may be subjected to two

interactions during its history: it can be absorbed or not. When not absorbed, the photon may be deviated from its initial direction and takes another direction, and even turns back toward its birthplace.

Several parameters describe and quantify the interactions of photons within matter. They define matter properties and how they perturb the photon propagation. It appears necessary to define them for the future developments in this thesis.

a. Absorption

The first parameter is the absorption coefficient (μ_a) [m^{-1}] of a given media. Let us consider the molecules, called chromophores, composing this media. A surface called effective cross-section σ_a [m^2], contained into these chromophores, absorbs light (see figure 2.1). The volume density of the medium containing the chromophores is ρ_a [m^{-3}] (i.e number of chromophores per volume of media). The absorption coefficient is thus defined by:

$$\mu_a = \rho_a . \sigma_a \tag{2.1}$$

Furthermore, the probability $P_{survival}$ of photon's survival after crossing a length L [m] within the media is:

$$P_{survival} = e^{-\mu_a . L} \tag{2.2}$$

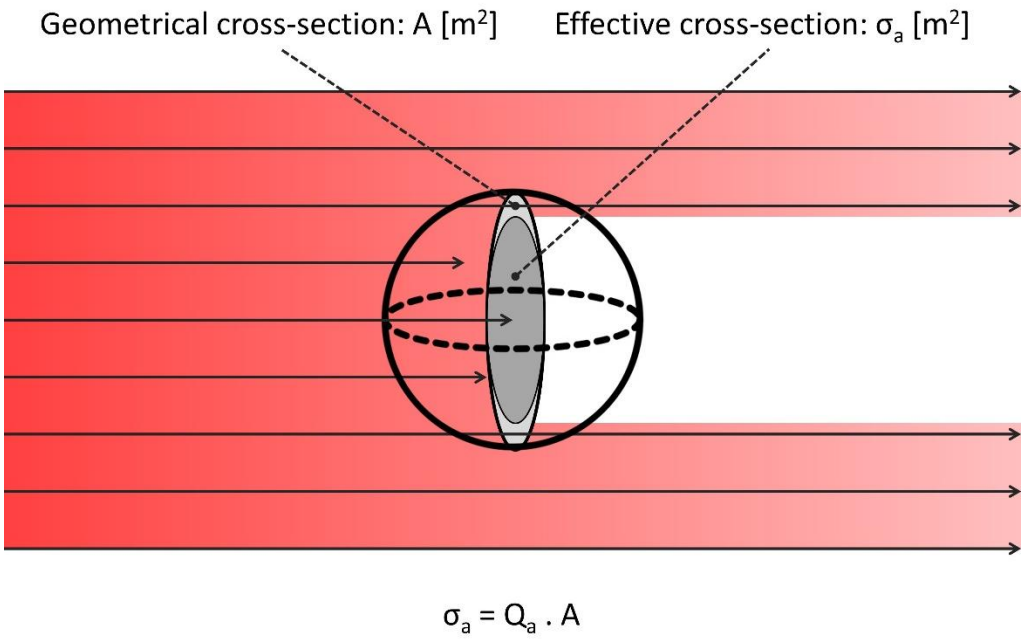

Figure 2.1: Light absorption process by a chromophore of a geometrical cross-section *A* [m^2] and an effective cross-section σ_a [m^2] linked by the absorption efficiency *Qa* [dimensionless].

b. Scattering

Light may be absorbed or deviated from its initial direction. The coefficient describing this phenomenon is named scattering coefficient. This phenomenon results from the interaction of a photon with an obstacle on its pathway. Mostly, the photon wavelength is not affected during this process. The term “elastic” is employed to describe this collision during which the total kinetic energy of the system photon – collided particle is conserved. This system can be considered as a harmonic oscillator model, i.e., two masses tied by a spring (see figure 2.2).

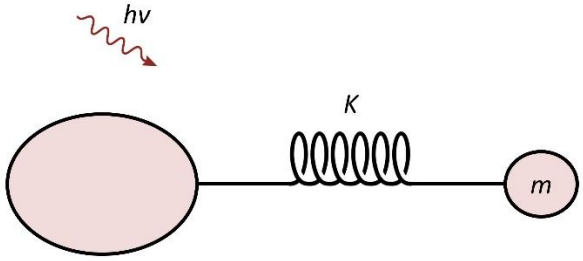

$$f_{resonance} = \frac{1}{2\pi} \cdot \sqrt{\frac{k}{m}}$$

Figure 2.2: Harmonic oscillator modeling the scattering process.

When the incident photon wavelength matches exactly with the resonant frequency of the harmonic oscillator system $f_{resonance}$, the entire energy of the incident photon is absorbed by the system. Also, if the incident photon wavelength does not match exactly with the resonant frequency of the harmonic oscillator system, the system enters in a forced oscillation leading to a very poor energy transfer. Nevertheless, an oscillating system reacts as an antenna and radiates its energy outward. Consequently, the incident photon can provoke oscillation of the mass-spring system, which remits energy in a different direction from the incident direction; the photon is scattered.

If the size of the obstacle is close to the photon wavelength, this one has a higher probability to be scattered. Two theories can be applied according to the size of the encountered structure. If the size of this latter is of the same scale as the incident photon wavelength, the Mie Theory describes the scattering process. If the size of the encountered structure is smaller than the length of the incident photon wavelength, the Rayleigh scattering theory describes scattering process (see figure 2.3). The Mie theory is a particular solution of Maxwell’s equations used to describe the elastic scattering. As for Rayleigh scattering, it

approximates the limit conditions of the Mie theory, especially for particles much smaller than the incident radiation wavelength.

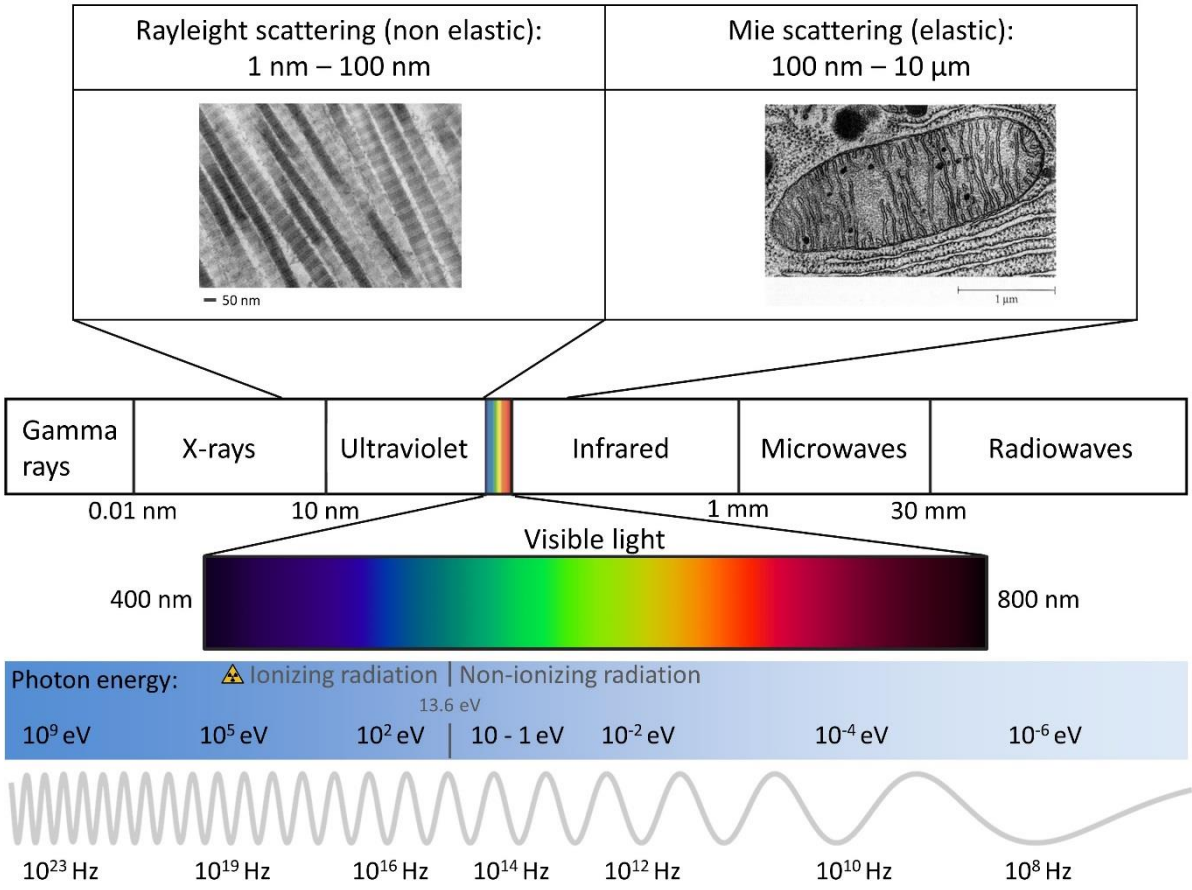

Figure 2.3: Relation between wavelength and associated scattering theory.

Regarding the wavelength scale mostly used in PDT (between 400 to 900 nm), the Mie theory is applied to explain the photon's behavior during the scattering.

The parameter that describes the scattering event is the scattering coefficient (μ_s) [m^{-1}]. Let us consider again a surface called effective cross-section σ_s [m^2] contained into a medium composed of several molecules (see figure 2.4). The volume density of the medium containing the chromophores is ρ_s [m^{-3}]. The scattering coefficient defines the cross-sectional area per unit volume of medium:

$$\mu_s = \rho_s . \sigma_s \tag{2.3}$$

Furthermore, the probability $P_{transmission}$ of photon crossing a length L [m] of this media without scattering event is:

$$P_{transmission} = e^{-\mu_s . L} \tag{2.4}$$

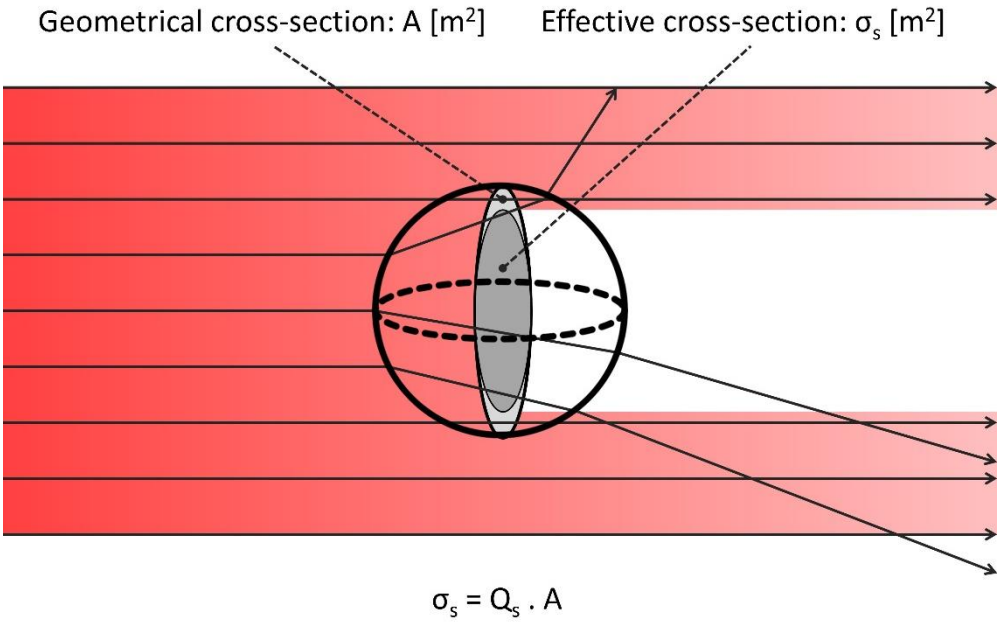

Figure 2.4: Scattering process by a chromophore.

The total attenuation coefficient μ_t is the sum of the absorption and scattering coefficients:

$$\mu_t = \mu_a + \mu_s \tag{2.5}$$

Finally, on an infinitesimal path length ΔL, the probability of a photon to interact (absorption or scattering process) is given by:

$$P_{interact} = e^{-\mu_t.\Delta L} \tag{2.6}$$

c. Anisotropy

After a scattering event, the photon has a new trajectory. The coefficient of anisotropy g [dimensionless] describes the behavior of the photon's direction, and more specifically the angle between the incident trajectory and the new one. Let us consider a photon scattered by a structure. The angle θ corresponds to the difference between the initial trajectory and the deviated one. The anisotropic coefficient defines the mean cosines value of the expected angle θ after a scattering event:

$$g = < cos(\theta) > \tag{2.7}$$

An ideal isotropic scattering process is described by g = 0 and a total forward scattering process is described by g = 1. The scattering phase function p(θ) [sr^{-1}] designates the photon probability to be scattered into a solid angle oriented at the angle θ according to the value of the anisotropy g (see figure 2.5). The scattering phase function was published for the first time

by Henyey and Greenstein in 1941 in their work on interstellar dust clouds [134]. The Henyey-Greenstein function enables to compute the scattering phase function p(θ) according to the value of the anisotropy g:

$$p(\theta) = \frac{1}{4\pi} . \frac{1 - g^2}{(1 + g^2 - 2g.\cos(\theta))^{3/2}} \tag{2.8}$$

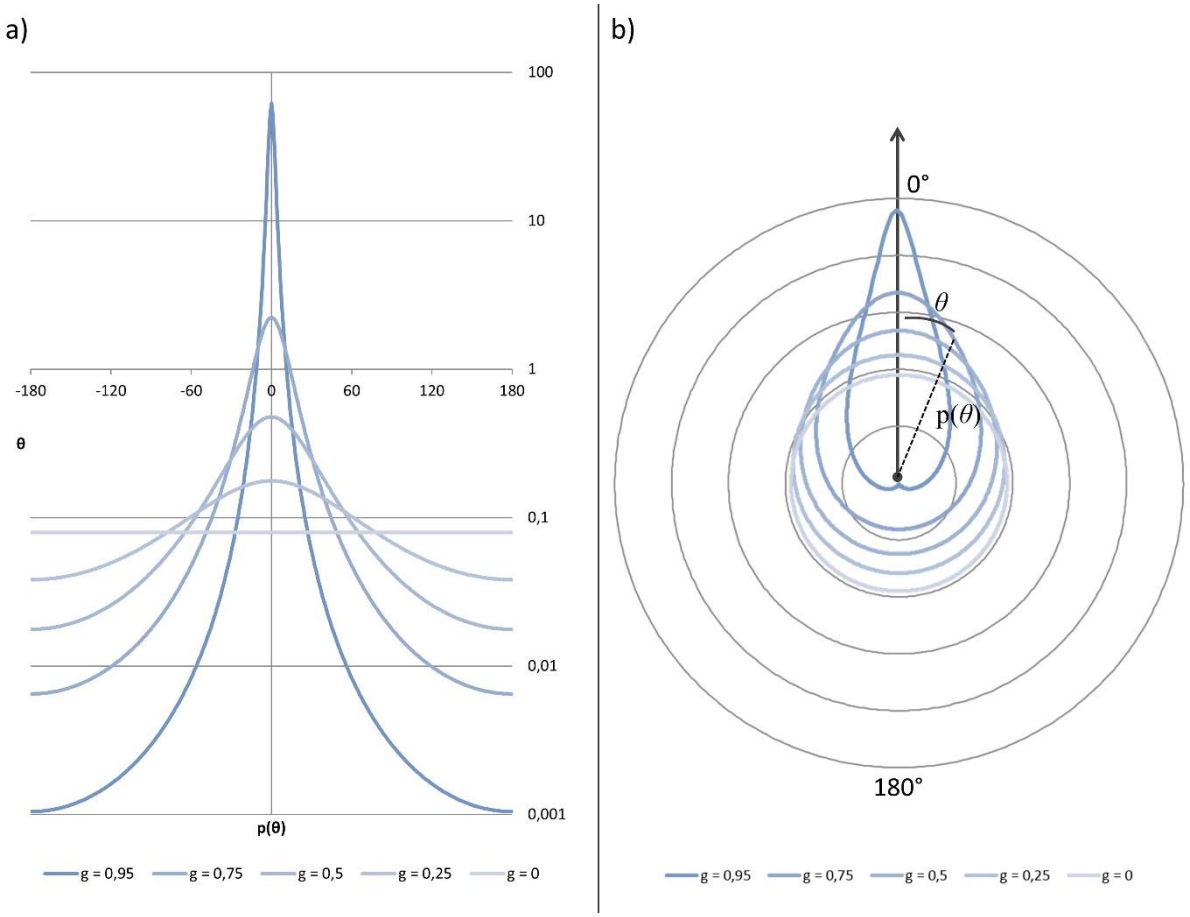

Figure 2.5: Henyey-Greenstein functions for different anisotropic values: plot a) and polar plot b) of the scattering phase function p(θ) [sr^{-1}] according to the angle θ (The forward direction along the original photon trajectory is 0° and the backward direction is 180°).

The anisotropic coefficient can be described as [135]:

$$g = \int_0^{\pi} p(\theta).\cos(\theta).2\pi.\sin(\theta).d\theta \tag{2.9}$$

This equation better represents the notion of probability (due to the scattering phase function) in the anisotropic coefficient (see figure 2.5).

The reduced scattering coefficient μ'_s [m^{-1}] is an important factor often used in optic to

take into account the anisotropy of the media:

$$\mu'_s = \mu_s.(1-g) \tag{2.10}$$

The inverse of the reduced scattering coefficient describes the mean distance of a photon according to the anisotropy of the medium. This shortcut, called reduced mean free path, is equal to several infinitesimal photon displacements in a high scattering media (the absorption coefficient must be negligible when compared to the scattering coefficient) (see figure 2.6).

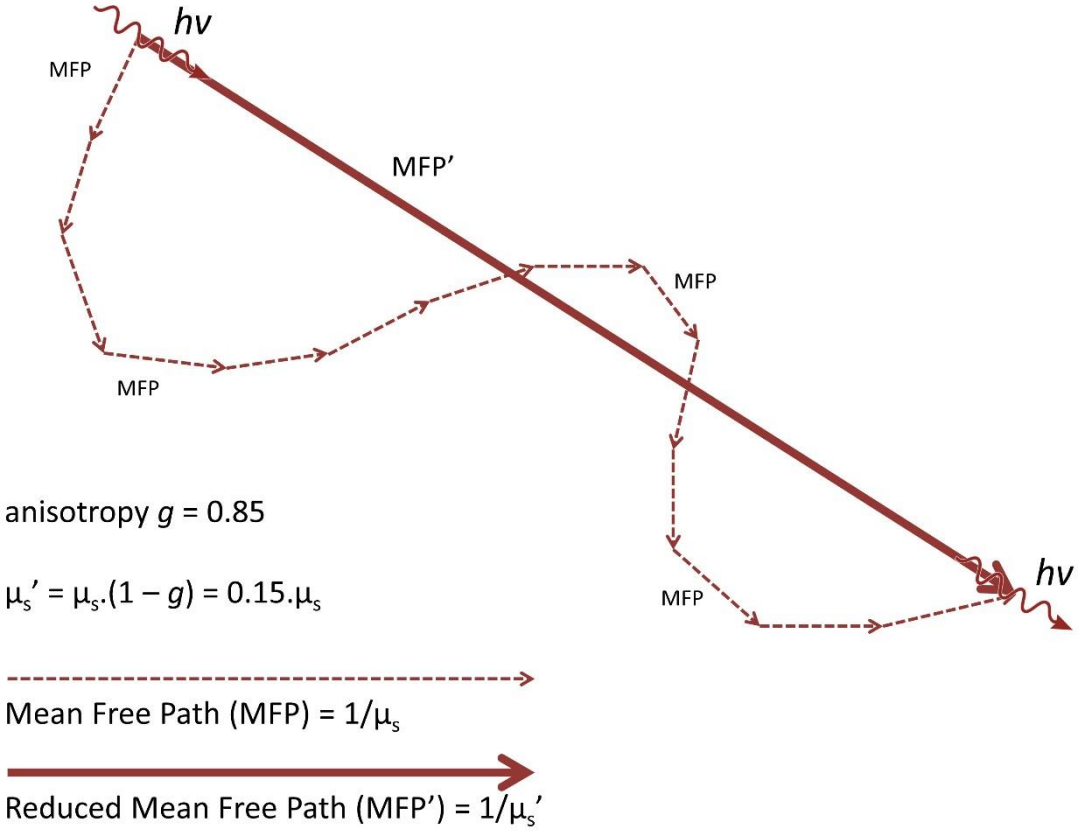

Figure 2.6: Mean free path versus reduced mean free path. The term "reduced" enables to extrapolate several progressions of one photon into one mean displacement.

The effective attenuation coefficient gathers absorption and scattering properties together:

$$\mu_{eff} = \sqrt{3.\mu_a.(\mu_a + \mu'_s)} \tag{2.11}$$

It is the simplest coefficient that can be obtained with experimental measurements. In all biological tissues, light power decreases exponentially according to the distance d [m] from the light source P_{source} [W]:

$$P(d) = P_{source}.e^{-d.\mu_{eff}} \tag{2.12}$$

d. Refraction and reflection

From a macroscopic point of view, light scattering can be defined with fluctuations of the refractive index [dimensionless]. This index characterizes a ratio between the phase velocity in the media considered v_{media} [m.s^{-1}] and the speed of light in vacuum c [m.s^{-1}]:

$$n = \frac{v_{media}}{c} \tag{2.13}$$

From a microscopic point of view, this difference is explained by the scattering events described previously, which induced small variations of the photon's path or bigger variations at the interface between two media owning different refractive index. Thus, at this interface, a part of the incident light beam may go through the second media with a different trajectory (refracted light) or be reflected at the interface (reflected light) (see figure 2.7). The incident angle $\theta_{incident}$, reflected $\theta_{reflected}$ angle (equal to $\theta_{incident}$) and refracted angle $\theta_{refracted}$ are determined according to the refractive indices of the first and second media (respectively, n_1 and n_2):

$$n_1 . \sin(\theta_{incident}) = n_2 . \sin(\theta_{refracted}) \tag{2.14}$$

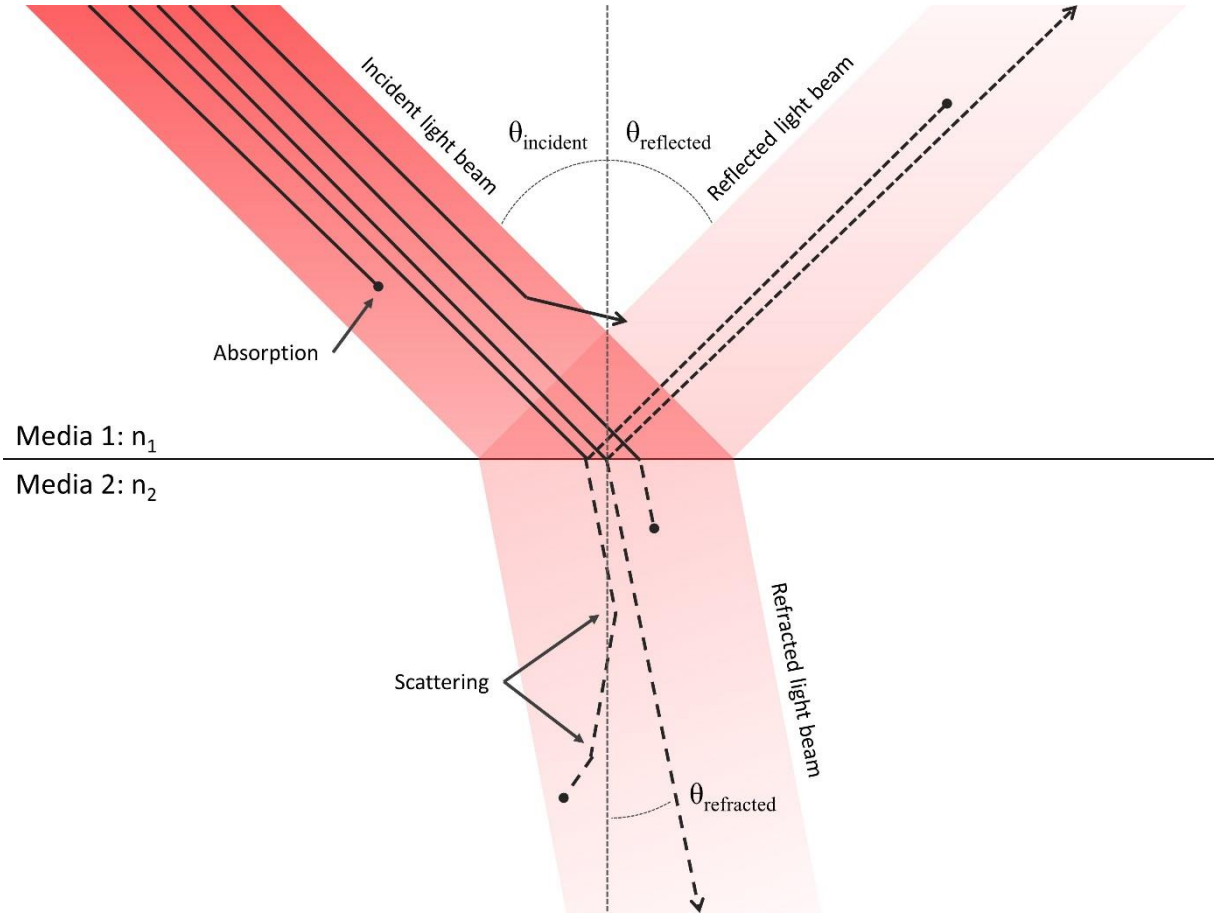

Figure 2.7: Summary of light interactions: reflection, refraction, scattering and absorption in two biological tissues with different optical properties.

2. Radiometric parameters

In this part, non-exhaustive definitions of radiometric parameters are given. Only parameters mostly used in PDT dosimetry were selected to be highlighted.

a. Light sources

Light sources are mostly defined according to their illumination type (e.g., in watt for frontal diffusors, in watt per centimeter for cylindrical diffusors). This trivial definition of the light source can be detailed in several other concepts used in biomedical optics.

The photon density N [photons.m^{-3}] emitted from this light source can be established. It characterizes the number of photons inside a unit volume (defined by a solid angle dω directed by the unit vector $\hat{u}$).

Using this photon density, the radiance term L [W.m^{-2}.sr^{-1}] introduces the notion of energy in this previous density. It represents the power per unit area (and not per unit volume) of photons crossing this area, which is oriented perpendicularly to the unit vector $\hat{s}$ and delimited by the solid angle $d\omega$ (see figure 2.8).

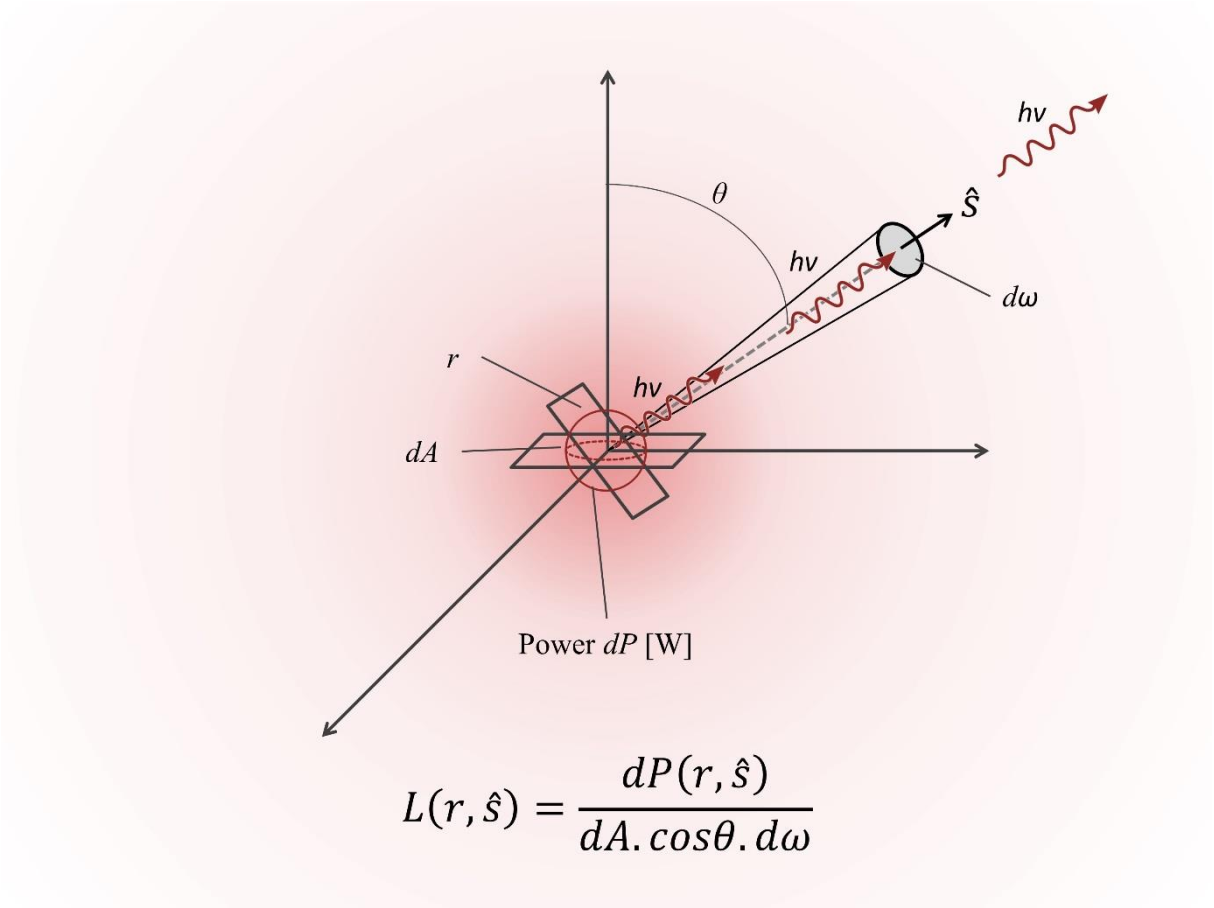

Figure 2.8: Radiance illustrated.

b. Irradiance and fluence rate

In biomedical optics, two similar but not identical notions related to the target and not to the light source must be defined. The irradiance and the fluence rate are both expressed in $W.m^{-2}$. As A.J. Welch et al. commented in their book chapter "Definitions and Overview of Tissue Optics [136]:

> "For the novice and even for many in the field, it goes against intuition that the fluence rate, φ [W/m^2] within tissue can be larger than the irradiance E0 [W/m^2]."

The irradiance defines the power incident delivered by a light beam on an area situated at the targeted tissue surface only, similarly to a light beam hitting a screen. This expression considers only the geometric configuration of the light source and the illuminated surface and is mainly employed in dermatology because most of illumination modalities are delivered topically. The amount of energy delivered per second at the surface of the skin can be expressed as an irradiance term.

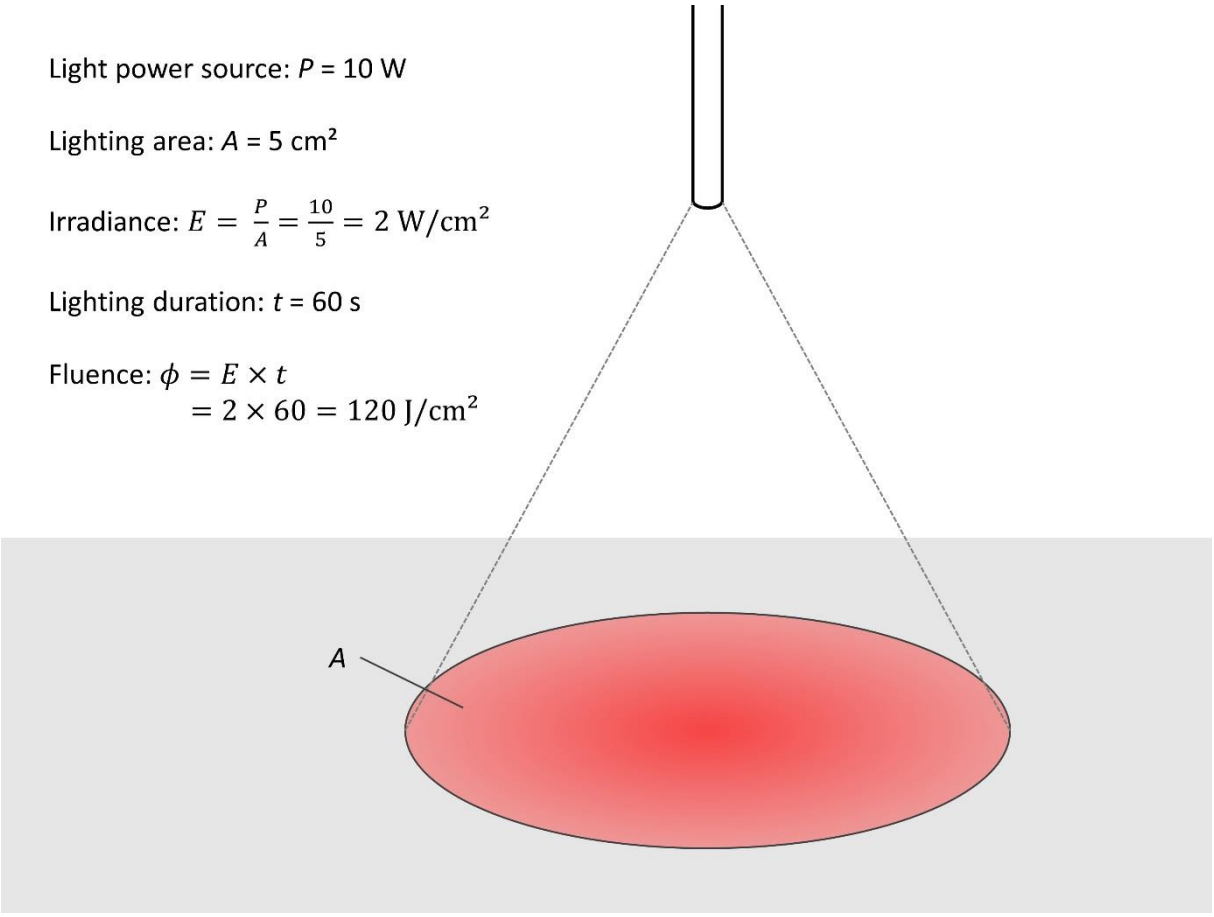

Figure 2.9: Irradiance computing illustrated. A light beam is emitted on a surface; the irradiance on the area containing the entire beam is computed.

Nevertheless, in many biomedical optics applications, the fluence rate has to be employed. Fluence rate considers the radiance obtained over all directions. It expresses the power incident delivered by a light beam inside a small sphere, on the cross-sectional area of this small sphere. Thus, the area can be situated not only on the surface but also inside tissues. Due to scattering events occurring in highly diffusing medium, one photon can cross several times the cross-sectional area where the fluence rate is estimated. This difference explains values of the fluence rate that can be higher than the irradiance, even if they are expressed both in the same unit [$W.m^{-2}$] [136, 137] (see figure 2.9).

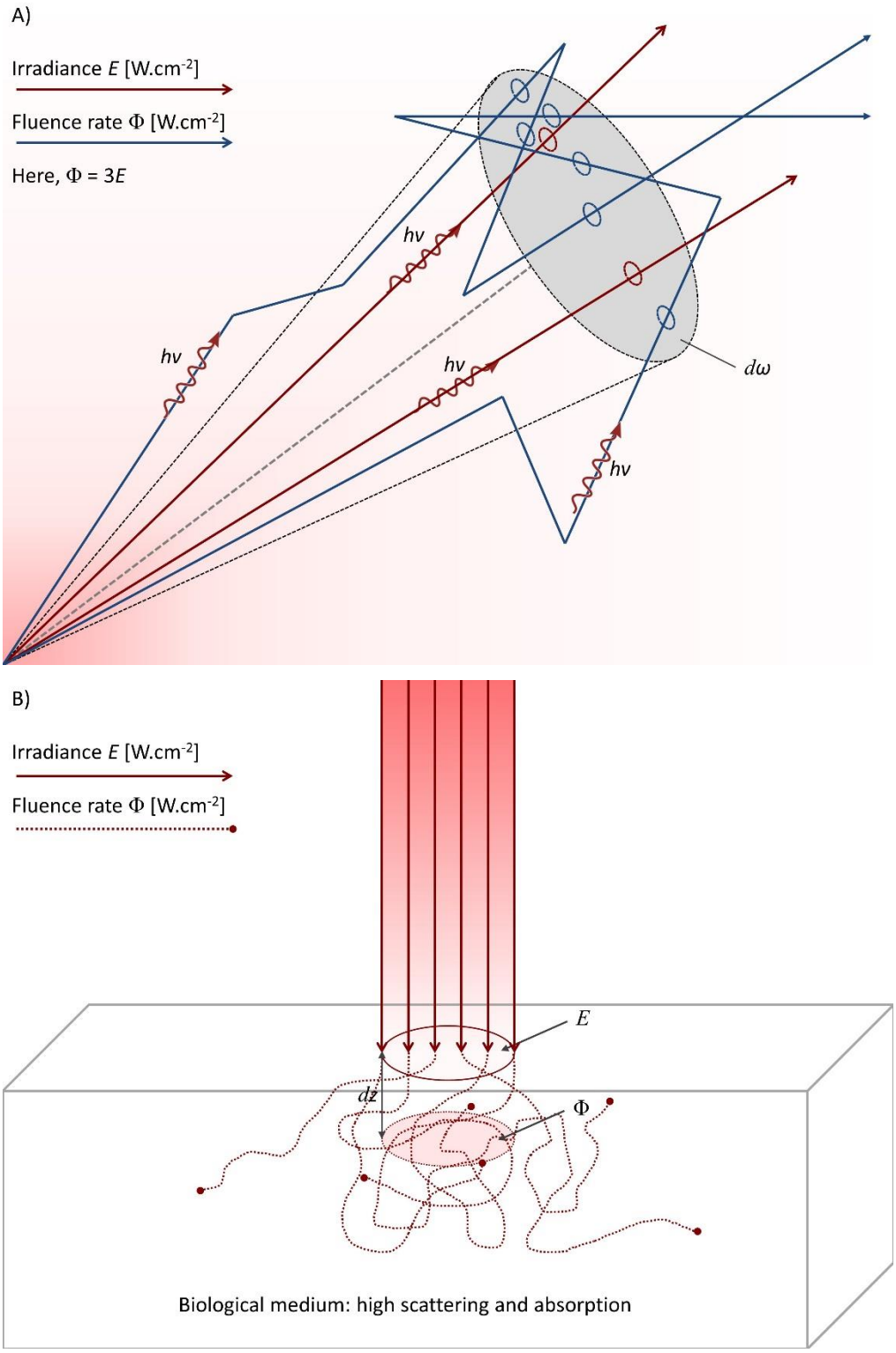

Figure 2.10: Irradiance versus fluence rate: in A), the fluence rate Φ is three times greater. than the irradiance E. In B), the irradiance E is defined as the power striking the surface. Conversely, the fluence rate Φ considers all photons distribution crossing the cross-sectional area. Due to the high scattering property of biological media, the fluence rate value is higher than the irradiance value.

c. Transmittance and reflectance

Transmittance and reflectance are mainly used in biomedical optics to calculate optical properties of a medium. These terms characterize the two light beams resulting from light interactions at the interface between two media: the reflected and the transmitted beam.

The reflectance R_t [dimensionless] is the sum of the specular reflection R_s [dimensionless] and the diffuse reflection R_d [dimensionless] (see figure 2.10):

$$R_t = R_s + R_d \tag{2.15}$$

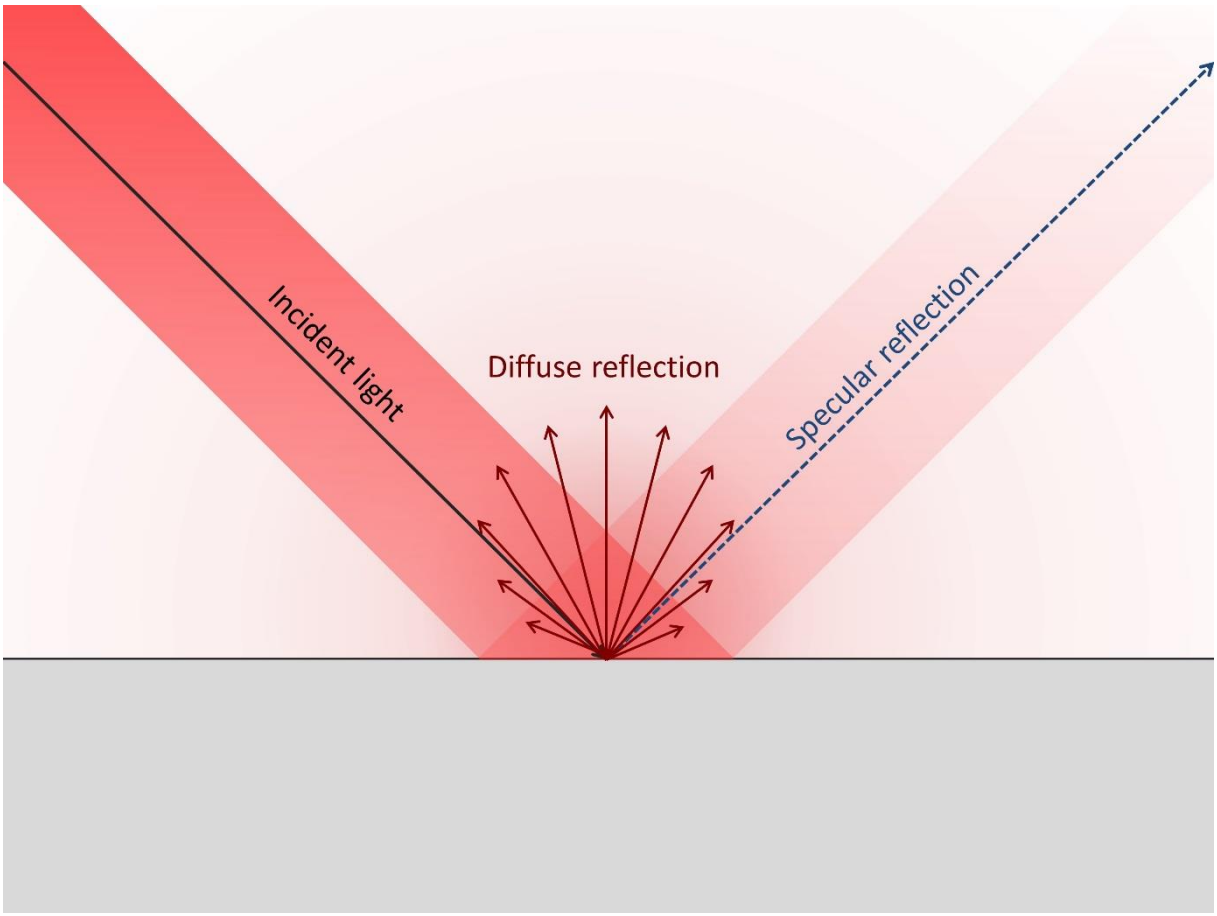

Figure 2.11: An incident light beam is reflected on a smooth surface considered as an ideal diffuse reflector: specular reflection and diffuse reflection rays are depicted.

Specular reflection assumes a perfect smooth interface able to reflect the same incident collimated light beam. Conversely, diffuse reflection considers the roughness of a more realistic interface, which can be encountered in biomedical optics.

The specular reflectance can be estimated using the Fresnel equation:

$$R_s = \frac{1}{2} \cdot \left[\frac{tan^2(\theta_1 - \theta_2)}{tan^2(\theta_1 + \theta_2)} + \frac{sin^2(\theta_1 - \theta_2)}{sin^2(\theta_1 + \theta_2)} \right] \text{ with } \theta_1 \neq 0 \quad (2.16)$$

When the incident angle θ_1 is null, i.e., the incident angle is perpendicular to the interface, the expression becomes:

$$R_s = \frac{(n_1 - n_2)^2}{(n_1 + n_2)^2} \text{ with } \theta_1 = 0 \quad (2.17)$$

Light transmission T [dimensionless] is the ratio of light that is not reflected at the interface and penetrates the second media, can be estimated using the specular reflectance:

$$T = 1 - R_s \quad (2.18)$$

Derived from the light transmission, the transmittance is the proportion of light absorbed by a medium sample with a known thickness.

II. PDT dosimetry: state of the art

In their review, Pogue et al. defines the dosimetry as [138]:

> "The quantitative planning and verification processes used to prescribe and verify a patient treatment, which will ensure that the targeted areas are given appropriate dose to kill the tissue, and to prevent over-treatment to normal tissues, avoiding morbidity issues."

In a PDT context, this dosimetry definition describes both the planning of the treatment delivery (or predictive dosimetry) and the monitoring during the treatment. Planning includes prediction of light propagation, PS concentration and tissue oxygen concentration prior to the treatment delivery (relative to patient treatment prescription). Monitoring is thus the verification of preoperative planning (or prescription). In this second paragraph, methods applied to perform the PDT dosimetry, both for planning and monitoring are listed. Regarding the planning, modeling of the light delivery, photosensitizer distribution and oxygen concentration are presented with a focus on light propagation computing. Then, monitoring approaches such as fluorescence and singlet oxygen detection are detailed in the last section.

1. Predictive dosimetry

Predictive dosimetry is composed of three features that are relative to the three major PDT components: the light propagation, the photosensitizer distribution and the oxygen concentration. Modeling these three parameters enables to plan the PDT treatment delivery.

a. Light delivery computing

Three different models may be used to compute the light distribution in steady-state inside biological media. The analytical models enable to estimate quickly the fluence rate distribution in a homogeneous medium. Numerical models are most often dedicated to compute the light propagation in more complex tissues. Monte-Carlo is a physical model used to compute light transport in heterogeneous media and can be consider as the reference model.

i. Analytical models

The analytical models allow estimating the fluence rate produced by a light source using mathematical equations. All developed models originate from the Boltzmann transport equation [139]:

$$\frac{1}{c}.\frac{\partial L(r,\hat{s},t)}{\partial t} + \nabla.L(r,\hat{s},t)\hat{s} = -(\mu_a + \mu_s)L(r,\hat{s},t) + \mu_s \iint_{4\pi} L(r,\hat{s}',t)f(\hat{s}\cdot\hat{s}')d\Omega' + Q(r,\hat{s}',t) \quad (2.19)$$

where c is the light velocity [m.s^{-1}], t is the time [s], $L(r,\hat{s},t)$ is the radiance [W.m^{-2}.sr^{-1}], $Q(r,\hat{s}',t)$ defines the power centered on the unit vector $\hat{s}$ at the r position and the normalized differential scattering cross-section $\iint_{4\pi} f(\hat{s}\cdot\hat{s}')d\Omega' = 1$

The Boltzmann transport equation (equation 2.19) can be simplified using the definition of the source $S(r,t)$, the fluence rate $\phi(r,t)$ and the flux $j(r,t)$:

$$S(r,t) \equiv \iint_{4\pi} Q(r,\hat{s},t)d\Omega$$
$$\phi(r,t) \equiv \iint_{4\pi} L(r,\hat{s},t)d\Omega \quad (2.20)$$
$$j(r,t) \equiv \iint_{4\pi} L(r,\hat{s},t)\hat{s}d\Omega$$

Using the Fick's law of diffusion, the flux can be written as:

$$j(r,t) = -D\nabla\phi(r,t)$$
$$\text{Where } D = \frac{1}{3[(1-g)\mu_s+\mu_a]} = \frac{1}{3[\mu'_s+\mu_a]} = \frac{1}{3\mu_{tr}} \quad (2.21)$$

Assuming the source as isotropic and in a steady state, the combination of these different expressions yields to the general diffusion equation in turbid medium with scattering property stronger than absorption:

$$\frac{1}{c}.\frac{\partial\phi(r,t)}{\partial t} = D\nabla^2\phi(r,t) - \mu_a(r)\phi(r,t) + S_0(r,t) \quad (2.22)$$

where c is the light velocity [m.s^{-1}], $\phi(r,t)$ is the fluence rate [W.m^{-2}], t is the time [s], D is the diffusion coefficient [m], $\mu_a(r)$ is the absorption coefficient [m^{-1}] and ∇^2 the Laplacien equal to the second derivative in x, y and z ($\nabla^2\phi(r,t) = \frac{\partial^2\phi(r,t)}{\partial x^2} + \frac{\partial^2\phi(r,t)}{\partial y^2} + \frac{\partial^2\phi(r,t)}{\partial z^2}$). This equation describes the wave propagation in space and time, emitted from a source $S_0(r,t)$.

In a PDT dosimetry context, the fluence rate is most often the main variable studied in order to obtain the fluence [J.m^{-2}] during the planed treatment. Consequently, only stationary problems are considered and are independent from the time t. The general diffusion equation can be simplified by dropping the t parameter and considering $\frac{\partial\phi(r,t)}{\partial t}$ equal to zero. This leads to the following equation:

$$S_0(r) = \mu_a(r)\phi(r) - D\nabla^2\phi(r) \tag{2.23}$$

which is the partial differential Helmholtz's equation [140, 141].

In stationary state and with a sufficient distance from light sources (considering superior to the reduced mean free path) or interfaces between several media, the Helmholtz equation can be simplified in:

$$D\nabla^2\phi(r) = \mu_a(r)\phi(r) \tag{2.24}$$

Using this equation (equation 2.24), several simple light sources geometries can be modeled. The easier model is the point source of power P with r the distance between the source and the position of the point where the fluence rate $\phi(r)$ is estimated:

$$\phi(r) = \frac{\phi(0)}{4\pi.D.r}.e^{\frac{-r}{\sqrt{D/\mu_a}}} \approx \frac{P.3(\mu_a + \mu'_s)}{4\pi.r}.e^{-r.\mu_{eff}} \tag{2.25}$$

More complex geometries can be modeled such as cylindrical light sources, i.e., cylindrical diffusor used in most interstitial PDT treatment. However, two equations can be found in the literature to estimate the fluence rate emitted from a light source of a length l in turbid media (equations 2.26 and 2.27). The first equation (equation 2.26) discretizes the diffusing part of the optical fiber as a sum of several point light sources [142-144]. Thus, calculation of the fluence rate at a distance r from the fiber is the sum of each light source contribution:

$$\phi(r) = \sum_{n=1}^{n_{sources}} P.\frac{3.\mu_s'}{4.\pi.r_n}.e^{-r_n.\mu_{eff}} \tag{2.26}$$

The second equation (equation 2.27) considers the whole fiber as a finite line light source with 2D cylindrical light emission characteristics [145, 146]. It computes the fluence rate values using the minimal distance r from the fiber:

$$\phi(r) = P.\sqrt{\frac{2.\delta}{\pi.r}}.\frac{e^{-r/\delta}}{2\pi.\mu_a.\delta^2} \tag{2.27}$$

where δ is the optical penetration depth [m] and is equal to $\sqrt{\frac{D}{\mu_a}}$.

Other equations (equations 2.28) enable to model planar or spherical light sources [145]:

$$\text{Planar: } \phi(r) = P.\frac{1}{2.\delta.\mu_a}.e^{-r/\delta}$$
$$\text{Spherical: } \phi(r) = P.\frac{\mu_{eff}}{4\pi.\mu_a.r}.e^{-r/\delta} \tag{2.28}$$

These equations allow to estimate light distribution of various light sources geometries during a very short computing time (see figure 2.11). It represents definitely the simplest approach to evaluate the light propagation and can be easily integrated in a TPS dedicated to PDT. Nonetheless, it remains difficult to take into account heterogeneities of tissues. Fluence rate estimation closed to light source (under the reduced mean free path) and closed to boundaries requires complex mathematical approximations that make the usage of analytical models not relevant in these cases.

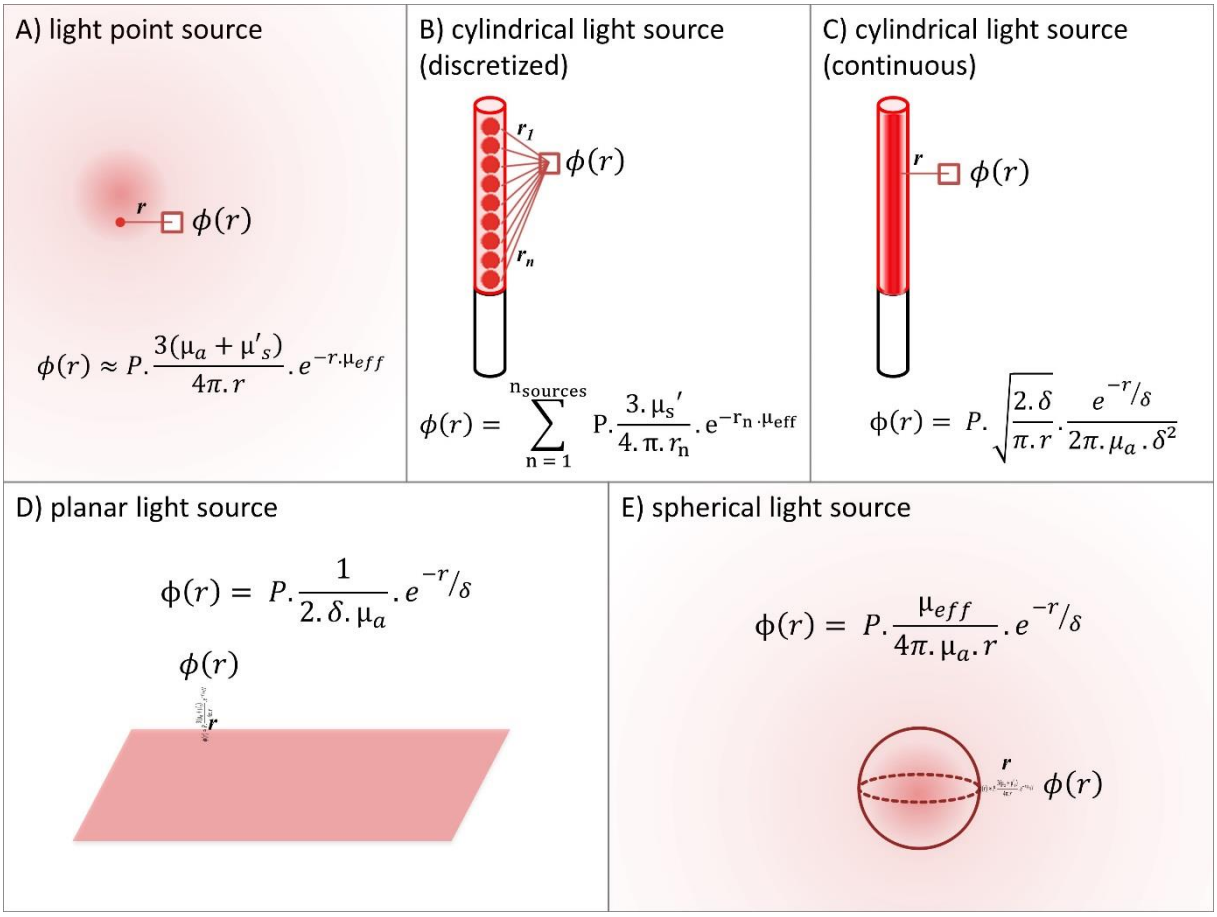

Figure 2.12: Analytical models estimate the fluence rate radiated from different types of light sources : A) light point source (equation 2.25) B) cylindrical light source considered as sum

of several light point sources (equation 2.26) C) cylindrical light source considered as a continuous light source (equation 2.27) D) planar light source and E) spherical light source (equations 2.28).

ii. Finite elements

Numerical analysis has been developed in order to resolve mathematical equations such as partial differential equation (PDE). This approach called "finite element" is largely used in engineering and physics, and subsequently in biomedical optics. Finite element can be used to solve PDE, such as the Helmholtz equation (equation 2.23). This method discretizes the space into a mesh in order to set boundaries conditions and enables to obtain numerical approximations. Currently, meshes are adapted to an expected resolution: a fine resolution is generally applied near to complex shape or close to light sources. Conversely, a coarser resolution is defined at a distance from complex geometries in order to reduce computing time. From this mesh, a resolving of diffusion equation is performed at each node constituting the mesh.

The three main element methods allowing to solve the diffusion equation are the finite difference, finite element and boundary element methods. All these methods mostly differ from the initial geometry of the mesh (see figure 2.13). The finite difference method discretizes the entire space into a Cartesian mesh. The finite element discretizes the region of interest in 2D with triangular elements or in 3D with tetrahedral elements. The boundary element discretizes boundaries of the different homogeneous parts of the region of interest in several nodes.

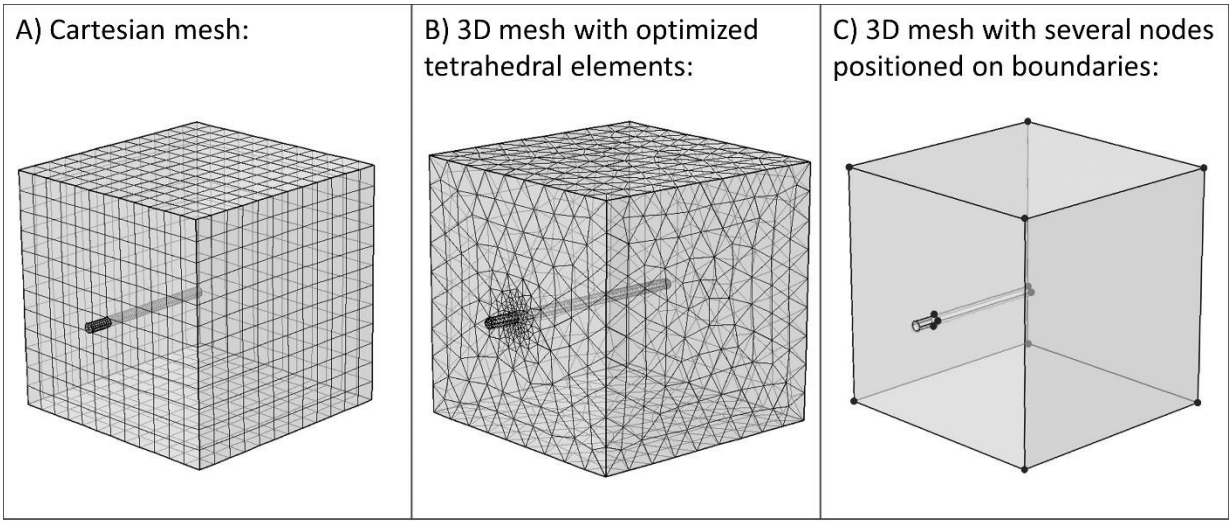

Figure 2.13: A) Cartesian mesh used in finite difference method B) 3D mesh with tetrahedral elements used in finite element method C) 3D mesh with several nodes used in boundary element method.

Since it enables an easier modeling of shapes and it is implemented in several major modeling software such as Comsol MultiPhysics® (COMSOL Inc., Burlington, USA), only the second approach called finite element method is described in this section. A full mathematical explanation of other methods would be out of the scope of this work. Several publications already describe in more details these methods [147-152].

The finite element method represents the most exploited method in PDE solving [153-159] (see figure 2.14). This method discretizes continuous PDE solving into discrete solutions according to Galerkin's method. A weak formulation of the PDE is solved at each node of the mesh. The Helmholtz equation H (equation 2.23) can be approximated by a linear combination of basis functions φ multiplied by coefficients α:

$$H \approx \sum_i \varphi_i . \alpha_i \tag{2.29}$$

From this simple consideration, a more complex model can be elaborated:

$$\langle -\nabla \cdot D\nabla \Phi_{\varphi_i} \rangle + \langle \mu_a . \Phi_{\varphi_i} \rangle = \langle S_{\varphi_i} \rangle \tag{2.30}$$

where the notation $\langle H \rangle$ designates the integration of the entire field in Hilbert spaces (space with finite or infinite dimensions) and Φ_{φ_i} is the discrete fluence evaluated at each node i weights φ_i. It does not appear necessary here to describe more in details the numerous mathematical steps to obtain the following equation (already described in [160-164]):

$$\Phi = [A]^{-1} S \tag{2.31}$$

where A is the matrix of the diffusion connectivity between basis functions and S is the vector of sources at each node. Interpolation between nodes is performed in order to produce a continuous matrix of the diffusion equation solving.

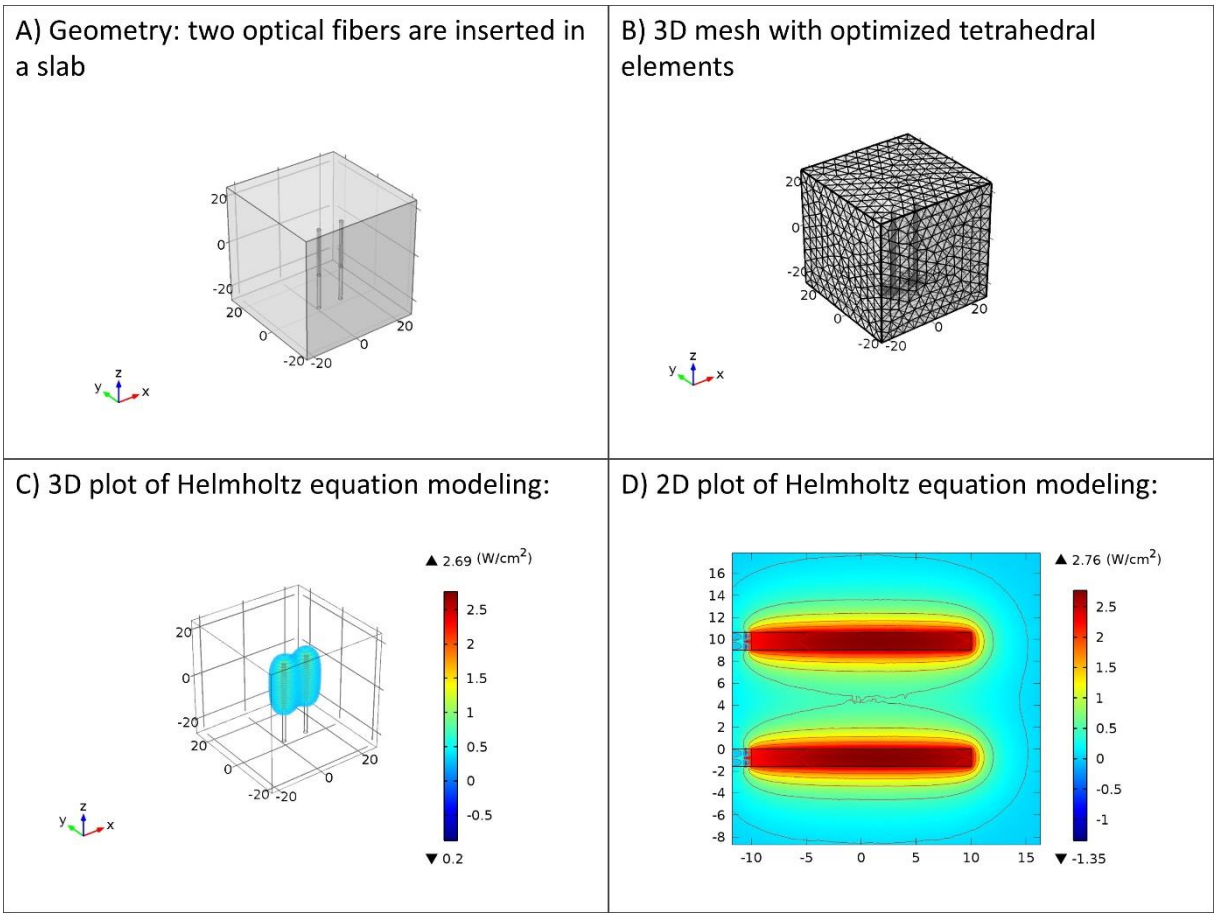

Figure 2.14: Illustration from Comsol MultiPhysics simulation using finite elements method to resolve different PDE. Here, the Helmholtz equation is solved: A) two cylindrical diffusers are defined as light source and B) an adaptive mesh is built around these cylinders in order to obtain an accurate results near boundaries (C and D).

iii. Monte-Carlo

The third model used to estimate the fluence rate in biological media is called Monte-Carlo method. This algorithm model is one of the most popular estimation algorithm and widely used in physics applications and particularly in particle physics simulations [165]. Thanks to its accuracy, this method is now in use in most TPS for planning high-energy photon radiation therapies. Wilson and Adam performed the first Monte-Carlo simulations of light (non-ionizing photons) transportation in a biological medium in 1983 [166]. Since then, Wang, Jacques and Prahl [167, 168] considerably improved Monte-Carlo performances and accuracy leading to several Monte-Carlo codes including the well-known MCML program (Monte-Carlo Multi-Layered) [169].

A well-known example to illustrate the Monte-Carlo method and understand the use of random numbers is the determination to the area of a lake A_{lake} situated in square site A_{site} of

known dimensions. A cannon fires x_{random} shots randomly in this square area. The number of balls remaining on the ground n_{ground} is determined. Thus, the number of balls fallen in the lake are $x_{random} - n_{ground}$. The area of the lake A_{lake} can be estimated from these numbers:

$$A_{lake} = \frac{x_{random} - n_{ground}}{x_{random}} . A_{site} \tag{2.32}$$

The estimation accuracy of the area of the lake A_{lake} improves by increasing the number of cannon fires x_{random} (see figure 2.15).

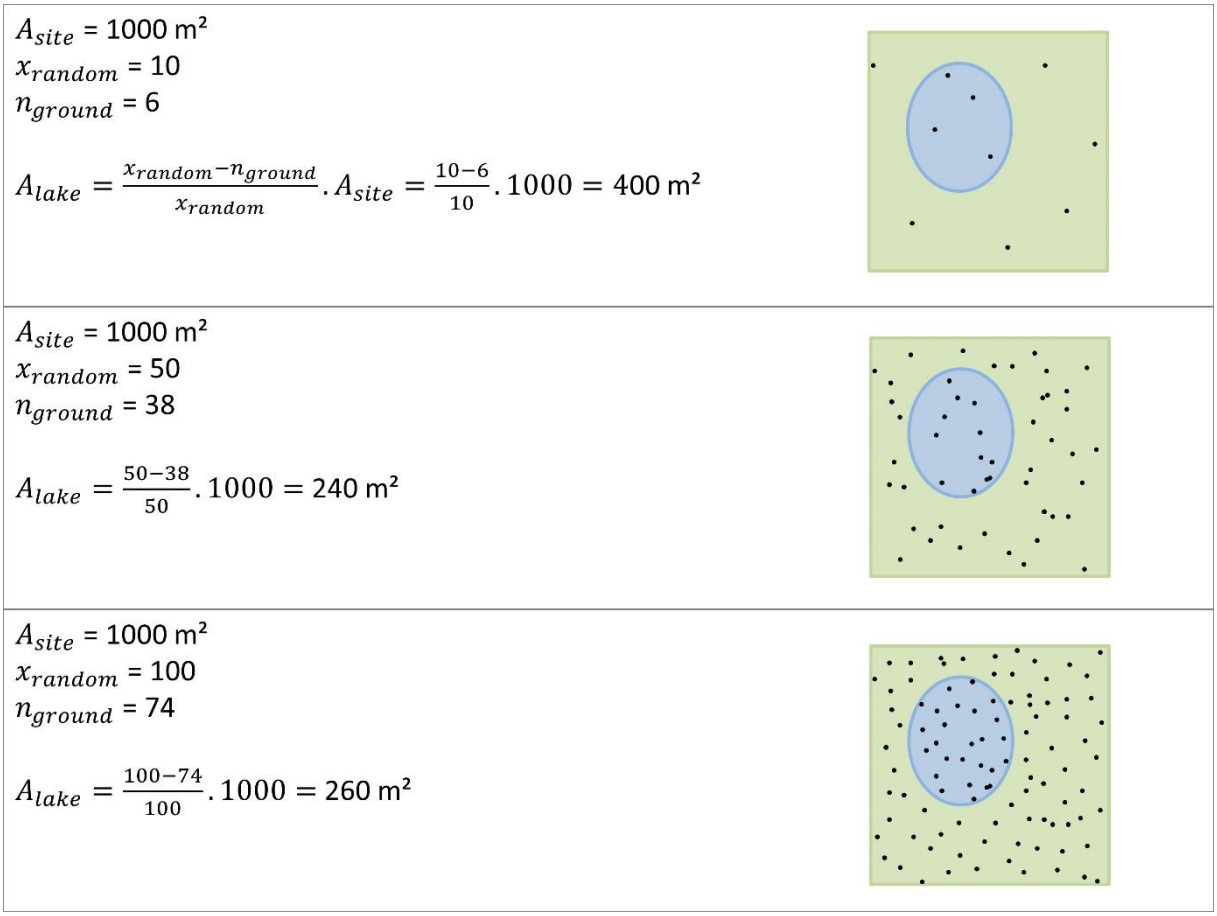

Figure 2.15: Illustration of the Monte-Carlo method. The area of the lake is determined from the number of balls fired randomly from a cannon fallen or not in the lake. Higher the number of balls fired is, better the estimation of the lake area is.

Similar approach can be used to model light propagation in matter. Indeed, using probabilities of interaction of photons with matter previously detailed, for a given photon, each event on its pathway can be randomly defined according to these probabilities. To model the propagation of light in matter, each photon pathway is computed from birth to death. Photons' life (creation, transport and absorption) is called *history* and each step of their

history is recorded. Random numbers are injected many times in the program to evaluate all probability distribution functions associated to all steps of photons' history. Accordingly, by transposing this random technic to the light propagation through matter, a large number of photons had to be randomly generated in order to tend toward a good estimation of the light absorption. Using all data collection of several millions of histories, light propagation through matter can be estimated.

The first part of the third chapter is dedicated to the description of the Monte-Carlo model, the standard algorithm and all computing improvements.

b. Photosensitizer distribution

The PS uptake in tissues remains the most crucial point for efficient PDT treatment. The modeling of the PS distribution into tissues before the PDT treatment is mainly governed by mathematical equations requiring precise knowledge of the PS pharmacokinetics [170, 171]. The rate of diffusion of a PS is determined by the concentration gradients and the diffusivity. This constant depends on the tissues properties and also on the chemical properties of the PS used in the treatment [172]. The Fick's first law describes the diffusion of matter in steady state:

$$J = -D.\frac{dM}{dx} \tag{2.33}$$

Where J is the flux vector indicating the direction of the PS, D is the diffusion coefficient through mater, M is the precursor drug (e.g., 5-ALA for PpIX) concentration and x is the depth in the media.

From this simple equation, more complex equations can derivate to describe the temporal evolution of the PS and its precursor [173] and lead to the concentration of photoactive compound accumulated in the target tissue.

Although a profound comprehension of the PS uptake within tissues remains essential, according to selectivity and specificity of a given PS, the modeling of its distribution in a dosimetry context may be secondary.

c. Singlet oxygen concentration

Initially, oxygen is a prerequisite to obtain a PDT response during the illumination of targeted areas. However, oxygen level may vary spatially and dynamically due to its consumption during a PDT treatment [174-177].

Singlet oxygen is the main cytotoxic agent provoking considerable damages in tumor cells

and represents a particular lever in PDT treatment efficacy. Thus, a strong effort has been made to develop a model able to predict the singlet oxygen concentration in tissues [178]. Because singlet oxygen distribution modeling depends on the reaction type implemented, most of developments have been concentrated on the type II reaction. Singlet oxygen creation requires several previous photochemical reactions and all species can be described by differential equations [174, 179] [180, 181]:

$$\begin{aligned}
\frac{d[S_0]}{dt} &= -k_0[S_0] - k_1[^1O_2]([S_0]+\delta) + k_2[T][^3O_2] + k_3[S_1] + k_4[T] \\
\frac{d[S_1]}{dt} &= -(k_3+k_5)[S_1] + k_0[S_0] \\
\frac{d[T]}{dt} &= -k_2[T][^3O_2] - k_4[T] + k_5[S_1] \\
\frac{d[^3O_2]}{dt} &= -S_\Delta k_2[T][^3O_2] + k_6[^1O_2] + P \\
\frac{d[^1O_2]}{dt} &= -k_1([S_0]+\delta)[^1O_2] + S_\Delta k_2[T][^3O_2] - k_6[^1O_2] - k_7[A][^1O_2] \\
\frac{d[A]}{dt} &= -k_7[A][^1O_2]
\end{aligned} \tag{2.34}$$

where [S_0], [S_1] and [T] are respectively the singlet and triplet PS concentration, and $[^3O_2]$ and $[^1O_2]$ are respectively the ground triplet and excited singlet state oxygen concentration, P and [A] are the oxygen supply term and the concentration of $[^1O_2]$ acceptor excluding PS molecule and δ is a low PS concentration correction term. The k_i parameters define different rates (photon absorption, decay excited to ground state or bimolecular rate of reaction) and are described in the Wang et al. study [180]. These six differential equations (equations 2.33) are then combined with the light diffusion equation and solved in order to obtain the concentration of the excited singlet state oxygen$[^1O_2]$, which induces the cytotoxic effects of PDT treatments. In the study of Liang et al., this method was implemented in the software Comsol Mutliphysics® dedicated to numerical analysis using finite element method [182]. This approach was evaluated on C3H mice treated with two PS: Photofrin and BPD Verteporfin. The authors also associated the concentration of excited singlet state oxygen to the size of necrotic areas predicted and measured. More recently, Qiu et al. correlated three parameters: the fluence rate, the fluence and the concentration of excited singlet state oxygen [183]. The authors argued that the parameter $[^1O_2]$ was the most accurate metric and could serve as a better predictive dosimetric quantity. Additionally, Lopez et al. described a new dosimetry metric: the tumor reactive single oxygen as a new dosimetry metric that represents

the amount of singlet oxygen per tumor volume that reacts with the molecules in the tumor [184]. The authors proposed in their study a model using the PPIX as PS in 5-ALA PDT treatment. This metric integrates fluence rate, optical properties, the oxygen consumption and the PS distribution.

2. Monitoring of the PDT treatment

Monitoring enables the evaluation of the treatment response during the illumination and the adaptation of the light delivery. With a strong uptake of tumor cells, fluorescence of the PS is the most intuitive marker to monitor the treatment response. Also, although it is still difficult to record, the monitoring of singlet oxygen luminescence is the most direct marker of the PDT dose.

a. Fluorescence detection

The emergence and now, the common practice of the fluorescence-guided resection (FGR) in clinical routine is the first application of PS fluorescence property [76, 185-189]. The use of 5-ALA (commercial name Gliolan®) as contrast agent in surgery of malignant glioma has been approved for human use in Europe, Asia, Australia and USA[1].

Thus, the measurement of the PS concentration before, during and after a PDT treatment can be included as an indicator in a clinical trial. This feature provides from direct in situ measurements of the fluorescence emitted by the PS [190-193]. Quantifying PS fluorescence has the potential to optimize PDT treatment parameters and also to monitor the PS concentration during treatment. According to PS used in the PDT treatment, high variability of concentration can appear between patients and tissues within the same tumor. Currently, spectroscopy technic is used to detect the PS fluorescence of the treated area. Several research teams have already developed several technological tools to detect this fluorescence such as fiber probe systems for deep PS distribution measurements [191, 194-198], CCD camera-based systems [199-206] and tomographic system for sub-surface PS distribution measurements only [96, 105, 207-209].

b. Singlet oxygen monitoring

[1]EUROPEAN PUBLIC ASSESSMENT REPORT (EPAR), *GLIOLAN EPAR, summary for the public* [online], available at http://www.ema.europa.eu/docs/en_GB/document_library/EPAR_-_Summary_for_the_public/human/000744/WC500021786.pdf (accessed July 02, 2017)

One of the most efficient approaches to predict PDT damages remains the measurement of singlet oxygen concentration's level [182, 193, 210]. During a PDT treatment, a luminescence of the singlet oxygen in the near infrared (approximately 1270 nm) appears. Nonetheless, a direct *in vivo* measurement of this signal remains challenging due to its weak amplitude and the very short lifetime of the molecule (approximately 50 ns). Using photomultiplier tubes [211-213] or other technologies [214-216], the signal is integrated during a part or the entire treatment time in order to collect enough photons to obtain a relevant metric related to PDT dose. Although this metric correlated closely damages due to PDT treatment, a practical system providing robust results for clinical routine seems no to be available yet.

Additionally, the oxygen partial pressure can also be used as a surrogate metric to correlate the PDT damages. Variations of the partial pressure of oxygen in the blood have an impact on the oxygenation of tissues where oxygen is required for PDT treatment [217-220]. The study of Li et al. demonstrates a correlation between singlet oxygen production and oxygen partial pressure during irradiation. A real-time multi-parameter detection system integrating PS florescence, luminescence of singlet oxygen, oxygen partial pressure should provide robust data to implement a complete dosimetric assessment and to monitor a PDT treatment efficiently.

Chapter conclusion

PDT dosimetry is a multifactor estimation to compute impact on tissues. Predictive dosimetry includes computing of light, of PS and oxygen distribution in biological tissues. Although it is highly time-consuming, Monte-Carlo remains the reference method to compute the propagation of light in heterogeneous media. Monitoring of the PDT treatment gathers several features (PS fluorescence, detection of singlet oxygen) to improve the "PDT dose" metric. Finally, a collaborative effort between contributions of biologists, chemists, physicists, and engineers would lead to define a comprehensive PDT dose [221]. In this thesis, a focus was achieved on the light distribution modeling using the Monte-Carlo method.

Chapter III
Monte-Carlo: from basics to PDT implementation

As detailed in chapter II, dosimetry requires an accurate estimation of light dose deposited in the matter. Accordingly, Monte-Carlo model that simulates the photons' interactions in the matter during their entire "life" is the prime candidate to be used in PDT dosimetry. After introducing the theory of the Monte-Carlo model, its implementation in the context of PDT is presented. Additionally, since the Monte-Carlo modelling is highly time-consuming, acceleration technics are described to make feasible its integration in a treatment planning system dedicated to PDT in clinical routine. Finally, a comprehensive experimental design is proposed to validate the implementation of the Monte-Carlo model achieved during this thesis.

I. Monte-Carlo model

The Monte-Carlo model simulates the propagation of photons through matter

according to physics laws. Photons are generated at a random position according to the light source location. Space is discretized according to matrix or grid of voxels and each photon pathway through different media and its progressive absorption are simulated at each voxel location. Thus, by generating a very large number of photons, a light dose (i.e., fluence [J/cm²]) is obtained using the recording of all photons' absorption inside each voxel of the grid.

1. Theory of the Monte-Carlo model

The Monte-Carlo algorithm describes the history of a photon from its "birth" or launch until its death. As an illustration, in figure 3.1, a photon is launched with an initial state and is propagated through different media. Several scattering and absorption events occur until the photon death.

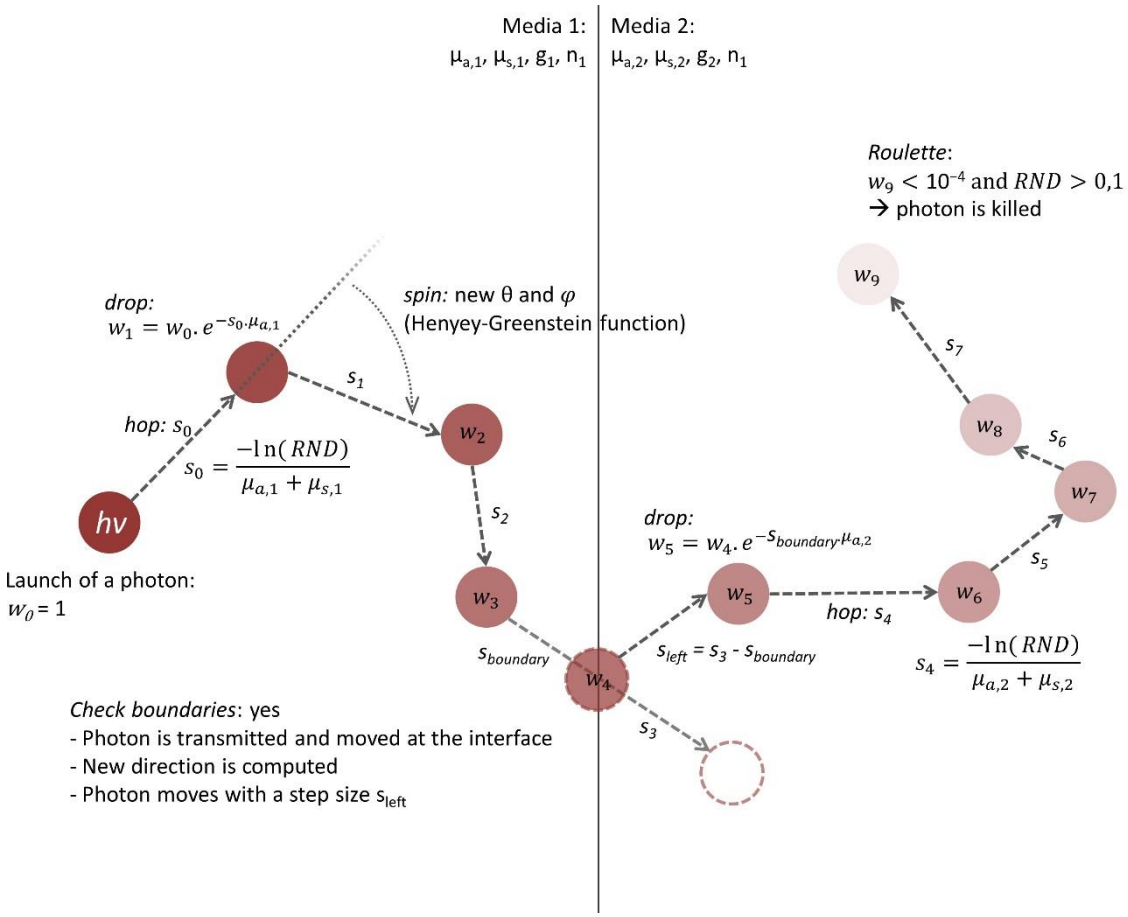

Figure 3.1: A photon history; from launch to termination.

a. Photon launch

Photons are defined by several features (equation 3.1) such as a position (*x*, *y*, *z* in

Cartesian coordinates), a direction (*ux*, *uy*, *uz* in Cartesian coordinates) and a weight *w* (dimensionless). This weight, initially set to 1.0, could be seen as a "health bar" where each collision (i.e., absorption event) decreases this gauge until death (i.e., *w* = 0.0). To simplify the comprehension of the model, the progression of only one photon will be described in this paragraph. However, each step of this photon's life is common to the others. Only the random characteristic leads to different pathways for each photon generated during the simulation.

$$\overrightarrow{photon} \stackrel{\text{def}}{=} \begin{pmatrix} \begin{pmatrix} x \\ y \\ z \end{pmatrix} \\ \begin{pmatrix} u_x \\ u_y \\ u_z \end{pmatrix} \\ w \end{pmatrix} \tag{3.1}$$

All different types of light sources can be modeled using these features (collimated uniform or Gaussian beam, focused or not, isotropic sources). Spherical or cylindrical diffusers are mainly used in interstitial or intraoperative PDT. These light sources are isotropic, i.e., photons are distributed uniformly around the point source. This non-preferential direction of photon direction is initially calculated using eq. 3.2:

$$\begin{aligned} u_x &= sin\,\theta.cos\,\varphi \\ u_y &= cos\,\theta.sin\,\varphi \\ u_z &= cos\,\theta \end{aligned} \tag{3.2}$$

where θ is the angle between trajectory vector and the *z* axis and φ is the angle between trajectory vector and the *x* axis.

To obtain an isotropic uniform distribution of photons, θ and φ are computed using a random number (RND):

$$\begin{aligned} cos\,\theta &= 2RND - 1 \\ sin\,\theta &= \sqrt{(1 - cos^2\theta)} \\ \varphi &= 2\pi.RND \end{aligned}$$

if $\varphi < \pi$ (3.3)

$$sin\,\varphi = \sqrt{(1 - cos^2\varphi)}$$

else

$$sin\,\varphi = -\sqrt{(1 - cos^2\varphi)}$$

Once the initial position and direction are computed for each photon, their propagation begins. According to the optical properties of the medium, photons cross a given distance called step size s_{photon} [m]. This step size denotes the displacement of photons through matter at each iteration of the algorithm (i.e., each step of the "photon's life") and is deduced from absorption and scattering coefficients through the probability *p(s)* (equation 3.4):

$$p(s) = \frac{e^{-\mu_t.s}}{\mu_t}$$

such as the probability density function is (3.4)

$$F(s) = \int_0^{\infty} \frac{e^{-\mu_t.s}}{\mu_t} ds = 1$$

where the total attenuation coefficient μ_t is the sum of the absorption and scattering coefficients.

Thus, for a given photon and its step size s_{photon}, the probability distribution function *F* becomes:

$$F(s_{photon}) = \int_0^{s_{photon}} \frac{e^{-\mu_t.s}}{\mu_t} ds = 1 - e^{-\mu_t.s_{photon}} \quad (3.5)$$

s_{photon}, describing the iterative photon pathway, is finally obtained by a random sampling of the distribution function *F* (equation 3.6):

$$F(s_{photon}) = 1 - e^{-\mu_t.s_{photon}} = RND$$
$$s_{photon} = \frac{-\ln(1 - RND)}{\mu_t} = \frac{-\ln(RND)}{\mu_t} \quad (3.6)$$

Once this first step length is computed, the photon begins its propagation through surrounding matter. Future interactions with media, defined by their optical properties, is iteratively computed from the *Hop-Drop-Spin* process.

b. *Hop-Drop-Spin* model description

The *Hop-Drop-Spin* sequence is the approach used to iteratively compute state and position of the photon along its trajectory. "Hop" designates the displacement of the photon, "Drop" describes to the absorption event and "Spin" defines the change of direction.

i. Hop

During a movement at a given step of its pathway, the photon may change of medium even if its step size is low (only several micrometers). Once the step size is computed, the

algorithm evaluates if the photon is changing of medium or not.

If not, a standard photon movement called "Hop" is achieved. The photon moves according to the step size s_i, the direction cosines ux_i, uy_i, uz_i and the coordinates x_i, y_i, z_i:

$$\begin{aligned} x_{i+1} &= x_i + s_i.u_{x,i} \\ y_{i+1} &= y_i + s_i.u_{y,i} \\ z_{i+1} &= z_i + s_i.u_{z,i} \end{aligned} \tag{3.7}$$

where $i \in [0; n]$, n represent the total number of the photon's displacements during its entire history.

Conversely, if the photon moves towards a medium with different optical coefficient, the photon is placed at the boundary of the first medium using the current direction cosines $u_{x,i}$, $u_{y,i}$, $u_{z,i}$ and current coordinates x_i, y_i, z_i:

$$\begin{aligned} x_{i+1} &= x_i + (s_i - s_{boundary}).u_{x,i} \\ y_{i+1} &= y_i + (s_i - s_{boundary}).u_{y,i} \\ z_{i+1} &= z_i + (s_i - s_{boundary}).u_{z,i} \end{aligned} \tag{3.8}$$

where $s_{boundary}$ is the step length between the current position and the boundary with the neighboring medium.

If the neighboring medium owns the same refractive index, no additional interaction can happen. However, when the refractive medium of the current medium n_1 is different from the surrounding medium n_2, the reflectance R must be evaluated to compute probability that the photon could be reflected at the interface or transmitted into the neighboring medium. This reflectance is computed using the Fresnel reflectance equation (equation 3.9):

$$\begin{aligned} R = \frac{(\sin\theta_1 \cos\theta_2 - \cos\theta_1 \sin\theta_2)^2}{2} \times \\ \frac{(\cos\theta_1 \cos\theta_2 + \sin\theta_1 \sin\theta_2)^2 + (\cos\theta_1 \cos\theta_2 - \sin\theta_1 \sin\theta_2)^2}{(\sin\theta_1 \cos\theta_2 - \cos\theta_1 \sin\theta_2)^2.(\sin\theta_1 \cos\theta_2 + \cos\theta_1 \sin\theta_2)^2} \end{aligned} \tag{3.9}$$

where θ_1 is the photon incident angle, θ_2 is the photon transmission angle through the second medium computed using the Snell–Descartes law and according to the refractive indices of the first and second media (equation 2.14).

Once the reflectance is computed, a random number between [0,1] is generated and compared to the reflectance value. If the random value is strictly superior to the reflectance value, the photon is transmitted to the second medium with the following direction:

$$u_{x,i+1} = u_{x,i}.\frac{n_1}{n_2} \tag{3.10}$$

$$u_{y,i+1} = u_{y,i}.\frac{n_1}{n_2}$$

if $\cos\theta_1 \approx 1$ (normal incidence)

$$u_{z,i+1} = \cos\theta_1$$

else if $\cos\theta_1 \approx 0$ (raking incidence)

$$u_{z,i+1} = 0$$

else

$$u_{z,i+1} = \cos\theta_2$$

If the random value is inferior to the reflectance value, the photon is reflected to the interface between the two media with the following direction cosines:

$$\begin{aligned} u_{x,i+1} &= u_{x,i} \\ u_{y,i+1} &= u_{y,i} \\ u_{z,i+1} &= -u_{z,i} \end{aligned} \tag{3.11}$$

ii. Drop

Once the "Hop" movement completed, the "Drop" (i.e., absorption) event occurs. After moving to its new position, the photon interacts with the tissue. A small proportion of its weight *w* [dimensionless] is decreased according to the size step s_i:

$$w_{i+1} = w_i.e^{-s_i.\mu_a} \tag{3.12}$$

The absorbed fraction of the photon by the medium has to be recorded in order to obtain the total fluence deposit by all photons generated. To accumulate these absorbed fractions, the entire space is discretized into voxels which generates a matrix called *Absorption*.

The absorption is then stored in the *Absorption* matrix at position *l*, *m*, *n*, which corresponds to the location where the absorption occurs:

$$Absorption[l,m,n]_i = Absorption[l,m,n]_{i-1} + w_i.(1 - e^{-s_i.\mu_a}) \tag{3.13}$$

iii. Spin

Once the "*Drop*" event completed, the photon is scattered into a new direction according to the optical properties of the medium, which corresponds to the "*Spin*" process. These new direction cosines are computed using the Henyey-Greenstein equation seen previously (equation 2.7). The function can be normalized over 4π sr (equation 3.14):

$$\int_0^{2\pi}\left\{\int_0^{\pi} p(\theta).sin(\theta).d\theta\right\}d\phi = 1 \tag{3.14}$$

Thus, the Henyey-Greenstein function becomes:

$$p(\theta) = \frac{1}{2}.\frac{1-g^2}{(1+g^2-2g.\cos(\theta))^{3/2}} \tag{3.15}$$

The new direction is obtained by inserting a random number *RND* in the previous equation (equation 3.15). New angles θ and φ provide from the sampling of the Henyey-Greenstein function:

$$\cos\theta = \frac{1+g^2-\left(\frac{1-g^2}{1-g+2g.RND}\right)^2}{2g} \tag{3.16}$$

$$\varphi = 2\pi.RND$$

New direction cosines $u_{x,i+1}$, $u_{y,i+1}$, $u_{z,i+1}$ are then computed following calculations:

$$u_{x,i+1} = \frac{\sin\theta\,.\left(u_{x,i}.u_{z,i}.\cos\varphi - u_{y,i}.\sin\varphi\right)}{\sqrt{1-{u_{z,i}}^2}} + u_{x,i}.cos\ \theta$$

$$u_{y,i+1} = \frac{\sin\theta\,.\left(u_{y,i}.u_{z,i}.\cos\varphi + u_{x,i}.\sin\varphi\right)}{\sqrt{1-{u_{z,i}}^2}} + u_{y,i}.cos\ \theta \tag{3.17}$$

$$u_{z,i+1} = -\sin\theta\,.\cos\varphi\,.\sqrt{1-{u_{z,i}}^2} + u_{z,i}.\cos\theta$$

When $u_{x,i}$= 0, $u_{y,i}$= 0, $u_{z,i}$± 1, new direction cosines $u_{x,i+1}$, $u_{y,i+1}$, $u_{z,i+1}$ are then computed following calculations:

$$u_{x,i+1} = sin\ \theta.cos\ \varphi$$

$$u_{y,i+1} = cos\ \theta.sin\ \varphi$$

if $u_{z,i} \geq 0$

$$u_{z,i+1} = cos\ \theta \tag{3.18}$$

else

$$u_{z,i+1} = -cos\ \theta$$

Using these new direction cosines, a new step size can be generated and photon can be considered for a new iteration.

c. Termination of the history

The photon keeps propagating using the *hop-drop-spin* sequence with a decrease of its weight *w* at each interaction. The *roulette* method is one of the most common used to finish the photon propagation. An arbitrary threshold value is defined (10^{-4} typically). When the photon's weight reaches a value lower than this threshold, the *roulette* algorithm is applied. A

random number *RND* is generated and compared to a chance value (typically 0.1). If the *RND* value is strictly superior to the chance value, the photon terminates its propagation. Conversely, if the *RND* value is inferior to the chance value, the photon carries on with a weight value increased by the inverse of the chance value (typically 10 times the last weight value).

$if(w_i < threshold)$

$if(RND \leq chance)$

$$w_{i+1} = \frac{w_i}{chance} \tag{3.19}$$

$else$

$$w_{i+1} = 0$$

Once the photon history is terminated, another photon is launched. The Monte Carlo simulation is repeated until the expected total number of photon $N_{photons}$ is reached.

d. Converting to fluence rate

Once all photon histories are completed, the *Absorption* matrix expressed in [photon_weight/voxel] must be converted to obtain the fluence rate matrix expected [J/cm²]. The *Absorption* matrix has to be normalized by the volume of voxels V_{voxel} [cm^3] and the total number of photon $N_{photons}$ in the simulation. Then, each voxel value of the resulting matrix [1/cm^3] must be divided by the absorption coefficient of the medium associated to obtain the fractional transport $Transport$ matrix [1/cm^2].

$$Transport[l,m,n] = \frac{Absorption[l,m,n]}{V_{voxel}.N_{photons}.\mu_a[l,m,n]} \tag{3.20}$$

Since each voxel can represent a different medium, heterogeneity of biological tissues is taken into account. Thus, a fluence rate matrix [W.cm^{-2}] is easily obtained by multiplying the $Transport$ matrix with the light power source [W].

The larger the number of simulated photon is, the longer the computing time is. The computing time also changes according to the optical properties of modeled tissues. If the absorption coefficient increases, the number of steps required to simulate a full photon history decreases. Conversely, if the scattering coefficient increases, the number of required steps to simulate a full photon history increases. On a sequential structure, a mean simulation time *t* can be estimated with the following calculation:

$$t = N_{photons}.t_{step}.N_{steps} = N_{photons}.t_{step}.\frac{\ln(threshold)}{\ln\left(\frac{\mu_s}{\mu_s+\mu_a}\right)} \tag{3.21}$$

Where t_{step} [s] is the mean time required to achieve a photon step, $N_{photons}$ is the number of photons simulated, N_{step} is the number of steps required for each photon and $threshold$ is typically 10^{-4}. Those factors are computed using previous Monte-Carlo simulations and are valid only for a given computing configuration.

For example, to compute 10^6 photons in a homogeneous medium composed with the absorption $\mu_a = 0.2$ cm^{-1} and scattering $\mu_s = 160$ cm^{-1} coefficients, which correspond to mean brain optical properties, (a mean t_{step} with such coefficients is approximately 700 ns[2]) and with a threshold fixed to 10^{-4}, the required mean time is about 65 minutes.

Finally, all these previously described steps are summarized in figure 3.2. A photon is launched and its step size is computed according to optical coefficients of the medium. Then, the *hop-drop-spin* sequence is computed to move through matter until the photon's death. This process is then repeated to reach a large number of generated photons.

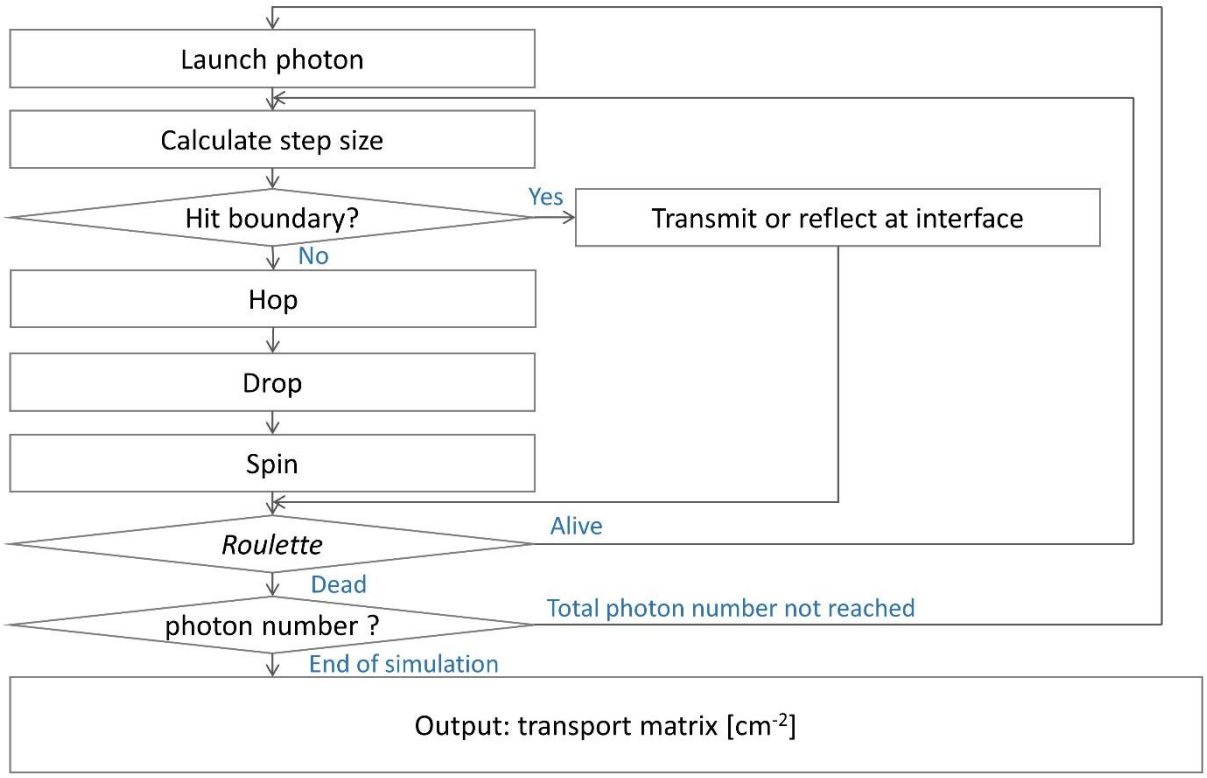

Figure 3.2: Flow-diagram of a standard steady-state Monte-Carlo simulation.

[2] Monte-Carlo simulation executed on a 2.80 GHz Intel Xeon CPU

2. Accelerated Monte-Carlo: state of the art

Although Monte-Carlo algorithm remains the reference method to model light propagation in turbid media, its use in clinical routine is constrained by the time needed to achieve accurate results. With the improvement of computing capacity and new technologies, some recent technics used to accelerate Monte-Carlo simulations are listed.

a. Sequential methods

Among them, some methods use the results of previous Monte-Carlo simulations or combine them with analytical methods in order to decrease the number of simulated photon required.

i. Scaling methods

The scaling methods are the first approaches in use to speed up Monte-Carlo simulations [222-225]. Single or few Monte-Carlo simulations, considered as *offline references*, are performed to record several features such as number of interactions, step sizes or photons' trajectories. These recordings are then modified *inline* by applying scaling relations in order to avoid to perform a whole Monte-Carlo simulation and to obtain a fast calculation of total reflectance and transmittance. A condensed version of monte-Carlo simulation was proposed by Graaff et al. in 1993 [226].

ii. Perturbation methods

Based on a similar idea, the perturbation method requests previous Monte-Carlo simulations to be achieved [227-239] to consider resolution in a heterogeneous medium. Several features deduced from previous Monte-Carlo simulation in homogeneous media are stored all along the path length, the exit weight and the number of interactions encountered during all photons histories. After collecting these data, inhomogeneities are introduced into the structure of the second Monte-Carlo simulation and impact the photon weight [227, 230, 233, 240].

iii. Hybrid methods

Another approach to accelerate Monte-Carlo simulation is to introduce analytical solutions in determined areas in order to avoid a full Monte-Carlo simulation on the whole

space. Flock et al. were the first to introduce the term of hybrid Monte-Carlo method [241]. Several previous Monte-Carlo simulations with different optical properties were aggregated in order to extract a function. This function is then injected into a diffusion theory solving to obtain better results. Tinet et al. continued in this idea and proposed a two stages semi-analytical Monte Carlo simulation [242, 243]. The first stage was dedicated to the information generator, i.e., to collect total reflectance and transmittance for each scattering event and to reintroduce them into the algorithm to decrease the required number of photons. The second stage used results obtained from the first one to calculate analytically photons propagation. At the same time, Wang et al. proposed a solution closest to the idea of hybridization of the Monte-Carlo method [244, 245]. Monte-Carlo solving was used to simulate the light propagation in areas close to the source and analytical equations were solved at large distance from the source. Alexandiakis et al. extended this idea to solve the photons migration in the frequency domain [246, 247]. Modulation of phase and amplitude occurred when light was reflected by turbid media and were used to characterize optical properties [248-250]. This discrimination technic was improved in other studies to differentiate high scattering from low scattering regions, isotropic from anisotropic regions or homogeneous from inhomogeneous regions [251-254].

b. CPU parallelism and Internet

i. CPU parallelism

The first published attempt to parallelize algorithm was Kirkby et al. in 1997 [255]. The authors proposed to build a network between several computers and parallelize Monte-Carlo simulation on these different CPU. Once 1000 photons were generated on all the computers, results were stored in a file on a disk that was accessible to all connected computers in the network. A maximum of 24 computers were declared because each of them had access to the common disk during one hour per day. However, with the advent of multiple Central Processing Unit (CPU) or multiprocessing, new possibilities to speed up Monte-Carlo simulations have emerged. Colasanti et al. developed a code addressed to multiple CPU contained into one unit computer. The high performances exhibited by this new type of processor (cost about 2500$) considerably speed-up the resolution of light transport [256]. Reported acceleration reduced the computing time by a factor equal to the number of CPU used. It ranged from a factor 100 for a number of 128 CPU to a factor 1000 for a number of 1024 processors, the maximum capacity available in 2000. A recent coprocessor (Intel Xeon

Phi) was used to simulate light propagation in turbid media [257].

ii. Internet-based parallelism

The Internet revolution has also strongly impacted performances of high computational algorithm. This technology recently used in treatment planning systems mostly dedicated to radiotherapy tends towards its application into the simulation of visible photons simulation [258-261]. Thus, using the mapReduce[3] environment provided by Google to facilitate development of parallel algorithm including cloud computing, Pratx et al. created a cloud version of the MC321 Monte-Carlo code by Steven Jacques [262, 263]. This monte-Carlo code simulated the photons propagation in steady state in a homogeneous and infinite medium and results could be stored in spherical, cylindrical and planar coordinates. Performances of the fastest approach described in the paper reached 2 minutes for simulating 100.10^6 photons, compared to 28 minutes for a single thread. A speed-up of 1258 was reported in comparison with a value of 1080 with the fastest Monte-Carlo method available in 2011 on a single computer. A peer-to-peer Monte-Carlo code was also developed by Doronin et al. in order to simulate photon transport in heterogeneous turbid media [264].

c. GPU acceleration

Recently, one major advancement in parallel computation was realized using the Graphics Processing Unit (GPU) to speed-up considerably Monte-Carlo simulations at a limited cost. The first article introducing this new technology was the study of Erik et al. in 2008 showing that a low-cost GPU (110$) could provide extreme acceleration [265]. Authors transposed a code used to simulate photons migration in a semi-infinite, homogenously scattering and non-absorbing medium in a Compute Unified Device Architecture (CUDA) architecture [224]. This platform, ownership of the trademark NVIDIA (NVIDIA Corporation, Santa Clara, CA, USA), was released in 2007 and enabled to develop a C, C++ or Fortran code in order to take advantage of the computing parallel possibilities offered by a GPU. To compare the performances of their code, authors simulated 500,000 photons in a White Monte-Carlo model (i.e., a Monte-Carlo simulation of a homogeneous medium with zero absorption) on both CPU and GPU. The speed-up was about 1000 times faster with the GPU: 8513 seconds for the CPU, 7.9 seconds for the GPU. Their work was enhanced two years later by proposing a GPU version of the MCML code [169] and optimizing fast access

[3] mapReduce: System and method for efficient large-scale data processing [online], available at: http://www.google.com/patents/US7650331 (accessed September 21, 2017)

memories. They reported a GPU acceleration of about 600 times faster than CPU version in heterogeneous media. The most popular GPU version of time-resolved photon propagation in a 3D turbid media was proposed by fang et al. in 2009 [266]. They claimed an improvement of 300 times faster than conventional CPU simulation. Other simulations were then developed using GPU parallelization. Martinsen et al. implemented a photons transport simulation through turbid media and reported an acceleration of 70 times faster than CPU only [267]. Several other studies also proposed to simulate photons through turbid media with several discrepancies [268-270]. Carbone et al. introduced the GPU computation in order to accelerate the solving of the forward problem to retrieve optical coefficients of inhomogeneities introduced in homogeneous medium [271]. Leung et al. simulated ultrasound-modulated light in turbid media with an improvement of 125 times of the standard computing time [272]. Powell et al. took the advantage of GPU acceleration to simulate acousto-optic effect in heterogeneous turbid media [273]. Yang et al. generated a diffuse reflectance value in 0.08ms in order to interpret quickly fiber-based and camera-based measurements of remitted light from biological tissues [274]. The more recent article, provided by Li et al. compared the performances of 3 different GPU in order to study the behavior of polarized photons as they propagate through complex biological tissues [275]. All these papers demonstrate a strong interest in this technology that provides the better cost-efficient choice to improve Monte-Carlo simulations performances.

II. GPU Monte-Carlo implementation

Monte-Carlo method is considered as the reference in the dosimetry computation for both ionizing and non-ionizing radiation. Because this technic is highly time-consuming in conventional central processing unit (CPU) implementation, several improvements have been developed to speed-up simulations. Among them, the use of GPU in order to parallelize algorithm provides a cost-efficient solution to accelerate Monte-Carlo method. In this paragraph, a parallel implementation of Monte-Carlo using GPU technology is described.

1. Monte-Carlo implementation

a. History

One of the most important methods for the computer performances improvement has been, for four decades, to increase the speed at which the processor's clock operated. Increasing this clock speed resulted in also increasing the number of operations performed per

second by the CPU. The multiplication of CPU in supercomputer has been the starting point of the new point of view in the escalation of computer power. Since 2005, instead of stretching the limits of processor's clock speed, the use of multi-core CPU (2 to 16 cores) has been allowing to strongly increase performances by parallelizing tasks. In 2006, the manufacturer NVIDIA unveiled the first GPU which was not dedicated to produce a feed of output images to a display but to enable general-purpose computation. Thus, this new electronic component could be seen as a multi-core CPU owning thousands of tiny processing units. Currently, general-purpose computing on graphics processing units (GPGPU) is on the rise in image processing, fluid dynamics and bioinformatics.

b. Introduction to parallel world

The main goal of parallelized implementation is to create an algorithm capable to be executed simultaneously in different processors in order to obtain the output in less time. To exemplify this concept, matrix calculation can be easily integrated in a parallel computing. Let us consider the sum of the two $m \times n$ matrices *A* and *B*:

$$\begin{bmatrix} a_{1,1} & \cdots & a_{1,n} \\ \vdots & \ddots & \vdots \\ a_{m,1} & \cdots & a_{m,n} \end{bmatrix} + \begin{bmatrix} b_{1,1} & \cdots & b_{1,n} \\ \vdots & \ddots & \vdots \\ b_{m,1} & \cdots & b_{m,n} \end{bmatrix} = \begin{bmatrix} a_{1,1} + b_{1,1} & \cdots & a_{1,n} + b_{1,n} \\ \vdots & \ddots & \vdots \\ a_{m,1} + b_{m,1} & \cdots & a_{m,n} + b_{m,n} \end{bmatrix} \quad (3.22)$$

From a sequential point of view, this sum requires $m \times n$ consecutive sums. If a sum takes t_{sum} time, this operation necessitates $t_{sum} \times m \times n$ without taking into account access time and reading/writing time on the hard disk drive that contains values of matrices. However, from a parallelized point of view, because all $m \times n$ sums are performed simultaneously, the entire computation takes only t_{sum} time. This example easily shows the gain provided by such implementation (see figure 3.3).

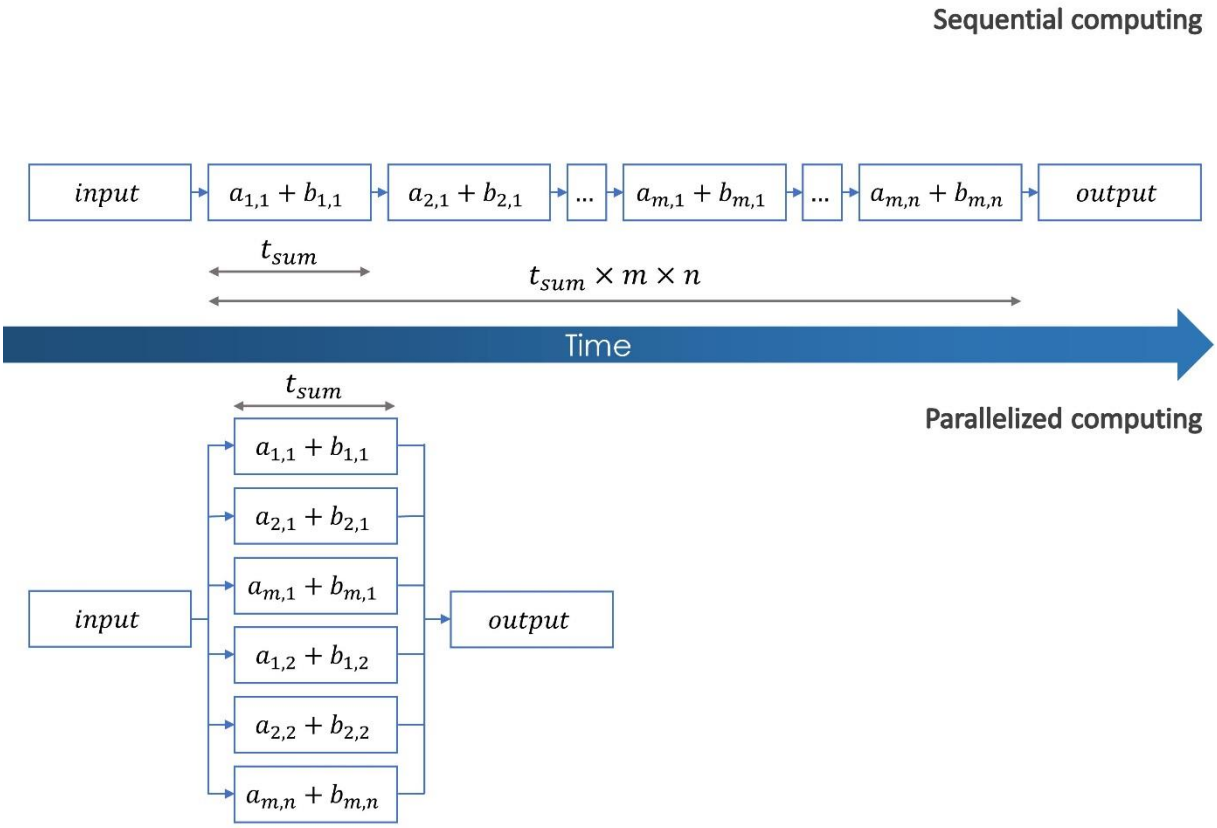

Figure 3.3: Sequential versus parallelized computing: time required to perform the sum of two $m \times n$ matrices is decreased of a $m \times n$ factor.

To be executed in parallel, a computer code must be cut into different independent processes. Several criteria have been defined to evaluate performances. Total computing time T is the sum of the sequential computing time T_S and parallel computing time T_P:

$$T = T_S + T_P \tag{3.23}$$

According to the Amdhal's law [276, 277], the minimum computing time T_{np} on a computer owning *np* processing units is equal to:

$$T_{np} = T_S + \frac{T_P}{np} \tag{3.24}$$

The acceleration A_{np} due to the parallelism is then defined as:

$$A_{np} = \frac{T}{T_{np}} = \frac{1}{(1-\alpha) + \frac{\alpha}{np}} \tag{3.25}$$

Where α is the proportion of execution time that benefits from parallelized implementation (e.g., according to a given code implemented, if 60% of its execution time could be subject of a speedup, α is equal to 0.6).

The parallelization efficiency E_{np} is the ratio of the acceleration A_{np} and the number of processing units *np*:

$$E_{np} = \frac{A_{np}}{np} = \frac{1}{(1-\alpha).np + \alpha} \tag{3.26}$$

As an example, if α= 0.99, which means that 99% of the entire programming code could be parallelized on a computer owning *np* = 99 processing units, the acceleration is equal to 50 and parallelization efficiency is equal to 0.51. Thus, the one percent of the programming code that cannot be parallelized takes the half time of the entire computing time.

Two rules must be validated in order to know whether a programming code can be parallelized or not. Firstly, the result must not be altered if a random permutation occurs between processing unit execution. If an inversion is made provoking the execution of the code in the unit execution *np* instead of the unit execution *np*-1, the output must not be affected. Secondly, two codes in execution must be totally independent. The output of the unit execution *np* must be not the entry of the unit execution *np*-1 (*data dependence*) and the output of the two units execution *np*-1 and *np* must not change the same variable (*output dependence*).

c. Architecture

The particularity of the GPGPU programming lies in the architecture of the device used. The term “Host” refers to the CPU and its memory; the “Device” to the GPU. Only the parallelized code is equally distributed into several unities called “kernel” as referred previously as the “tiny processing units” and located in the device (see figure 3.4). Each kernel instance is called “thread”. Several kernels constitute a “block” and several blocks constitute a “grid”. In some cases, it can be useful to define several grids. It is commonly used to illustrate this interlocking in 2D or 3D. However, no determined organization of kernels is defined in the device. This compartmentalization of the GPU memory is defined according to hierarchy of electronic components embedded in the printed circuit board of the graphic processor.

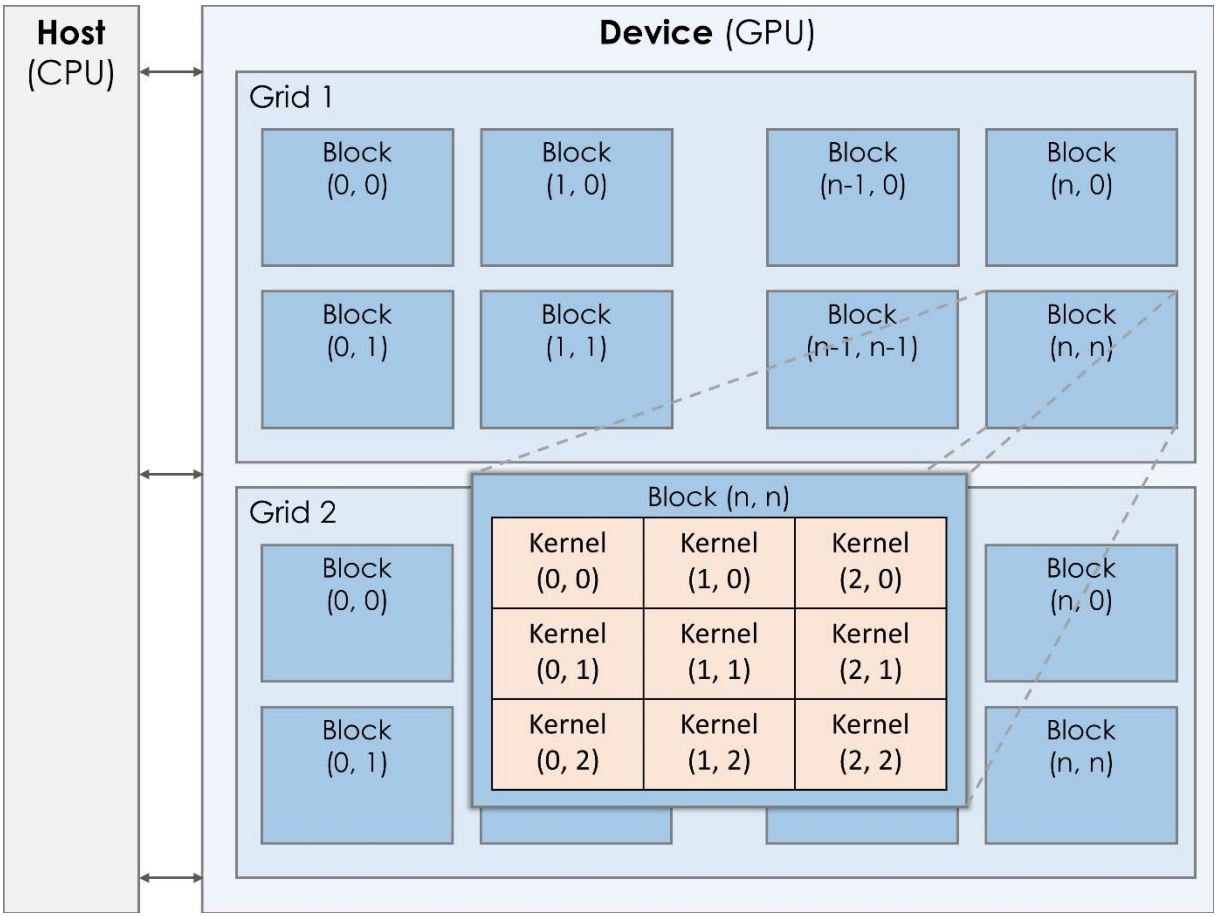

Figure 3.4: Each kernel hosts the parallel part of the code; several kernels are gathered into a block and all blocks constitute a grid.

While the CPU memory can be considered as unique, the GPU memory is divided into six different memories as follows (see figure 3.5):

- Global memory: this is the largest memory available in the device. The main asset is that stored data are visible from all kernels in the device and can store large amount of data. Each thread can read and write in this memory but the access is very slow.
- Constant memory: this one holds only data that will remain constant during the execution of the code. Thus, its authorization is in read-only, which allows a more rapid access to constant data.
- Texture memory: similar to the constant one, it can be used when memory access exhibits a strong dependence with local neighbor threads. When all read accesses in a warp (merging of 32 threads) are physically adjacent, texture memory can decrease memory traffic and increase performances in comparison to the global memory.

These next three memory types are visible to the host which can read and write.

- Local memory: it is contained into each block and is visible only to one thread.

Threads have read and write access to this memory.

- Register: this one owns the same specifications as the local memory. The space available is smaller than the local memory but, because registers reside on the GPU chip, the access to data is very fast.
- Shared memory: this memory resides also on the GPU chip but is visible to all threads contained in a block in a fast read and write access.

Using all these six different memories efficiently, program performances can be optimized and the parallelization efficiency improved.

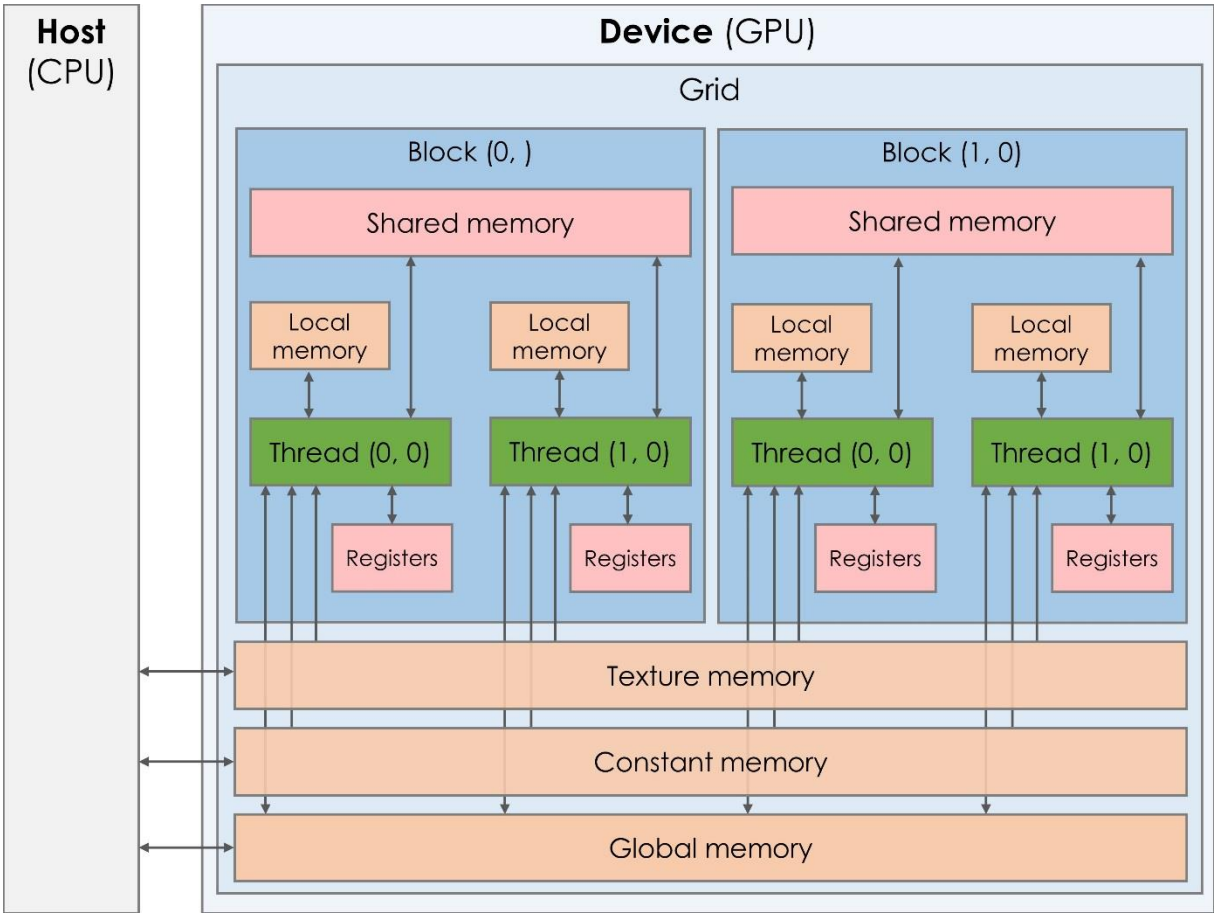

Figure 3.5: The six different memories constituting the device memory and their read and write access.

2. Parallel Monte-Carlo

a. Parallel computing platform

Numerous parallel computing platforms have been developed to communicate with the device. Among them, two are commonly used to develop applications on GPGPU: Compute Unified Device Architecture (CUDA) and Open Computing Language (OpenCL).

In 2007, the American company NVIDIA, mostly known for its GPU production, released the CUDA platform. This parallel computing platform and application programming interface (API) was developed to facilitate the communication with GPU and introduce the use of kernels as processing units. CUDA was elaborated with programming languages such as C, C++, and Fortran. This platform can only work with the use of NVIDIA GPU. In return, NVIDIA provides a well-integrated library allowing an easier control of GPU programming.

In 2008, Apple Inc. developed a proposal of framework dedicated to GPGPU. In 2009, the Khronos Group, a non-profit technology consortium, released the initial version of this framework. OpenCL was elaborated with C and C++ programming languages. The main difference with its CUDA rival lies in the opening to other GPU brands such as AMD. The use of OpenCL does not require a NVIDIA GPU. However, codes developed on this platform will not run optimally on all of them without strong optimization work.

b. Implementation

Our Monte-Carlo method has been designed toward its implementation in a future treatment planning system (TPS) dedicated to photodynamic therapy for glioblastoma (GBM) treatment as introduced previously in chapter I. Monte-Carlo simulations rely on segmented MRI examinations for which each voxel is classified according to the type of biological medium it belongs to (white matter, grey matter, tumor, edema, necrosis). This data represents a 3D matrix in which light sources are modelled according their location and shape, basically one or several cylindrical diffusers.

Structures of Fang et al. [266] and the *mcxyz* CPU code by Jacques et al. inspired our GPU Monte-Carlo method [278, 279]. Several input features are required to execute the simulation. 12 parameters are written in a first text file:

- Number of voxels on each axis (*Nx*, *Ny*, *Nz*),
- Voxels size on each axis (*dx*, *dy*, *dz*),
- Coordinates of a first point, localized on the x, y and z-axis, corresponding to the beginning of the cylindrical diffuser (x_{in}, y_{in}, z_{in}),
- Coordinates of a second point, localized on the x, y and z-axis, corresponding to the end of the cylindrical diffuser (x_{out}, y_{out}, z_{out}).

The matrix corresponding to the segmentation output (i.e., biological medium of each voxel) is also stored in constant memory. This matrix is composed of *Nx.Ny.Nz* indices. Each index refers to a lookup table in which optical properties of each medium type are stored.

Each thread generated on the GPU runs an entire photon history (from its birth with initial properties to its death by the *roulette* process) (see figure 3.6). Thus, depending on hardware capacities, several photon histories are simultaneously launched. Propagation process is the same as presented in chapter II, namely:

- A photon is first created at a random position between the two extremities (x_{in}, y_{in}, z_{in}), and (x_{out}, y_{out}, z_{out}) the diffusing part of the cylindrical diffuser inserted into the brain's patient, orientated isotropically (i.e., uniformity in all orientations around the source) and with a weight of 1,
- A step size is computed using optical properties where the photon belongs,
    - If the photon does not cross boundaries of the voxel, it moves to its next location and loses weight according to the length of its step size and absorption property of the voxel
    - If the photon crosses boundaries of the voxel, it moves at this boundary, loses weight according to the length of its distance to the voxel's boundary and absorption property of the voxel and a remaining step size is computed to continue its propagation,
    - This last step is repeated until the photon has traveled the total remaining step size,
- A new random direction is computed using optical properties,
- Steps are repeated (from the generation of the step size) until the roulette algorithm kills the photon or the photon exits the entire volume.

Depending on hardware capacities, the required number of simulated photons is most of the time largely superior to the number of kernels available. Thus, once a kernel finished its photon history, another photon propagation thread is repeated in the same kernel. Every kernel repeats the entire simulation process until the expected number of photons is reached to obtain an accurate result.

The output of the simulation is the *Nx.Ny.Nz* Absorption matrix [photon_weight/bin], which is normalized to obtain the transport matrix [cm^{-2}] and multiplied with the power source [W] to finally obtain the fluence rate [$W.cm^{-2}$].

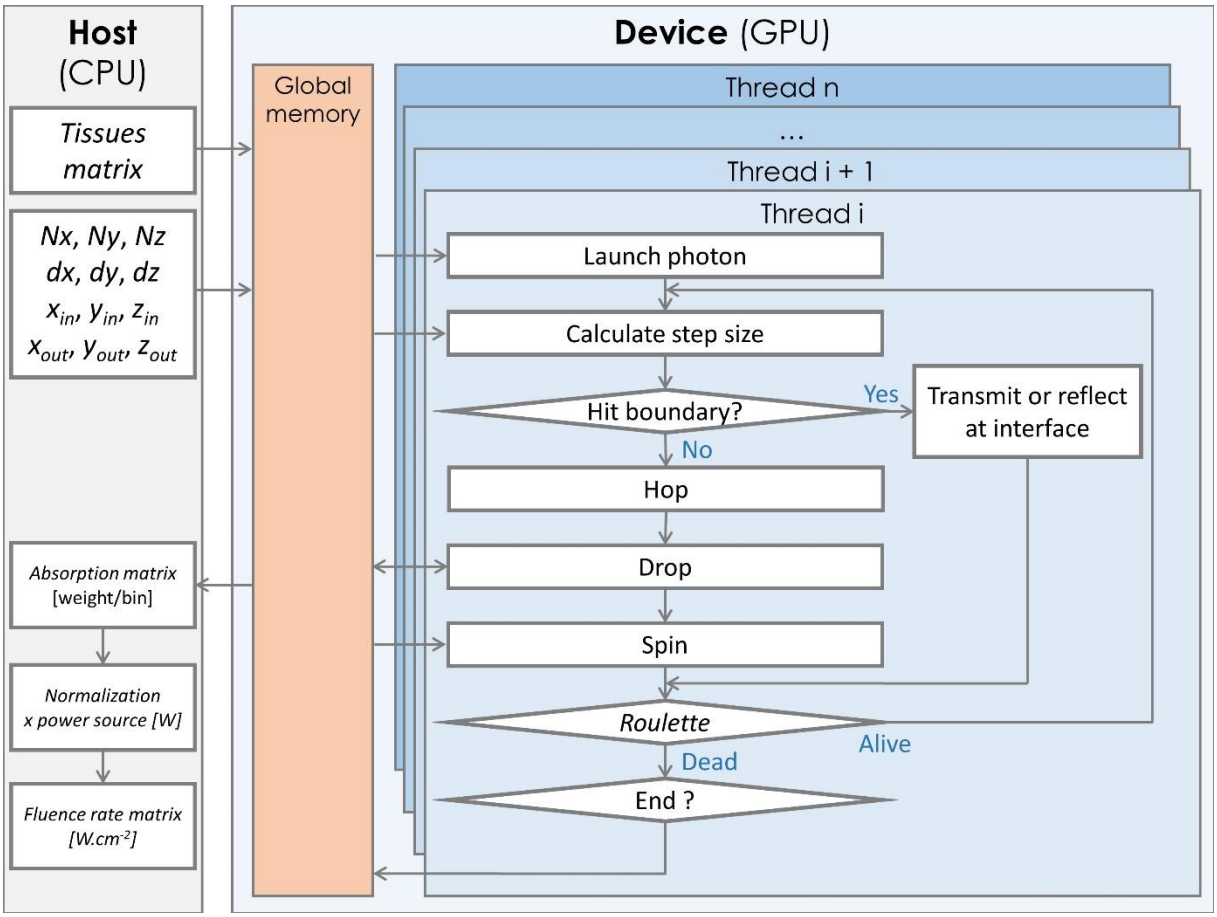

Figure 3.6: Pipeline of the GPU Monte-Carlo simulation dedicated to interstitial photodynamic therapy (iPDT) for glioblastoma treatment.

3. Particularities of Parallelized Monte-Carlo

Due to the rapid execution and to the high number of parallelized tasks, specific errors of GPU programming can occur during the simulation. Here is a list of main issues encountered during the development of the Monte-Carlo code.

a. Random number generator

The very essence of Monte-Carlo method lies in the random characteristic of the algorithm. An efficient random number generator in a CPU programming is essential. In GPU programming, the generation of random number is a very critical part due to the high number of randomization needed by each thread. Because generating a pure random number by using only a computer is unrealizable, pseudo-random number generators (PRNG) have been developed to produce numbers whose properties approximate those of sequences of real random numbers [280]. Among them, the Mersenne Twister algorithm is the most famous PRNG and is used in numerous applications requiring generation of random number [281]. In

2011, one of the authors released a lighter version of the Mersenne Twister dedicated to the GPGPU computing called “Tiny Mersenne Twister” [282].
This PRNG provides a lighter implementation than the classical Mersenne Twister algorithm and is optimized to GPGPU requiring large state generators. Moreover, it has been evaluated using the strict statistical test “TestU01” provided by L’ecuyer et al. [283] and results reported pretty good quality of the outputs. Although, the initial Tiny Mersenne Twister own a period of generated sequences of 2^{19937}-1 iterations, the tiny version owns one of 2^{127}-1. Besides its correct performances, this particular PRNG has been selected and implemented in the Monte-Carlo mostly because it is available on OpenCL and CUDA platforms.
The PRNG is seeded in each thread using the time corresponding to the program’s launch and the index of the thread in order to obtain a different seed in every thread.

b. Atomic operation

The atomicity property is the second critical point in GPU Monte-Carlo. This term designates an operation (in most cases addition, subtraction, multiplication or division) performed by two or more threads on the same allocated memory location and at the same time. The probability of such an addressing conflict is important due to the numerous threads created in a GPU program. In the global memory, which is visible for every thread, several threads can expect to write in the same allocated memory location. When a large number of threads read and write on the same global memory location concurrently, which is the case in the “drop” event typically, part of concurrent threads will not succeed to write in the global memory. If this property is not taken into account, absorption can be underestimated.
To circumvent this issue, atomic operations have been created to allow this accumulation on the same memory location without any loss and to ensure the integrity of results. For example, if a thread reads a data at a given address in global or shared memory, modifies the contained value and writes back the result to the same address, no other thread can access this address during this operation. Thus, this modification is guaranteed to be performed without competitive issue from other threads. However, these operations are computationally expensive and slow down the acceleration due to waiting threads during an atomic process.

c. Synchronization

Because photons propagation in Monte-Carlo method is governed by random properties, a photon propagated in a thread *i* and another photon propagated in the thread *i+1*

will not terminate their history at the same time. To counterbalance this probable time interval, the device can synchronize all the threads that are contained in the same block. When the thread *i* reaches the synchronize command, it stops its computing until all threads contained in its block also reaches this command. Thus, this barrier allows to keep a homogeneous progression of the threads during the simulation.

d. Memories optimization

The last step to improve performances and rapidity of the execution is the optimization of the memory's allocation. Although the constant memory is relatively small (i.e., 65536 bytes, approximately 8 Mo), it remains sufficiently large to store the 12 input variables (48 octets). Conversely, matrix containing indices of tissues owns the same dimensions as MRI standard volume, i.e., 256x256x150 voxels. This matrix is approximately 40Mo and cannot be sent into the constant memory. Also, because absorption matrix will be constantly modified during the execution and owns the same dimensions as the tissue matrix, these two matrixes must be stored into the global memory. Texture memory cannot be used because there is no spatial dependence between threads.

Regarding the number of grids, blocks and threads per block, no law is currently available to compute the optimal configuration. Several tests must be performed to evaluate the best configuration. Moreover, this arrangement is only optimal for a given GPU. That is why a list of recommended GPU is often provided with particular GPU program.

III. Model validation

Once the GPU Monte-Carlo implemented, a comparison with experimental measurements is expected to validate results. This paragraph details the methodology used to assess the results of Monte Carlo algorithm from experimental measurements. Additionally, optimization of the performances to produce fast Monte-Carlo simulations (such as memories optimization and programming language) is highlighted.

1. Phantom creation

A phantom of known optical properties is firstly created. Several types of phantom are used to mimic precise optical properties, such as optical polymer gels [284-286], silicone [287, 288], Al2O3 powders [289, 290] or 3D printing [291, 292]

However, the most popular and easier way to build such a phantom is to mix Intralipid liquid,

India ink and water [194, 293-296]. This type of phantom is usually applied as a biological tissue modelling in light dosimetry experimentations. The concentration of Intralipid controls the scattering coefficient because the absorption coefficient is negligible. Conversely, India ink only affects the absorption coefficient, and not the scattering one. Thus, mixing with the right quantity of Intralipid liquid and India ink in water solution, a phantom with controlled optical properties can be elaborated.

Such phantoms have already been extensively studied, and calculations of quantities to be mixed relied on the multi-center study of Spinelli et al. [296], published in 2014. In this paper, the same optical phantom based on Intralipid and India ink was characterized using nine different methods in nine different research laboratories from six countries. They evaluated the absorption and scattering properties at three different near infrared wavelengths (633, 750 and 830nm). By exploiting results of each laboratory, reference values at these three wavelengths for the intrinsic absorption coefficient of India ink and the intrinsic reduced scattering coefficient of Intralipid concentrated at 20% were determined with an uncertainty of respectively approximately 2% or better, depending on the wavelength considered, and 1%,. Using these values, they proposed a mathematical model to obtain masses of India ink and Intralipid:

$$m_{ink} = \frac{\mu_a}{\varepsilon_{a,ink}} . m_{tot}$$

$$m_{il} = \frac{\mu'_s}{\varepsilon'_{s,il}} . m_{tot} \qquad (3.27)$$

$$m_{water} = m_{tot} - m_{ink} - m_{il}$$

where m_{ink} is the mass of India ink [g], m_{il} is the mass of Intralipid [g], m_{water} is the mass of water [g], m_{tot} is the total mass of the phantom [g], $\varepsilon_{a,ink}$ is the intrinsic absorption coefficient of India ink [m^{-1}], $\varepsilon_{s,il}$ is the intrinsic scattering coefficient of Intralipid [m^{-1}], μ_a and μ'_s are the desired absorption and reduced scattering coefficients of the phantom.

Values of absorption μ_a = 0.02 mm^{-1} and reduced scattering μ'_s = 2 mm^{-1} correspond to mean optical properties of normal human brain tissues with infiltrated glioma cells [75, 117, 297, 298]. These values will be considered as references in this study.

Thus, for $\varepsilon_{a,ink}$ = 384 ± 8 mm^{-1}, $\varepsilon'_{s,il}$ = 26.3 ± 0.4 mm^{-1}, μ_a = 0.02 mm^{-1}, μ'_s = 2 mm^{-1} and m_{tot} = 1000 mg, masses of India ink, Intralipid 20% and water are respectively m_{ink} = 0.052g, m_{il} = 76.046g and m_{water} = 923.902g.

2. Monte-Carlo validation by comparison with experimental measurements: materiel and methods

A specific experimental design was set-up to characterize the fluence rate emitted by different cylindrical diffusors commonly used in PDT treatment within the created phantom.

a. Calibration factor

The only variable that can be measured in light dosimetry experiment is the light power [W]. To convert this power value $P_{measured}$ [W] into fluence rate value ϕ_{medium} [W.cm^{-2}], a calibration factor CF_{medium} dependent of the surrounding medium must be calculated to enable this conversion:

$$\phi_{\text{medium}} = \text{CF}_{medium} . \text{P}_{\text{measured}} \quad (3.28)$$

In their two papers, Marijnissen and Star provide a complete methodology to obtain this calibration factor CF_{medium} [299, 300] which is recommended by the American Association of Physicists in Medicine (AAPM) [301, 302]. This factor is the combination of a calibration factor determined firstly in the air CF_{air} and four other corrective coefficients.

$$\text{CF}_{medium} = \text{CF}_{air} . \text{F}_n . \text{F}_p . \text{F}_b . \text{F}_i \quad (3.29)$$

where F_n is a correction factor enabling to compensate the loss of light due to interface between the sensor and the surrounding medium using their respective refractive indices [dimensionless].

F_p is a perturbation correction [dimensionless].

F_b is a correction of the collection photons loss due to the surface occupied by the fiber on the detection sphere [dimensionless].

F_i is a correction of the sensor non-homogeneity response [dimensionless].

Combining these empirical and theoretical factors, a calibration factor CF_{media} can be estimated for a given biological medium and for a given isotropic probe in order to obtain fluence rate value ϕ_{medium} [W.cm^{-2}] in this medium:

$$\phi_{\text{medium}} = \text{P}_{\text{measured}} . \text{CF}_{air} . \text{F}_n . \text{F}_p . \text{F}_b . \text{F}_i \quad (3.30)$$

First, a calibration factor in air CF_{air} must be determined (see figure 3.7). A bare fiber was fixed on an experimental optical bench and connected to a 630nm laser source. In the other side of the optical bench, two detectors were placed in front to the output of the bare fiber. The first sensor is an isotropic probe (IP85, Medlight, Ecublens, Switzerland) which will be used in future power measurements. The sensor was fixed on a rotating support enabling to vary the angle θ between incident beam and tip axe. The second is a flat sensor

(818-SL, Newport, Irvine, CA, USA) whose size of the detection cell is 1cm². Direct measurement with this last sensor enables to obtain an estimation of the irradiance [W.cm^{-2}]. Thus, measuring the power collected at the same location with both the isotropic probe (a mean is performed according to the irradiation angle θ) $P_{mean\_isotropic}$ and the flat sensor, a calibration factor in air CF_{air} can be estimated:

$$CF_{air} = \frac{P_{flat}}{P_{mean\_isotropic}} \tag{3.31}$$

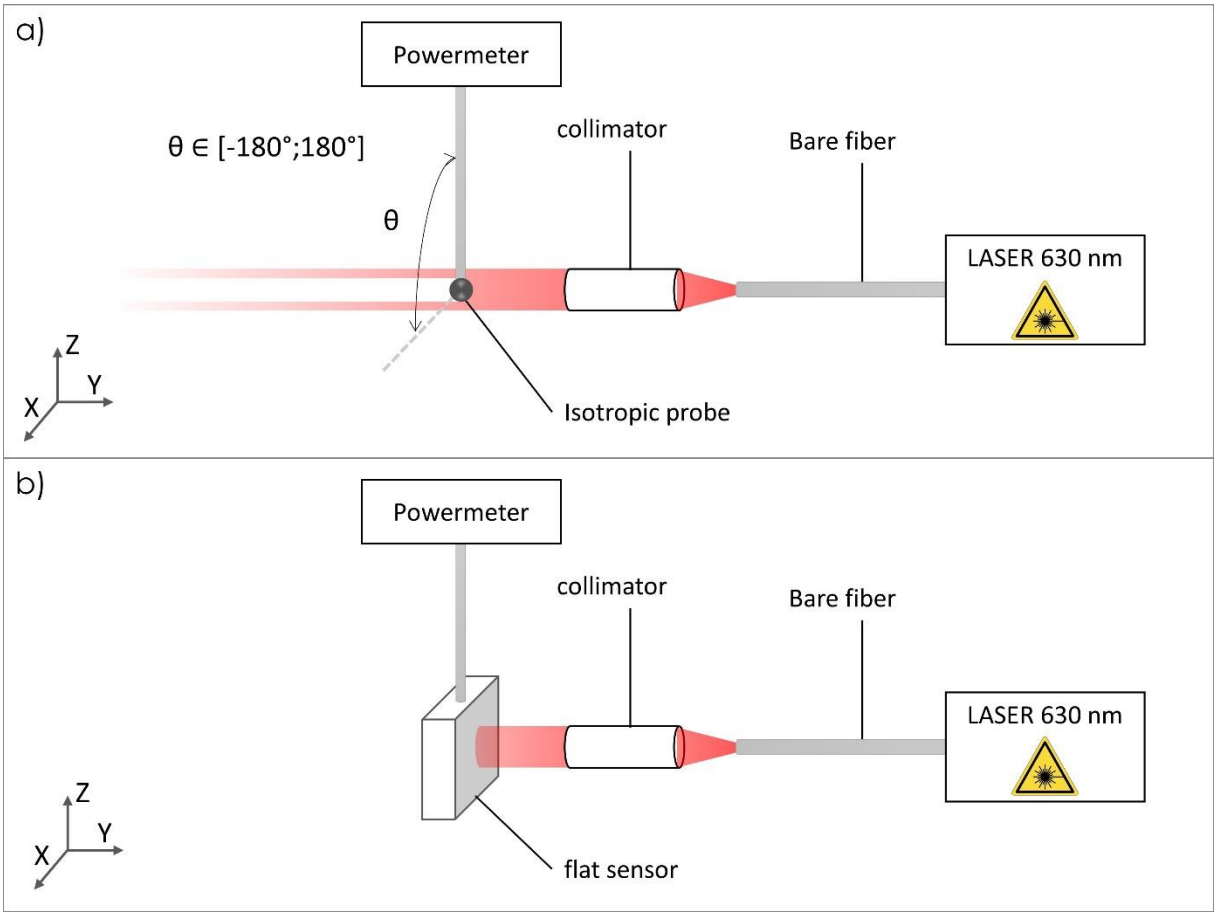

Figure 3.7: Optical bench for calibration factor in air estimation.

The correction factors F_n, F_b and F_p were determined from the papers of Marijnissen et al. [299, 300]. The non-homogeneity response factor F_i was determined from the standard deviation of measurements using the isotropic probe according to the irradiation angle θ.

b. Phantom measurements procedure

A cylindrical diffuser is inserted in a 15x15x15 cm black box (to avoid light reflection) and fixed so that it is as straight as possible. A sensor (IP85, Medlight, Ecublens, Switzerland) is fixed to a mobile support and located at precise coordinates, e.g., against the

cylindrical diffuser (see figure 3.8). Once the sensor and the optical fiber are placed, the phantom pours inside the black box in order to fill it entirely. A 635 nm laser source is then connected to the SMA connector of the fiber.

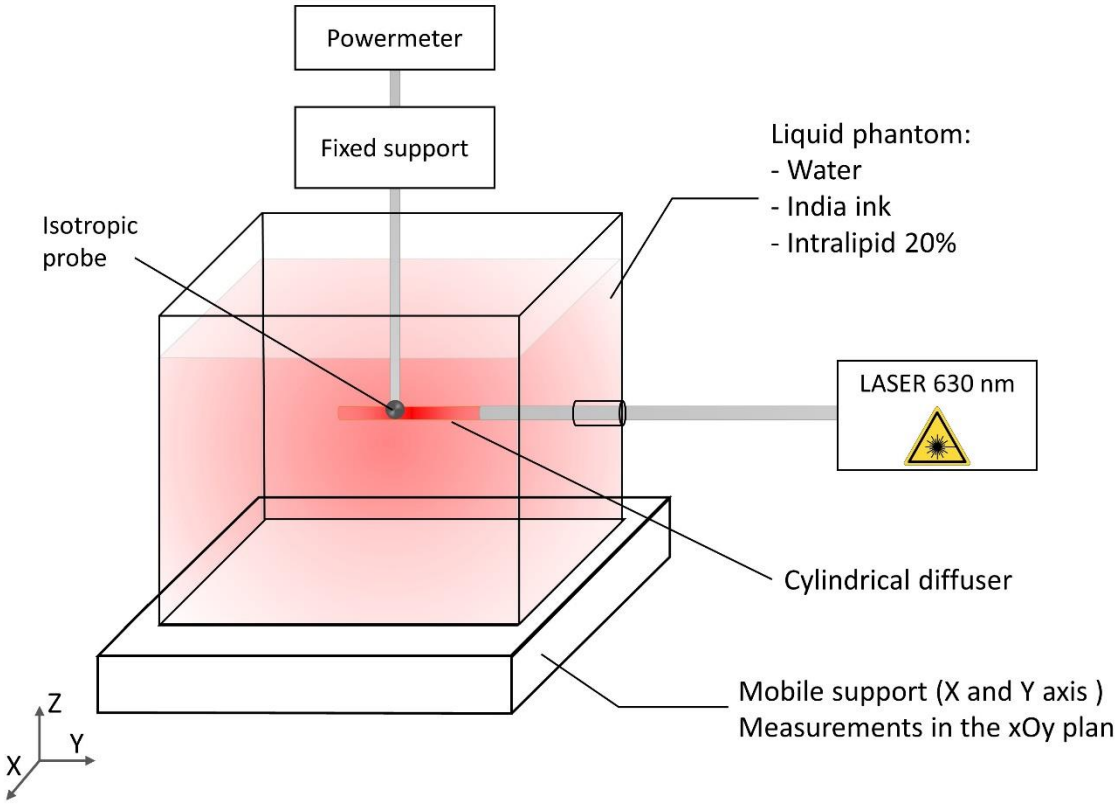

Figure 3.8: Experimental plan for light power measurements in the phantom.

Power measurements are realized according to the horizontal cut plane of the cylindrical diffuser. With a step size of one millimeter, the sensor is moved from the beginning to the end of the cylindrical diffuser (y axis) and until it reaches a 1 cm distance from light source (x axis) (see figure 3.9).

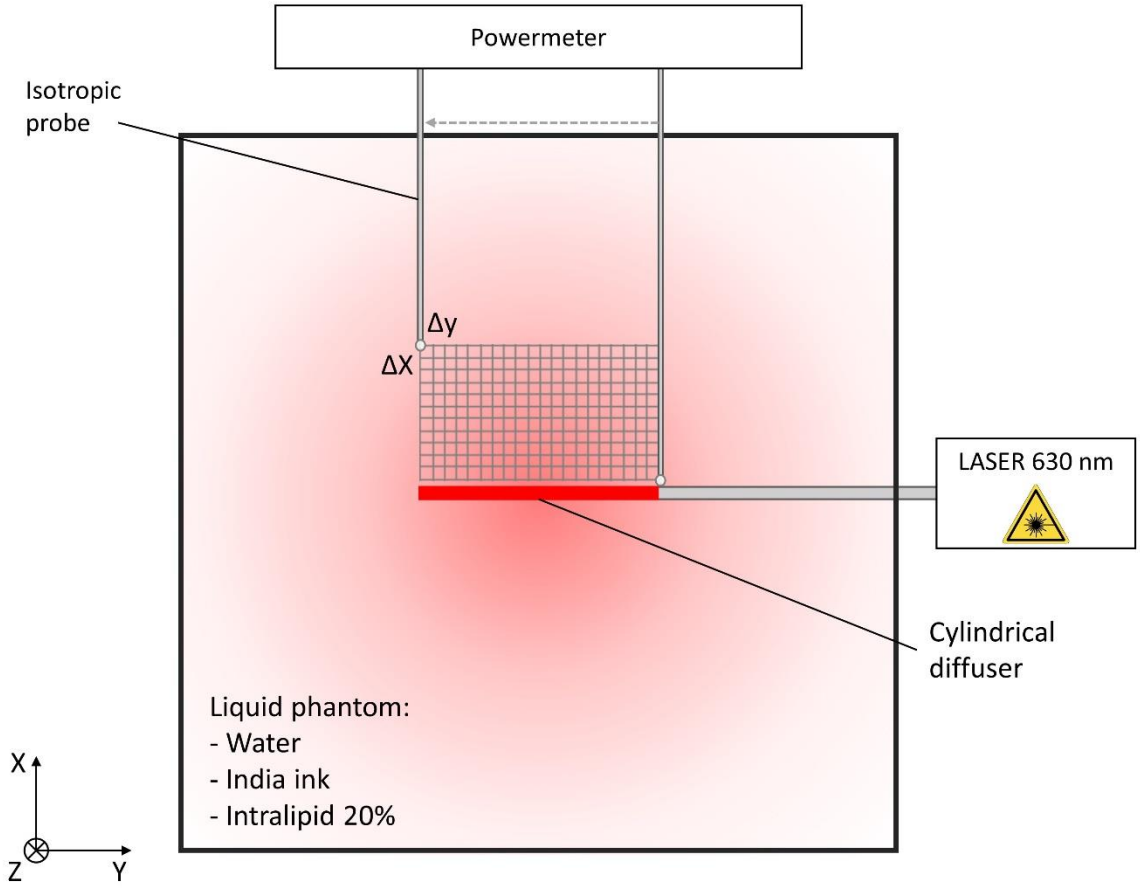

Figure 3.9: Grid of power measurements positions.

A power of 500mW was emitted from the laser source. Once the power had been measured [W], the value was multiplied to the calibration factor in order to obtain a fluence rate value [$W.cm^{-2}$].

c. Comparison with Monte-Carlo simulation

The same optical properties (absorption, scattering and anisotropy) were applied to compare experimentals' results with Monte-Carlo results. Because it depends mostly on the Intralipid liquid, the anisotropy coefficient was deduced from the equation provided by the study of Aernouts et al. [294]. They provided an empirical equation to estimate the value of anisotropy coefficient of Intralipid liquid according to wavelength:

$$g(\lambda) = a.\left(\frac{1-f}{1+e^{c(\lambda+d)}}+f\right)+b\left(\frac{1-h}{1+e^{c(\lambda+d)}}+h\right)\lambda \quad (3.32)$$

where a = 1.094, b = $-5.653.10^{-4}$, c = $5.3.10^{-3}$, d = $\frac{a(f-1)}{b(h-1)}$, f = 0.3516 and h = 0.1933

Using these coefficients and for a wavelength of 635 nm, the corresponding anisotropy used was approximately 0.733.

In order to obtain a reduced scattering coefficient μ_s' of 20 cm^{-1}, a scattering coefficient was deduced using the anisotropy value previously computed:

$$\mu_s = \frac{\mu_s'}{(1-g)} \tag{3.33}$$

Thus, a homogeneous medium has been implemented with the following optical properties:

- Absorption coefficient: μ_a = 0.2 cm^{-1}
- Scattering coefficient: μ_s = 74.074 cm^{-1}
- Scattering reduced coefficient: μ_s' = 74.074 cm^{-1}
- Anisotropy coefficient: g = 0.733

In each simulation, 10^7 photons were launched isotropically in the surrounding medium. The cylindrical diffuser modeled was placed at the center of the 40x40x80 slab (see figure 3.10).

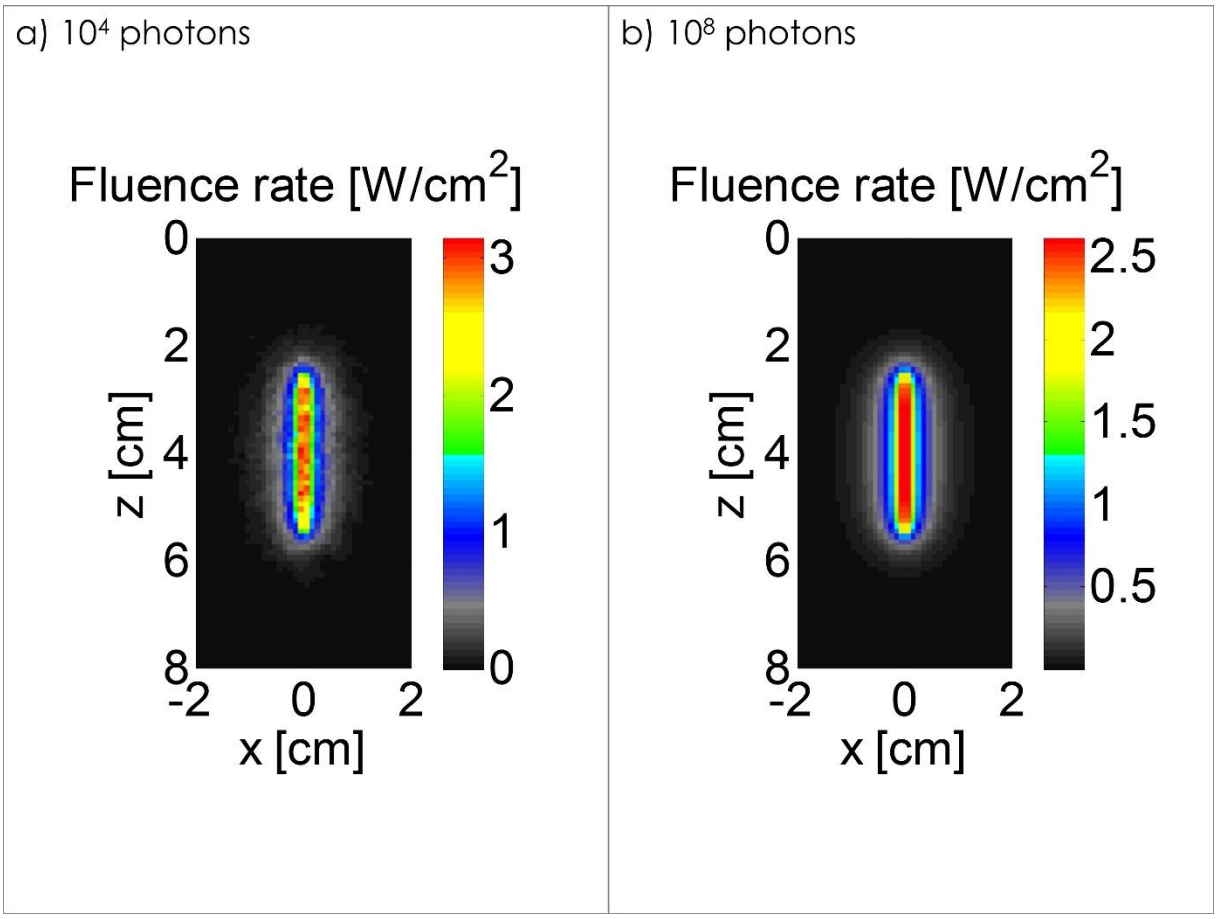

Figure 3.10: Monte-Carlo simulations of a 40 mm cylindrical diffuser in a homogeneous medium: a) 10^4 photons and b) 10^8 photons were launched during each simulation.

To compare results provided from both experimental fluence rate measurements ϕ_{exp} defined as reference and Monte-Carlo simulation $\phi_{MonteCarlo}$, relative deviation was defined

as metric:

$$Relative\ deviation\ (\%) = \frac{\phi_{\mathrm{exp}}(\mathrm{d}) - \phi_{\mathrm{MonteCarlo}}(\mathrm{d})}{\phi_{\mathrm{exp}}(\mathrm{d})} \quad (3.34)$$

Metric values were extracted each of 1 mm from the light source to a distance of approximately 8 mm. After this distance, power measurements were under the microwatt scale. Also, the diameter of the isotropic probe (approximately 0.85 mm) and cylindrical diffuser diameter have been considered to compare fluence rate values to the same distance *d* to the light source.

Five different cylindrical diffusers have been used to compare Monte-Carlo to experimental measurements (see table 3.1).

Manufacturer and model of the fiber	**Length of the tip (mm)**	**Diameter (mm)**	**Core diameter (µm)**	**Numerical aperture (dimensionless)**	**Efficiency measured**
Biolitec, CD 603-20	20	1.65	600	0.37	93%
Medlight, RD-ML 25	25	1	400	0.37	87%
Medlight, RD 30	30	0.98	500	0.48	71%
Medlight, RD-ML 40	40	1	400	0.37	87%
Medlight, RD-ML 50	50	1	400	0.37	87%

Table 3.1: Characteristics of the five cylindrical diffusers used in experiments

These five cylindrical diffusers, from two main optical fibers manufacturers (Medlight, Ecublens, Switzerland and Biolitec GmbH, Jena, Germany) represents the standard optical fiber dimensions used in interstitial PDT.

3. Monte-Carlo validation by comparison with experimental measurements: results

a. Calibration factor

The calibration factor CF_{medium} was estimated using the following values of correction factors $\mathrm{F}_n, \mathrm{F}_b, \mathrm{F}_p$ and F_i (see table 3.2 and figure 3.11). This value is only valid for the isotropic probe and the phantom that will be used in the future experimentations.

	Correction factors (standard deviation)
$\mathrm{F_b}$ (dimensionless)	1.055 ± 0.005
$\mathrm{F_p}$ (dimensionless)	1.03 ± 0.02

F_n (dimensionless)	1.535 ± 0.05
F_i (dimensionless)	1.052 ± 0.04
CF_{air} (cm^{-2})	29411
CF_{medium} (cm^{-2})	51608.78 ± 4890.08

Table 3.2: Calibration factor estimation CF_{medium} for power measurement conversion into fluence rate values.

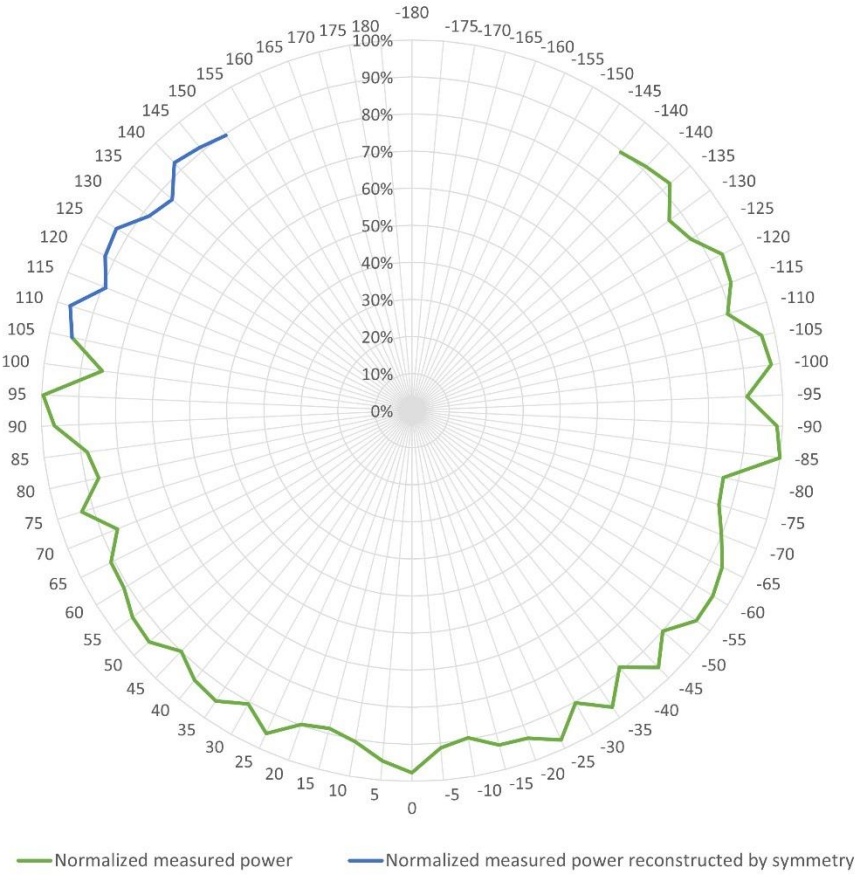

Figure 3.11: Diagram showing the normalized power measured (in nW) according to the incident angle between the probe and the laser beam.

b. Power measurements

The illumination profiles of the five cylindrical diffusers are illustrated in the figure 3.12. Because cylindrical diffusers do not emit perfectly the light all along the diffusing part [303, 304], mean of fluence rate values computed from the beginning to the end of the diffusing tip for different distance to the source were compared to Monte-Carlo simulations.

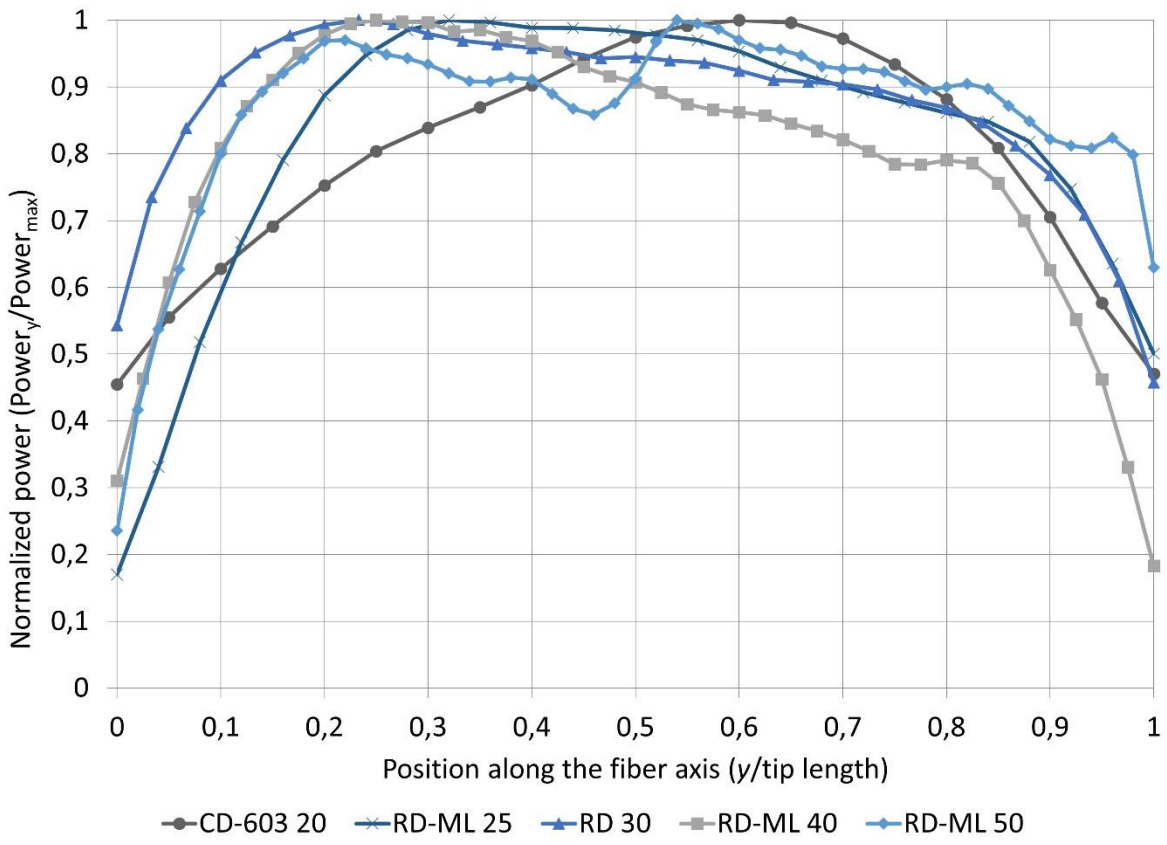

Figure 3.12: Normalized illumination profile of the five cylindrical diffusers described in the table 3.1. The power emitted by the five cylindrical diffusers was measured along each tip. Power measurements were normalized according to each maximum power.

Using the calibration factor previously described, each power measurements have been converted into fluence rate values. Mean relative deviations were obtained according to distances to the fiber tip (see figure 3.13).

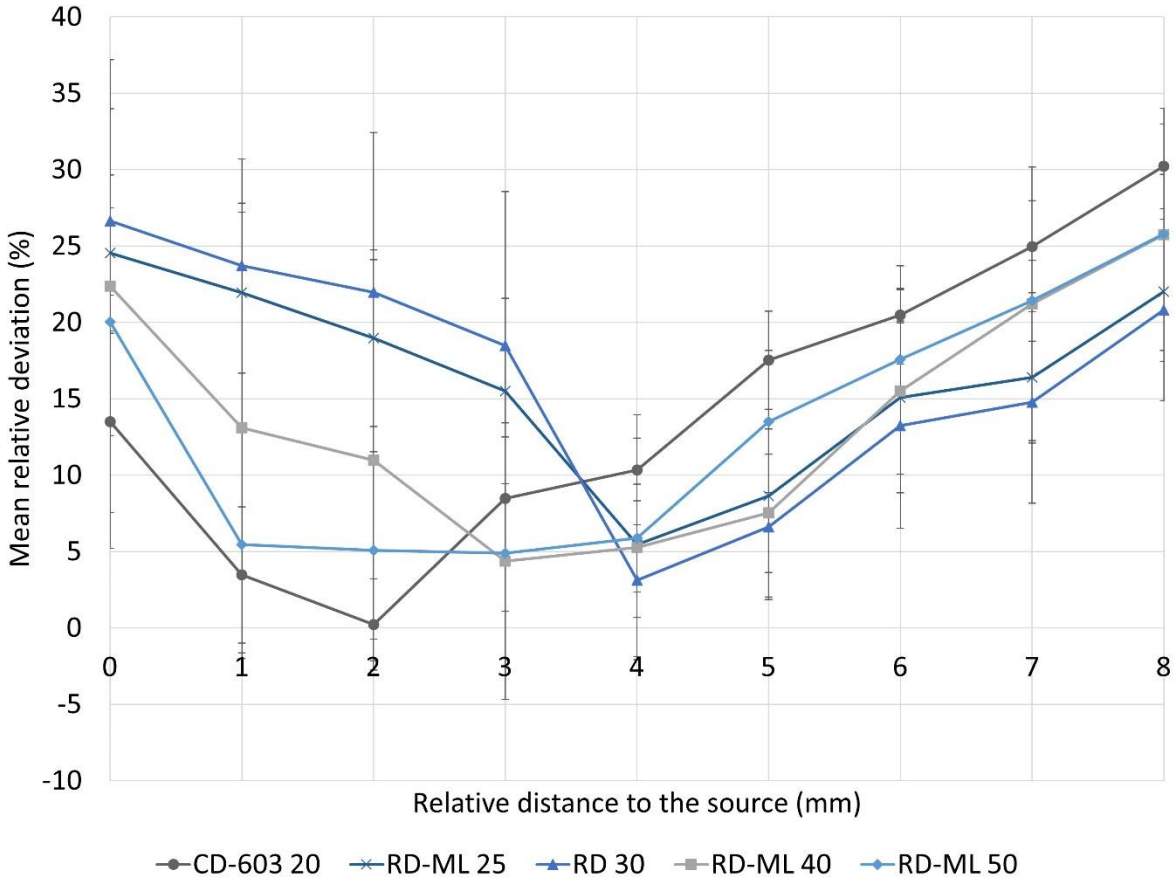

Figure 3.13: Mean relative deviation according to relative distances to the fiber tip.

By computing the mean of all means relative deviations for each cylindrical diffusers and independently from the distance to the light source, a total mean value of all experimentations of approximately 14.97 % ± 6.16 was computed (see table 3.3).

Manufacturer and model of the fiber	**Mean relative deviations (standard deviation)**
Biolitec, CD 603-20	13.29 (4.88)
Medlight, RD-ML 25	14.01 (9.81)
Medlight, RD 30	16.60 (7.12)
Medlight, RD-ML 40	16.51 (5.02)
Medlight, RD-ML 50	14.36 (3.95)
Total mean	**14.97 (6.16)**

Table 3.3: Mean relative deviation and standard deviation for each cylindrical diffusers.

4. Performances

All the following tests were realized with a NVIDIA GPU Quadro K620. This GPU has the following features (see table 3.4):

Device 0: "Quadro K620"	
CUDA Driver Version / Runtime Version	7.50 / 4.0
CUDA Capability Major/Minor version number:	5.0
Total amount of global memory:	2048 MBytes (2147483648 bytes)
GPU Clock Speed:	1.12 GHz
Memory Clock rate:	900.00 Mhz
Total amount of constant memory:	65536 bytes
Total amount of shared memory per block:	49152 bytes
Total number of registers available per block:	65536
Maximum sizes of each dimension of a block:	1024 x 1024 x 64
Maximum sizes of each dimension of a grid:	2147483647 x 65535 x 65535

Table 3.4: K620 GPU features provided by the "Device Query" program sample developed by NVIDIA.

a. Optimization of the execution speed

Several configurations have been tested to obtain the fastest execution of Monte-Carlo simulation regarding the number of blocks and threads used per block. A homogeneous medium has been implemented with the following optical properties:

- Absorption coefficient: $\mu_a = 0.1\ cm^{-1}$
- Scattering coefficient: $\mu_s = 100\ cm^{-1}$
- Anisotropy coefficient: $g = 0.8$

102400 photons were generated to simulate a 40 mm cylindrical diffuser placed at the center of a 40x40x80 mm homogeneous slab constituted of the medium previously described.
First, the number of blocks has been varied from 1 to 1024. The number of threads per block was fixed to 512 during all simulations. Mean computing time of the GPU part only was recorded. Results are presented in the following table 3.5:

Blocks	Mean time (ms)	Threads generated
1	5364.194 (26.82)	512
2	2708.338 (16.52)	1024
4	2715.358 (22.20)	2048
8	2095.402 (16.51)	4096
16	2124.522 (23.45)	8192

32	**2026.826 (8.38)**	**16384**
64	2097.168 (16.25)	32768
128	2217.3 (17.88)	65536
256	2345.622 (8.43)	131072
512	2343.858 (17.29)	262144
1024	2343.77 (14.80)	524288

Table 3.5: Mean computing times of one Monte-Carlo simulation (standard deviation), according to the number of block used. 512 threads were implemented in each block in all simulations.

Strong dependence of computing time is observed according to the number of blocks employed. In the case of the GPU previously described and used here, the number of 32 blocks appears as the best solution to improve GPU performances.

Once the number of 32 blocks was fixed, the number of threads per block has been varied from 8 to 512. The same simulation conditions were implemented.

Threads per block	**Mean time (ms)**	**Threads generated**
8	6676.506 (35.07)	256
16	4304.988 (24.61)	512
32	2646.69 (26.53)	1024
64	1777.518 (25.38)	2048
128	1787.228 (46.83)	4096
256	**1761.98 (5.83)**	**8192**
512	2035.524 (25.94)	16384

Table 3.6: Mean computing times of one Monte-Carlo simulation, and standard deviation associated in parentheses, according to the number of block used. 512 threads were implemented in each block in all simulations.

Thus, the fastest and most stable configuration for this GPU configuration is to divide the grid into 32 blocks with 256 threads per block which generates 8192 threads for each simulation (see table 3.6).

With this configuration, the time required to perform the same Monte-Carlo simulation takes approximately 1341.35s. The resulting acceleration and efficiency, defined previously by the Amdhal's law, are approximately 661.7991 and 0.0808 respectively. Using this results, the proportion of execution time α that benefits from parallelized implementation is approximately 0.9986.

b. Fluctuations

The minimal photons' number that must be generated to obtain an accurate result (less than ten percent of error with a very large photon number) was evaluated. The number of photons was varied from 10^5 to 10^7 using the same properties as defined previously. A homogeneous medium was implemented with the following optical properties:

- Absorption coefficient: $\mu_a = 0.1$ cm^{-1}
- Scattering coefficient: $\mu_s = 100$ cm^{-1}
- Anisotropy coefficient: $g = 0.8$

A 30 mm cylindrical diffuser was implemented at the center of this slab. Fluence rate values ϕ were extracted along the cross section of the cylindrical diffuser's center. Relative error was computed at several distances *d* from the center of the source. The reference simulation used 10^8 photons. Five different total numbers of photons (10^4, 10^5, 10^6, 10^7, 5.10^7) were compared.

$$relative\ error\ (\%) = \frac{\phi_{reference}(d) - \phi_{measured}(d)}{\phi_{reference}(d)} \tag{3.35}$$

Number of photons	Time (ms)	Mean error	Standard deviation	Max error
1.00E+08	557132	*Reference*	*Reference*	*Reference*
5.00E+07	85913.2	2.1%	2.4%	9.8%
1.00E+07	162005	2.0%	2.4%	8.9%
1.00E+06	16347.6	2.8%	2.9%	10.1%
1.00E+05	1787.87	5.9%	4.7%	16.7%
1.00E+04	196.866	24.5%	31.5%	145.6%

Table 3.7: Relative errors computed for five different total numbers of photons generated during one simulation.

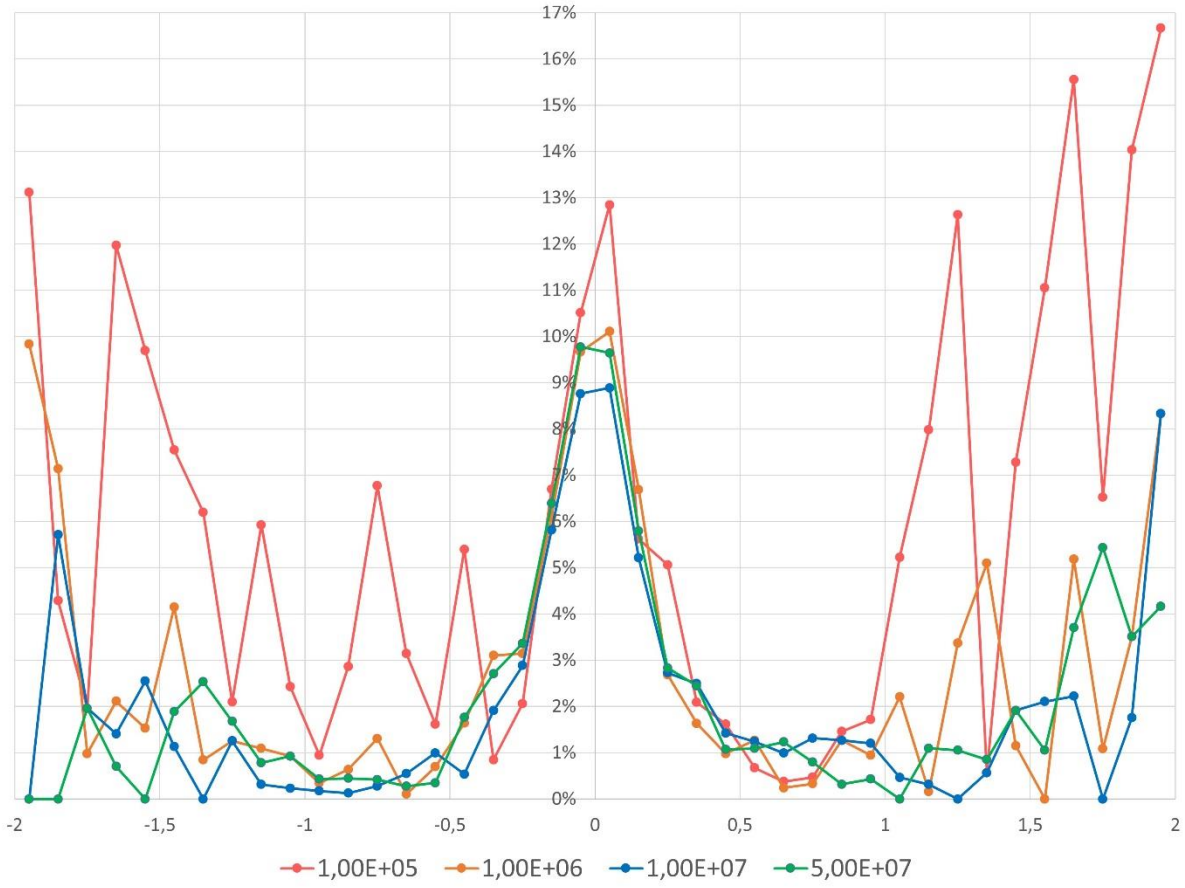

Figure 3.14: Relative errors of several Monte-Carlo simulations using different total numbers of photons generated (10^5 to 5.10^7).

The more propagated the photons are, the more accurate the estimation of the solution is (see table 3.7 and figure 3.10). The reference simulation took nearly thirty minutes to achieve the entire simulation. When multiplying this computing time by the number of cylindrical diffusers modeled, such a large computing time is not reasonable in a clinical routine context. However, the value of 10^6 photons brings acceptable results, i.e., a maximum error at ten percent, during a short computing time of a couple tens of seconds. Gain obtained with larger number of generated photons (such as 10^7) appears as too weak in comparison with the strong loss of performances (computing time is multiplied by ten).

c. Comparison between OpenCL and CUDA

The same Monte-Carlo algorithm has also been implemented in OpenCL platform. A comparison of performances obtained by both CUDA and OpenCL has been performed. The same simulation of a 40 mm cylindrical diffuser inserted inside a homogeneous medium was implemented with the following optical properties:

- Absorption coefficient: $\mu_a = 0.1\ cm^{-1}$
- Scattering coefficient: $\mu_s = 100\ cm^{-1}$
- Anisotropy coefficient: $g = 0.8$

102400 photons were generated on each simulation. 32 blocks with 256 threads per block which induces to generate 8192 threads, have been declared in CUDA and OpenCL. The following computing times have been measured:

Platform	Mean computing time (ms)
CUDA	1761.98 (5,83)
OpenCL	13185.6 (152.66)

Table 3.8: Mean computing times of Monte-Carlo simulation computed by both CUDA and OpenCL platform using the same computing parameters.

Although the OpenCL platform enables all GPU as device, development and optimization is much more challenging than CUDA. Moreover, using the same algorithm with the same computing parameters, OpenCL reveals to be more than seven times slower than the CUDA simulation (see table 3.8).

Discussion and chapter conclusion

Several different approaches enable to compute the propagation of light. Among them, Monte-Carlo remains the reference method. Despite its high accuracy, this method remains so far little used mainly because of the long computing time required to perform a whole simulation. With recent high computing capacities and technologies enabling the parallel computing, Monte-Carlo method can now reach a computing time acceptable for clinical routine.

This chapter introduces a programming code fully dedicated to the GPU modeling of cylindrical diffusers used in PDT is described. To evaluate the output of the algorithm, i.e., the fluence rate emitted from light sources, a phantom has been created to mimic particular optical properties. Experimental results were compared to Monte-Carlo simulations and a mean relative deviation of approximately 14.97% enabled to validate the accuracy of the Monte-Carlo model.

Although the value of the total mean could appear as high, it fits with the recommendations of the AAPM [301, 302] and enables to validate the accuracy of the Monte-Carlo model proposed:

> “the potential variations in the many factors that affect PDT can easily

exceed a minor 10% to 20% error in light dosimetry." [302]

Several biases could be noticed to explain these mean relative deviations:

- The precision of the weighting of every compound to create the optical phantom is critical. Particularly, the mass of India ink injected into the phantom is low but has a strong impact on absorption coefficient. A slight measurement error during the weighting of the India ink can provoke a shift in the phantom absorption.
- The precision of the isotropic probe location in the phantom according to the cylindrical diffusers position was evaluated manually. Once the liquid optical phantom was poured inside the black box, the isotropic probe could not be seen. It was then impossible to check the position of the bulb during the experiment.
- The efficiency of the cylindrical diffusers used has been evaluated using three different laser systems: Ceralas (Biolitec, Jena, Germany), DIOMED 630 PDT (DIOMED, Cambridge, United Kingdom) and ML7710-630-6K (Modulight, Tampere, Finland). The mean of the three efficiencies measured was used to weight the Monte-Carlo simulations.
- The inhomogeneity of illumination profiles of the cylindrical diffusers was measured on each diffuser tip and shows a strong diversity of illumination profiles. Ideally, this heterogeneity should be measured and considered during planning therapy in order to reach a more relevant dosimetry.
- The optical coefficients used in the Monte-Carlo simulations to simulate the phantom are based on forecasting that the phantom is composed of these same coefficients.
- The non-realistic modeling of a cylindrical diffuser in the Monte-Carlo simulations impacts the results. The non-diffusing part and the numerical aperture of each cylindrical diffuser should be considered to obtain a more realistic modeling. These characteristics influence the light distribution.

In clinical context, the strong optical heterogeneity of brain tissues, and particularly in the GBM, induces multiple perturbations for light propagation. Also, optical coefficients provided by different studies [305, 306] of the different structures encountered in patient's brain show strong variations. It appears then difficult to plan the real light propagation through those heterogeneous structures using optical coefficients measured on other brains. Nevertheless, the Monte-Carlo simulation remains the best alternative to reach an accurate estimation of the light distribution.

Regarding speedup gained with GPU implementation, optimization of performances

leads to an acceleration of approximately 660 faster than the CPU version. Although it remains difficult to compare this value to other accelerations noticed in other articles [257, 265-275, 307] (different computing capacities and simulations), the acceleration provided by the Monte-Carlo presented in this thesis provides a sufficient acceleration to enable its use in clinical routine.

Chapter IV
Practical application to the interstitial dosimetry

For non-resectable GBM, newly diagnosed or relapse, interstitial photodynamic therapy (iPDT) may be preferred as alternative treatment modality. This surgical procedure aims for inserting light sources directly inside the tumor and requires the use of a treatment planning system (TPS) before entering the operating theater.

A proof of concept of a TPS dedicated to the stereotactic iPDT treatment of GBM is introduced in this chapter. The two key points in the procedure planning are the stereotactic localization and the dosimetry. These two sections are evaluated and the respective methodologies are described.

Since this first version is only a proof of concept, forthcoming developments are then proposed, particularly the integration of the GPU Monte-Carlo method presented in chapter III.

I. A treatment planning system

For unresectable GBM cases, iPDT may be preferred [19, 117, 118, 297, 308]. Since this procedure requires to plan the positioning of light sources to compute the light exposure

duration, a TPS dedicated to this modality is highly expected.

1. Interstitial PDT procedure

According to the literature, a minority [93] to 23%-38% [92] of GBM are non-resectable (newly diagnosed or relapsing). In these cases, iPDT [117, 308-311] may be achievable. This modality lies on the insertion of optical fibers directly into the tumor targeted. Because of strong light absorption in biological tissues, the diffusing sources located at the tip of the optical fibers have to be placed near or inside the tumor under stereotactic conditions to maximize the treated volume. Preliminary results have shown positive outcomes [118]. The treatment strategy (see figure 4.1) includes the PDT treatment after its planning with the help of a TPS. Using imagery (MRI and CT-Scan modalities mainly), the GBM is segmented and classified to identify organs at risk and areas to treat. Then, cylindrical diffusers insertion is simulated within the Leksell stereotactic frame of reference. Once the treatment is planned, the procedure starts with the administration of the precursor of the PS (5-ALA) several hours before the illumination in order to have a sufficient concentration of PS (PpIX) to provoke a PDT effect on tumor cells. Optical fibers are then inserted in patient's brain and illuminate surrounding tissues during a given treatment time as planned before the procedure. Once the PDT procedure ended, radiation therapy and chemotherapy are delivered to the patient to decrease recurrence risks (standard of care).

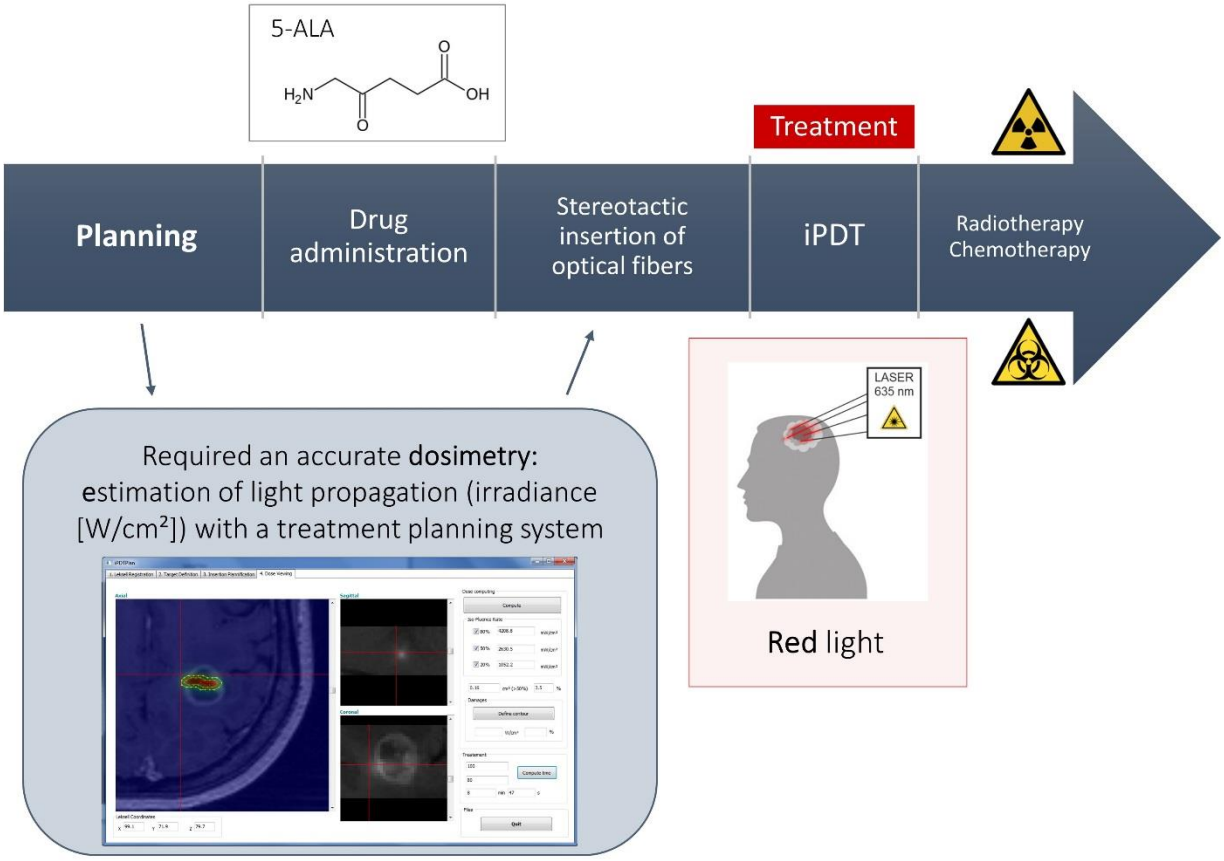

Figure 4.1: Surgical workflow including the 5-ALA iPDT procedure.

2. Proof of concept

A TPS is highly recommended to plan an iPDT procedure and for optimization of the light delivery and maximization of the treated volume. Once this modeling is completed, the illumination duration is computed in order to deposit a given therapeutic fluence value [$J.cm^{-2}$]. In this paragraph, a description of the developed software, the validation of the stereotactic registration and dosimetry model implemented is presented [312].

a. *iPDT-Plan*: a proof of concept

This software, named *iPDT-Plan*, includes stereotactic registration of medical images (digital imaging and communications in medicine, DICOM), manual delineation of the tumor target, light source insertion and dosimetry modeling.

The software was implemented with the integrated development environment C++ Builder XE8 (Embarcadero, Austin, TX, USA) and the environment ArtiMED[4] developed at the ONCO-THAI Lab. This environment provides data management, mathematics and image

[4] "ArtiMED: a medical imaging collaborative platform", ONCO-THAI, http://www.onco-thai.fr/index.php?option=com_content&view=article&id=6&Itemid=140&lang=en (July 21, 2017)

processing tools. Named *iPDT-Plan*, this first TPS implementation provides an user-interface composed of four main tabs corresponding to the typical planning workflow (see figure 4.2) [102, 103, 308, 312].

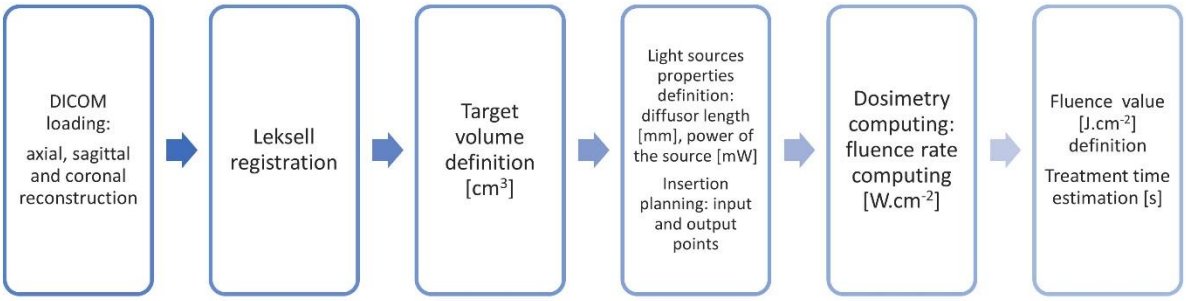

Figure 4.2: Workflow of the *iPDT-Plan* TPS.

The first tab is dedicated to DICOM viewing and stereotactic localization. Axial, sagittal and coronal views are displayed. As previously described in chapter I (III, 2, a - Instrumentation), stereotactic surgery methods have been developed to plan accurate tools insertion into brain patients [109, 113, 114]. For iPDT purpose, the Leksell frame (Elekta®, Stockholm, Sweden) was preferred because of its common use in stereotactic neurosurgical procedures (Biopsies, Stereo-Electro-Encephalograms, Deep Brain Stimulation, Gamma-knife radiosurgery) [313-316]. The locations of fibers in CT or MR imaging space can be converted into the Leksell space, defined by a frame set-up on the patient's head.

After a target is manually delineated, the surgeon or medical physicist is able to simulate different treatment configurations through the placement of cylindrical diffusers inside the target volume. To simulate the fibers insertion, the diffuser length [mm], the power of the source [mW], and the input and output points (i.e., entry point into the skull and ending point into the brain) must be defined. Vascular structures and optic fibers collision is a major concern in this stereotactic procedure. Specific visualization tools are thus required to enable visual inspection of the fiber trajectory and thus limit damages to the vascular tree. The fiber trajectory within the volume may be represented in two ways (see figure 4.3). When the whole trajectory is contained in only one axial image, it is represented by two distinct parts: the diffusing part, symbolized here by a red continuous line, and the non-diffusing part, symbolized here by a cyan continuous segment. Additionally, when the trajectory crosses several planes, the projection of the trajectory on the displayed plane is symbolized here by a discontinuous segment navy blue (see figure 4.3). Thus, it is possible to visualize the progression of the fiber inside the patient's brain. Entry and ending points are directly

converted into 3D Leksell frame coordinates to be used with the stereotactic Leksell System (Elekta, Stockholm, Sweden) or for their programming on a neurosurgical robot.

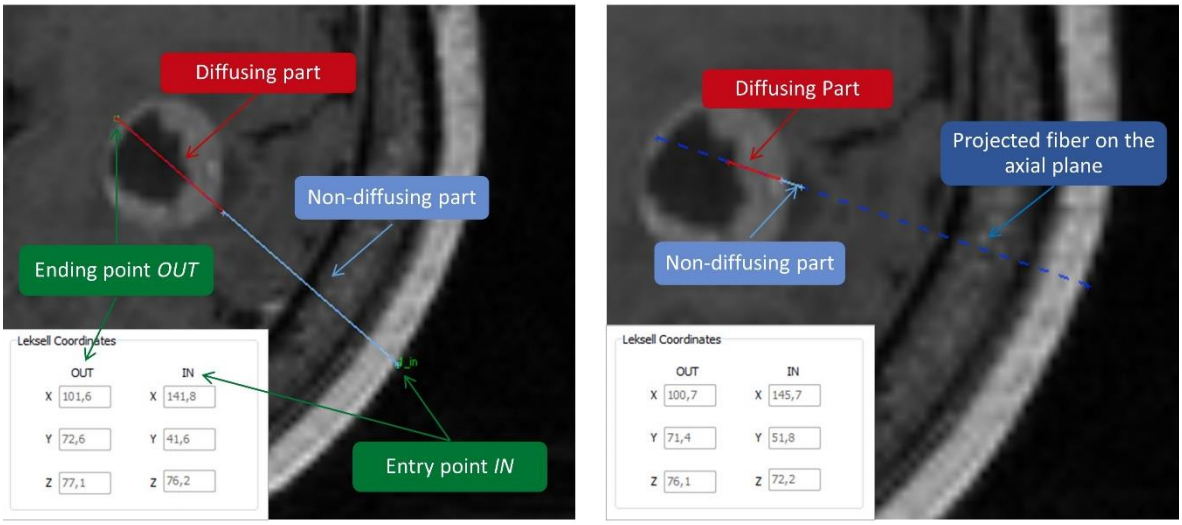

Figure 4.3: On the left, a 20 mm cylindrical diffuser is displayed and contained in only one axial image, represented by two distinct parts: the diffusing tip (red continuous segment) and non-diffusing part (cyan continuous segment). On the right, a 20 mm cylindrical diffuser is also inserted with a trajectory crossing several planes. Three different parts appear: the diffusing part (red continuous segment), the non-diffusing part contained in the visualized plane (cyan continuous segment) and the projection on the axial image of the non-diffusing part (navy blue discontinuous segment).

For a given treatment configuration (number, type and location of the cylindrical diffusers, power emitted by light sources), dosimetry modeling and lighting duration estimation are computed to provide a fluence rate map [W/cm²] which is superimposed on the images.

Using the fluence rate matrix [$W.cm^{-2}$], treatment duration is estimated to deposit a fluence value [$J.cm^{-2}$] on a target pre-determined by the user. The larger the target is, the longer the treatment duration to obtain a PDT effect on the treated volume is.

b. Stereotactic frame registration

As previously described, the Leksell stereotactic frame (Elekta®, Stockholm, Sweden) is used to localize point in the 3D Leksell space from imaging (CT or MRI). Translation from imaging space to the Leksell space is achieved through an MR- or CT-indicator box clipped onto the frame during the exams. Radio-opaque rods representing the characteristic “N” of the

Leksell frame were included inside at least two sides of the box. Thus, these six rods appear as points in the axial plane of the patient imagery (see figure 4.4). To perform a Leksell localization of the DICOM set, these rods have to be located on all images. Two collections of points in R^3 were created: the first P_{IMA} represents four points on *n* slices in the imaging modality (i.e., CT or MRI) coordinates, and the second $P_{Leksell}$ represents the theoretical positions of the same four points in the Leksell frame coordinates. A matrix *A* allows the conversion of P_{IMA} in $P_{Leksell}$:

$$P_{Leksell} = A \,.\, P_{IMA} \tag{4.1}$$

For a given slice, the four points enclosed in red circles (see figure 4.4) form a rectangle 190 x120 mm in length and the intersection of diagonals is situated on *x* = *y* = 100 mm Leksell coordinates. They also own the same *x* and *y* Leksell frame coordinates. The two points enclosed in a blue circle (see figure 4.4) indicate the location of the diagonal rod of the Leksell frame. These two points move, respectively, along the lines [1, 2] and [3, 4] according to the axial imaging modality slice location. Thus, the *z* Leksell coordinate can be determined using the two lengths $L_{1,2}$ and $L_{3,4}$ as mentioned in figure 4.4. An addition of 40 mm on the z-axis is due to the extra height of the frame mount. Thus, for a given slice *n*, the Leksell coordinates $p_{Leskell,i}$ of the four points 1, 2, 3 and 4 can be computed as follows:

$$p_{Leksel,1,n} = \begin{cases} 100 - \left(\frac{190}{2}\right) = 5\ mm \\ 100 + \left(\frac{120}{2}\right) = 160\ mm \\ 40 + L_{1,2}\ mm \end{cases} \quad p_{Leksell,3,n} = \begin{cases} 100 + \left(\frac{190}{2}\right) = 195\ mm \\ 100 + \left(\frac{120}{2}\right) = 160\ mm \\ 40 + L_{1,2}\ mm \end{cases} \tag{4.2}$$

$$p_{Leksell,2,n} = \begin{cases} 100 - \left(\frac{190}{2}\right) = 5\ mm \\ 100 - \left(\frac{120}{2}\right) = 40\ mm \\ 40 + L_{3,4}\ mm \end{cases} \quad p_{Leksell,4,n} = \begin{cases} 100 + \left(\frac{190}{2}\right) = 195\ mm \\ 100 - \left(\frac{120}{2}\right) = 40\ mm \\ 40 + L_{3,4}\ mm \end{cases} \tag{4.3}$$

P_{IMA} and $P_{Leksell}$ are thus composed of 4*n* 3D (x,y,z) elements:

$$P_{IMA} = \begin{Bmatrix} x_{IMA,1,1} & y_{IMA,1,1} & z_{IMA,1,1} \\ x_{IMA,2,1} & y_{IMA,2,1} & z_{IMA,2,1} \\ x_{IMA,3,1} & y_{IMA,3,1} & z_{IMA,3,1} \\ x_{IMA,4,1} & y_{IMA,4,1} & z_{IMA,4,1} \\ \vdots & \vdots & \vdots \\ x_{IMA,1,k} & y_{IMA,1,k} & z_{IMA,1,k} \\ x_{IMA,2,k} & y_{IMA,2,k} & z_{IMA,2,k} \\ x_{IMA,3,k} & y_{IMA,3,k} & z_{IMA,3,k} \\ x_{IMA,4,k} & y_{IMA,4,k} & z_{IMA,4,k} \\ \vdots & \vdots & \vdots \\ x_{IMA,1,n} & y_{IMA,1,n} & z_{IMA,1,n} \\ x_{IMA,2,n} & y_{IMA,2,n} & z_{IMA,2,n} \\ x_{IMA,3,n} & y_{IMA,3,n} & z_{IMA,3,n} \\ x_{IMA,4,n} & y_{IMA,4,n} & z_{IMA,4,n} \end{Bmatrix} \quad P_{Leksell} = \begin{Bmatrix} x_{Leksell,1,1} & y_{Leksell,1,1} & z_{Leksell,1,1} \\ x_{Leksell,2,1} & y_{Leksell,2,1} & z_{Leksell,2,1} \\ x_{Leksell,3,1} & y_{Leksell,3,1} & z_{Leksell,3,1} \\ x_{Leksell,4,1} & y_{Leksell,4,1} & z_{Leksell,4,1} \\ \vdots & \vdots & \vdots \\ x_{Leksell,1,k} & y_{Leksell,1,k} & z_{Leksell,1,k} \\ x_{Leksell,2,k} & y_{Leksell,2,k} & z_{Leksell,2,k} \\ x_{Leksell,3,k} & y_{Leksell,3,k} & z_{Leksell,3,k} \\ x_{Leksell,4,k} & y_{Leksell,4,k} & z_{Leksell,4,k} \\ \vdots & \vdots & \vdots \\ x_{Leksell,1,n} & y_{Leksell,1,n} & z_{Leksell,1,n} \\ x_{Leksell,2,n} & y_{Leksell,2,n} & z_{Leksell,2,n} \\ x_{Leksell,3,n} & y_{Leksell,3,n} & z_{Leksell,3,n} \\ x_{Leksell,4,n} & y_{Leksell,4,n} & z_{Leksell,4,n} \end{Bmatrix} \tag{4.4}$$

With these two vectors, a 3x3 covariance matrix *S* is built:

$$S = \begin{pmatrix} Cov(P_{IMA}(:,1), P_{Leksell}(:,1)) & Cov(P_{IMA}(:,2), P_{Leksell}(:,1)) & Cov(P_{IMA}(:,3), P_{Leksell}(:,1)) \\ Cov(P_{IMA}(:,1), P_{Leksell}(:,2)) & Cov(P_{IMA}(:,2), P_{Leksell}(:,2)) & Cov(P_{IMA}(:,3), P_{Leksell}(:,2)) \\ Cov(P_{IMA}(:,1), P_{Leksell}(:,3)) & Cov(P_{IMA}(:,2), P_{Leksell}(:,3)) & Cov(P_{IMA}(:,3), P_{Leksell}(:,3)) \end{pmatrix} \tag{4.5}$$

Using the trace Tr_S of the *S* matrix, a 4x4 matrix *Q* is created from these two data sets:

$$Q = \begin{bmatrix} Tr_S & S_{1,2} - S_{2,1} & S_{2,0} - S_{0,2} & S_{0,1} - S_{1,0} \\ S_{1,2} - S_{2,1} & 2 \times S_{0,0} - Tr_S & S_{0,1} + S_{1,0} & S_{0,2} + S_{2,0} \\ S_{2,0} - S_{0,2} & S_{1,0} + S_{0,1} & 2 \times S_{1,1} - Tr_S & S_{1,2} + S_{2,1} \\ S_{0,1} - S_{1,0} & S_{2,0} + S_{0,2} & S_{2,1} + S_{1,2} & 2 \times S_{2,2} - Tr_S \end{bmatrix} \tag{4.6}$$

Eigen vectors are computed from the *Q* matrix and enable the building of a quaternion *q* expressed as $q = a + b + c + d$ where *a, b, c, d* are normalized real parts of the maximum eigen values from the eigen vector. With this quaternion, a matrix A which enables the conversion of image coordinates into Leksell coordinates is created:

$$A = \begin{bmatrix} a^2 + b^2 - c^2 - d^2 & 2bc - 2ad & 2ac + 2bd & t_x \\ 2ad + 2bc & a^2 - b^2 + c^2 - d^2 & 2cd - 2ab & t_y \\ 2bd - 2ac & 2ab + 2cd & a^2 - b^2 - c^2 + d^2 & t_z \\ 0 & 0 & 0 & 1 \end{bmatrix} \tag{4.7}$$

where:

$$\begin{aligned} t_x &= \overline{P_{IMA.x}} - (A_{0,0}.\overline{P_{Leksell.x}} + A_{0,1}.\overline{P_{Leksell.y}} + A_{0,2}.\overline{P_{Leksell.z}}) \\ t_y &= \overline{P_{IMA.y}} - (A_{1,0}.\overline{P_{Leksell.x}} + A_{1,1}.\overline{P_{Leksell.y}} + A_{1,2}.\overline{P_{Leksell.z}}) \\ t_z &= \overline{P_{IMA.z}} - (A_{2,0}.\overline{P_{Leksell.x}} + A_{2,1}.\overline{P_{Leksell.y}} + A_{2,2}.\overline{P_{Leksell.z}}) \end{aligned} \tag{4.8}$$

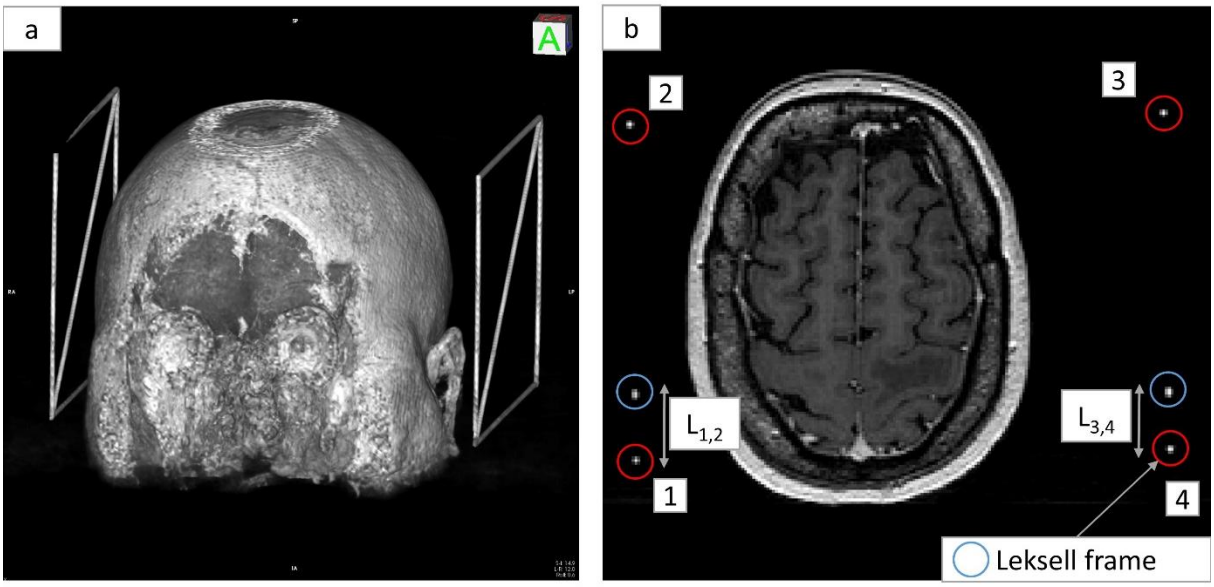

Figure 4.4: a) 3D rendering showing the Leksell frame to the left and right side of the patient's head. b) MRI exams showing the six dots (enclosed in circles) matching the 6 radio-opaque rods included inside the Leksell frame.

c. Dosimetry

The model implemented is an analytical model of light distribution (see chapter II, II, 1, a, *i* – Analytical models). This method discretizes the diffusing part of the optical fiber as a sum of several *n*-light point sources [142-144] (equation 2.26). Thus, calculation of the fluence rate at a distance *d* from the fiber is the sum of each light source contribution.

$$\phi(d) = \sum_{n=1}^{n_{sources}} \frac{P}{L_{diffuser\ length}} . \frac{3.\mu_s'}{4.\pi.d_n} . e^{-d_n . \mu_{eff}} . dl \qquad (4.9)$$

where P is the power of the source [W], $L_{diffuser\ length}$ is the cylindrical diffuser length [mm], *dl* is the constant step length of discretization between two light point sources [mm], d_n is the distance to the *n*-light point source [mm] where $n = \frac{L_{diffuser\ length}}{dl}$, μ_a, μ_s', μ_{eff} are the absorption, reduced scattering and effective attenuation coefficients respectively [mm^{-1}].

This fluence rate estimation is computed on each voxel of the space. The coefficients used are provided from a previous study of Beck et al. in 2007 [117] and confirmed by a more recent study of Tedford et al. in 2015 [317]. They correspond to a normal brain tissue infiltrated by GBM tumor cells: $\mu_a = 0.2\ cm^{-1}$ and $\mu_s' = 20\ cm^{-1}$.

To evaluate this analytical model, the results were compared to the Monte-Carlo model presented in chapter III.

To compare these models, a common metric (equation 4.11) was used. The fluence rate ϕ was estimated at the distance value *d* from the center of the source for each simulation (see figure 4.5). The distance called the reduced Mean Free Path (MFP') is defined as the inverse of the sum of absorption and reduced scattering coefficient:

$$\mathrm{MFP}' = \frac{1}{\mu_a + \mu_s'} \tag{4.10}$$

In this case, with μ_a = 0.02 mm^{-1} and μ_s' = 2 mm^{-1}, the MFP' is close to 0.50 mm. At distances below this MFP´, analytical light propagation models become inaccurate [145]. Thus, the fluence rate estimation started from 0.75 mm to avoid outlier values due to their exponential factor (i.e., when the distance d is close to zero). The relative deviation between Monte-Carlo ϕ_{MC} and the analytical model $\phi_{analytical}$ was then computed (equation 4.11):

$$\text{Relative deviation (\%)} = \frac{\phi_{MC}(d) - \phi_{analytical}(d)}{\phi_{MC}(d)} \tag{4.11}$$

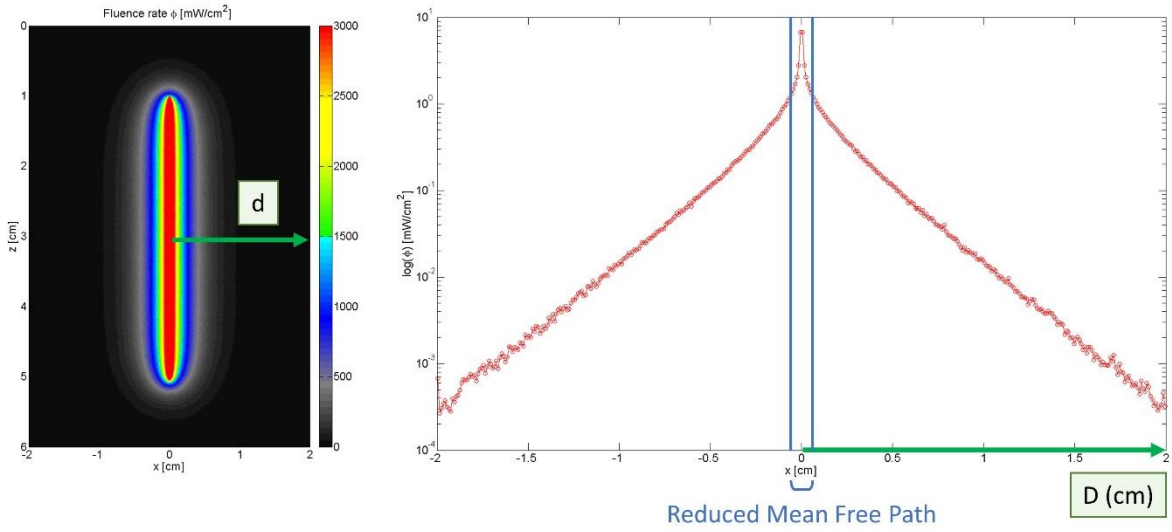

Figure 4.5: A 2D cross section map (on the left) and 1D line scan plot (on the right) of fluence rate values for a 40 mm length diffuser computed with Monte-Carlo method. At distances below this MFP´, the analytical light propagation models become inaccurate.

Several Monte-Carlo simulations were computed to evaluate the fluence rate distribution from different diffuser lengths (10, 15, 20, 30, 40 and 50 mm). Metric values were extracted each 1 mm from the center of the light source to a distance of 10 mm (figure 4.5). Analytical model was implemented in Matlab software (MathWorks, Natick, USA).

First, the mean relative deviations for each distance *d* (between 0.75 mm to 10 mm) were computed over six different diffuser lengths. Subsequently, the mean relative deviations for all six different diffusers were computed over each distance *d* (between 0.75 mm to 10 mm).

d. Sensitivity study

Fluence rates computed from different analytical models were expected to be very sensitive to optical coefficients of the considered media, particularly when the strong heterogeneity of GBM tissues led to a wide range of optical coefficients (see table 4.5). This sensitivity was evaluated with indices called the Sobol indices S_i [318, 319].
The estimation of the first-order Sobol index of input parameters X_i requires evaluating the ratio between conditional and total variance (equation 4.12).

$$S_i = \frac{V_i}{\mathrm{V}(Y)} = \frac{\mathrm{V}(\mathrm{E}[\mathrm{Y}|X_i])}{\mathrm{V}(Y)} \tag{4.12}$$

This index quantifies the sensitivity of the output *Y* due to the variation of the input X_i.
Higher-order Sobol indices quantify the sensitivity of the output *Y* variance to the interaction of n-input parameters $X_{i\ldots n}$. The second-order Sobol index estimates the output *Y* sensitivity to X_i and X_j inputs parameter (equation 4.13).

$$S_{ij} = \frac{\mathrm{V}\left(\mathrm{E}\left[\mathrm{Y}\middle|X_i, X_j\right]\right) - V_i - V_j}{\mathrm{V}(Y)} \tag{4.13}$$

The sensitivity package provided by the Comprehensive R Archive Network[5] was implemented in the statistical software R. This library provides different functions for sensitivity analysis computation, including Sobol indices computation by the Monte-Carlo method. The variance V_i can be developed as (equation 4.14):

$$V_i = \mathrm{V}(\mathrm{E}[Y|X_i]) = \mathrm{E}[\mathrm{E}[Y|X_i]^2] - \mathrm{E}\left[\mathrm{E}[Y|X_i]\right]^2 = U_i - \mathrm{E}[Y]^2 \tag{4.14}$$

A randomization method estimates U_i using typical variance computing using two N-dimension random samples of input parameters $\tilde{X}_{(N)}^{(1)}$ and $\tilde{X}_{(N)}^{(2)}$, with X_i constant:

[5] Sensitivity: Global Sensitivity Analysis of Model Outputs, CRAN [online] https://CRAN.R-project.org/package=sensitivity (accessed August 28, 2017)

$$\widehat{U_i} = \frac{1}{N}\sum_{k=1}^{N} \frac{f\left(x_{k1}^{(1)}, \ldots, x_{k(i-1)}^{(1)}, x_{ki}^{(1)}, x_{k(i+1)}^{(1)}, \ldots, x_{kp}^{(1)}\right)}{f(x_{k1}^{(2)}, \ldots, x_{k(i-1)}^{(2)}, x_{ki}^{(1)}, x_{k(i+1)}^{(2)}, \ldots, x_{kp}^{(2)})} \tag{4.15}$$

First-order Sobol indices $\hat{S}_i$ can then be estimated as:

$$\hat{S}_i = \frac{\widehat{V_i}}{\hat{V}} = \frac{\widehat{U_i} - \widehat{f_0}^2}{\hat{V}} \text{ (8) with } \widehat{f_0} = \frac{1}{N}\sum_{k=1}^{N} f\left(x_{k1}, \ldots, x_{kp}\right)$$

and (4.16)

$$\hat{V} = \frac{1}{N}\sum_{k=1}^{N} f^2\left(x_{k1}, \ldots, x_{kp}\right) - \widehat{f_0}^2$$

The same process was applied to estimate the second-order Sobol index; two N-dimension random samples of input parameters $\tilde{X}_{(N)}^{(1)}$ and $\tilde{X}_{(N)}^{(2)}$ are injected in the *f* function with X_i and X_j constants:

$$\widehat{U_i} = \frac{1}{N}\sum_{k=1}^{N} \frac{f\left(x_{k1}^{(1)}, \ldots, x_{k(i-1)}^{(1)}, x_{ki}^{(1)}, x_{k(i+1)}^{(1)}, \ldots, x_{k(j-1)}^{(1)}, x_{kj}^{(1)}, x_{k(j+1)}^{(1)}, \ldots, x_{kp}^{(1)}\right)}{f\left(x_{k1}^{(2)}, \ldots, x_{k(i-1)}^{(2)}, x_{ki}^{(1)}, x_{k(i+1)}^{(2)}, \ldots, x_{k(j-1)}^{(2)}, x_{kj}^{(1)}, x_{k(j+1)}^{(2)}, \ldots, x_{kp}^{(2)}\right)} \tag{4.17}$$

Second-order Sobol indices $\hat{S}_{ij}$ can then be estimated as:

$$\hat{S}_{ij} = \frac{\widehat{V_{ij}}}{\hat{V}} = \frac{\widehat{U_{ij}} - \widehat{f_0}^2 - \hat{V}_i - \hat{V}_j}{\hat{V}} \tag{4.18}$$

As reported by Zhang et al. [319], the parameters and their limits must be carefully defined. In this study, two parameters were included in the sensitivity analysis: absorption and reduced scattering coefficient. Thus, two N-dimension samples ($\tilde{X}_{(N)}^{(1)}$ and $\tilde{X}_{(N)}^{(2)}$) of absorption and reduced scattering coefficients were created. Random values of optical coefficients were generated with a range of ± 50% from the mean value presented previous (i.e., μ_a = 0.02 mm^{-1} and μ_s' = 2 mm^{-1}): between 0.01 to 0.03 mm^{-1} for the absorption coefficient and 1 to 3 mm^{-1} for the reduced scattering coefficient. The Sobol function provided in the "sensitivity" package was applied with a sample size of N = 100,000 and 1000 bootstrap replications. First, second and total-order sensitivity indices were generated and analyzed. The analytical model was implemented with a 40 mm diffuser length. Indeed, the diffuser length can be considered as a constant because the power, defined in W/mm, must be divided by the diffuser length.

Furthermore, the light source power was not considered as a parameter because it does not affect light propagation in tissues.

3. Results

a. Validation of the stereotactic registration

A phantom model was developed in order to evaluate the Leksell registration. A 15 cm^3 cube of polymethyl methacrylate (PMMA) was designed with three rods (see figure 4.6). Thirteen radio-opaque marbles spaced 10 mm apart were inserted into these three rods.

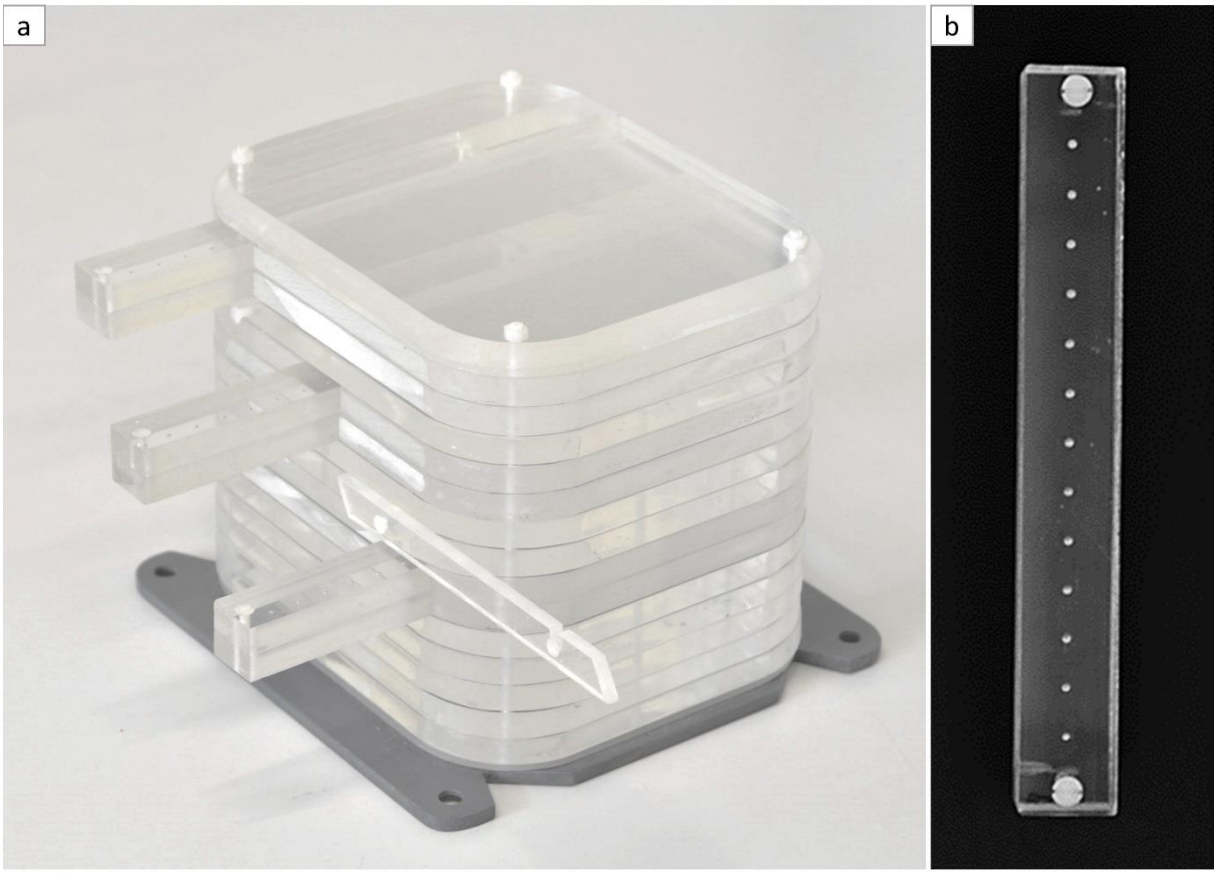

Figure 4.6: a) A phantom model designed to simulate the head of the patient was fixed on a Leksell frame. b) PMMA rod with 13 radio-opaque marbles spaced 10 mm apart.

This phantom was then fixed to a Leksell frame and imaged by CT (see figure 4.7). The coordinates of each marble in the Leksell frame were computed by both the *iPDT-Plan* and the Leksell GammaPlan® (Elekta, Stockholm, Sweden) defined as ground truth. The metric to evaluate the Leksell registration implemented in *iPDT-Plan* was the distance *d* [mm] between Leksell coordinates of the same marble obtained by the *iPDT-Plan* and the

GammaPlan®:

$$d = \sqrt{(x_{iPDT} - x_{GammaPlan})^2 + (y_{iPDT} - y_{GammaPlan})^2 + (z_{iPDT} - z_{GammaPlan})^2} \quad (4.19)$$

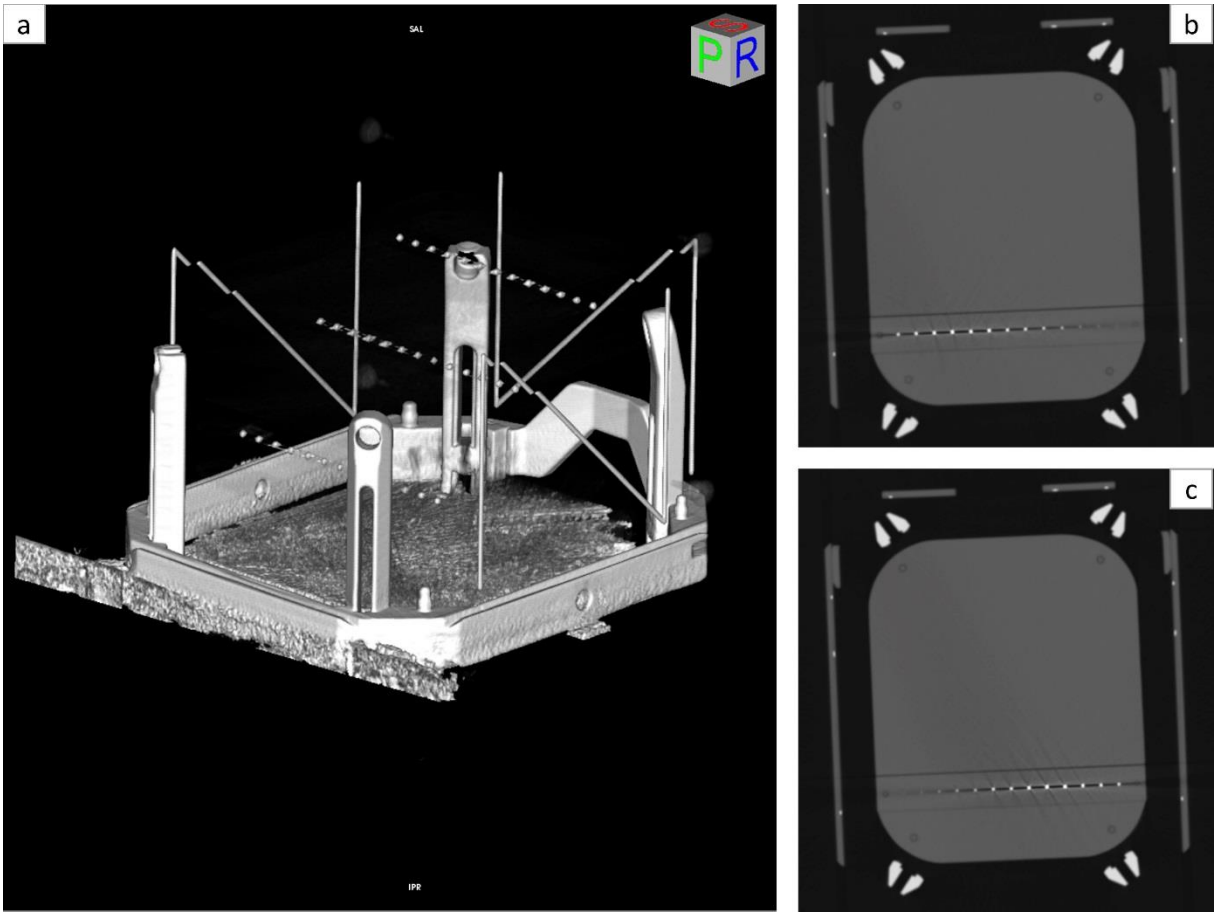

Figure 4.7: a) 3D reconstruction of the CT phantom where the 39 radio-opaque marbles appear inside the Leksell frame. b) and c) CT slices of the phantom with 13 radio-opaque marbles appear in high-level contrast.

Distances [mm] were computed for each marble inserted in the phantom model (see table 4.1). The mean distance computed was 0.8 ± 0.3 mm (maximum = 1.8 mm).

Markers	**1**	**2**	**3**	**4**	**5**	**6**	**7**	**8**	**9**	**10**	**11**	**12**	**13**
Rod 1	1.0	0.3	0.2	0.6	0.7	0.7	0.9	1.4	0.5	0.7	1.1	0.6	0.5
Rod 2	1.8	1.2	1.3	1.3	1.5	1.1	0.6	0.7	0.8	1.2	0.9	1.3	1.1
Rod 3	0.5	0.4	0.8	1.0	0.9	0.7	0.7	0.9	0.5	0.5	0.6	0.8	0.7

Table 4.1: Distances [mm] between Leksell coordinates of the radio-opaque marbles obtained by the TPS and the GammaPlan® (Elekta, Stockholm, Sweden).

b. Dosimetry evaluation

Figure 4.8 represents the mean relative deviation estimated over the six diffuser lengths (i.e., 10, 15, 20, 30, 40 and 50 mm) for each distance *d*. Mean relative deviation values are summarized in table 4.2.

The mean of all mean relative deviations summarized in table 4.2 equals 1.23% (2.48%).

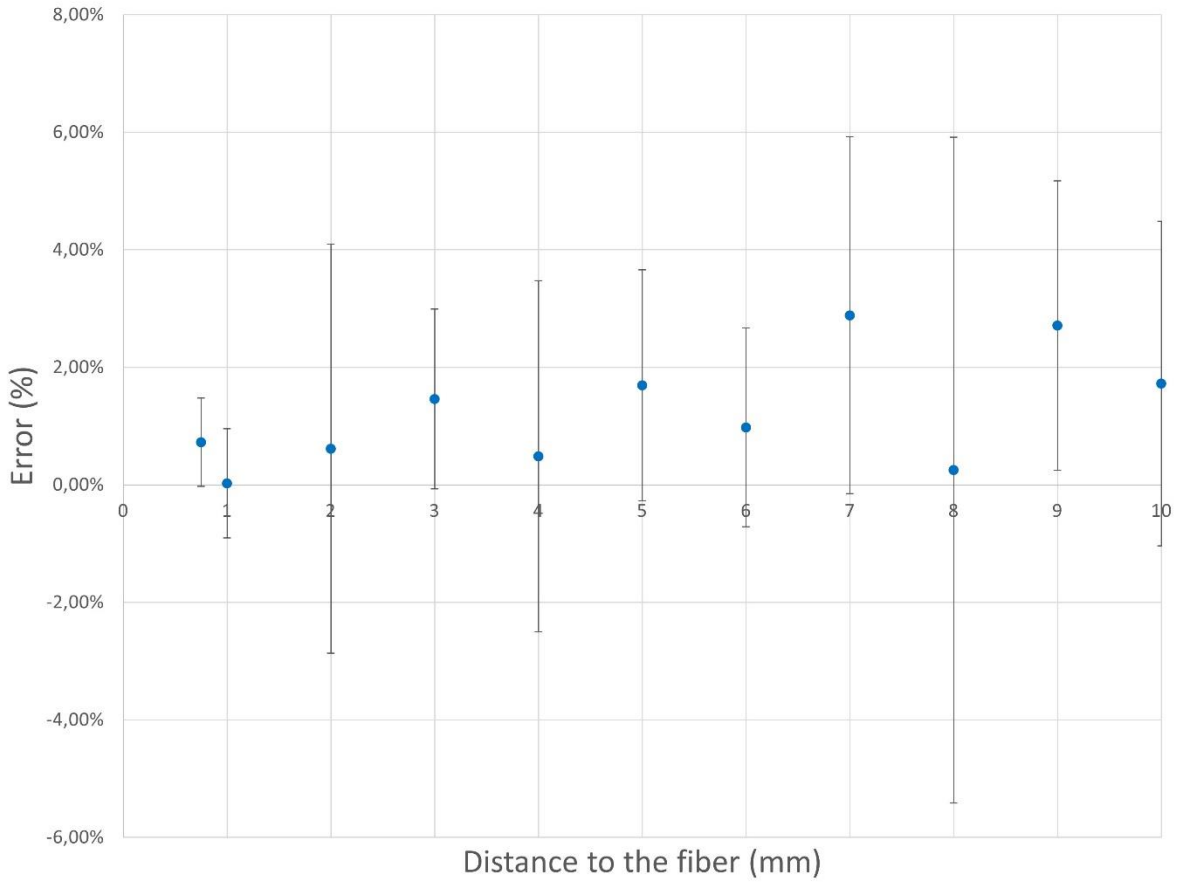

Figure 4.8: Data points are the mean relative deviations of fluence rate values computed by the analytical model, calculated for each distance d (0.75 mm to 10 mm) over all six different source lengths.

d (mm)	Mean (SD)	Max deviation
0.75	0.72% (0.75%)	1.98%
1	0.03% (0.93%)	2.55%
2	0.61% (3.48%)	9.36%
3	1.46% (1.53%)	4.32%
4	0.49% (2.99%)	7.08%
5	1.69% (1.96%)	5.51%
6	0.98% (1.69%)	4.70%
7	2.89% (3.03%)	7.61%
8	0.25% (5.67%)	15.38%

9	2.71% (2.46%)	7.89%
10	1.72% (2.76%)	8.00%

Table 4.2: Relative deviation computed at different distances from the source; the mean is computed for all source lengths at a given distance d.

Figure 4.9 represents the relative deviation where the mean is estimated of all distances *d* to the source for each diffuser length simulated, summarized in table 4.3. The mean value of relative deviations equals 2.53% (2.09%).

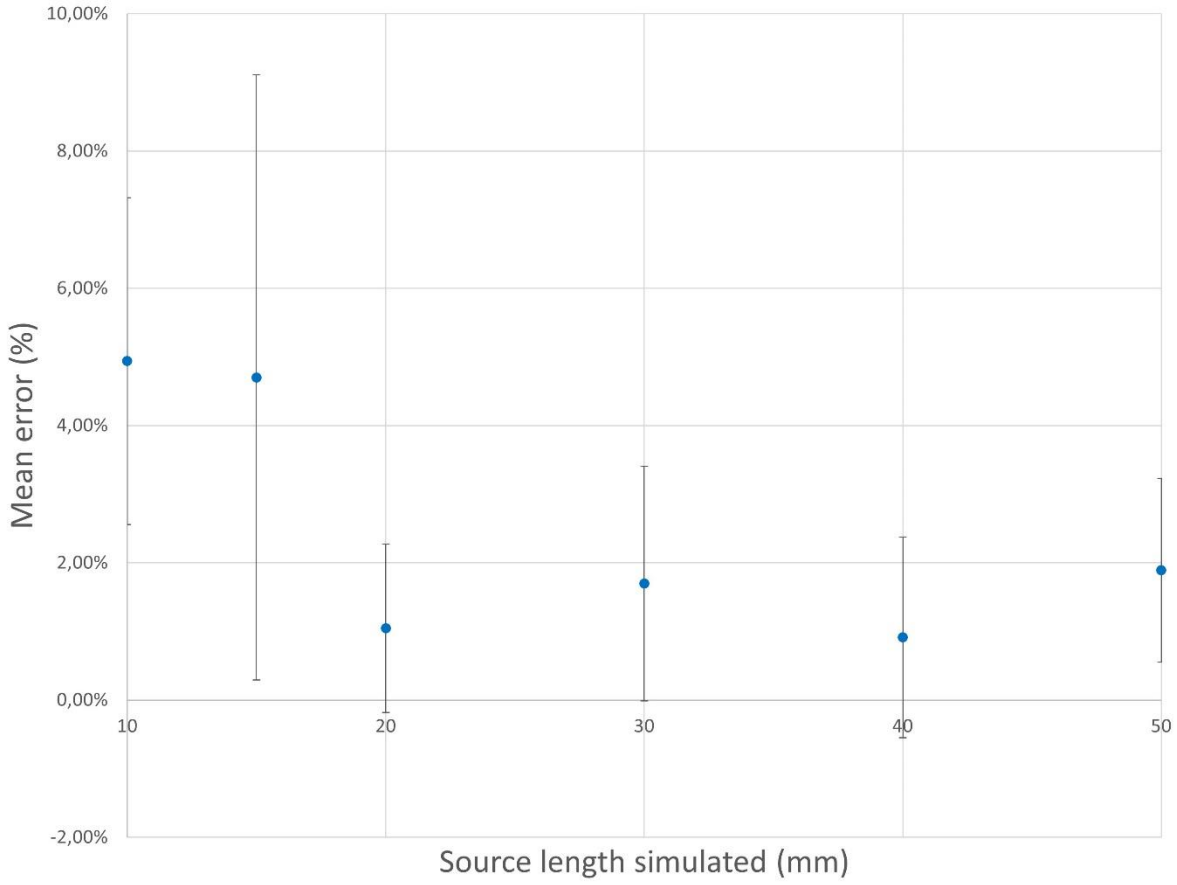

Figure 4.9: Data points are the mean relative deviations of fluence rate values computed by the analytical method, calculated for all six different source lengths over each distance d (0.75 mm to 10 mm).

Source length (mm)	Mean (SD)	Max deviation
10	4.94% (2.38%)	8.00%
15	4.70% (4.41%)	15.38%
20	1.05% (1.23%)	4.24%
30	1.70% (1.71%)	5.56%
40	0.91% (1.46%)	5.00%

50	1.89% (1.34%)	4.49%

Table 4.3: Relative deviation computed for different source lengths; the mean is computed for all distances.

c. Sensitivity study results

Sobol indices computed from the analytical model were illustrated according to the distance to the light source on figures 4.10, 4.11 and 4.12. Figure 4.10 shows the first-order Sobol indices due to absorption coefficient variation. Figure 4.11 shows the first-order Sobol indices due to the reduced scattering coefficient variation. Figure 4.12 shows the second-order Sobol indices estimating the output sensitivity to absorption and reduced scattering coefficients. Table 4.4 summarizes the first-order and total-effect indices of each parameter (absorption and reduced-scattering coefficient). In this case, the total-effect index is the sum of the first- and second-order Sobol indices. These indices provide global sensitivity, which is the sensitivity of the parameter alone and interaction sensitivity with all other parameters.

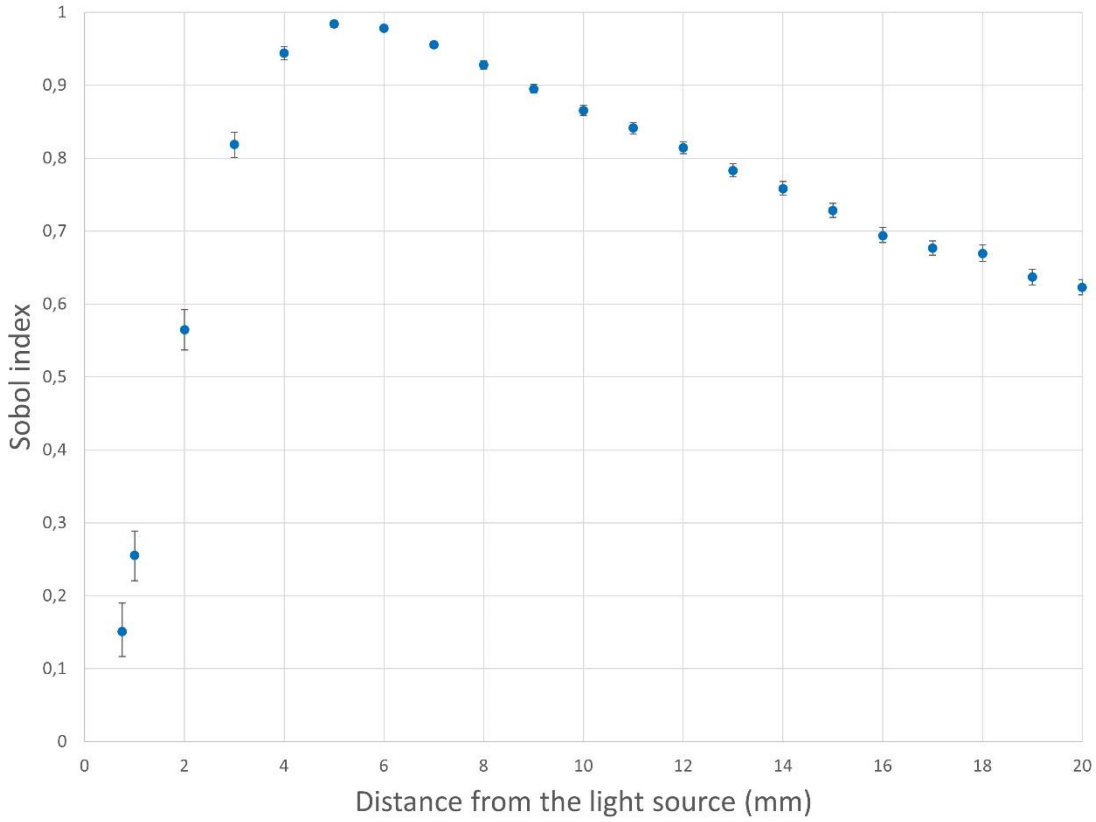

Figure 4.10: First-order Sobol indices (S_{μ_a}) for different distances to the light source. These Sobol indices quantify the contribution to the analytical model variance to the effect of absorption coefficient variation.

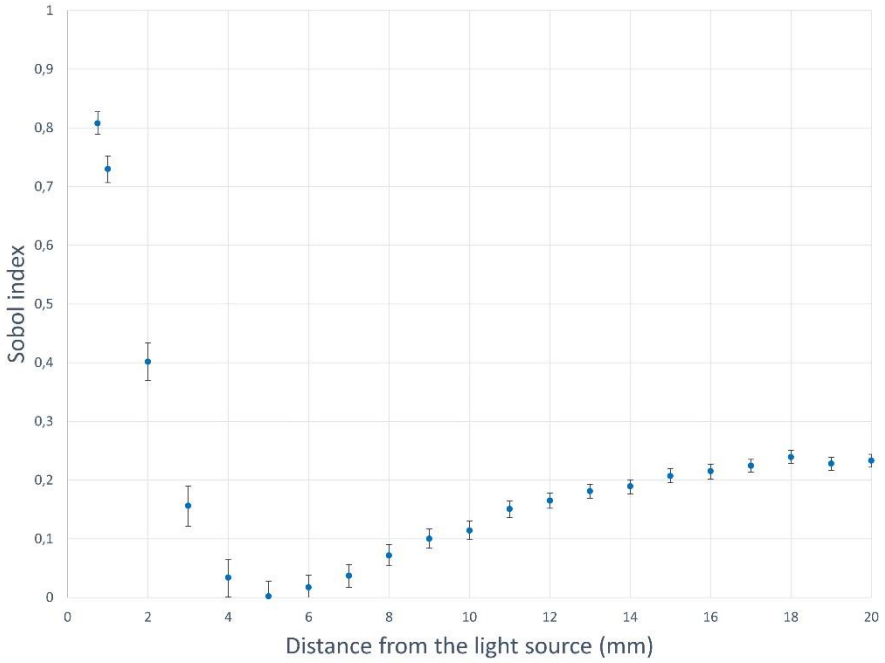

Figure 4.11: First-order Sobol indices ($S_{\mu_s'}$) for different distances from the light source. These Sobol indices quantify the contribution of the analytical model variance to the effect of reduced scattering coefficient variation.

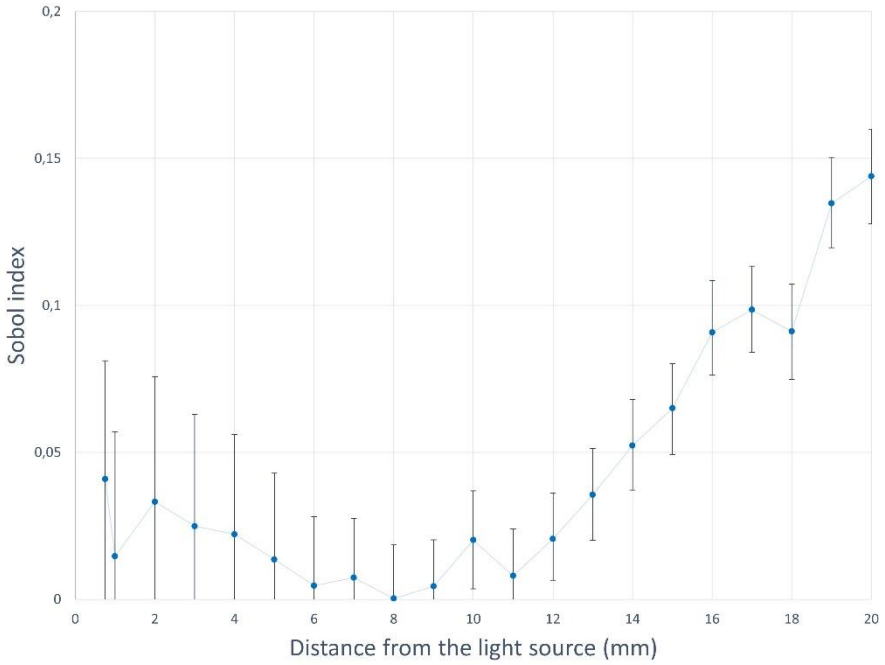

Figure 4.12: Second-order Sobol indices ($S_{\mu_a\mu_s'}$) for different distances to the light source. These Sobol indices quantify the sensitivity of the analytical model variance to the interaction of reduced scattering and absorption coefficients variations.

distance (mm)	S_{μ_a}	S_{Ti}	$S_{\mu_s'}$	S_{Ti}
0.75	0.285	0.287	0.713	0.715
1	0.354	0.371	0.629	0.646
2	0.663	0.702	0.299	0.337
3	0.853	0.924	0.077	0.147
4	0.959	0.986	0.014	0.041
5	0.984	0.998	0.002	0.016
6	0.974	0.992	0.008	0.026
7	0.951	0.957	0.043	0.050
8	0.921	0.939	0.061	0.079
9	0.892	0.897	0.103	0.108
10	0.855	0.862	0.138	0.145
11	0.823	0.843	0.157	0.177
12	0.794	0.834	0.166	0.206
13	0.770	0.811	0.189	0.230
14	0.753	0.801	0.199	0.247
15	0.711	0.789	0.211	0.289
16	0.695	0.782	0.218	0.305
17	0.680	0.767	0.233	0.320
18	0.647	0.768	0.232	0.353
19	0.619	0.760	0.240	0.381
20	0.597	0.755	0.245	0.403

Table 4.4: First-order ($S_{\mu_a}$and ($S_{\mu_s'}$) and total-effect Sobol indices (S_{Ti}).

4. Discussion

The use of a standard stereotactic procedure would facilitate the iPDT integration in a standard neurosurgery environment. Regarding the stereotactic registration algorithm implemented in the *iPDT-Plan*, its validation shows results close to the registration embedded in the Leksell GammaPlan® (Elekta, Stockholm, Sweden). The mean distance was 0.8 ± 0.3 mm, which is under the standard MRI resolution (i.e., one millimeter) commonly used in treatment planning.

As implemented in this study for μ_a = 0.02 mm^{-1} and μ_s' = 2 mm^{-1}, this analytical method (equation 4.9) shows an accurate estimation of light distribution, especially for a source length longer than 20 mm compared with the Monte-Carlo results. As detailed, the mean relative deviation of source length variations was approximately 1.23%, which is acceptable for a use as estimation of light propagation in a homogeneous medium, at a distance greater than the MFP' from the light source.

Regarding the sensitivity study, the reduced scattering coefficient is the most influential on analytical model variance close to the light source (approximately 70% to 80%). Conversely, beyond a distance to the light source of 3 mm, the absorption coefficient becomes the most influential parameter on the analytical model. At a distance of 5 mm, approximately 98% of the analytical model variance is due to the effect of the reduced scattering coefficient. First-order Sobol indices can be considered as total-effect indices between 0.75 mm and 10 mm from the light source, whereas the second-order Sobol indices are negligible. Between 10 mm and 20 mm from the light source, the impact of absorption coefficient on output variance remains constant, (approximately 20%) and the effect of reduced scattering decreases slowly (from 85% to 60%). Thus, the interaction between the absorption and the reduced scattering coefficient cannot be overlooked.

Since the analytical model implemented in the TPS does not consider the heterogeneity characteristic of GBM, the necessity to replace it by the Monte-Carlo model appears as highly recommended.

II. Forthcoming developments and improvements

Although this first attempt to design a TPS dedicated to the stereotactic iPDT of GBM enables keys steps to plan an entire iPDT procedure, several developments could be performed to improve the dosimetry part mainly, particularly to include the GPU Monte-Carlo model presented in Chapter III.

1. Automatic segmentation

A major advantage of the use of analytical models lies in its simplicity of implementation in a TPS. As seen previously, GBM is strongly heterogeneous, and the analytical models cannot consider this characteristic, which remains a major drawback.
As shown in Chapter III, the improvement of parallel GPU computing that drastically decreases the computing time [266, 268, 320] ensured strong enthusiasm for developing the Monte-Carlo method for PDT planning [102, 266]. With the implementation of an automatic tissue segmentation methods [321, 322] in the workflow of the iPDT-Plan (figure 4.1), the GPU Monte-Carlo model presented in chapter III could be used to compute the fluence rate according to optical coefficients for each voxel of the MRI volume used for planning.

Currently, the dosimetry model does not consider heterogeneity of target tissues. The entire space is considered as a homogeneous biological medium. A major improvement of the

TPS will have to include an automatic segmentation of different parts of GBM, e.g., necrotic signal, enhancing and non-enhancing tumor and edema as proposed by the software BraTumIA (Brain Tumor Image Analysis) [70]. This segmentation method, based on a decision forest classifier, modeled a map of the tumor cells distribution in tissue using four different MRI modalities: T1, T1-Gadolinium, T2 and FLAIR [323]. From this map, distinction between four main biological tissue types is performed. Adding this fast automatic segmentation method in the actual workflow of the *iPDT-Plan* would enable to take advantage of Monte-Carlo possibilities, in particular to model light propagation in heterogeneous turbid medium. Thus, each voxel would represent a specific biological tissue with specific optical coefficient values (see table 4.5) at the segmentation output. Thus, the GBM heterogeneity would be considered.

Tissue	**Absorption: μ_a (cm^{-1})**	**Scattering: μ_s (cm^{-1})**	**Anisotropy: g**	**Refractive index: n**	**Wavelength [nm]**	**Reference**
GBM cells infiltrated	0.2	160	0.875	1.4	633	[75, 99, 117, 188]
White matter	1.58 0.8	51 409	0.96 0.84	1.4	633 630	[305] [324]
Grey matter	2.63 0.2	60.2 90	0.88 0.89	1.4	633 630	[305] [324]
Necrotic core	0.7	147	0.85	1.4	630	[325]
Edema	0.2	184	0.875	1.4	633	[326]
Skull	0.4	350	0.92	1.55	650	[327, 328]
Standard brain	0.29	127	0.9	1.4	660	[327]

Table 4.5: Optical coefficients properties according to tissue type.

Presently, this software is not available in command-line interface and cannot be easily integrated in the *iPDT-Plan* workflow. Although, numerous algorithms can differentiate accurately different parts of brain structures, segmentation of brain tumors remains challenging, more particularly in the GBM case due to its strong heterogeneity [329].

2. Treatment optimization

The development of a computer-based optimization process occurring after the planning of cylindrical diffusers insertion would simplify the planning procedure. This also facilitates the standardization of PDT treatments, which enables to achieve better comparison between clinical studies.

Similarly to stereo-electroencephalography (SEEG) procedures [330, 331]procedures which safety optimization have been recently proposed, iPDT planning for brain tumor therapy should include safety constraints during the optimization process. Indeed, SEEG planning tends to optimize the intracranial electrode implantation in order to maximize the recording volume, while constraining trajectories to safe paths. After the target points are defined, algorithm optimization computes possible trajectories and their associated risks. Similar technologies may be used for iPDT. From fiber locations with associated risk along their path, light propagation in tissues might be computed to enable a global optimization process to illuminate a maximum of tissue volume while keeping trajectory safe.

3. Additional parameters integration

As previously developed in the second chapter (II, 2 – additional features for dosimetry planning), estimation of the distribution of light delivery is a major but not the only one component of PDT dosimetry. Photosensitizer and tissue oxygen concentrations should also be integrated in the workflow to obtain at least an explicit dosimetry of the PDT treatment planned. Thus, obtaining a complete dosimetry in clinic is a very challenging task which requires acquisition of several data before and during the surgical procedure with multiple probes insertion. Also, implicit features such as fluorescence and singlet oxygen assessment during the treatment could improve TPS dedicated to PDT. Presence of blood or cerebrospinal fluid can strongly affect the absorption of light during a PDT treatment. This alteration modifies the fluence deposited in tissue and, as a consequence, the PDT outcomes. However, it remains difficult to prevent such perturbations on tissues optical properties and to integrate them into light distribution computing.

Finally, in analytical solutions, presence of non-diffusing part, numerical aperture and inhomogeneity of light distribution along the cylindrical diffusers are not considered. These features also influence the light emission. As Vesselov et al. showed in their study [332], strong difference can appear between theoretical and experimental irradiation measurements from different manufacturers. Ideally, the efficiency and longitudinal, polar and azimuthal

emission of each light source should be added into the fluence rate computation workflow to reach a more realistic model.

Chapter conclusion

A proof of concept of a TPS dedicated to the stereotactic iPDT is presented. This first attempt enables to plan the insertion of cylindrical diffusers and locate them in the Leksell frame, commonly used in neurosurgery. The stereotactic registration method used is described and its accuracy was evaluated by comparing its localization with the native commercial solution. Also, a simple dosimetry model based on analytical model, implemented in the software, enables to estimate light propagation in brain's patient. This model was compared to Monte-Carlo model to validate its accuracy. A sensitivity study was performed to evaluate the impact of absorption and scattering properties variations on the variance of the analytical model, as in GBM tissues.

Finally, several future developments are suggested, particularly to include a segmentation algorithm, which is mandatory for implementing the GPU Monte-Carlo model in the TPS workflow.

Chapter V

Intraoperative PDT: toward the clinical trial

Important pre-clinical studies have been carried out in order to optimize the PDT delivery within the framework of the GBM treatment project at the ONCO-ThAI laboratory. Thus, moving forward a clinical application of PDT was therefore a logical outcome. This last

chapter presents a new lighting device dedicated to intraoperative GBM photodynamic treatment and for which the Monte-Carlo implementation presented in chapter III was deeply involved during the evaluation phase.

A short overview of previous clinical trials investigating intraoperative approach of PDT for GBM is first presented. Regarding the methodology expected to be seamless with the usual neurosurgery approach, a new lighting device was designed during this thesis and that includes specific expectations. Additionally, specific methodologies were developed to calibrate and assess the device in terms of mechanic and dosimetry. Indeed, the calibration lead to a transfer function associated with the device and that provides fast, robust and easy treatment duration prescription to induce a PDT response.

Furthermore, a comprehensive experimental design has been worked out prior to the clinical trial and results are reported in this chapter.

Finally, the setup of the clinical trial and first patient's results are introduced. Possible technological improvements and research perspectives are discussed.

I. Design and development of the prototype

1. Previous experiments

As previously described in the first chapter (II, 2 – Standard of care), when achievable, maximum tumor resection is expected according to the standard management of GBM [72]. Fluorescence guided resection (FGR) leads to 2 months-increase of the progression free survival median (PFS). However, even if the surgery is complete (no more visible fluorescence or no more MRI signal highlighting the GBM), spread tumor cells usually remains within the healthy parenchyma. Because of these invading tumor cells, radiation therapy and concomitant and adjuvant chemotherapy fail to definitely cure the tumor and relapse is always occurring in the cavity margin in 85% of cases, [76, 333, 334]. A therapy to treat resection borders is highly expected to maximize the local control.

Illumination of the resection cavity remains challenging since the device has to suit the shape of the cavity. In that context, a deformable balloon is expected to meet this requirement. As presented in chapter I (III, 3, a – Instrumentation), several devices have been designed in the past: inflatable balloon with different light sources [121-123, 132, 335], optical fiber coupled to a reflector in order to maximize light in the surgical cavity or LASER light source coupled to the surgical microscope and enabling a step by step illumination [124]. Moseley et al. described the only study using ALA as precursor [122, 132]. For this study, both 5-ALA

and Photofrin® were considered and repetitive PDT was evaluated. 5-ALA was used for the FGR procedure and PpIX was activated with the first illumination. The following illuminations (post-operative) were used to activate Photofrin®, which has a longer half-life than 5-ALA. The diffuser was created from a catheter balloon with a fiber and a cylindrical diffuser tip coupled to a Diomed PDT laser at 630 nm. Thus, none of these previous studies used 5-ALA as primary PS precursor to provoke a PDT effect on areas bordering the resection cavity.

2. Description of a new concept of intraoperative PDT procedure

To be more acceptable for both surgeon and patients, intraoperative PDT has to be fully embedded within the usual surgical workflow. Consequently, the concept of our new therapeutic approach was to deliver 5-ALA PDT intraoperatively early after FGR. Accordingly, PDT added at the end of surgery achieved with FGR enables the treatment of the areas bordering the resection cavity while maintaining a maximal but safe resection (see figure 5.1).

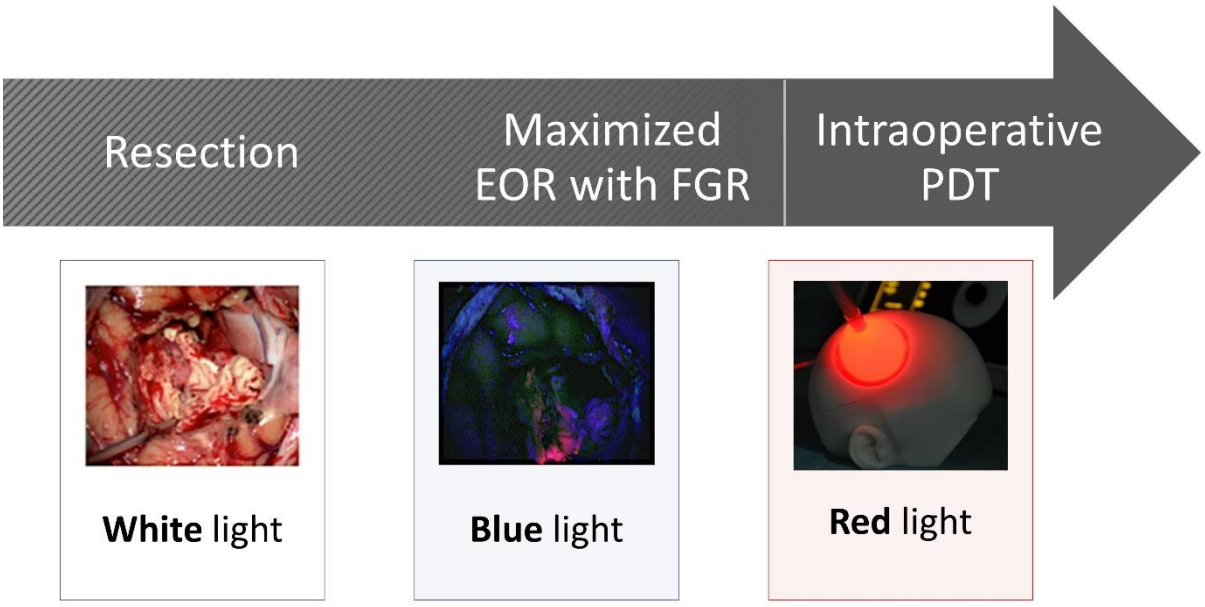

Figure 5.1: Surgical workflow including 5-ALA PDT early after FGR achieved to maximize the extent of resection (EOR).

To make feasible intraoperative PDT, illumination of the surgical cavity must be carried out by a specific device diffusing a 635 nm LASER light homogenously to a sufficient irradiance.

Intraoperative PDT takes advantage of the presence of the PS which is already approved and administered to the patient for FGR purpose [76]. The proposed treatment strategy can fit into the current standard of care applied in first intention of care (see figure 5.2) [72]. Thus, intraoperative 5-ALA PDT is more ethically acceptable in comparison with interstitial PDT on resectable tumor.

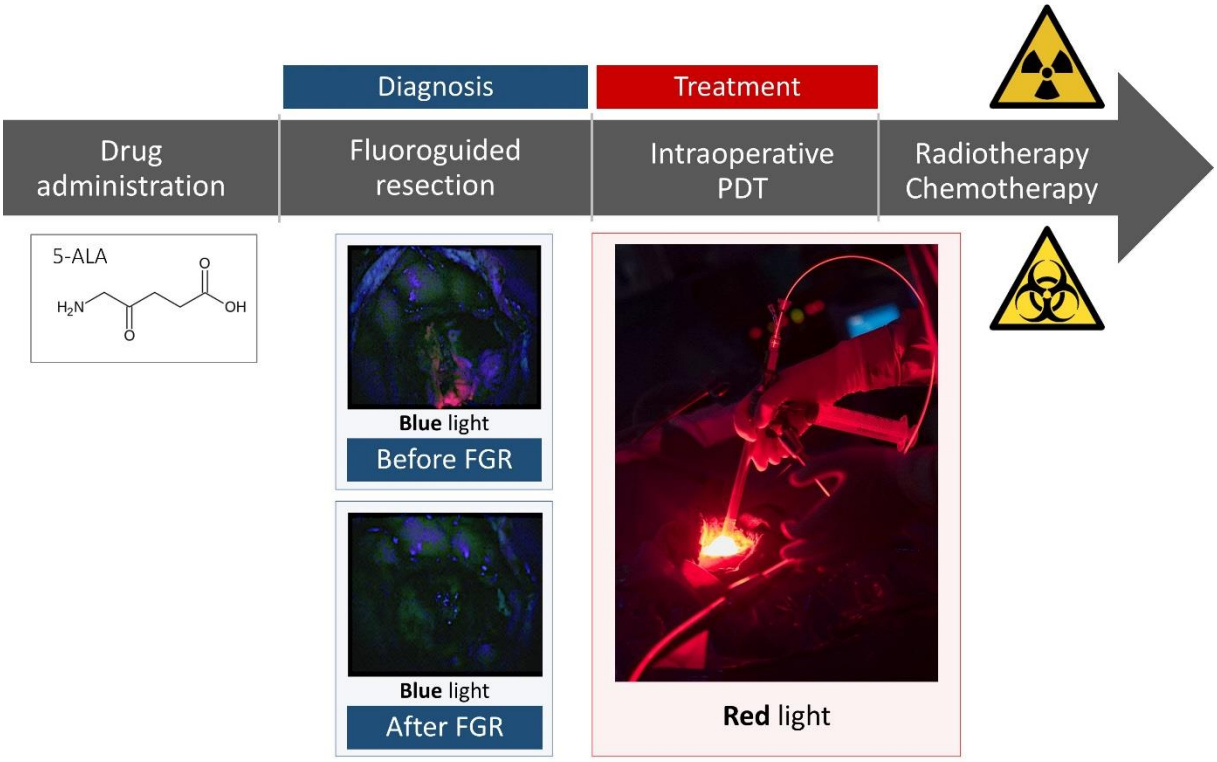

Figure 5.2: Workflow of the intraoperative PDT procedure.

First, the precursor of the photosensitizer (5-ALA) is administered to the patient several hours before surgery. Standard resection surgery is performed in order to remove as much tumor tissues as possible. When the surgeon judges it necessary, blue light is turned on to illuminate the resection cavity. The PS, concentrated in the tumor tissue, emits a pink fluorescence (see figure 5.2). This technic helps to better distinguish the healthy brain from remaining tumor tissue. In this case, the PS is used as a contrast agent for visual diagnosis. The resection is ended when no remaining fluorescence is observed or to preserve functional areas. However, even if no fluorescence in the cavity is observed, remaining tumor cells around and deeper in the cavity are still present with PpIX uptake, but at a concentration limiting their visualization through the microscope. These remaining cells that are not

macroscopically visible are the main target of the PDT treatment in that context. Thus, the PDT procedure is achieved early after the FGR. Here, PS is thus repurposed as a therapeutic agent to obtain a PDT effect. After the PDT procedure, as recommended by the standard of care, radio and chemotherapy are delivered to the patient to decrease recurrence risks.

To set-up an intraoperative PDT procedure, a lighting device has to be placed inside the surgery cavity and its inflation must be controlled by neurosurgeon until it reaches the cavity boundaries. The device must illuminate homogeneously the surrounding tissues with the help of an optical fiber. The treatment time enabling to achieve a therapeutic fluence value in surrounding brain tissues has to be easily and quickly computed.

For that purpose, a new lighting device was designed according to the comprehensive specifications drawn up in agreement with neurosurgeons from the Neurosurgery Department of the University Hospital of Lille. Additionally, a transfer function was built-up to enable real time dosimetry in the operating room according to the volume of the surgical cavity after gross tumor resection.

The medical device had to meet the following main requirements:

- Having a spherical or ovoid shape,
- Owning a diameter up to 10 cm,
- Enabling a conformability to the cavity,
- Ensuring a biocompatibility with brain tissue,
- Avoiding liquid injection in brain tissues,
- Integrating a diffusing optical fiber at its center,
- Being transparent to the light emitted by the LASER during the PDT treatment,
- Allowing an easy setting up,
- Enabling an acceptable illumination time.

Despite of the Herloon© balloon manufactured by B-Braun® Aesculap® (Tuttlingen, Germany) is neither dedicated to PDT nor neurosurgery, it meets several criteria of the specifications. Thus, to speed-up approval by ethical committees, this already CE marked and commercialized device was adapted for a PDT and served as basis for the design of the light applicator.

3. Medical device design

The device consists of two parts (see figure 5.3). The first one is the Herloon© balloon coupled to a trocar that is usually used during endoscopic intervention in which tissue needs

to be separated in the extraperitoneal space. This device is built from a sterilizable trocar body and a single-use only transparent balloon. A sluice gate is added to the trocar, allowing fluid insertion to inflate the balloon. The inflation of the balloon ranges from a 4 cm diameter for 40 mL of diffusing solution to a 9 cm diameter for 500 mL of injected diffusing solution. A silicone valve terminates the trocar to ensure permeability and pressure inside the device.

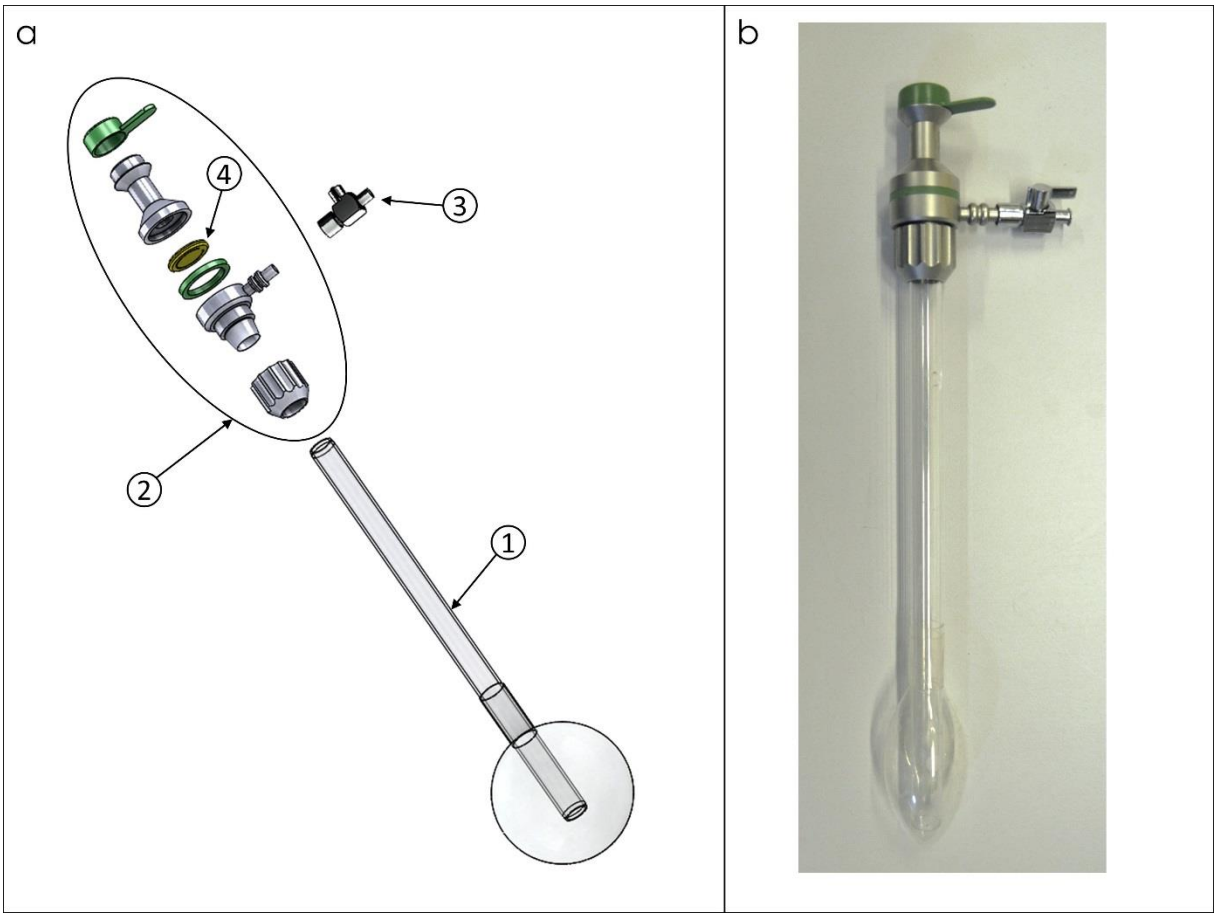

Figure 5.3: (a) Expanded view of the Herloon® device: an inflatable balloon (1) is inserted into the trocar body (2); a sluice gate allows fluid insertion (3) and a flap valve selectively close or open the internal passage of the fiber guide while ensuring its tightness. (b) Assembled view of the first part of the device: the Herloon© balloon commercialized by B-Braun® Aesculap®.

The second part, referred to as the optical fiber guide, was developed in the laboratory ONCO-THAI. This guide was built from an 8 mm diameter borosilicate glass tube closed at one end and inserted in a 10 mm stainless steel tube (see figure 5.4). This guide enables the positioning of the optical fiber at the balloon's center while ensuring complete permeability. The optical fiber inserted in the guide is a 70 mm long cylindrical diffuser (RD-ML 70, Medlight, Ecublens, Switzerland) that approximately matches the balloon length in its

deflated state. Finally, a screw thread fixed at the top of the guide allows tightening of the optical fiber inside the guide. The fiber guide is entirely compatible with the ethylene oxide sterilization process.

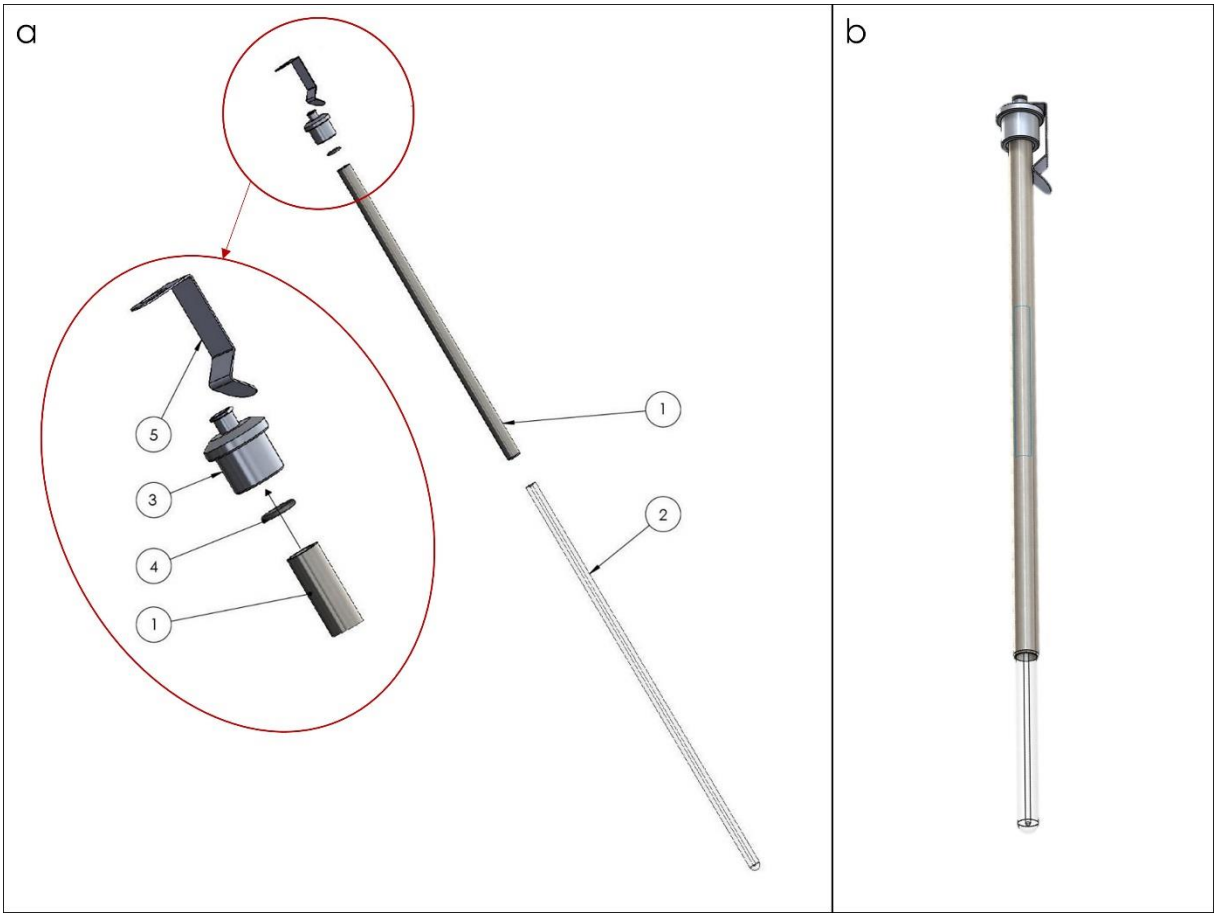

Figure 5.4: (a) Expanded view of the fiber guide: a borosilicate glass tube (2) is inserted into the stainless steel tube (1); a stainless steel luer adaptor (3), a PTFE seal for impermeability (5) and a stainless steel spring tab (5) hold the fiber guide against the trocar. (b) Assembled view of the fiber guide.

To set up the whole lighting applicator, a single-use balloon is first inserted into the trocar. Then, the fiber guide hosting the 70 mm long cylindrical diffuser is inserted into the fiber guide (see figure 5.5) and is placed in the trocar balloon. After being assembled, the device is set on a frame and guided inside the surgical cavity by neurosurgeon. The balloon is filled with an emulsion composed of a 20% Intralipid® (Fresenius Kabi France, Sèvres, France) diluted at a concentration of 0.1% until its wall reaches the brain-patient boundaries. This emulsion exhibits weak absorption and strong diffusion at a laser light wavelength of 635 nm [122, 132, 335] and increases homogeneity of the light emitted from the source.

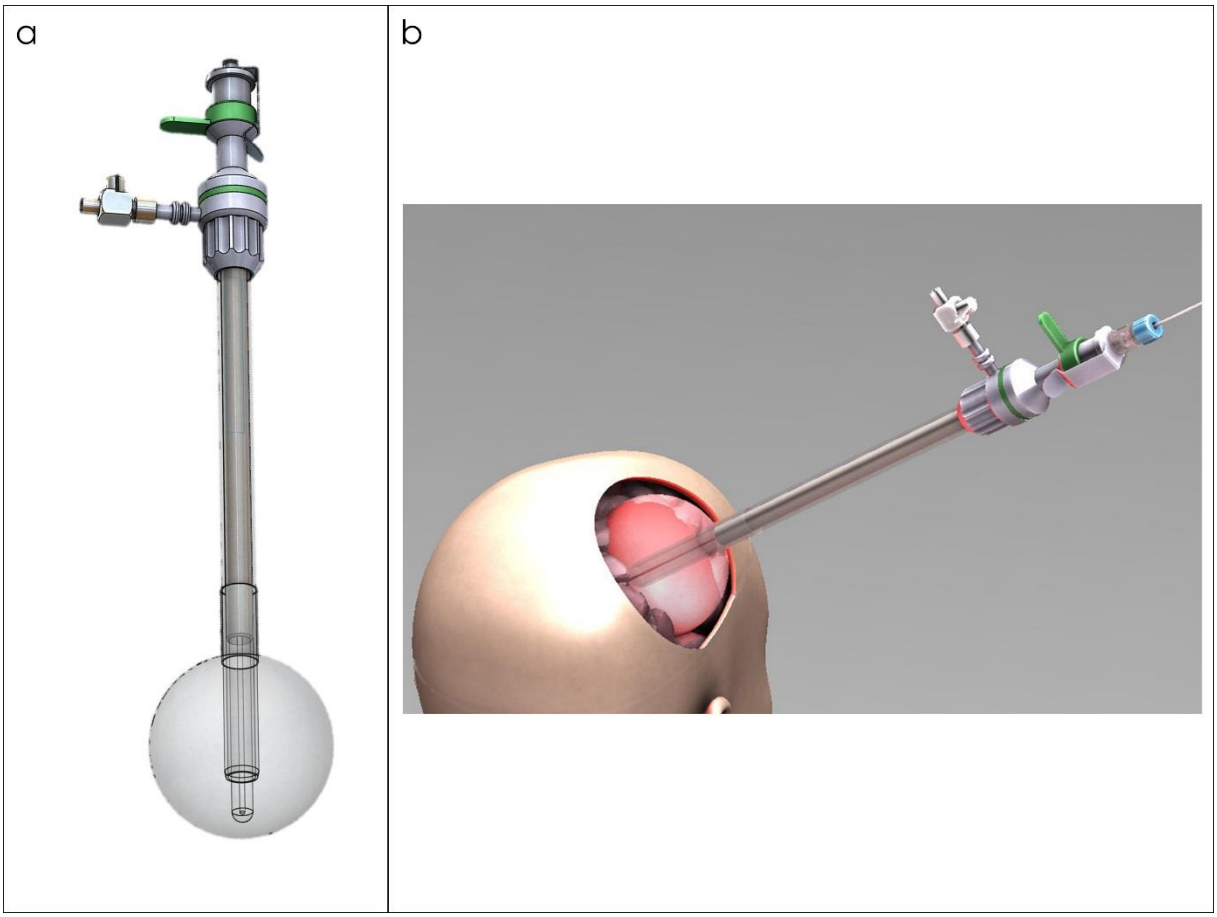

Figure 5.5: (a) Complete lighting applicator (part one and two assembled) (b) Perspective view (generated by SolidWorks®) of the whole system: the fiber guide and the single-use balloon are inserted into the trocar; the whole device is placed into a surgical cavity.

II. Calibration

The main purpose of the calibration was to model a transfer function so that the treatment duration can be predicted from an abacus according to the quantity of diffusing solution injected into the balloon. Indeed, the higher the quantity of liquid injected is, the larger the balloon diameter is and the longer the treatment duration has to be for a given therapeutic fluence. The treatment time, deduced from the abacus, is expected to lead to a therapeutic fluence of 25 J/cm² at 5 mm inside surrounding brain tissues.

The propagation of the light emitted from the balloon was quantified using several ex vivo experiments. To mimic clinical treatment conditions, calf brains were used due to their optical properties (absorption and reduced scattering coefficients of 0.19 cm^{-1} and 20.09 cm^{-1}, respectively [305]) close to those of human brains (absorption and reduced scattering coefficients of 0.20 cm^{-1} and 20 cm^{-1}, respectively) [117, 336, 337]. Additionally, these experiments were compared with *in silico* experiments from Monte-Carlo simulations using

the algorithm implemented and detailed in chapter III.

1. Calibration of the measuring system

Before measuring fluence rate in calf brain using the same methodology and measurement chain than the Monte-Carlo validation experiments (III.2 Monte-Carlo validation by comparison with experimental measurements) calibration of the measuring system were achieved.

Indeed, as presented in chapter III (III, 2, a - Calibration factor), power measurements had to be converted to achieve the dosimetry of the device. Basically, a calibration factor CF_{brain} was computed in order to convert power values measured in the calf brain $P_{measured}$ [W] into fluence rate values ϕ_{brain} [W.cm^{-2}]:

$$\phi_{brain} = CF_{brain} . P_{measured} \quad (5.1)$$

The same methodology as used in chapter III was applied using Marijnissen and Star papers [299, 300]. Thus, four correction factors F_n, F_p, F_b, F_i and the calibration factor CF_{air} in air was estimated to obtain the calibration factor CF_{brain} in calf brains.

$$\phi_{brain} = P_{measured} . CF_{air} . F_n . F_p . F_b . F_i \quad (5.2)$$

where F_n is a correction factor enabling to compensate the loss of light due to the interface sensor/surrounding calf brain using the refractive index of the calf brain around the isotropic probe (dimensionless). F_p is a perturbation correction [dimensionless]. F_b is a correction of the detection's photons' loss due to the surface occupied by the fiber on the detection sphere [dimensionless]. F_i is a correction of the sensor's non-homogeneity response [dimensionless].

All factors were estimated using the experimental protocol already described in the third chapter (II, 2, a - Calibration factor).

2. Ex-vivo measurements

Prior to the experiments, fresh calf brains were prepared by dissecting out the cerebellum, the brain stem and the corpus callosum to improve the homogeneity of the studied tissues. The entire lighting applicator was fixed to a black box to avoid reflections and the balloon part was placed at the center of the box. Several pieces of calf brain were arranged in such a way that the balloon was entirely surrounded by tissues (see figure 5.6).

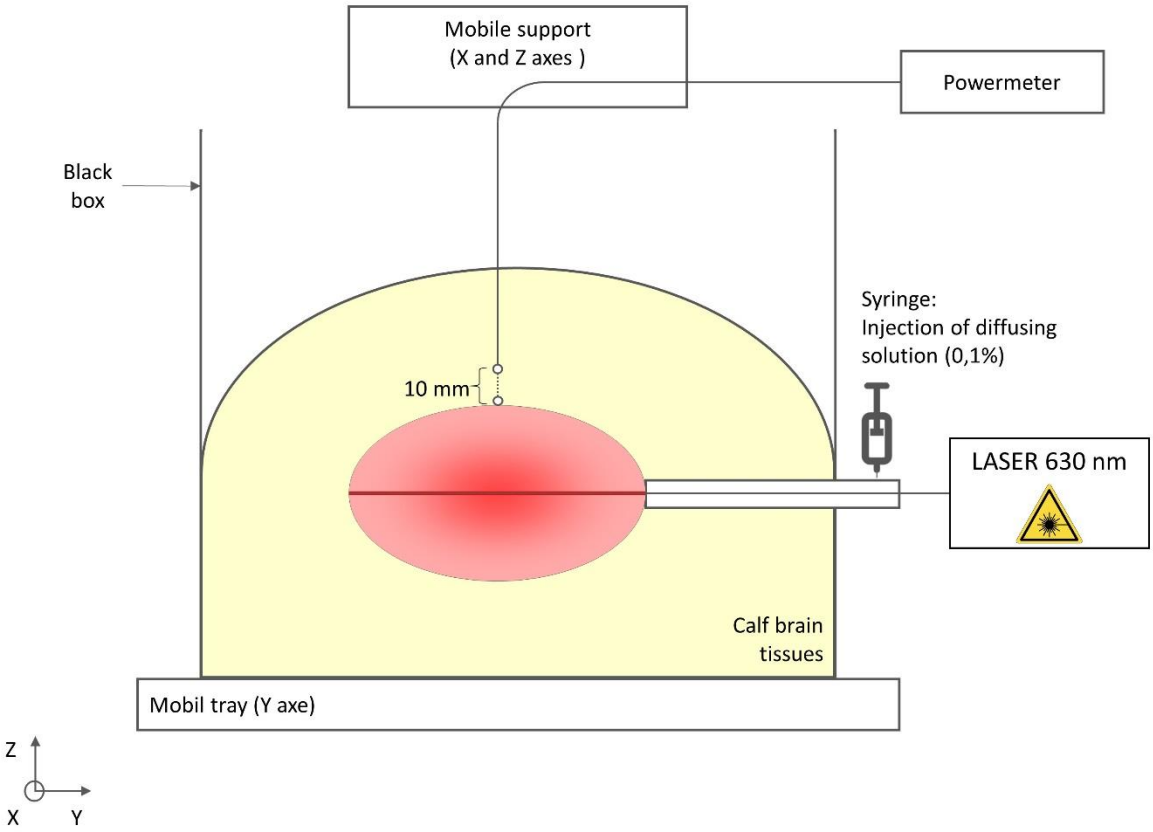

Figure 5.6: Experimental plan for fluence rate measurements inside calf brains.

An isotropic probe (IP85, Medlight, Ecublens, Switzerland) was inserted into the brain until it touched the balloon's wall for the first measure. Then, the probe was pulled upward in 1 mm steps until the probe was 10 mm from the balloon's wall. These measurements were repeated at 15 different positions around the balloon to decrease the variability due to the strong heterogeneity of the tissues (see figure 5.7).

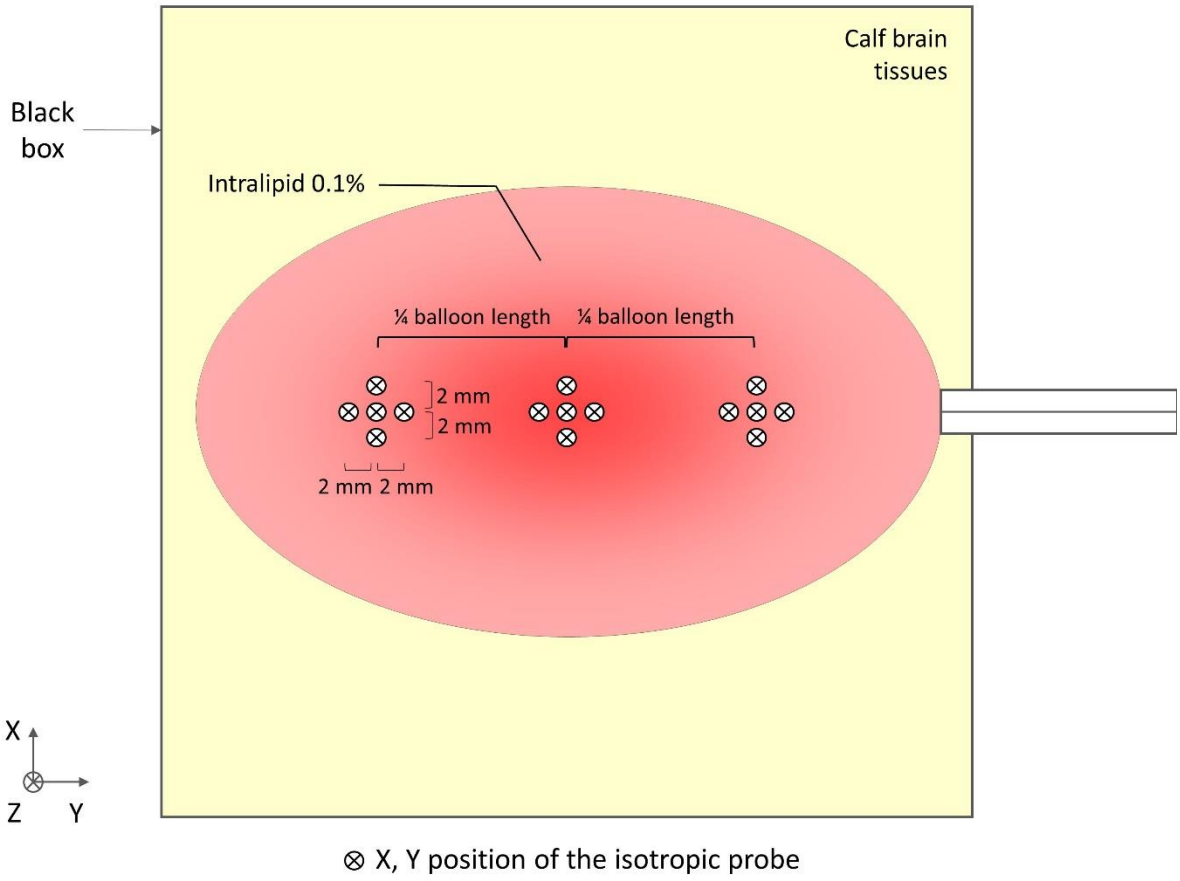

Figure 5.7: Locations of the 15 measurement positions around the balloon.

Once measurements completed, power measurements were converted into fluence rates values. A fluence value was fixed against the balloon wall in order to obtain a fluence value close to 25J/cm² at 5mm depth inside tissue. Using this fluence value, treatment times were computed according to the volume of diffusing solution injected in the device.

To verify the validity of measurements, Monte-Carlo simulations were performed using balloon's dimension. The same protocol was used to compute treatment times according to the balloon's volume. Thus, the two transfer functions (ex-vivo and Monte-Carlo) were compared. Additionally, the difference between irradiance and fluence rate as previously introduced in chapter II is illustrated.

3. PpIX concentration impact on optical coefficients

It is known that a PS might induce a change in optical coefficients according to its concentration in tissues. Therefore, PpIX impact was evaluated using the equation described by Vignion-Dewalle et al. [338].

The accumulation of PpIX does not affect the total reduced scattering coefficient. However,

the absorption coefficient is the sum of the calf brain absorption coefficient $\mu_{a,brain}$ and the PpIX absorption coefficient $\mu_{a,PpIX}$:

$$\mu_{a,total} = \mu_{a,brain} + \mu_{a,PpIX} \quad (5.3)$$

where $\mu_{a,total}$ is the absorption coefficient due to the brain and PS absorption (cm^{-1}), $\mu_{a,brain}$ is the absorption coefficient of the calf brain (cm^{-1}), and $\mu_{a,PpIX}$ is the absorption coefficient of PpIX (cm^{-1}).

The PpIX absorption coefficient $\mu_{a,PpIX}$ can be expressed according to the PpIX concentration C_{PpIX} and its molar extinction coefficient ε_{PpIX} at the precise wavelength λ:

$$\mu_{a,PpIX,\lambda} = \varepsilon_{PpIX,\lambda}.C_{PpIX} \quad (5.4)$$

where $\mu_{a,PpIX,\lambda}$ is the PpIX absorption coefficient at wavelength λ (cm^{-1}), C_{PpIX} is the PpIX concentration ($mol.L^{-1}$), and $\varepsilon_{PpIX,\lambda}$ is the molar extinction coefficient of the PpIX at wavelength λ ($L.mol^{-1}.cm^{-1}$)

Thus, the PpIX absorption coefficient can be computed in brain tissues with high PpIX concentration at 635 nm. The value of the PpIX molar extinction coefficient at 405 nm is known [339]. The PpIX absorption coefficients at 405 nm and 635 nm of a sample of an unknown concentration were determined from the absorption spectrum measured by the Research Center for Automatic Control of Nancy (CRAN) (see figure 5.8).

$$\mu_{a,PpIX,635} = \frac{\mu_{a,PpIX,CRAN,635}}{\mu_{a,PpIX,CRAN,405}}.\varepsilon_{PpIX,405}.C_{PpIX} \quad (5.5)$$

where $\mu_{a,PpIX,635}$ is the PpIX absorption coefficient at a wavelength of 635 nm (cm^{-1}), $\mu_{a,PpIX,CRAN,635}$ is the PpIX absorption coefficient of a sample of unknown concentration at a wavelength of 635 nm (cm^{-1}), $\mu_{a,PpIX,CRAN,405}$ is the PpIX absorption coefficient of a sample of unknown concentration at a wavelength of 405 nm (cm^{-1}), $\varepsilon_{PpIX,405}$ is the molar extinction coefficient of PpIX at a wavelength of 405 nm ($L.mol^{-1}.cm^{-1}$), and C_{PpIX} is the PpIX concentration ($mol.L^{-1}$).

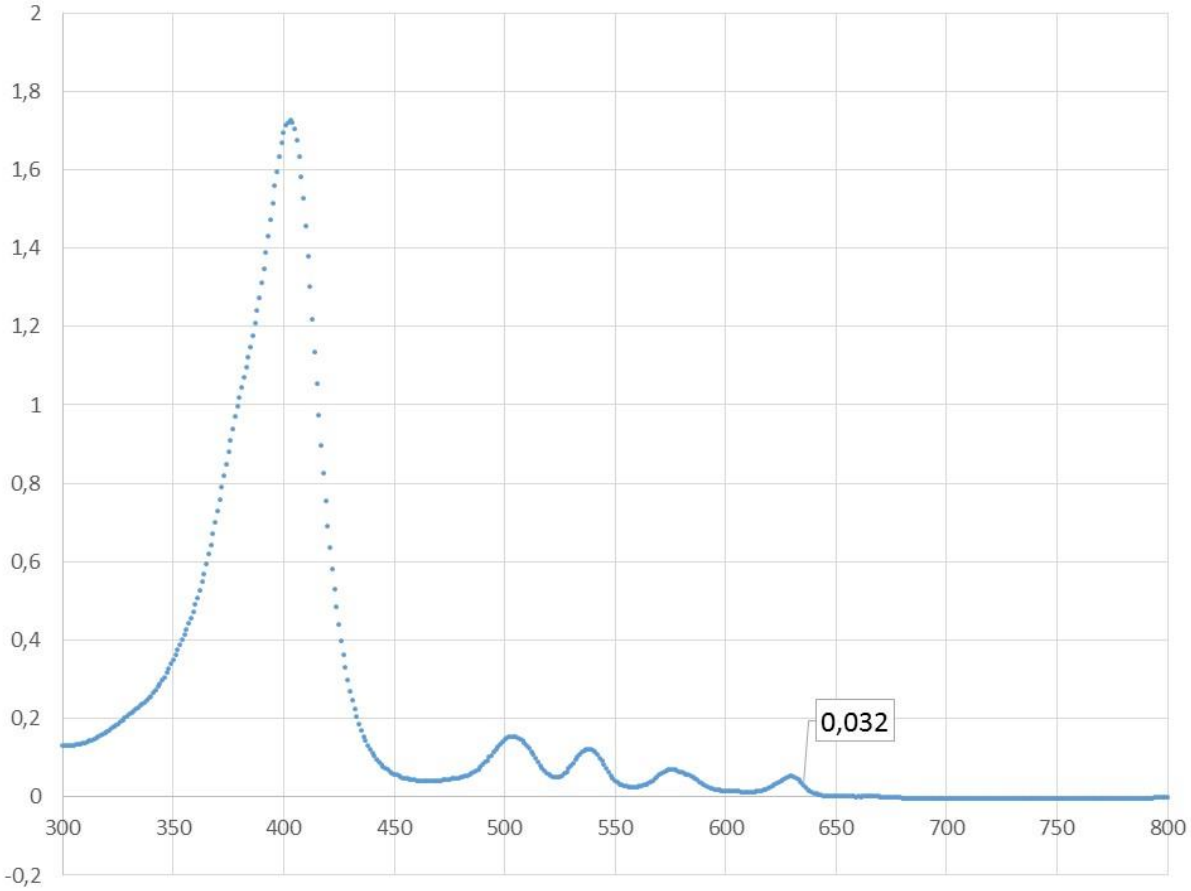

Figure 5.8: PpIX absorption spectrum.

III. Quality assessment and characterization

Several quality controls and characterization procedures were achieved in order to ensure the safety of the device. All these tests were used as technical reports for the setup of the clinical trial detailed later in this chapter.

1. Mechanical assessment

The behavior of the lighting device within a surgical cavity (pressure against the healthy parenchyma, conformity to the cavity) was studied by mean of a specific phantom with similar brain mechanical properties. Computerized Tomography (CT) images were acquired to evidence the conformity of the balloon when inflated in the surgical cavity.

a. Brain mechanical properties

The purpose was to evaluate the mechanical behavior of the device and its ability to fit

into the surgery cavity. Two features can characterize mechanical properties in elastic domain: the Young's modulus and Poisson's ratio.

The Young's modulus describes the elastic behavior of a solid material. It represents the relationship between stress [$N.m^{-2}$ or Pa] and strain [dimensionless] in continuum mechanics. A low Young's modulus (approximately kPa) describes a flexible material; contrariwise, a stiff material has a high Young's modulus (approximately GPa).

The Poisson's ratio describes the ratio of transverse strain to axial strain. Its value varies between 0 and 0.5. A high Poisson's ratio defines a material that can be deformed; contrariwise, a material resistant to deformations or that breaks without showing any elongation owns a low Poisson's ratio.

Human brain has already been mechanically characterized, including Young's modulus and Poisson's ratio (see table 5.1).

References	Young's modulus (kPa)	Poisson's ratio
Miga et al., 2000 [340]	2.100	0.45
Miller et al., 2000 [341]	3.24	0.499
Ferrant et al., 2001 [342]	3.0	0.45
Soza et al., 2005 [343]	8.196 – 8.863	0.452 – 0.461
Budday et al., 2015 [344]	1.389 – 1.895	0.5
Stewart et al., 2017 [345]	0.17 – 16.06 (brain tumors)	0.4 – 0.496

Table 5.1: Young's modulus and Poisson's ratio of human brain.

However, although those studies show Young's modulus and Poisson's ratio of human brain, a complete characterization of mechanical properties involves other features mainly because human brain does not belong to elastic domain but to hyper-elastic domain.

b. Gel phantom

In this study, the Young's modulus is the only evaluation criterion. A gel phantom was produced in order to mimic the mechanical properties of human brain and to enable the evaluation of the lighting device. According to the literature, a mean Young's modulus (without distinction on white and grey matter) is approximately 4.44 kPa and a mean Poisson's ratio is approximately 0.47.

The selected matter to create such a phantom is Power gel® (Cellpack, Villmergen, Switzerland). This bi-component gel (e.g., component A and component B) is initially used to

protect and make electrical installation watertight. Adapting the mixing of A and B enables to change the Young's modulus of the gel and thus to obtain a Young's modulus close to human brain.

Four samples of different A:B ratio have been produced: (1:1.05), (1:1.08), (1:1.10) and (1:1.12) (see figure 5.9). Inside these four samples, three tensile specimens have been cut out. Twelve tensile specimens have been produced and characterized using extensometer. This technic measures changes in the length of a material. Two points were drawn on each tensile specimen. By applying forces on each side of the tensile specimens, the two points were tracking by video during the test. Using positions of each point, graphs showing the nominal stress according to the stretch were plotted. Then, from each curve, the Yeoh's model has been used to obtain Young's modulus value. The Yeoh's model is a phenomenological model dedicated to hyper-elastic nonlinear materials with nearly incompressible deformations [346, 347].

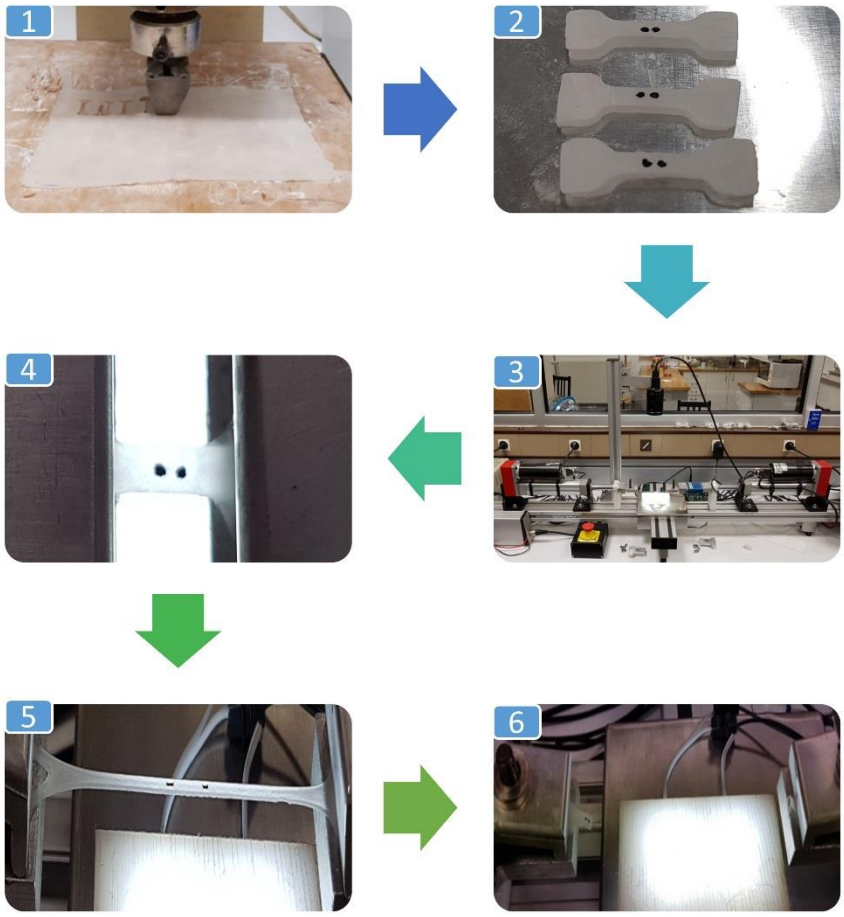

Figure 5.9: Mechanical tests: 1) cut out of the tensile specimens, 2) marking of the two points of the tensile specimens 3) mechanical bench used for tensile test: 4) the tensile specimen is fixed between two jaws and 5) stretched until 6) it breaks.

c. Phantom creation

Once the correct gel mixing ratio was obtained, a mold of a brain including a surgical cavity was created to build-up the final brain phantom.

The shape of the phantom was designed from images of a patient harboring a tumor. To best mimic the usability of the lighting device within a surgical cavity, MR images acquired intraoperatively on the intraoperative MRI of the neurosurgery department of University Hospital of Lille were used.

Post-processing was achieved on the MITK software (Medical Imaging Interaction Toolkit) that enabled to manually delineate brain and other parts of patient's head (such as skull, fat, eyes, nose and ears) (see figure 5.10).

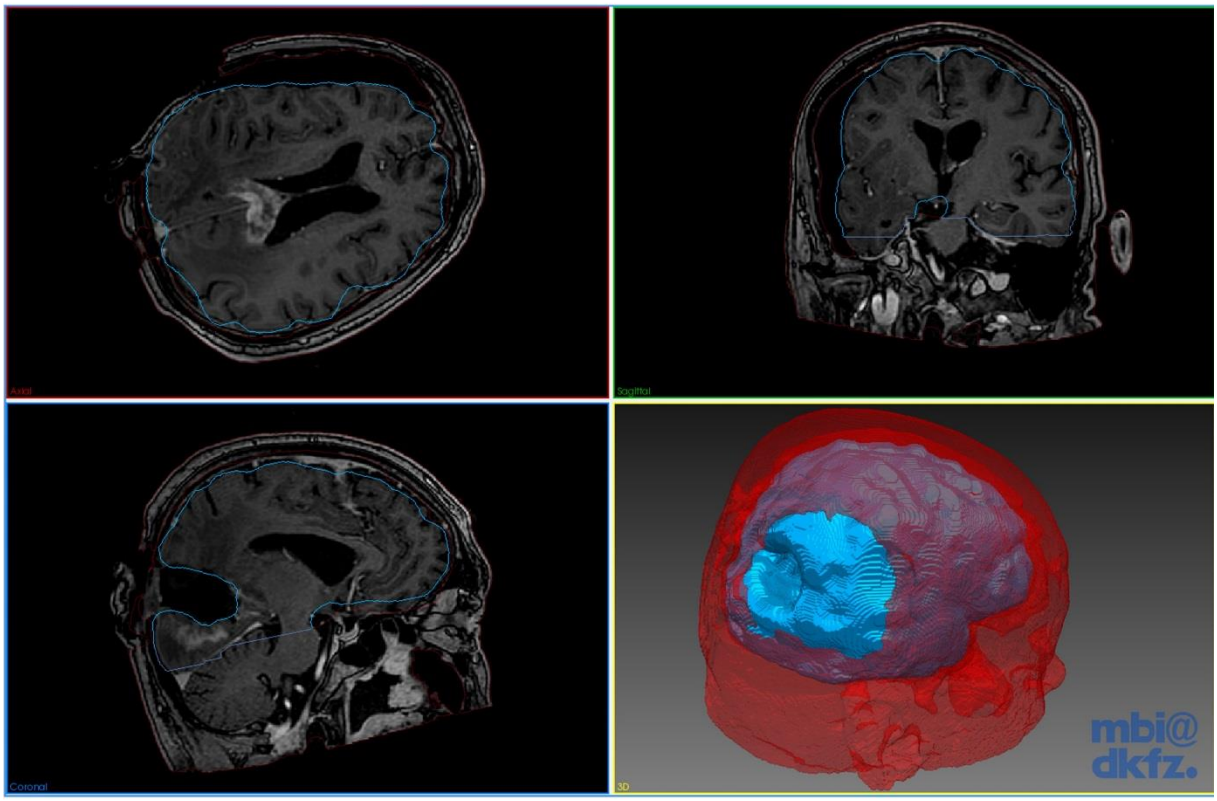

Figure 5.10: Screenshot of the MITK software: axial, sagittal and coronal view of an intraoperative MRI. 3D reconstruction of the brain's patient in blue and other tissues in red (such as skull, fat, eyes, nose, ears).

From the segmentation results, polygon models have been generated and exported in Polygon File Format in order to be processed in the software SolidWorks® (Dassault

Systemes, Vélizy-Villacoublay, France) for 3D printing in AM3300 polymer. Both, a head (see figure 5.11) and a waste mold of the brain negative were 3D printed. Using the suitable concentration mixing, the gel was poured into the waste mold. At the end, the resulting phantom gel owned exactly the same shape of the brain with the surgery cavity previously segmented.

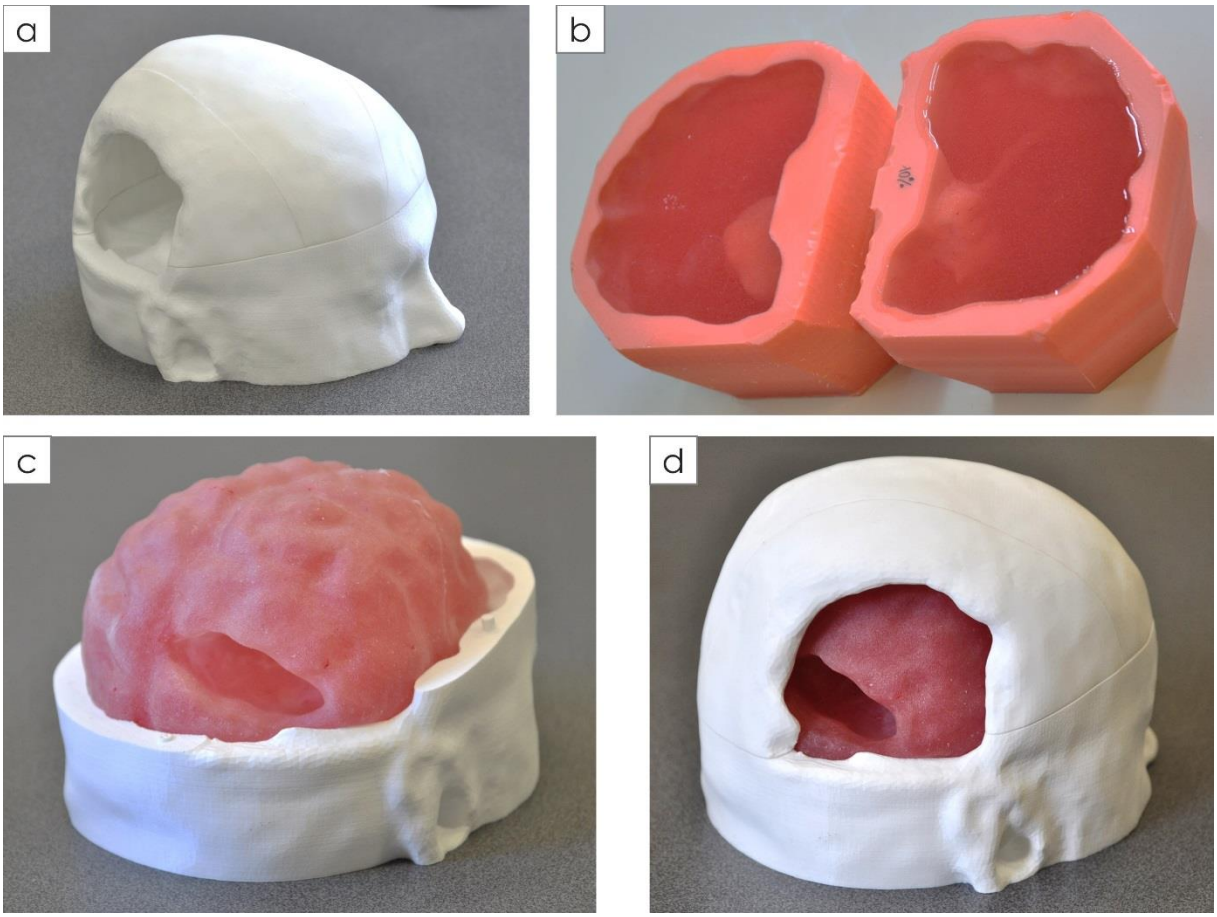

Figure 5.11: a) Skull 3D printed b) 3D printed mold filled with gel with a (1:1.10) mixing c) and d) phantom of the brain placed inside its skull 3D printed.

d. Phantom imaging

The phantom was imaged using CT-scan (see figure 5.12). The lighting applicator was placed inside the surgery cavity and filled by iodine solution in order to obtain a strong contrast between the balloon and the phantom's brain.

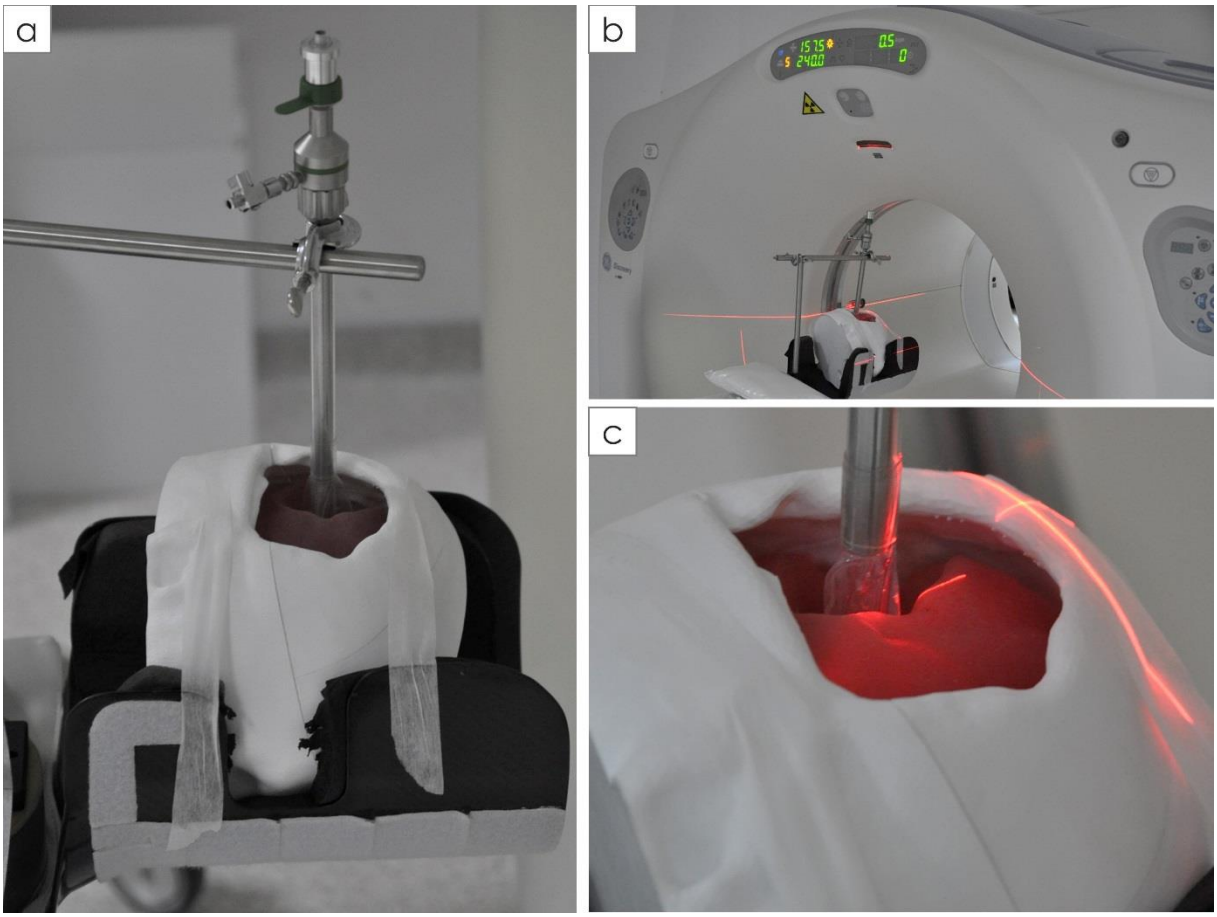

Figure 5.12: a) and b) The phantom was placed inside a CT-scan. c) The lighting applicator was inserted into the resection cavity and filled with iodine until the balloon's wall reached the boundaries of the cavity.

Using this sequence, a conformation coefficient τ [%] was computed:

$$\tau = \frac{A_{contact}}{A_{cavity}} \tag{5.6}$$

where $A_{contact}$ is the area where the balloon touches the brain's phantom and A_{cavity} is the area of the cavity.

2. Additional safety tests

In addition to the mechanical assessment of the device, several additional tests were performed to assess the safety of the device before being approved for a clinical trial.

a. Homogeneity of the light distribution

The homogeneity of the distribution along the balloon was evaluated. A flat sensor (818-SL, Newport, Irvine, CA, USA) was placed against the balloon at five different locations

(see figure 5.13). The irradiance was measured according to five different quantities of diffusing solution injected into the device (100, 200, 300, 400 and 500mL). For each volume, the irradiance was normalized.

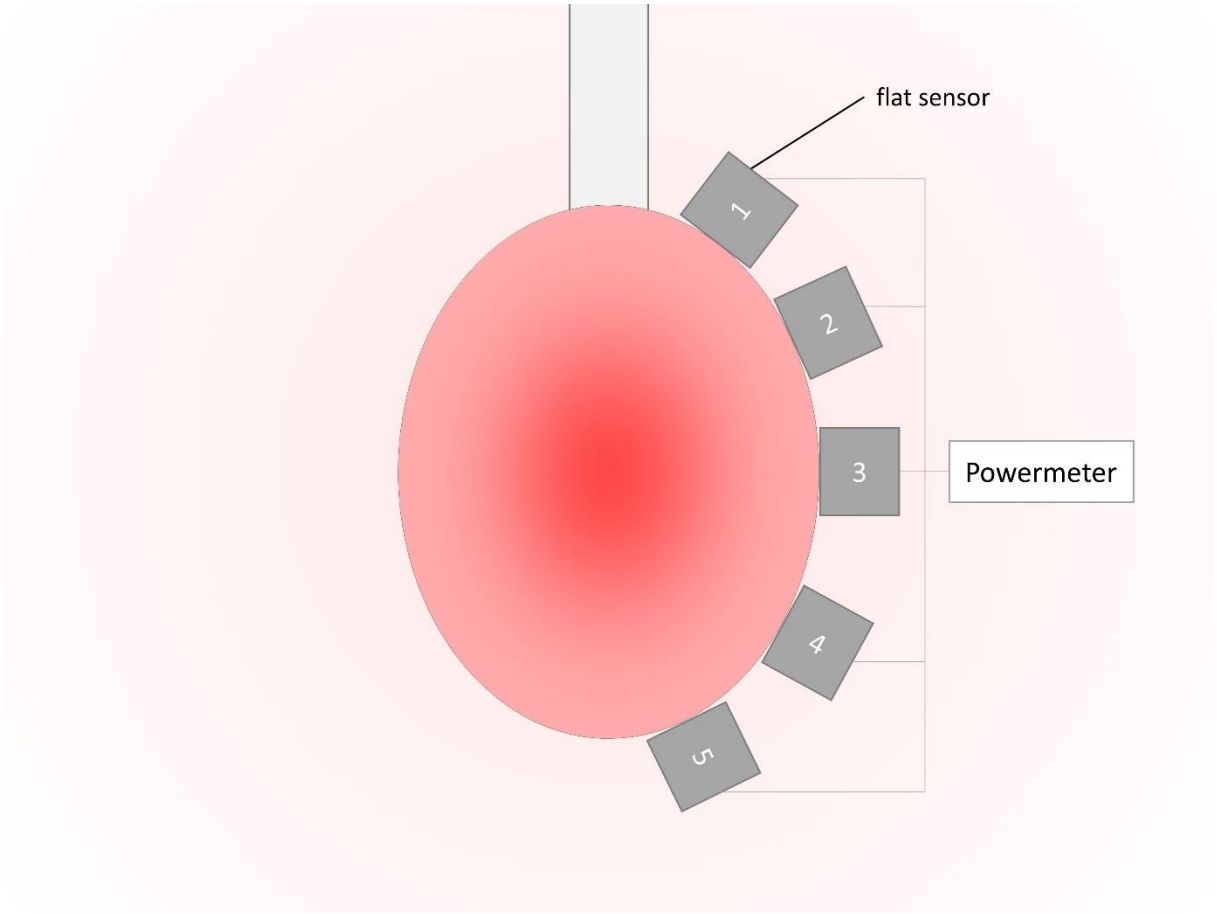

Figure 5.13: Light distribution homogeneity assessment.

b. Fluid leakage

For safety purpose, fluid leakage is prohibited and must be controlled. To assess this safety, the device was fixed to a support during two hours and filled at the maximal volume studied (500 mL). A visual inspection was performed during the test to observe any fluid leakage.

c. Thermal variations

The temperature elevation was also investigated to evaluate the temperature rising risk of surrounding brain tissues (see figure 5.14). The balloon was filled with 500 mL of diffusing solution and then immersed in a hot-water bath adjusted to 37°C. The LASER has emitted a continuous power of 2 W for two hours. The temperature was measured with a thermographic camera.

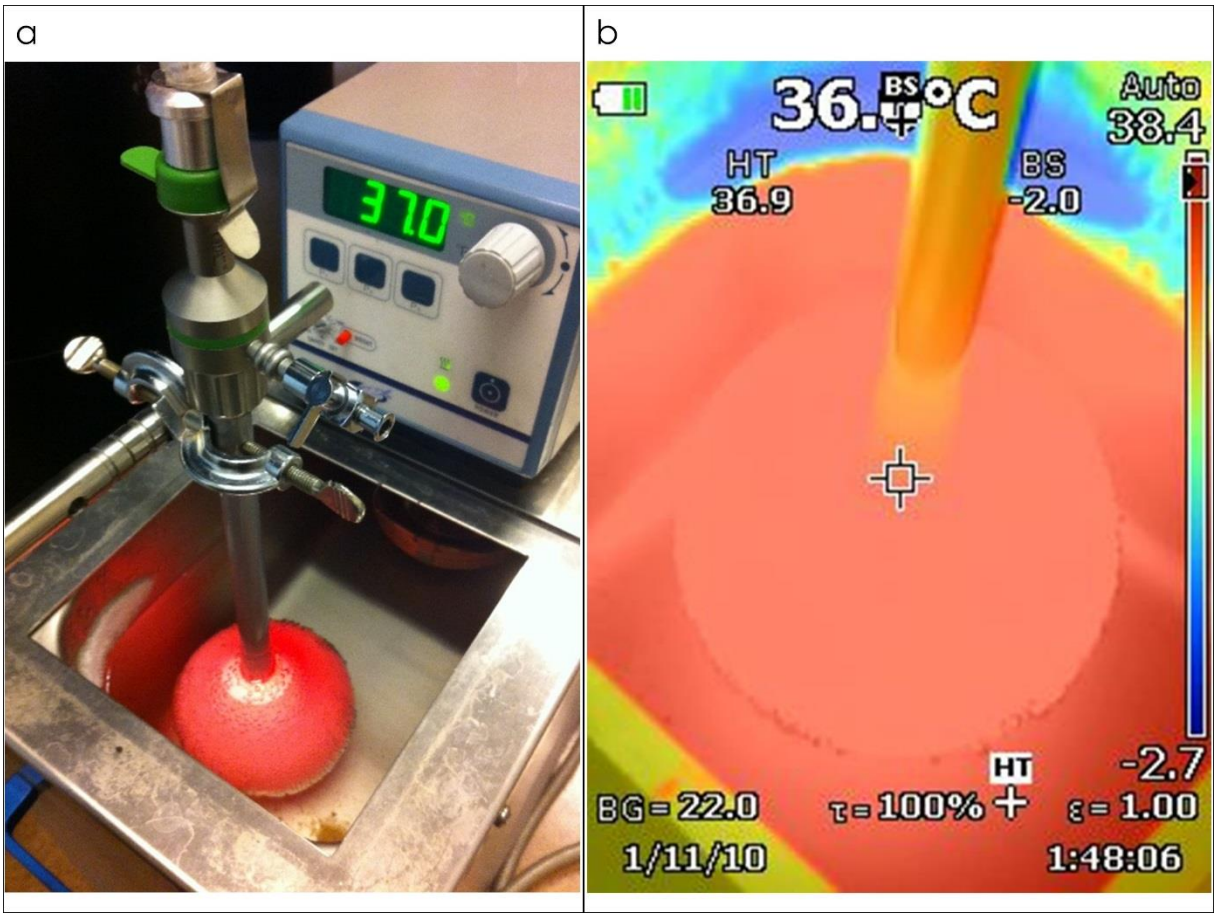

Figure 5.14: (a) Picture of the experimental set-up of temperature measurement: the balloon was filled with 500 mL of diffusing solution and immersed in a hot-water bath adjusted to 37°C. (b) Screenshot of the thermographic camera: the laser emitted a continuous power of 2 W for two hours.

d. Robustness

Finally, the maximal volume of diffusing solution admissible inside the balloon had to be evaluated. The device was fixed in suspension to a support. Diffusing solution was then injected in 50 mL steps until the balloon's wall teared.

IV. Results

1. Dosimetry

a. Calibration factor in calf brains

The calibration factor CF_{brain} was estimated using the following values of correction factors F_n, F_b, F_p and F_i (see table 5.2). The correction factors F_n, F_b and F_p were determined

from the papers of Marijnissen et al. [299, 300]. The non-homogeneity response factor F_i was determined from the standard deviation of measurements where the isotropic probe is irradiated according several irradiation angle θ (figure 3.7).

F_b (dimensionless)	1.0625 (0.005)
F_p (dimensionless)	1.03 (0.02)
F_n (dimensionless)	1.55 (0.05)
F_i (dimensionless)	1.0237 (0.07)
CF_{air} (cm^{-2})	31721
CF_{media} (cm^{-2})	55082.98 (6872.20)

Table 5.2: Calibration factor estimation for power measurement conversion into fluence rate values.

This calibration factor value is only valid for the isotropic probe used during the power measurements and calf brains.

b. Transfer function

A power of 2 W was emitted from the output of the 70 mm cylindrical diffuser. Figure 5.15 shows all fluence rate [mW/cm²] curves measured around the device for the different balloon volumes (40 mL to 500 mL) at different depth from balloon's border [mm].

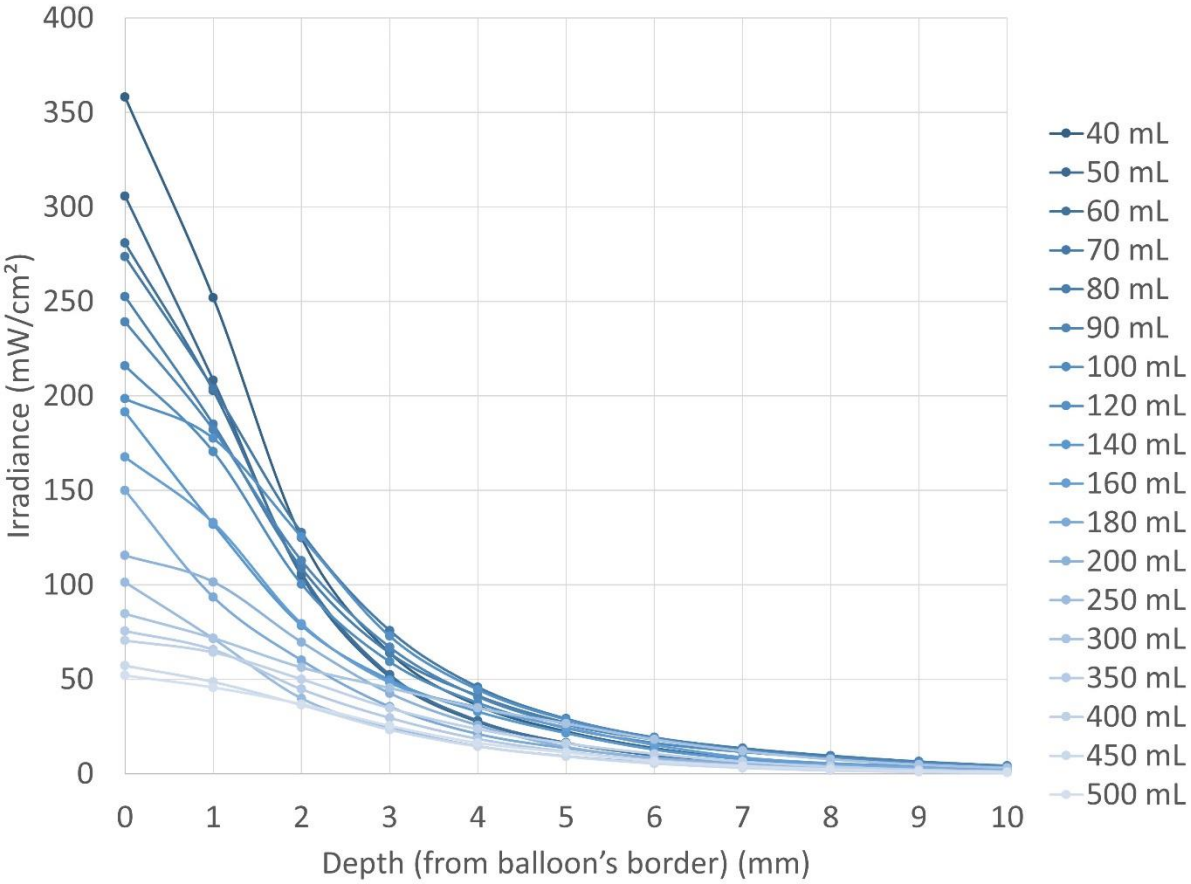

Figure 5.15: Fluence rate [mW/cm²] curves measured in calf brain tissues at different distances from the balloon's wall [mm] and for different balloon volumes.

Then, fluence values were deduced from these fluence rate data. For a value of 200 J/cm² defined against the balloon's wall for each balloon volume, a fluence value close to 25 J/cm² at a 5 mm depth, independent of the balloon volume is obtained (see figure 5.16). The fluence value of 25J/cm², defined as critical value, has been showing therapeutic PDT effect on several previous studies [348-351].

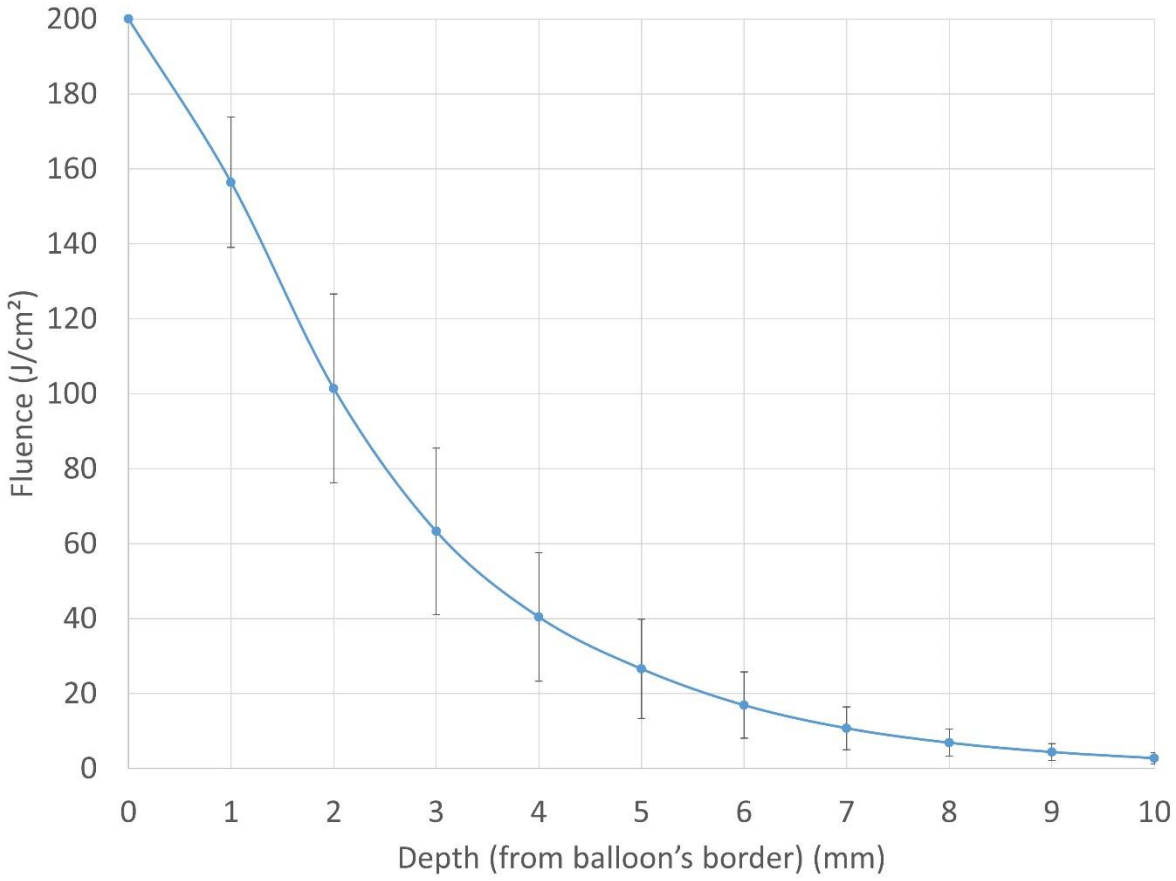

Figure 5.16: Fluence [J/cm²] computed at different distances from the balloon's wall [mm] by normalizing fluence curves for each balloon volume at 200J/cm².

The lighting duration for each balloon volume is computed by setting a fluence value of 200J/cm² against the balloon wall. Thus, a transfer function was defined to determine the lighting duration necessary to obtain a fluence value of 200J/cm² against the balloon wall and consequently, 25 J/cm² at a distance of 5 mm from the balloon wall depending on the volume of diffusing solution injected into the balloon (see figure 5.17).

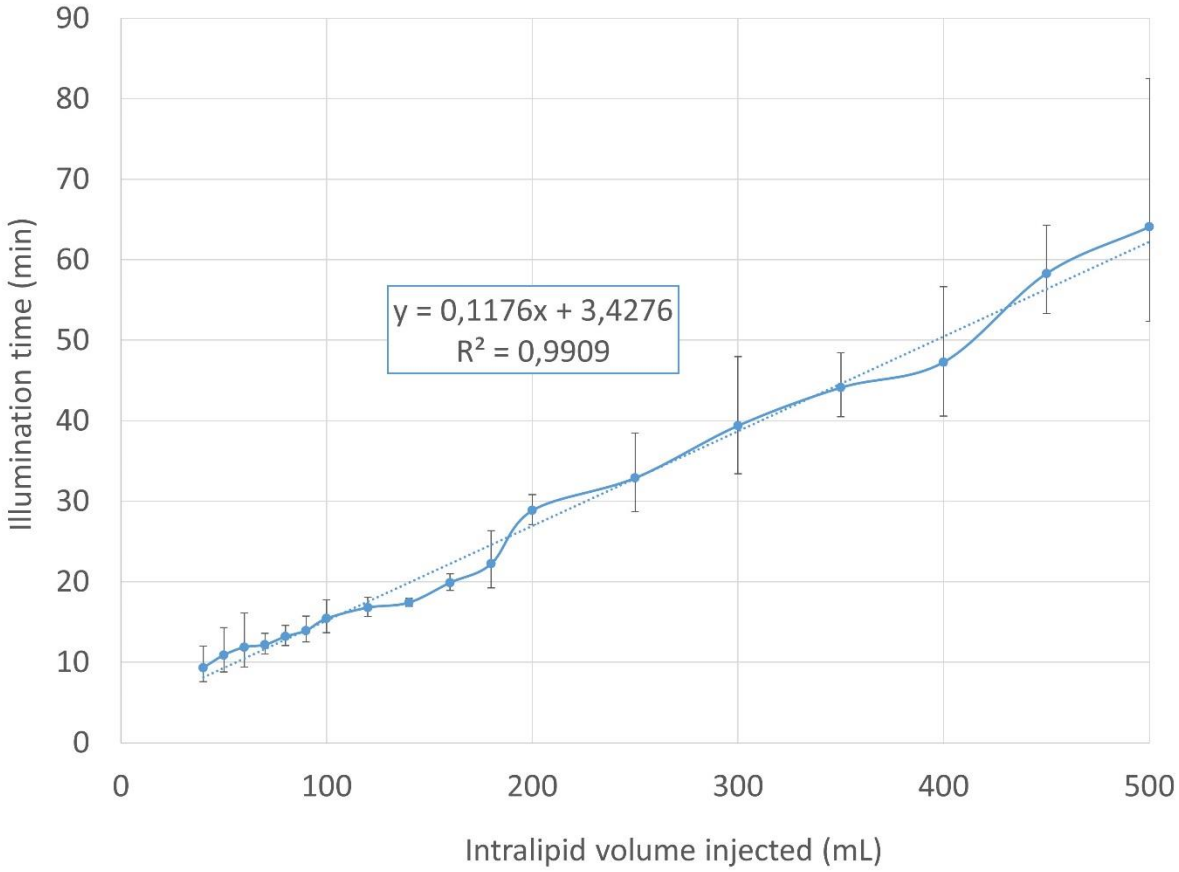

Figure 5.17: Transfer function of lighting duration (minutes) necessary to obtain a therapeutic fluence value of 25 J/cm² at a distance of 5 mm from the balloon's wall depending on the volume of diffusing solution injected into the device.

Using a linear regression, the following empirical equation can easily determine the treatment time $t_{treatment}$ according to the volume injected into the device $V_{DiffusingLiquid}$ to fit the surgical cavity and thus reach a therapeutic fluence value of 25J/cm² at 5 mm depth inside brain tissues.

$$t_{treatment} = 0.1176 \times V_{DiffusingLiquid} + 3.4276 \quad (5.7)$$

c. Monte-Carlo validation

Since Monte-Carlo model (previously described in chapter III) has been validated in homogeneous medium, it appears relevant to evaluate its results in a modeling where several media with different optical properties are involved. Several simulations were performed to evaluate the relevancy of irradiance values obtained from power measurements and also to validate the model in heterogeneous environment. Ten volumes of diffusing solution injected

were simulated: from 50 mL to 500 mL with a step of 50 mL. The balloon was designed with an ellipsoid shape. Dimensions of each configuration were measured (see table 5.3):

Volume of diffusing solution injected [mL]	**Width [cm]**	**Length [cm]**	**Volume of the ellipsoid [cm^3]**
50	4.1	7.2	63.37
100	5.1	7.5	102.14
150	5.9	8.0	145.81
200	6.4	8.7	186.59
250	6.9	9.1	226.85
300	7.2	9.6	260.58
350	7.8	10.5	334.49
400	8.5	11.1	419.91
450	8.7	11.5	455.76
500	8.9	11.8	489.4

Table 5.3: Balloon dimensions used to generate ellipsoid during Monte-Carlo simulations.

Using these dimensions and their respective optical properties, four different materials were modelled: standard brain tissues with glioma cells infiltrated, diffusing solution, stainless steel tube and borosilicate glass tube that composed the device (see figure 5.18). The 70 mm cylindrical diffuser (RD-ML 70, Medlight, Ecublens, Switzerland) were placed at the center of the borosilicate glass.

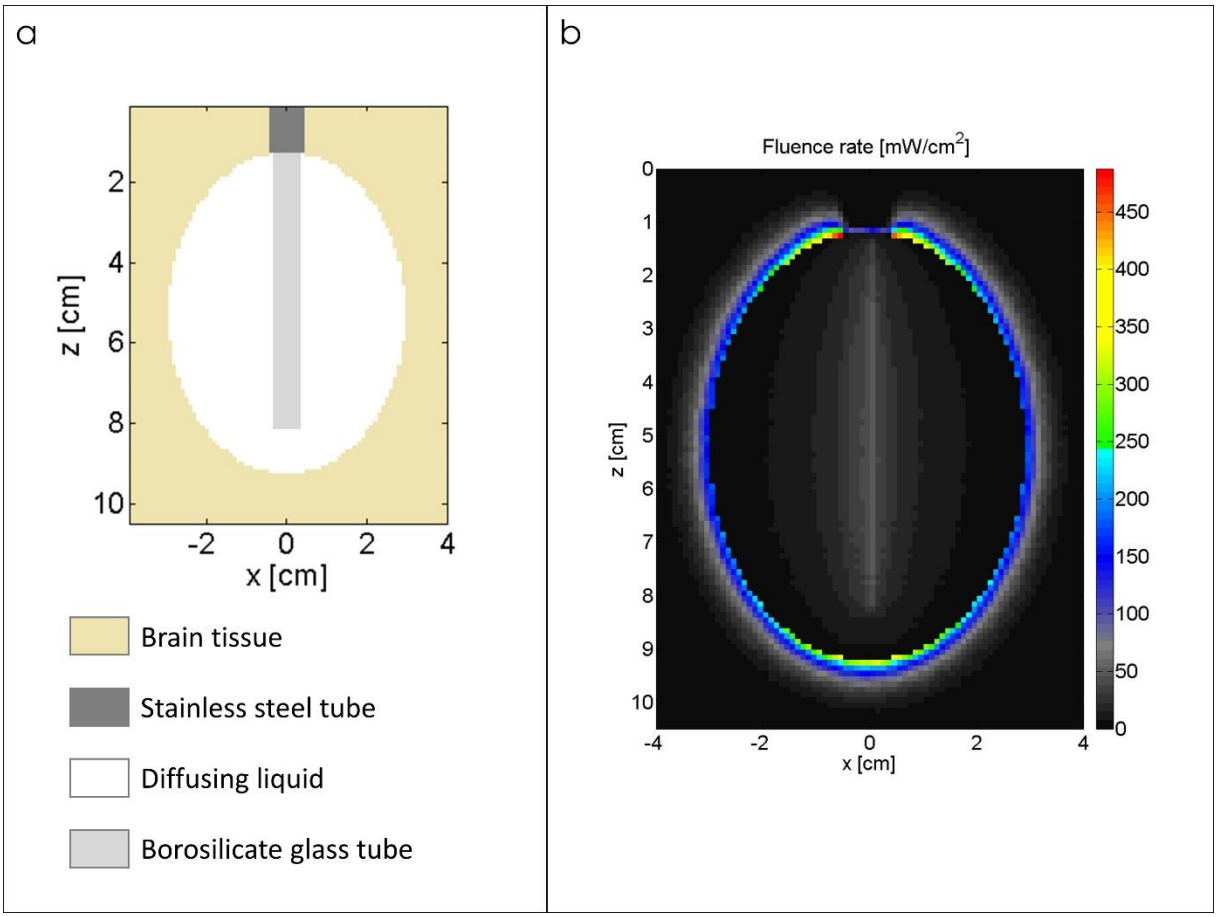

Figure 5.18: a) Modeling of the device filled with 150 mL of diffusing solution. The 70 mm long cylindrical diffuser was located at the center of the borosilicate glass tube. b) 2D cross section map of fluence rate values resulted from the Monte-Carlo simulation.

Relative error between fluence rate values against the balloon's wall obtained from power measurements and Monte-Carlo method were computed (see table 5.4).

Volume of the Balloon [mL]	**Fluence rate at balloon border [mW/cm^2]**		**Error [%]**
	Monte-Carlo simulation	**Ex vivo experiments**	
50	280.82 (18.47)	305.79 (72.86)	8.89%
100	192.93 (4.86)	215.94 (27.98)	11.93%
150	175.45 (21.13)	179.52 (7.02)	2.13%
200	139.06 (6.54)	115.54 (7.42)	16.91%
250	118.30 (6.42)	101.36 (14.74)	14.44%
300	98.23 (20.56)	84.65 (15.15)	13.82
350	86.06 (14.32)	75.56 (6.76)	12.19
400	66.28 (14.82)	70.50 (11.66)	6.38
450	59.53 (22.37)	57.19 (5.33)	3.93
500	53.10 (11.13)	52.02 (11.63)	2.03

Mean error (%)			**9.29%**

Table 5.4: Comparison of fluence rates obtained from Monte-Carlo simulations and ex vivo measurements.

By fixing a fluence value of 200 J/cm² against the balloon's wall, a transfer function has been generated from the Monte-Carlo results (see figure 5.19). The relative error between the two transfer functions equals to 9.998%.

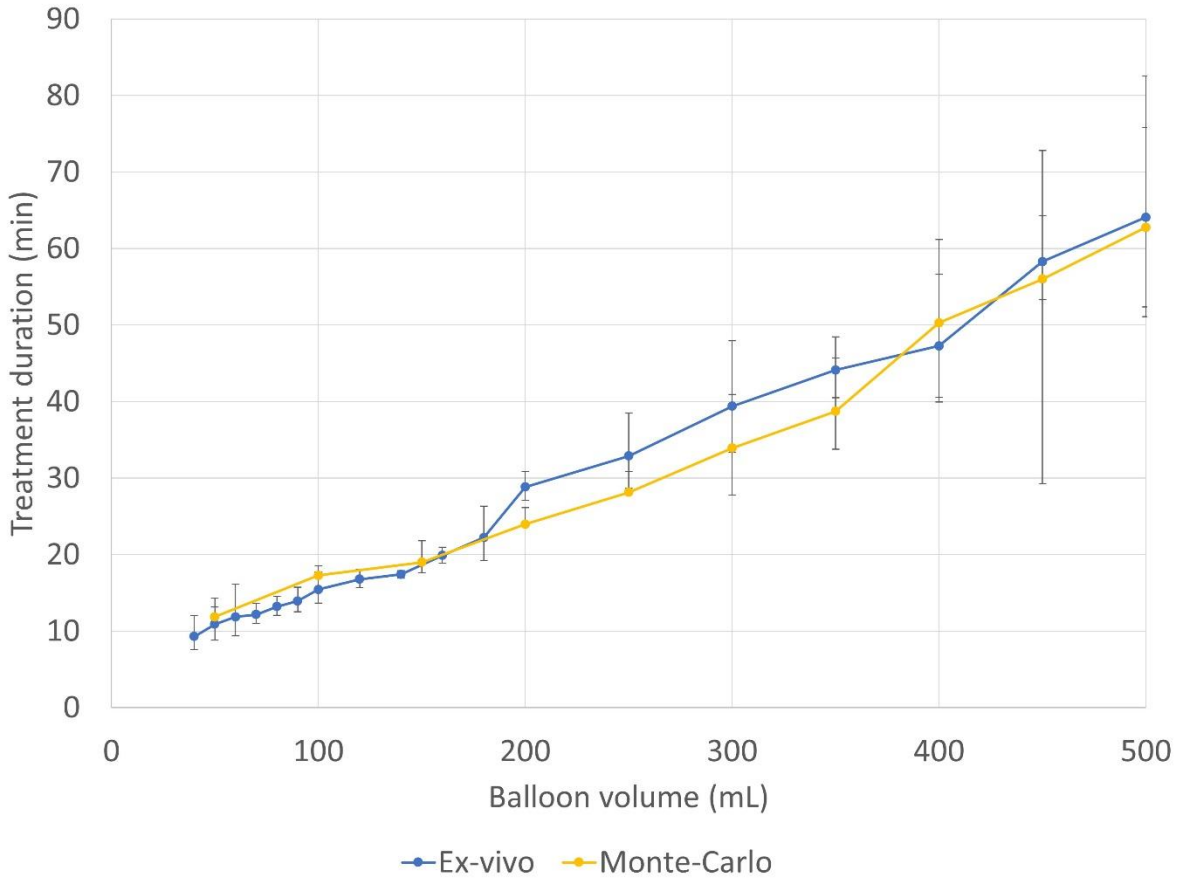

Figure 5.19: Transfer functions computed from ex-vivo measurements and Monte-Carlo model: normalizing a fluence value of 200J/cm² against the balloon's wall.

As an illustration of the difference between the irradiance and the fluence rate, Figure 5.20 shows a plot of the ratio of the fluence rate measured in the brain to the irradiance as a function of the depth for different balloon states.

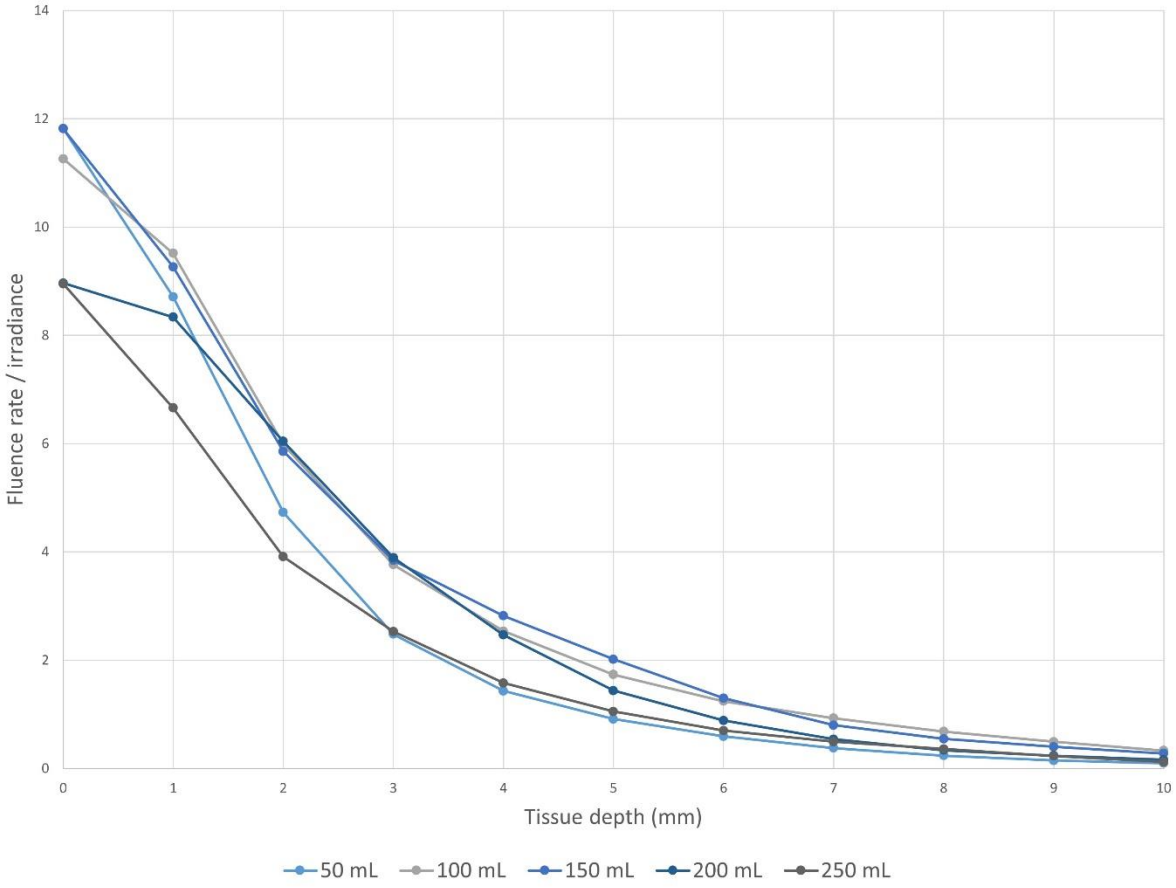

Figure 5.20: Plot of the ratio of the fluence rate measured in the brain and the irradiance as a function of the depth for different balloon states.

d. PpIX impact on optical coefficients

In the study of Valdes et al. [352], a PpIX concentration of 4.523 µg/mL (approximately 8.039 mol.L^{-1}) was observed in GBM tissue with a high level of fluorescence and PpIX accumulation. Using this concentration and at 635 nm, the PpIX absorption coefficient was estimated to be 0.0187 cm^{-1} in a way that the total absorption coefficient was only increased of 8.5% ($\mu_{a,total} = 0.2187\ cm^{-1}$). PpIX impact on optical properties is negligible at 635 nm.

2. Mechanical tests results

a. Evaluation of the phantom Young's modulus

Figure 5.21 shows the curves obtained from the eleven tensile specimens characterization using extensometer: 3 tensile specimens of (1:1.12), (1:1.10), (1:1.08) and

two tensile specimens of (1:1.05) (one (1:1.05) tensile specimen has teared during the test). The same stretching had been applied on each tensile specimen. Nominal stress [48] is plotted according to the stretch [mm]. Modeling using Yeoh's model is superimpose on each acquisition.

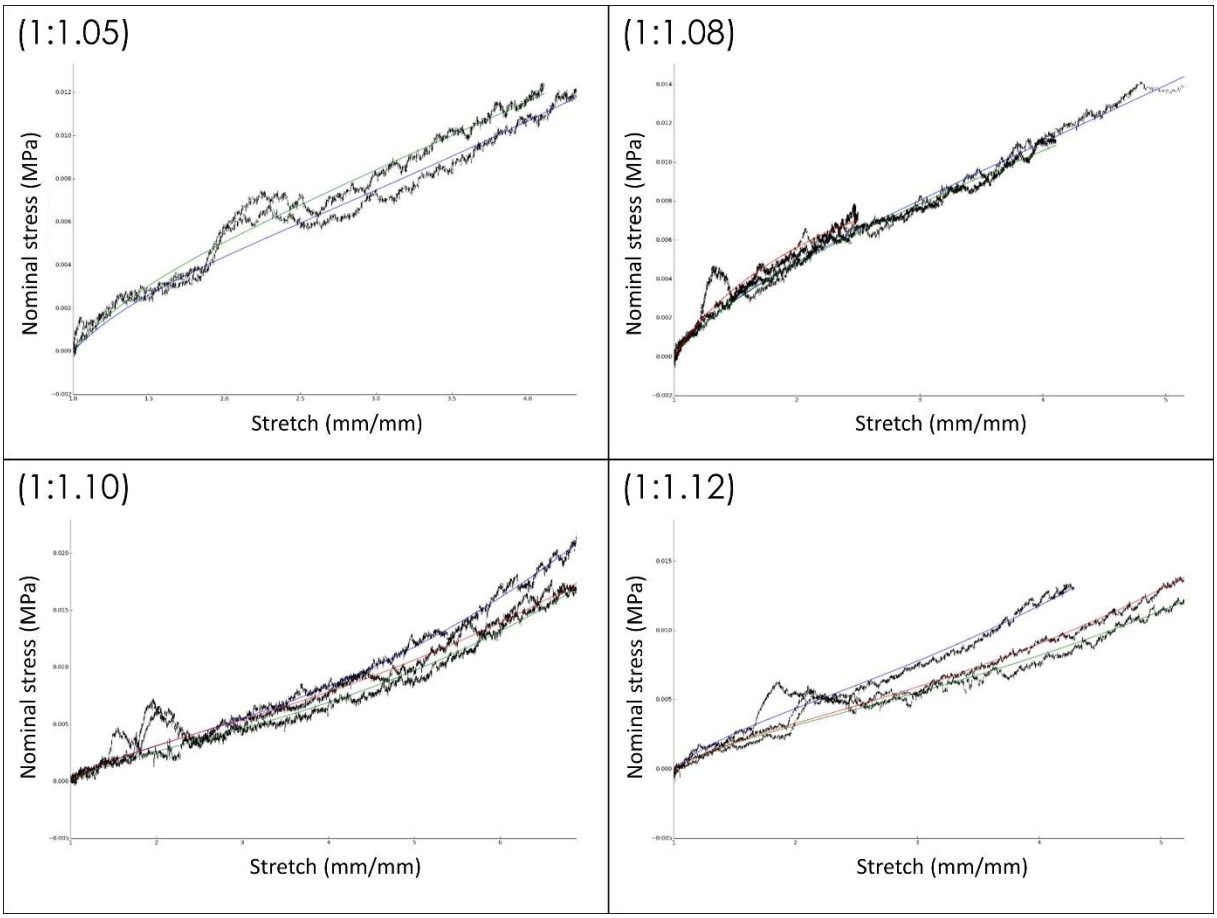

Figure 5.21: Curves obtained from the eleven tensile specimens characterization using extensometer. Black curves represent the data acquisition and color curves are each Yeoh's model fitted to data.

Young's modulus has been computed using Yeoh's model for each mixing (see table 5.5).

Mixing proportion of B (%)	**(1:1.12)**	**(1:1.10)**	**(1:1.08)**	**(1:1.05)**
Young's modulus of tensile specimen 1 (kPa)	7.21	5.14	8.31	7.40
Young's modulus of tensile specimen 2 (kPa)	5.23	4.35	8.24	8.63
Young's modulus of tensile specimen 3 (kPa)	5.42	5.27	10.22	-
Mean Young's modulus (kPa)	**5.96**	**4.92**	**8.92**	**8.01**

Table 5.5: Comparison of fluence rates obtained from Monte-Carlo simulations and ex-vivo measurements.

Although Young's modulus does not seem to follow a linear regression, the scale of values matches well with Young's modulus observed in the literature. Because the Young's modulus value for the (1:1.10) mixing (4.92 kPa) is the closest of the one obtained for the brain in the literature (4.44 kPa), the mechanical phantom was chosen to be constituted of a (1:1.10) mixing to best mimic mechanical properties of human brain.

b. Conformation to the cavity topology

Once the phantom placed in the CT-scan, the balloon was filled incrementally with 40, 60, 70, 80 and 90 mL of diluted iodine solution. The volume of 70 mL of iodine solution injected into the device allowed a good fitting of the cavity resection (see figure 5.22).

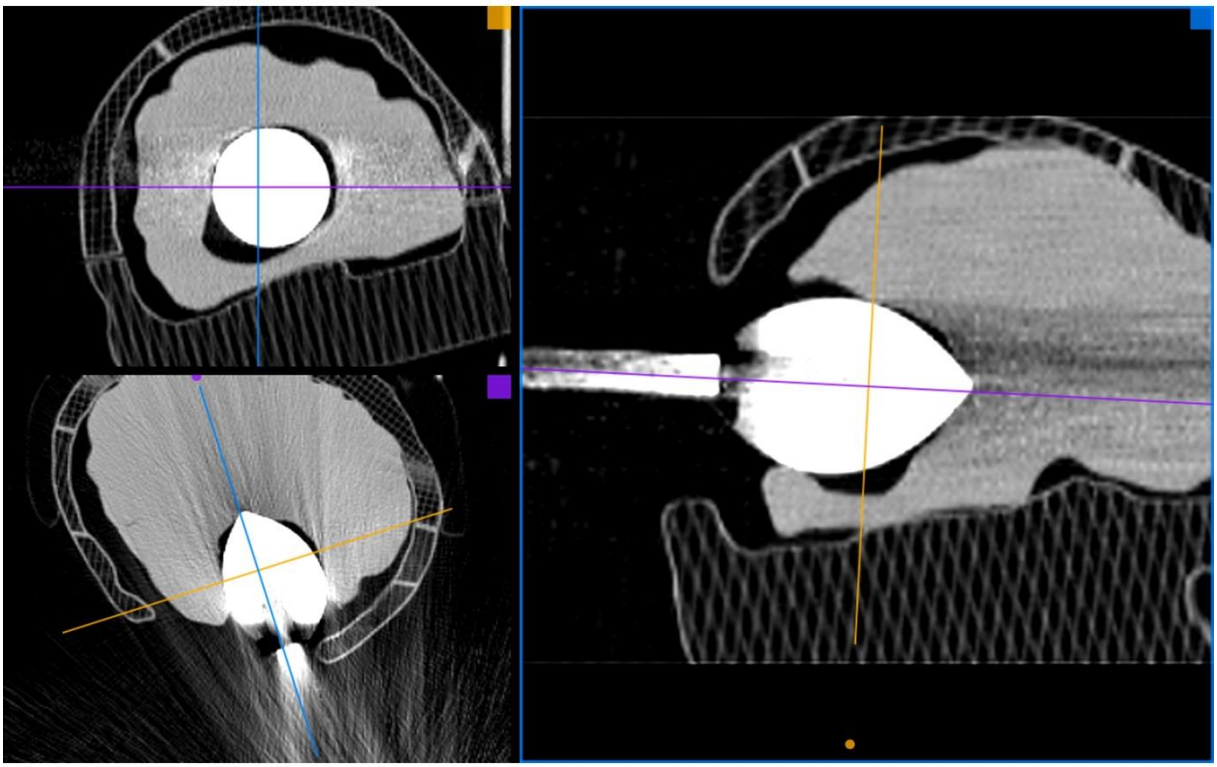

Figure 5.22: Multiplanar reconstruction of the CT-scan imaging. The balloon was filled with 70 mL of iodine solution.

The size of the cavity was approximately 80.93 cm^3. By delineating each slice of the CT volume, the conformation coefficient was evaluated equal to:

$$\tau = \frac{19.59\ cm^2}{62.07\ cm^2} = 31.56\ \%$$

3. Results of additional tests

a. Homogeneity of the light distribution

The irradiance measurements were normalized for each five quantities of diffusing solution injected into the device (100, 200, 300, 400 and 500mL) (see figure 5.23).

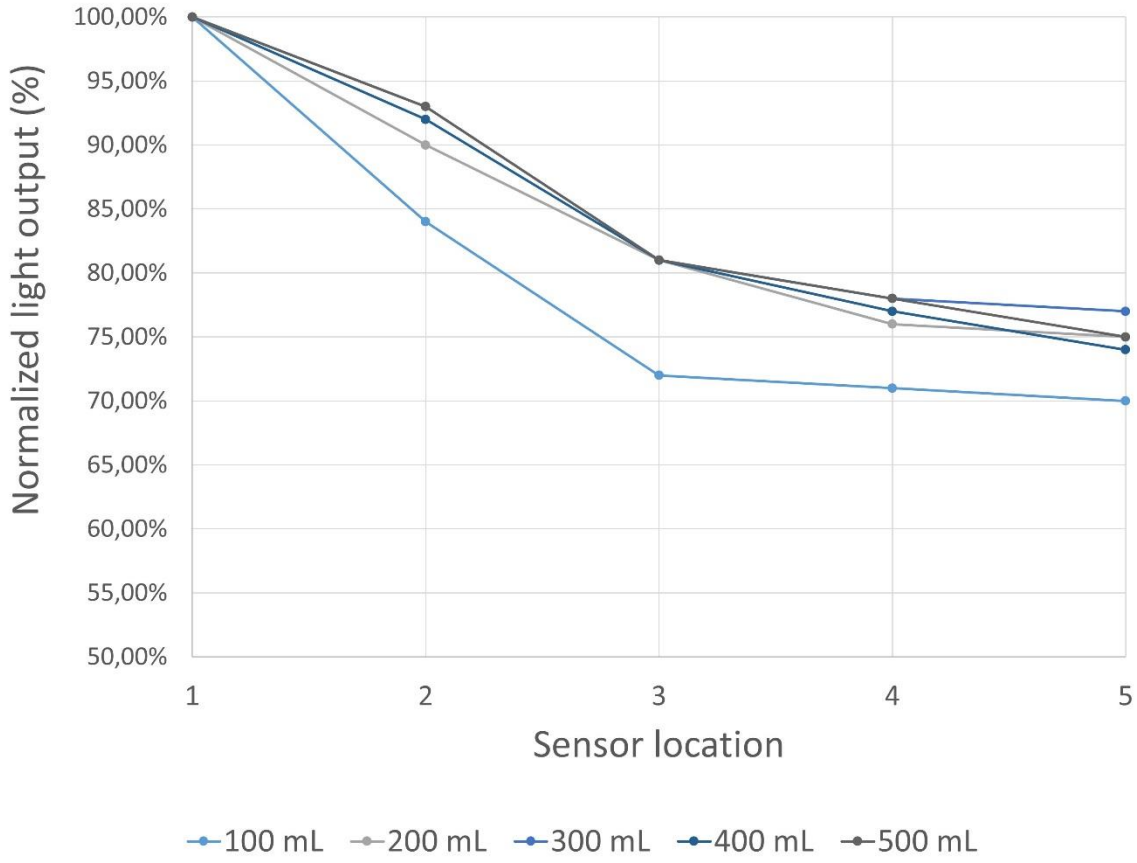

Figure 5.23: Normalized light output around the balloon's wall according to the diffusing solution injected [mL].

b. Fluid leakage

Regarding to the fluid leakage evaluation, no leakage has been observed during the two hours under maximal pressure (500 mL of diffusing liquid injected into the device).

c. Thermal variations

Regarding the temperature measurements, no temperature elevation has been observed during the experiments. Thus, the temperature elevation due to the device during treatment

can be considered acceptable.

d. Robustness

Regarding to the robustness evaluation, a maximal volume of 1600 mL of diffusing solution has been injected into the device until balloon breakage.

V. Clinical evaluation

1. Setting up of the clinical trial

Once the lighting applicator was characterized and validated, a phase one clinical trial has been investigated to evaluate the innocuousness of the procedure. This key milestone in the development of a medical device required several studies and particular methodology.

Thus, the pilot study has been setting up to assess feasibility and safety of intraoperative 5-ALA PDT procedure for the treatment of newly diagnosed GBM. This phase one clinical trial is monocentric, prospective is leaded by Pr. Reyns as principal investigator and Dr. Vermandel as scientific coordinator.

The primary endpoint is to assess the feasibility of intraoperative PDT early after the surgical resection of GBM without unacceptable and unexpected toxicities.

The secondary endpoints are the evaluation of:

- progression-free survival (PFS),
- overall survival (OS),
- treatment response on MRI, every three months until tumor relapse,
- toxicity every three months until tumor relapse and follow-up of serious unexpected event potentially linked to patient's death,
- quality of life, every three months until tumor relapse.

Enrollment of 10 patients is expected over a period of 12 months. Approximately 150 new cases of GBM are diagnosed each year in the Lille Hospital. Complete resection is usually feasible for more than a half of these cases. Evaluation criteria have been established in order to evaluate objectively the results obtained. The main criterion that enables the validation of primary endpoint, is the evaluation of the patients' proportion receiving full PDT treatment (expected to be at least 70%), according to the following requirements:

- achievement of the full PDT treatment with an acceptable tolerance due to the PDT itself;
    - no serious infection,

- no neurologic impairments leading to severe disabilities,
- status epilepticus,
- patient's death during post-operatory phase.

Secondary criteria that enable to validate secondary endpoints, are:

- OS determined from diagnosis date until death date,
- PFS determined from diagnosis date until relapse date. No other PDT procedure will be proposed as secondary treatment.
- Assessment of quality of life using a questionnaire in pre-treatment and post-treatment at 3, 6 and 12 months after treatment during neurosurgery consult,
- Treatment response on MRI at 3, 6 and 12 months after treatment.

A user manual has been written describing the setting procedure from the device assembly until the end to the treatment. A technical report has been edited describing all different parts of the device; characterization and safety tests were realized to insure its harmlessness. Materials and their biocompatibility have been defined. Ex-vivo experiments and sterilization process were also presented. Risks analysis was achieved in accordance with the European directive 93/42 EEC on medical devices and according to the European standard EN ISO 14971: 2007. Other reports had to be written to complete the application to authorities, such as investigator brochure, case report form or record sheets to organize the quality control system.

All these documents were submitted to the two French competent authorities, e.g., the ANSM ("*Agence Nationale de Sécurité du Médicament et des Produits de Santé*") and the ethical committee CPP ("*Comité de Protection des Personnes*") for technical (benefits and risks) and ethical aspects approvals respectively.

2. First patients

On September 22nd and December 26th of 2016, the CPP and ANSM approved the setting of the clinical trial. The first patient has been enrolled on 5th May of 2017. In the meantime, a patient test using 3D printed patient's head harboring a surgery cavity had been programmed to achieve a complete procedure with the neurosurgery team and rectify issues that could have appeared (see figure 5.24).

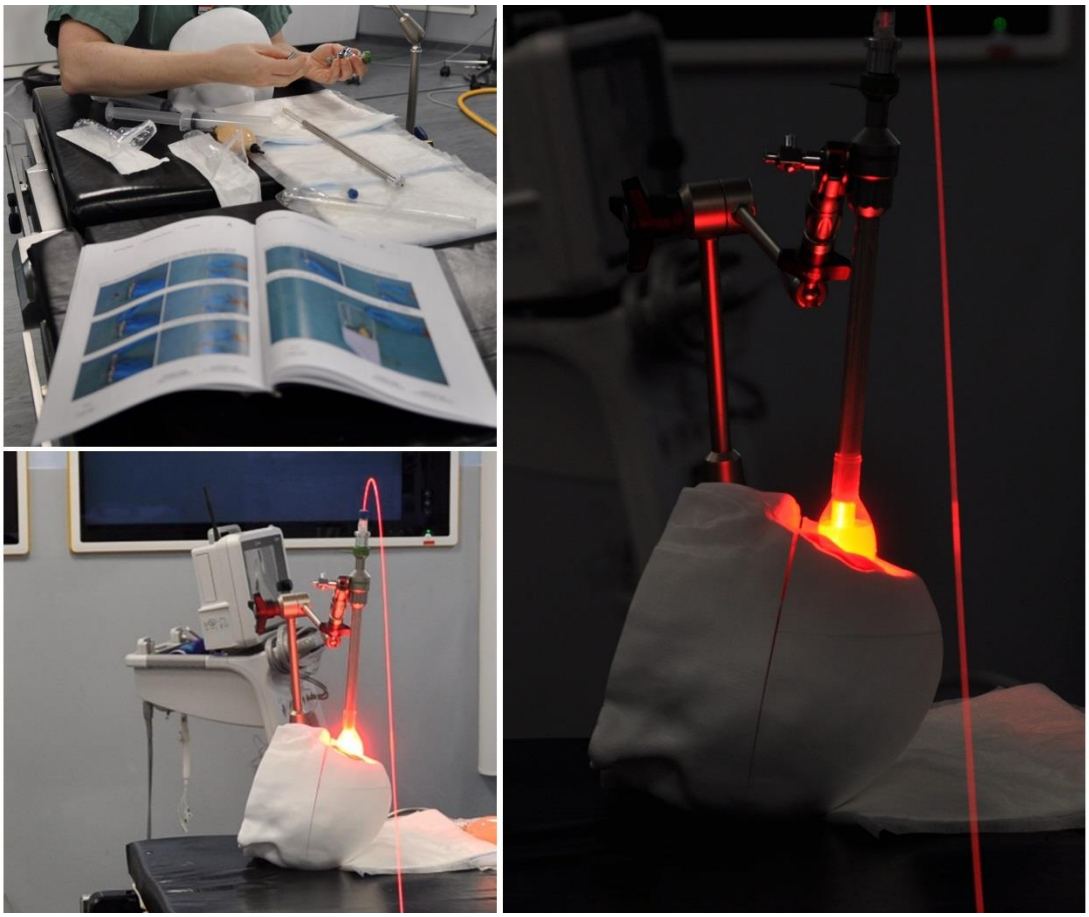

Figure 5.24: Patient test: setting up using the manual user and treatment of 3D printed patient's head.

At this time, five patients have been treated with intraoperative PDT (see figure 5.25). Several features of the PDT procedures have been measured (see table 5.6).

Patient number	**Volume of diffusing solution injected [mL]**	**Total illumination time [s]**	**Light dose delivered by the LASER [J]**	**Setting time [min]**	**Remaining fluorescence**
1	54	587	1804	5	Complete resection, remaining fluorescence
2	59	620	1741	4	Complete resection, no

					remaining fluorescence
3	110	980	2736	12	Complete resection, no remaining fluorescence
4	95	785	2231	10	Complete resection, no remaining fluorescence
5	30	417	1163	5	Complete resection, remaining fluorescence

Table 5.6: Treatment parameters of the four patients enrolled in the INDYGO clinical trial.

Figure 5.25: Operating room during PDT procedure of the third patient treatment.

VI. Discussion

1. Dosimetry and mechanic assessment

Currently, despite interstitial PDT being more frequently referenced in the literature, it is mainly dedicated to recurrent or non-operable GBM. Population with recurrent GBM is non-homogeneous since patients receive multimodal treatment, highlighting PDT effects remains difficult. Moreover, this technique remains difficult to perform for a large GBM (>3.5 cm).

This study demonstrated that a value of 0.2 cm^{-1} appears to be an absorption coefficient close to mean human brain optical properties, without considering gliomas cells infiltration [117, 305, 336]. Based on this value, modeling of the function transfer with Monte-Carlo is close to the one based on ex vivo experiments. This similarity reinforces the validity of the transfer function applied to the intraoperative PDT. However, ex vivo experiments could not be performed after 5-ALA administration, and modelling PpIX metabolism was not achievable. Thus, the impact of the absence of PpIX in the biological sample was evaluated prior to experiments. Indeed, differences in the absorption coefficients with and without PpIX might lead to different fluence rates. Nevertheless, the PpIX absorption coefficient in this condition and at 635 nm is only responsible for an increase of 8.5% in the total absorption coefficient, and the impact of PpIX was thus considered negligible for ex-vivo experiments. Moreover, the tissue surrounding the balloon would have a lower PpIX uptake than resected tumor tissues and the corresponding PpIX impact should still be more modest, confirming the assumption that the ex vivo model used in this study suited well the characterization of the device.

Regarding the precision of converting power measurements into fluence rate values, the calibration factor requires several constants including the refraction index of the medium surrounding the probe. This data strongly increases the calibration factor estimated in the air. The impact of the standard deviation of the calibration factor in the biological medium induces a standard deviation of 62 seconds for the illumination time (approximately 11% of the treatment duration for a mean cavity volume considered in this study). This value remains low compared with the total illumination time needed to treat one patient. A slight influence of calf brain oxidation on the power measurements, which cannot be quantified, was observed. However, to minimize this variable, fresh specimens preserved by refrigeration

were employed during the experiments.

The fluence rate values obtained from power measurements could appear high because of confusion with irradiance. Indeed, the fluence rate (W/cm²) can be larger than the irradiance (W/cm²), especially in the brain which is a highly scattering medium [136]. Monte-Carlo simulations confirmed this observation. In particular, with the device modeled in 3D, fluence rate values were close to values measured in the ex-vivo model. A mean error of 9.29% was obtained (see table 4.4) and remains satisfactory in regards to the assumption of a homogenous brain tissue used for Monte-Carlo and the slight difference in balloon shape that may occur in ex-vivo experiments. Finally, this mean error remains in the range of error presented in a document by the *American Association of Physicists in Medicine*, in which an error between 10 to 20% for that purpose is acceptable [302, 353].

Neurosurgery experts have validated the average lighting duration achievable by the device for most of the surgical cavities observed in the neurosurgery department of the University hospital of Lille. Indeed, the additional surgery time of 30 to 45 minutes required to deliver intraoperative PDT is considered to have limited risk for the patient. The additional operating time is acceptable for the range of volumes injected. Several studies reported a fluence value of 25 J/cm² to study PDT effect with 5-ALA [348-350] on GBM cells [351], and a photodynamic effect is expected to be observed at least within 5 mm of the cavity margin.

Regarding the mechanic assessment of the device, the value of the conformation coefficient could appear as weak: approximately 32% of the cavity surface was in contact with the balloon wall with 70 mL of diffusing liquid injected in the device. The conformation was improved with higher quantity of diffusing liquid injected: a maximum of 90 mL of diffusing liquid was injected during the test. However, this quantity was not relevant as clinical case reproduction because the compression of surrounding tissues was too high and could provoke ischemia.

The space between the balloon's wall and brain tissues, up to 15 mm in the present case, is composed of air, which does not absorb or scatter the light emitted. Thus, the dosimetry model achieved with the assumption of the balloon entirely surrounded by brain tissues still remains acceptable. Nevertheless, this impact should be quantified using several Monte-Carlo modeling of cavities imaged with intraoperative MRI. By obtaining the location and the quantity of diffusing solution injected, a 3D model of the device could be reconstructed inside the cavity. Heterogeneity of the light distribution in the cavity's margins could be modeled.

2. Clinical feedback

Although several studies have already reported intraoperative PDT, some experimental conditions have changed since the last trial, and more particularly the PS administered to the patient. In the last clinical trial in 2007 [122, 132], the drug administered was Photofrin® (Pinnacle Biologics™, Chicago, IL, United States). This first-generation PS had some disadvantages, including low absorbance at 630 nm and poor selectivity for tumor cells, leading to the necrosis of healthy tissues [354]. With the new generation of PSs, the selectivity and reactivity have been improved. In the surgical procedure investigated, the precursor 5-ALA (Gliolan-Medac, Germany) is administered to the patient, which induces a strong PpIX uptake in tumor cells [39, 355]. With the application of the device soon after FGR, improvement in the local control of direct PDT effects and an immune response with indirect PDT effects are expected. Including the 5-ALA PDT inside the SOC makes this trial a world premiere.

Additionally, investigating the impact of PDT on the patient's immune system is highly expected. Indeed, exosomes [356], which may be potential biomarkers of the PDT effect, can be massively released spontaneously by tumors after PDT treatment. Observing its evolution in the course of the management of the patient, the efficacy of PDT treatment could be related to the amount of exosomes. Such an analysis would enable to carry out immune-monitoring of patients by controlling the various immune populations (e.g., T lymphocytes, B lymphocytes, Regulatory T cell).

VII. Forthcoming improvements

1. Treatment monitoring

a. Intraoperative measurements

As mentioned in chapter II (II, 3 – monitoring and assessment of the dosimetry), fluorescence measurement can be a marker of the PS uptake during treatment and can enable to optimize PDT treatment parameters. Inserting one or several isotropic probes (IP85, Medlight, Ecublens, Switzerland) during the illumination would allow to record the light inside brain tissues [191, 194-198]. Spectroscopy technic can detect the fluorescence peak and monitor its intensity during the procedure. Also, by modifying the depth insertion of the probe, optical properties of surrounding tissues can be estimated. Regarding the singlet oxygen monitoring, a direct measurement of the very weak luminescence peak in the near

infrared can only be performed using the right equipment.

b. "Smart balloon": photo-acoustic imaging

Recent studies show an interest in the photo-acoustic technology to imaging changes in biological tissues [357, 358]. This imaging modality is based on the emission of ultrasonic waves by biological tissues irradiated. When laser beam is absorbed by a tissue, this energy absorption produces a local heat increase. A fast thermo-elastic expansion is created, leading to a displacement of particles that causes a pressure wave. By recording these waves with transducers, it is possible to determine the localization of the wave's origin and the type of absorbing material. With the miniaturization of transducer technology, capacitive micromachined ultrasonic transducers (CMUT), which can reach a size of 10 to 100 µm, could be placed around the surface of the balloon to perform a real-time monitoring of the PDT treatment. One of the main features monitored is the blood oxygen saturation. Photoacoustic tomography is used to record vascular damage due to PDT treatment in a high resolution (approximately 100 µm or less). However, to obtain such data, additional laser sources are necessary to excite molecules targeted: 750 and 850 nm for the study of Mallidi et al. [359] or 560 and 576 nm for the study of Shao et al. [358]. Although this technology can provide depth imaging of PDT impact during the illumination, it still remains far from being used in clinic.

2. Lighting fabrics

Another perspective of improvement lies in the use of light emitting fabric for intraoperative PDT. This technology already evaluated in dermatology clinical trial [360, 361] could be adapted to intracavitarly PDT treatment. The term of "light blanket" has already been used in intracavitarly context [362-364]. However, the technology was different from the actual light emitting fabric. The light blanket was composed of a series of parallel cylindrical diffusers, fixed with a polyethylene blanket and two other layers (a diffusing solution compartment and a reflector). The light emitting fabric uses the Fresnel conditions to emit light. If an optical fiber is bended beyond a critical angle θ_c (Brewster's angle which depend on the refractive indices of optical fiber materials), the light leaves the optical fiber:

$$\theta_c = \arcsin\left(\frac{n_2}{n_1}\right) \tag{5.8}$$

where n_1 and n_2 are respectively the refractive indices of the fiber core and surrounding cladding.

Using different weaving technics of optical fibers optimized for the light leak, called side emitting optical fiber, lighting fabric of different surface areas can be obtained. The main advantage of this technology is its easy conformation to all different topologies of treatment surface, including intracavitarly treatment. Nevertheless, current light emitting fabrics used in dermatology reach an irradiance of approximately 18 mW/cm². To perform a PDT treatment with such a system in order to replace the actual proposed balloon device, optimization had to be performed to increase the irradiance delivered. Also, in clinical context, these fabrics would have to be sterilized. Strict restrictions are applied with class III medical device (medical device in direct contact with central nervous system). Although this alternative seems to be interesting, several challenging studies had to be achieved to evaluate it in a clinical trial dedicated to intraoperative PDT GBM treatment.

Chapter conclusion

Unfortunately, the PDT effect on GBM is still not evidenced because of the poor reproducibility of the procedure from one center to another, the multi-modality treatment when considering only the recurrent GBM population and the low inclusion numbers in the past trials.

In this chapter, a new device and the associated procedure is proposed in order to facilitate the incorporation of intraoperative PDT into the standard surgical workflow. The innovation is better assimilated when its users are involved in its design for they adapt it to their expectations. Thus, the design of this new device aimed to simplify the PDT procedure for the neurosurgeon with a seamless methodology suitable for the standard surgical workflow which also limited the dosimetry issue during surgery. In such a manner, and thanks to a highly reproducible procedure, the effects of PDT should be better highlighted on a larger and more homogeneous population of only newly diagnosed GBM patients.

Although the device presented here could be improved, in particular with its adaptability to the cavity, this lighting delivery system is a first step towards future larger clinical trials and a future integration in the GBM standard of care.

General conclusion

The main purpose of this thesis work was to provide technologies to enable the GBM treatment with PDT. In order to include the totality of patients harboring GBM (resectable and unresectable cases), two different guidelines have been elaborated.

For unresectable tumors, the stereotactic iPDT is proposed. Because such a surgical procedure had to be planned, a TPS dedicated to this technic must have been developed. Currently, no TPS dedicated to iPDT for GBM treatment is available. In Chapter IV, a proof of concept of such a software is presented. Although several improvements are needed, it enables both the localization of cylindrical diffusers in the stereotactic Leksell frame usually used in neurosurgery and the estimation of the light propagation emitted from these light sources without considering the heterogeneity of GBM tissues. In order to improve this estimation, Monte-Carlo method, often used as reference to compute the light distribution, should be include into the workflow. However, because the main drawback of this model lies in the large time required to perform an entire simulation, its use in clinical routine remains an issue.

The improvement of parallel computing using GPU that drastically decreases the computing time [266, 268, 320] ensured strong enthusiasm for developing the Monte-Carlo method for PDT planning [102, 266]. With the assistance of an automatic tissue segmentation method dedicated to GBM [321, 322], the Monte-Carlo method proposed in chapter III can model the fluence rate according to optical coefficients for each voxel of the MRI volume used for planning. Thus, the fluence rate values computed may consider the optical heterogeneity.

Although results of the GPU Monte-Carlo validation are in accordance with the AAPM's recommendations, the accuracy of the Monte-Carlo model could be improved by considering the illumination profile of the cylindrical diffusers used in the treatment. Further validation tests with heterogeneous phantoms could enable a deeper validation of the outputs' algorithm. Regarding the performances, the reported acceleration (approximately 660 times) is in accordance with the literature. The time required to compute the light propagated from a cylindrical diffuser is now sufficiently fast to be integrated in clinical routine.

For resectable GBM cases, an intraoperative PDT modality treatment is proposed early after FGR. In Chapter V, a new device dedicated and its inclusion into the standard of care are described. The main asset of the proposed surgical procedure is to provide a straightforward use of the device and a surgical procedure suitable for the standard surgical workflow. The

device has been characterized using several *ex vivo* experiments. With these results, a dosimetry model has been generated to easily deduce the treatment duration according indirectly to the size of the cavity surgery. The resulting transfer function displays a linear relation between the quantity of diffusing liquid used to inflate the device in order to fit the cavity's size and the treatment duration. The computed time enables to emit sufficient light to induce a PDT effect at least at 5 mm depth inside surrounding brain tissues of the cavity.

This dosimetry model has been validated by Monte-Carlo simulation. The same transfer function has been generated from Monte-Carlo simulation. An error of 9.998% between ex vivo and Monte-Carlo results was obtained.

This device can fit into large surgical bed (>150cm^3). However, as the mechanical assessment and clinical evaluation show, when the device is placed in a small cavity, the balloon is not completely inserted. The impact on the deposit light during the treatment is negligible and a PDT effect is still expected at margins resection. To circumvent this issue, other devices such as light emitting fabrics should be assessed.

As previously announced in the introduction, the essential goal of research in medicine is patient's treatment. Accordingly, the feasibility of the delivering 5-ALA PDT for the treatment of newly diagnosed GBM is currently under evaluation in the world premiere INDYGO clinical trial (*ClinicalTrials.gov identifier*: NCT03048240). Ten patients will be recruited in this phase one clinical trial.

To conclude, this thesis moves the PDT treatment of GBM to a new step. Although previous results show inspiring outcomes, including some long-sustaining response patients, the effects of PDT should be better highlighted on a larger and more homogeneous population of newly diagnosed GBM patients only.

A strong and multidisciplinary effort should be conducted to propose a combined therapeutic solution, particularly with PDT and immunotherapies, in order to find a cure for brain cancer.

References

1. Fisher, T., et al., *Mechanisms operative in the antitumor activity of temozolomide in glioblastoma multiforme.* Cancer J, 2007. **13**(5): p. 335-44.
2. Ostrom, Q.T., et al., *The epidemiology of glioma in adults: a "state of the science" review.* Neuro-Oncology, 2014.
3. Sathornsumetee, S., J.N. Rich, and D.A. Reardon, *Diagnosis and treatment of high-grade astrocytoma.* Neurol Clin, 2007. **25**(4): p. 1111-39, x.
4. Jordan, J.T., et al., *Glioblastoma care in the elderly.* Cancer, 2016. **122**(2): p. 189-97.
5. Ohgaki, H. and P. Kleihues, *Population-Based Studies on Incidence, Survival Rates, and Genetic Alterations in Astrocytic and Oligodendroglial Gliomas.* Journal of Neuropathology & Experimental Neurology, 2005. **64**(6): p. 479-489.
6. Ostrom, Q.T., et al., *Epidemiology of Gliomas*, in *Current Understanding and Treatment of Gliomas*, J. Raizer and A. Parsa, Editors. 2015, Springer International Publishing: Cham. p. 1-14.
7. Thakkar, J.P., et al., *Epidemiologic and molecular prognostic review of glioblastoma.* Cancer Epidemiol Biomarkers Prev, 2014. **23**(10): p. 1985-96.
8. Omuro, A. and L.M. DeAngelis, *Glioblastoma and other malignant gliomas: A clinical review.* JAMA, 2013. **310**(17): p. 1842-1850.
9. Popat, K., K. McQueen, and T.W. Feeley, *The global burden of cancer.* Best Practice & Research Clinical Anaesthesiology, 2013. **27**(4): p. 399-408.
10. Daniell, M.D. and J.S. Hill, *A HISTORY OF PHOTODYNAMIC THERAPY.* Australian and New Zealand Journal of Surgery, 1991. **61**(5): p. 340-348.
11. Diamond, I., et al., *Photodynamic therapy of malignant tumours.* Lancet, 1972. **2**(7788): p. 1175-7.
12. Perria, C., et al., *First attempts at the photodynamic treatment of human gliomas.* J Neurosurg Sci, 1980. **24**(3-4): p. 119-29.
13. Einstein, A., *On the quantum mechanics of radiation.* Physikalische Zeitschrift, 1917. **18**: p. 121-128.
14. Kleppner, D., *Rereading Einstein on radiation.* Revista Brasileira de Ensino de Física, 2005. **27**(1): p. 87-91.
15. Gould, R.G. *The LASER, light amplification by stimulated emission of radiation*. in *The Ann Arbor conference on optical pumping, the University of Michigan*. 1959.

16. Maiman, T.H., *Stimulated optical radiation in ruby.* Nature, 1960. **187**: p. 2.
17. Maiman, T., *Optical and microwave-optical experiments in ruby.* Physical review letters, 1960. **4**(11): p. 564.
18. Stratonnikov, A.A., G.A. Meerovich, and V.B. Loschenov. *Photobleaching of photosensitizers applied for photodynamic therapy*. 2000.
19. Johansson, A., et al., *Protoporphyrin IX fluorescence and photobleaching during interstitial photodynamic therapy of malignant gliomas for early treatment prognosis.* Lasers in Surgery and Medicine, 2013. **45**(4): p. 225-34.
20. Robinson, D.J., et al., *Fluorescence photobleaching of ALA-induced protoporphyrin IX during photodynamic therapy of normal hairless mouse skin: the effect of light dose and irradiance and the resulting biological effect.* Photochem Photobiol, 1998. **67**(1): p. 140-9.
21. Farrell, T.J., et al., *Modeling of photosensitizer fluorescence emission and photobleaching for photodynamic therapy dosimetry.* Appl Opt, 1998. **37**(31): p. 7168-83.
22. Ma, L., S. Bagdonas, and J. Moan, *The photosensitizing effect of the photoproduct of protoporphyrin IX.* Journal of Photochemistry and Photobiology B: Biology, 2001. **60**(2): p. 108-113.
23. Juzenas, P., et al., *Fluorescence spectroscopy of normal mouse skin exposed to 5-aminolaevulinic acid and red light.* J Photochem Photobiol B, 2001. **61**(1-2): p. 78-86.
24. Bagdonas, S., et al., *Phototransformations of 5-Aminolevulinic Acid–induced Protoporphyrin IX in vitro: A Spectroscopic Study*¶. Photochemistry and Photobiology, 2000. **72**(2): p. 186-192.
25. Kessel, D., et al. *Pharmacokinetics of Photofrin II distribution in man*. 1991.
26. Orenstein, A., et al., *A comparative study of tissue distribution and photodynamic therapy selectivity of chlorin e6, Photofrin II and ALA-induced protoporphyrin IX in a colon carcinoma model.* British Journal of Cancer, 1996. **73**(8): p. 937-944.
27. Pahernik, S.A., et al., *Distribution and pharmacokinetics of Photofrin® in human bile duct cancer.* Journal of Photochemistry and Photobiology B: Biology, 1998. **47**(1): p. 58-62.
28. Stylli, S.S., et al., *Photodynamic therapy of brain tumours: evaluation of porphyrin uptake versus clinical outcome.* J Clin Neurosci, 2004. **11**(6): p. 584-96.
29. Wachowska, M., et al., *Aminolevulinic Acid (ALA) as a Prodrug in Photodynamic Therapy of Cancer.* Molecules, 2011. **16**(5): p. 4140.

30. Bechet, D., et al., *Multifunctional ultrasmall nanoplatforms for vascular-targeted interstitial photodynamic therapy of brain tumors guided by real-time MRI.* Nanomedicine: Nanotechnology, Biology and Medicine, 2014. **11**(3): p. 657-670.
31. Savarimuthu, W.P., et al., *Protoporphyrin IX-Gold Nanoparticle Conjugates for Targeted Photodynamic Therapy--An In-Vitro Study*. J Nanosci Nanotechnol, 2015. **15**(8): p. 5577-84.
32. Benachour, H., et al., *Multifunctional Peptide-conjugated hybrid silica nanoparticles for photodynamic therapy and MRI.* Theranostics, 2012. **2**(9): p. 889-904.
33. Bobyk, L., et al., *Photoactivation of gold nanoparticles for glioma treatment.* Nanomedicine, 2013. **9**(7): p. 1089-97.
34. Castano, A.P., T.N. Demidova, and M.R. Hamblin, *Mechanisms in photodynamic therapy: part one—-photosensitizers, photochemistry and cellular localization.* Photodiagnosis and photodynamic therapy, 2004. **1**(4): p. 279-293.
35. Tappeiner, H.V. and A. Jodlbauer, *Die sensibilisierende Wirkung fluoreszierender Substanzen*. 1907, Leipzig: Verlag FCW Vogel.
36. Mordon, S., *Lasers thérapeutiques : bases fondamentales*, ed. C.e.D. esthétique. 2006, Paris: Elsevier Masson.
37. Marchal, S., *Stratégies pro-apoptotiques appliquées au traitement photodynamique avec le Foscan® de modèles précliniques d'adénocarcinome humain*. 2008, Université Henri Poincaré - Nancy I.
38. Kostron, H., T. Fiegele, and E. Akatuna, *Combination of FOSCAN® mediated fluorescence guided resection and photodynamic treatment as new therapeutic concept for malignant brain tumors.* Medical Laser Application, 2006. **21**(4): p. 285-290.
39. Tetard, M.C., et al., *Experimental use of Photodynamic Therapy in high grade gliomas: a review focused on 5-aminolevulinic acid.* Photodiagnosis Photodyn Ther, 2014. **11**(3): p. 19.
40. Angell-Petersen, E., et al., *Influence of light fluence rate on the effects of photodynamic therapy in an orthotopic rat glioma model.* J Neurosurg, 2006. **104**(1): p. 109-17.
41. Medlight. *Medlight SA Switzerland*. 2017 15/05/2017]; Available from: http://www.medlight.com/.
42. Peng, Q. and J.M. Nesland, *Effects of Photodynamic Therapy on Tumor Stroma.* Ultrastructural Pathology, 2004. **28**(5-6): p. 333-340.

43. Pazos, M.d.C. and H.B. Nader, *Effect of photodynamic therapy on the extracellular matrix and associated components.* Brazilian Journal of Medical and Biological Research, 2007. **40**: p. 1025-1035.
44. Robertson, C.A., D.H. Evans, and H. Abrahamse, *Photodynamic therapy (PDT): A short review on cellular mechanisms and cancer research applications for PDT.* Journal of Photochemistry and Photobiology B: Biology, 2009. **96**(1): p. 1-8.
45. Bhuvaneswari, R., et al., *The effect of photodynamic therapy on tumor angiogenesis.* Cellular and Molecular Life Sciences, 2009. **66**(14): p. 2275-2283.
46. Kawczyk-Krupka, A., et al., *ALA-induced photodynamic effect on viability, apoptosis and secretion of S100 protein, secreted by colon cancer cells in vitro.* Photodiagnosis and Photodynamic Therapy, 2016. **15**: p. 218-227.
47. Sharwani, A., et al., *Photodynamic therapy down-regulates the invasion promoting factors in human oral cancer.* Archives of Oral Biology, 2006. **51**(12): p. 1104-1111.
48. Kawczyk-Krupka, A., et al., *ALA-induced photodynamic effect on vitality, apoptosis, and secretion of vascular endothelial growth factor (VEGF) by colon cancer cells in normoxic environment in vitro.* Photodiagnosis and Photodynamic Therapy, 2015. **13**: p. 308-315.
49. Xie, Y., et al., *Effect of 5-ALA-PDT on VEGF and PCNA expression in human NPC-bearing nude mice.* Oncol Rep, 2009. **22**(6): p. 1365-71.
50. Yi, W., et al., *Photodynamic therapy mediated by 5-aminolevulinic acid suppresses gliomas growth by decreasing the microvessels.* Journal of Huazhong University of Science and Technology [Medical Sciences], 2015. **35**(2): p. 259-264.
51. Maeding, N., T. Verwanger, and B. Krammer, *Boosting Tumor-Specific Immunity Using PDT.* Cancers, 2016. **8**(10): p. 91.
52. Yang, Y., Y. Hu, and H. Wang, *Targeting Antitumor Immune Response for Enhancing the Efficacy of Photodynamic Therapy of Cancer: Recent Advances and Future Perspectives.* Oxidative Medicine and Cellular Longevity, 2016. **2016**: p. 5274084.
53. Wachowska, M., A. Muchowicz, and U. Demkow, *Immunological aspects of antitumor photodynamic therapy outcome.* Central-European Journal of Immunology, 2015. **40**(4): p. 481-485.
54. Pizova, K., et al., *Photodynamic therapy for enhancing antitumour immunity.* Biomedical papers, 2012. **156**(2): p. 93-102.
55. Castano, A.P., T.N. Demidova, and M.R. Hamblin, *Mechanisms in photodynamic therapy: Part three—Photosensitizer pharmacokinetics, biodistribution, tumor*

localization and modes of tumor destruction. Photodiagnosis and photodynamic therapy, 2005. **2**(2): p. 91-106.

56. Zhu, T.C. and J.C. Finlay, *The role of photodynamic therapy (PDT) physics.* Med Phys, 2008. **35**(7): p. 3127-36.
57. Louis, D.N., et al., *The 2016 World Health Organization Classification of Tumors of the Central Nervous System: a summary.* Acta Neuropathologica, 2016. **131**(6): p. 803-820.
58. Asklund, T., et al., *Brain tumors in Sweden: data from a population-based registry 1999-2012.* Acta Oncol, 2015. **54**(3): p. 377-84.
59. Brodbelt, A., et al., *Glioblastoma in England: 2007-2011.* Eur J Cancer, 2015. **51**(4): p. 533-42.
60. Gramatzki, D., et al., *Glioblastoma in the Canton of Zurich, Switzerland revisited: 2005 to 2009.* Cancer, 2016. **122**(14): p. 2206-15.
61. Muquit, S., R. Parks, and S. Basu, *Socio-economic characteristics of patients with glioblastoma multiforme.* J Neurooncol, 2015. **125**(2): p. 325-9.
62. Nava, F., et al., *Survival effect of first- and second-line treatments for patients with primary glioblastoma: a cohort study from a prospective registry, 1997-2010.* Neuro Oncol, 2014. **16**(5): p. 719-27.
63. Ostrom, Q.T., et al., *CBTRUS statistical report: Primary brain and central nervous system tumors diagnosed in the United States in 2006-2010.* Neuro Oncol, 2013. **15 Suppl 2**: p. ii1-56.
64. Chen, J.-R., et al., *Isocitrate Dehydrogenase (IDH)1/2 Mutations as Prognostic Markers in Patients With Glioblastomas.* Medicine, 2016. **95**(9): p. e2583.
65. Ricard, D., et al., *Primary brain tumours in adults.* Lancet, 2012. **379**(9830): p. 1984-96.
66. Michel Lacroix, et al., *A multivariate analysis of 416 patients with glioblastoma multiforme: prognosis, extent of resection, and survival.* Journal of Neurosurgery, 2001. **95**(2): p. 190-198.
67. Shah, B.K., A. Bista, and S. Sharma, *Survival Trends in Elderly Patients with Glioblastoma in the United States: a Population-based Study.* Anticancer Res, 2016. **36**(9): p. 4883-6.
68. Johnson, D.R. and B.P. O'Neill, *Glioblastoma survival in the United States before and during the temozolomide era.* J Neurooncol, 2012. **107**(2): p. 359-64.
69. Stupp, R., et al., *Radiotherapy plus concomitant and adjuvant temozolomide for*

glioblastoma. N Engl J Med, 2005. **352**(10): p. 987-96.

70. Rios Velazquez, E., et al., *Fully automatic GBM segmentation in the TCGA-GBM dataset: Prognosis and correlation with VASARI features.* Scientific Reports, 2015. **5**: p. 16822.
71. Aldape, K., et al., *Glioblastoma: pathology, molecular mechanisms and markers.* Acta Neuropathol, 2015. **129**(6): p. 829-48.
72. Stupp, R., et al., *High-grade glioma: ESMO Clinical Practice Guidelines for diagnosis, treatment and follow-up.* Ann Oncol, 2014. **25 Suppl 3**: p. iii93-101.
73. Kuhnt, D., et al., *Correlation of the extent of tumor volume resection and patient survival in surgery of glioblastoma multiforme with high-field intraoperative MRI guidance.* Neuro-Oncology, 2011. **13**(12): p. 1339-1348.
74. Stummer, W., et al., *Extent of resection and survival in glioblastoma multiforme: identification of and adjustment for bias.* Neurosurgery, 2008. **62**(3): p. 564-76; discussion 564-76.
75. Stepp, H., et al., *ALA and Malignant Glioma: Fluorescence-Guided Resection and Photodynamic Treatment.* Journal of Environmental Pathology, Toxicology and Oncology, 2007. **26**(2): p. 157-164.
76. Leroy, H.A., et al., *Fluorescence guided resection and glioblastoma in 2015: A review.* Lasers in Surgery and Medicine, 2015. **47**(5): p. 441-51.
77. Guyotat, J., et al., *5-Aminolevulinic Acid-Protoporphyrin IX Fluorescence-Guided Surgery of High-Grade Gliomas: A Systematic Review.* Adv Tech Stand Neurosurg, 2016(43): p. 61-90.
78. Gadji, M., et al., *Is the 1p/19q deletion a diagnostic marker of oligodendrogliomas?* Cancer Genetics and Cytogenetics, 2009. **194**(1): p. 12-22.
79. Zhao, J., W. Ma, and H. Zhao, *Loss of heterozygosity 1p/19q and survival in glioma: a meta-analysis.* Neuro-Oncology, 2014. **16**(1): p. 103-112.
80. Lathia, J.D., et al., *Cancer stem cells in glioblastoma.* Genes & Development, 2015. **29**(12): p. 1203-1217.
81. Swetha J. Sundar, et al., *The role of cancer stem cells in glioblastoma.* Neurosurgical Focus, 2014. **37**(6): p. E6.
82. Thomas, A.A., et al., *Emerging therapies for glioblastoma.* JAMA Neurology, 2014. **71**(11): p. 1437-1444.
83. Cohen-Inbar, O., Z. Xu, and J.P. Sheehan, *Focused ultrasound-aided immunomodulation in glioblastoma multiforme: a therapeutic concept.* Journal of

Therapeutic Ultrasound, 2016. **4**: p. 2.

84. Hung, A.L., T. Garzon-Muvdi, and M. Lim, *Biomarkers and Immunotherapeutic Targets in Glioblastoma.* World Neurosurgery, 2017. **102**: p. 494-506.
85. Lee, D.H., et al., *Advances in epigenetic glioblastoma therapy.* Oncotarget, 2017. **8**(11): p. 18577-18589.
86. Yang, F.Y. and S.C. Horng. *Chemotherapy of glioblastoma by targeted liposomal platinum compounds with focused ultrasound*. in *2013 35th Annual International Conference of the IEEE Engineering in Medicine and Biology Society (EMBC)*. 2013.
87. Phenix, C.P., et al., *High intensity focused ultrasound technology, its scope and applications in therapy and drug delivery.* J Pharm Pharm Sci, 2014. **17**(1): p. 136-53.
88. Yang, F.Y., et al., *Treating glioblastoma multiforme with selective high-dose liposomal doxorubicin chemotherapy induced by repeated focused ultrasound.* Int J Nanomedicine, 2012. **7**: p. 965-74.
89. Feng-Yi Yang, G.-L.L., Shih-Cheng Horng, Tien-Kuei Chang, Shih-Yen Wu, Tai-Tong Wong, and a.H.-E. Wang, *Pulsed High-Intensity Focused Ultrasound Enhances the Relative Permeability of the Blood–Tumor Barrier in a Glioma-Bearing Rat Model.* IEEE TRANSACTIONS ON ULTRASONICS, FERROELECTRICS, AND FREQUENCY CONTROL, 2011. **58**(5): p. 7.
90. von Neubeck, C., et al., *Glioblastoma multiforme: emerging treatments and stratification markers beyond new drugs.* The British Journal of Radiology, 2015. **88**(1053): p. 20150354.
91. Laws, E.R.J., et al., *Photoradiation Therapy in the Treatment of Malignant Brain Tumors: A Phase I (Feasibility) Study.* Neurosurgery, 1981. **9**(6): p. 672-678.
92. Fazeny-Dorner, B., et al., *Survival and prognostic factors of patients with unresectable glioblastoma multiforme.* Anticancer Drugs, 2003. **14**(4): p. 305-12.
93. Paquette, B., et al., *Prognostic value of health-related quality of life for death risk stratification in patients with unresectable glioblastoma.* Cancer Med, 2016. **5**(8): p. 1753-64.
94. Mirimanoff, R.O., et al., *Radiotherapy and temozolomide for newly diagnosed glioblastoma: recursive partitioning analysis of the EORTC 26981/22981-NCIC CE3 phase III randomized trial.* J Clin Oncol, 2006. **24**(16): p. 2563-9.
95. Johansson, A., et al., *In vivo measurement of parameters of dosimetric importance during interstitial photodynamic therapy of thick skin tumors.* Journal of Biomedical Optics, 2006. **11**(3): p. 034029-034029-10.

96. Johansson, A., et al., *Realtime light dosimetry software tools for interstitial photodynamic therapy of the human prostate.* Medical Physics, 2007. **34**(11): p. 4309-4321.
97. Wolfsen, H., et al., *Bare fiber photodynamic therapy using porfimer sodium for esophageal disease.* Photodiagnosis and Photodynamic Therapy, 2006. **3**(2): p. 87-92.
98. Tetard, M.C., et al., *Interstitial 5-ALA photodynamic therapy and glioblastoma: preclinical model development and preliminary results.* Photodiagnosis Photodyn Ther, 2015.
99. J. Beck, T., et al. *Clinical Determination of Tissue Optical Properties in vivo by Spatially Resolved Reflectance Measurements*. in *Photon Migration and Diffuse-Light Imaging*. 2003. Munich: Optical Society of America.
100. Baran, T.M. and T.H. Foster, *Comparison of flat cleaved and cylindrical diffusing fibers as treatment sources for interstitial photodynamic therapy.* Med Phys, 2014. **41**(2): p. 022701.
101. Sandell, J., et al., *A Treatment Planning System for Pleural PDT.* Proceedings of SPIE--the International Society for Optical Engineering, 2010. **7551**: p. 75510C.
102. Cassidy, J., V. Betz, and L. Lilge, *Treatment plan evaluation for interstitial photodynamic therapy in a mouse model by Monte Carlo simulation with FullMonte.* Frontiers in Physics, 2015. **3**: p. 1-10.
103. Cassidy, J., V. Betz, and L. Lilge. *Monte Carlo fluence simulation for prospective evaluation of interstitial photodynamic therapy treatment plans*. in *Proc. SPIE Optical Methods for Tumor Treatment and Detection: Mechanisms and Techniques in Photodynamic Therapy XXIV*. 2015.
104. Betrouni, N., et al., *An image guided treatment platform for prostate cancer photodynamic therapy.* Conf Proc IEEE Eng Med Biol Soc, 2013. **2013**: p. 370-3.
105. Swartling, J., et al., *System for interstitial photodynamic therapy with online dosimetry: first clinical experiences of prostate cancer.* J Biomed Opt, 2010. **15**(5): p. 058003.
106. Davidson, S.R., et al., *Treatment planning and dose analysis for interstitial photodynamic therapy of prostate cancer.* Phys Med Biol, 2009. **54**(8): p. 2293-313.
107. Rahman, M., G.J. Murad, and J. Mocco, *Early history of the stereotactic apparatus in neurosurgery.* Neurosurg Focus, 2009. **27**(3): p. E12.
108. SPIEGEL, E.A., et al., *Stereotaxic Apparatus for Operations on the Human Brain.* Science, 1947. **106**(2754): p. 349-350.

109. Leksell, L., *The stereotaxic method and radiosurgery of the brain.* Acta Chir Scand, 1951. **102**(4): p. 316-9.
110. Talairach, J., *[Stereotaxic radiologic explorations]*. Rev Neurol (Paris), 1954. **90**(5): p. 556-84.
111. Talairach, J. and P. Tournoux, *[Stereotaxic localization of central gray nuclei]*. Neurochirurgia (Stuttg), 1958. **1**(1): p. 88-93.
112. Talairach, J. and P. Tournoux, *Co-planar Stereotaxic Atlas of the Human Brain: 3-dimensional Proportional System : an Approach to Cerebral Imaging*. 1988: G. Thieme.
113. Iida, K. and H. Otsubo, *Stereoelectroencephalography: Indication and Efficacy.* Neurologia medico-chirurgica, 2017. **advpub**.
114. Brandmeir, N.J., et al., *The comparative accuracy of the ROSA stereotactic robot across a wide range of clinical applications and registration techniques.* Journal of Robotic Surgery, 2017.
115. Powers, S.K., et al., *Stereotactic intratumoral photodynamic therapy for recurrent malignant brain tumors.* Neurosurgery, 1991. **29**(5): p. 688-95; discussion 695-6.
116. Krishnamurthy, S., et al., *Optimal light dose for interstitial photodynamic therapy in treatment for malignant brain tumors.* Lasers Surg Med, 2000. **27**(3): p. 224-34.
117. Beck, T.J., et al., *Interstitial photodynamic therapy of nonresectable malignant glioma recurrences using 5-aminolevulinic acid induced protoporphyrin IX*. Lasers in Surgery and Medicine, 2007. **39**(5): p. 386-93.
118. Stummer, W., et al., *Long-sustaining response in a patient with non-resectable, distant recurrence of glioblastoma multiforme treated by interstitial photodynamic therapy using 5-ALA: case report.* Journal of Neurooncology, 2008. **87**(1): p. 103-9.
119. McCulloch, G.A., et al., *Phototherapy in malignant brain tumors.* Prog Clin Biol Res, 1984. **170**: p. 709-17.
120. Muller, P.J. and B.C. Wilson, *Photodynamic therapy: cavitary photoillumination of malignant cerebral tumours using a laser coupled inflatable balloon.* Can J Neurol Sci, 1985. **12**(4): p. 371-3.
121. Dwyer, P.J., et al., *Optical integrating balloon device for photodynamic therapy.* Lasers in Surgery and Medicine, 2000. **26**(1): p. 58-66.
122. Moseley, H., et al., *In vitro light distributions from intracranial PDT balloons.* Photodiagnosis Photodyn Ther, 2007. **4**(3): p. 213-20.
123. Schmidt, M.H., et al., *Light-emitting diodes as a light source for intraoperative*

photodynamic therapy. Neurosurgery, 1996. **38**(3): p. 552-6; discussion 556-7.

124. Akimoto, J., J. Haraoka, and K. Aizawa, *Preliminary clinical report on safety and efficacy of photodynamic therapy using talaporfin sodium for malignant gliomas.* Photodiagnosis Photodyn Ther, 2012. **9**(2): p. 91-9.
125. Kaye, A.H., G. Morstyn, and D. Brownbill, *Adjuvant high-dose photoradiation therapy in the treatment of cerebral glioma: a phase 1-2 study.* J Neurosurg, 1987. **67**(4): p. 500-5.
126. Perria, C., et al., *Photodynamic therapy of malignant brain tumors: clinical results of, difficulties with, questions about, and future prospects for the neurosurgical applications.* Neurosurgery, 1988. **23**(5): p. 557-63.
127. Kostron, H., A. Obwegeser, and R. Jakober, *Photodynamic therapy in neurosurgery: a review.* J Photochem Photobiol B, 1996. **36**(2): p. 157-68.
128. Rosenthal, M.A., et al., *Promising survival in patients with high-grade gliomas following therapy with a novel boronated porphyrin.* J Clin Neurosci, 2003. **10**(4): p. 425-7.
129. Schmidt, M.H., et al., *Evaluation of photodynamic therapy near functional brain tissue in patients with recurrent brain tumors.* J Neurooncol, 2004. **67**(1-2): p. 201-7.
130. Stylli, S.S., et al., *Photodynamic therapy of high grade glioma - long term survival.* Journal of Clinical Neuroscience, 2005. **12**(4): p. 389-98.
131. Muller, P.J. and B.C. Wilson, *Photodynamic therapy of brain tumors—A work in progress.* Lasers in Surgery and Medicine, 2006. **38**(5): p. 384-389.
132. Eljamel, M.S., C. Goodman, and H. Moseley, *ALA and Photofrin fluorescence-guided resection and repetitive PDT in glioblastoma multiforme: a single centre Phase III randomised controlled trial.* Lasers Med Sci, 2008. **23**(4): p. 361-7.
133. Muragaki, Y., et al., *Phase II clinical study on intraoperative photodynamic therapy with talaporfin sodium and semiconductor laser in patients with malignant brain tumors.* J Neurosurg, 2013. **119**(4): p. 845-52.
134. Henyey, L.G. and J.L. Greenstein, *Diffuse radiation in the Galaxy.* Astrophysical Journal 1941. **93**: p. 70-93.
135. Binzoni, T., et al., *The use of the Henyey-Greenstein phase function in Monte Carlo simulations in biomedical optics.* Phys Med Biol, 2006. **51**(17): p. N313-22.
136. Welch, A.J., M.J.C. van Gemert, and W.M. Star, *Definitions and Overview of Tissue Optics*, in *Optical-Thermal Response of Laser-Irradiated Tissue*, A.J. Welch and M.J.C. van Gemert, Editors. 2011, Springer Netherlands: Dordrecht. p. 27-64.

137. Jacques, S.L., *How tissue optics affect dosimetry of photodynamic therapy.* Journal of Biomedical Optics, 2010. **15**(5): p. 051608-051608-6.
138. Pogue, B.W., et al., *Revisiting photodynamic therapy dosimetry: reductionist & surrogate approaches to facilitate clinical success.* Phys Med Biol, 2016. **61**(7): p. R57-89.
139. Haskell, R.C., et al., *Boundary conditions for the diffusion equation in radiative transfer.* Journal of the Optical Society of America A, 1994. **11**(10): p. 2727-2741.
140. Mottin, S., G. Panasenko, and S.S. Ganesh, *Multiscale Modeling of Light Absorption in Tissues: Limitations of Classical Homogenization Approach.* PLoS ONE, 2010. **5**(12): p. e14350.
141. Rangogni, R., *The solution of the non-homogeneous Helmholtz equation by means of the boundary element method.* Applied Mathematical Modelling, 1984. **8**(6): p. 442-444.
142. Sandell, J.L. and T.C. Zhu, *A review of in-vivo optical properties of human tissues and its impact on PDT.* Journal of Biophotonics, 2011. **4**(11-12): p. 773-87.
143. Dimofte, A., et al., *Determination of optical properties in heterogeneous turbid media using a cylindrical diffusing fiber.* Physics in Medecine and Biology, 2012. **57**(19): p. 6025-46.
144. Dimofte, A., J.C. Finlay, and T.C. Zhu, *A method for determination of the absorption and scattering properties interstitially in turbid media.* Physics in Medecine and Biology, 2005. **50**(10): p. 2291-311.
145. Jacques, S.L. and B.W. Pogue, *Tutorial on diffuse light transport.* Journal of Biomedical Optics, 2008. **13**(4): p. 041302.
146. Liang, X., K.K. Wang, and T.C. Zhu, *Feasibility of interstitial diffuse optical tomography using cylindrical diffusing fibers for prostate PDT.* Physics in Medecine and Biology, 2013. **58**(10): p. 3461-80.
147. Dehghan, M., *Fully implicit finite differences methods for two-dimensional diffusion with a non-local boundary condition.* Journal of Computational and Applied Mathematics, 1999. **106**(2): p. 255-269.
148. Karatay, I. and S.R. Bayramoglu, *High-Order Compact Difference Scheme for the Numerical Solution of Time Fractional Heat Equations.* The Scientific World Journal, 2014. **2014**: p. 642989.
149. Pogue, B.W., et al., *Initial assessment of a simple system for frequency domain diffuse optical tomography.* Phys Med Biol, 1995. **40**(10): p. 1709-29.

150. Srinivasan, S., et al., *A boundary element approach for image-guided near-infrared absorption and scatter estimation.* Med Phys, 2007. **34**(11): p. 4545-57.
151. Sikora, J., et al., *Diffuse photon propagation in multilayered geometries.* Phys Med Biol, 2006. **51**(3): p. 497-516.
152. Fedele, F., et al., *Fluorescence photon migration by the boundary element method.* Journal of Computational Physics, 2005. **210**(1): p. 109-132.
153. Marqa, M.F., S. Mordon, and N. Betrouni, *Laser interstitial thermotherapy of small breast fibroadenomas: numerical simulations.* Lasers Surg Med, 2012. **44**(10): p. 832-9.
154. Oakley, E., et al., *A new finite element approach for near real-time simulation of light propagation in locally advanced head and neck tumors.* Lasers in Surgery and Medicine, 2015. **47**(1): p. 60-67.
155. Arridge, S.R., et al., *A finite element approach for modeling photon transport in tissue.* Med Phys, 1993. **20**(2 Pt 1): p. 299-309.
156. Okada, E., et al., *Experimental validation of Monte Carlo and finite-element methods for the estimation of the optical path length in inhomogeneous tissue.* Appl Opt, 1996. **35**(19): p. 3362-71.
157. Mohammed, Y. and J.F. Verhey, *A finite element method model to simulate laser interstitial thermo therapy in anatomical inhomogeneous regions.* BioMedical Engineering OnLine, 2005. **4**: p. 2-2.
158. Schweiger, M., et al., *The finite element method for the propagation of light in scattering media: boundary and source conditions.* Med Phys, 1995. **22**(11 Pt 1): p. 1779-92.
159. Schweiger, M. and S.R. Arridge, *The finite-element method for the propagation of light in scattering media: frequency domain case.* Med Phys, 1997. **24**(6): p. 895-902.
160. Arridge, S.R., *Methods in diffuse optical imaging.* Philosophical Transactions of the Royal Society A: Mathematical, Physical and Engineering Sciences, 2011. **369**(1955): p. 4558-4576.
161. Arridge, S.R. and J.C. Hebden, *Optical imaging in medicine: II. Modelling and reconstruction.* Physics in Medicine and Biology, 1997. **42**(5): p. 841.
162. Paulsen, K.D. and H. Jiang, *Spatially varying optical property reconstruction using a finite element diffusion equation approximation.* Medical Physics, 1995. **22**(6): p. 691-701.
163. Qin, C., et al., *Galerkin-based meshless methods for photon transport in the biological*

tissue. Optics Express, 2008. **16**(25): p. 20317-20333.

164. Chakrabarty, S.P. and F.B. Hanson, *Distributed parameters deterministic model for treatment of brain tumors using Galerkin finite element method.* Mathematical Biosciences, 2009. **219**(2): p. 129-141.
165. Metropolis, N., *The Beginning of the Monte Carlo Method.* Los Alamos Science, 1987.
166. Wilson, B.C. and G. Adam, *A Monte Carlo model for the absorption and flux distributions of light in tissue.* Med Phys, 1983. **10**(6): p. 824-30.
167. Lihong Wang, S.L.J., *Monte Carlo Modeling of Light Transport in Multi-layered Tissues in Standard C*. 1992.
168. Prahl, S.A., et al., *A Monte Carlo Model of Light Propagation in Tissue*, in *SPIE Proceedings of Dosimetry of Laser Radiation in Medicine and Biology*, G.J.M.a.D.H. Sliney, Editor. 1989, SPIE Optical Engineering Press: Bellingham, Washington. p. 102-111.
169. Wang, L., S.L. Jacques, and L. Zheng, *MCML—Monte Carlo modeling of light transport in multi-layered tissues.* Computer Methods and Programs in Biomedicine, 1995. **47**(2): p. 131-146.
170. de Blois, A.W., et al., *In vivo pharmacokinetics of protoporphyrin IX accumulation following intracutaneous injection of 5-aminolevulinic acid.* J Photochem Photobiol B, 2001. **61**(1-2): p. 21-9.
171. Plaetzer, K., et al., *Photophysics and photochemistry of photodynamic therapy: fundamental aspects.* Lasers Med Sci, 2009. **24**(2): p. 259-68.
172. Svaasand, L.O., et al., *Light and drug distribution with topically administered photosensitizers.* Lasers in Medical Science, 1996. **11**(4): p. 261-265.
173. Salas-García, I., F. Fanjul-Vélez, and J.L. Arce-Diego, *Photosensitizer absorption coefficient modeling and necrosis prediction during photodynamic therapy.* Journal of Photochemistry and Photobiology B: Biology, 2012. **114**: p. 79-86.
174. Foster, T.H. and L. Gao, *Dosimetry in photodynamic therapy: oxygen and the critical importance of capillary density.* Radiation Research, 1992. **130**(3): p. 379-83.
175. Zhu, T.C., J.C. Finlay, and S.M. Hahn, *Determination of the distribution of light, optical properties, drug concentration, and tissue oxygenation in-vivo in human prostate during motexafin lutetium-mediated photodynamic therapy.* Journal of Photochemistry and Photobiology B: Biology, 2005. **79**(3): p. 231-41.
176. Jarvi, M.T., et al., *The influence of oxygen depletion and photosensitizer triplet-state*

dynamics during photodynamic therapy on accurate singlet oxygen luminescence monitoring and analysis of treatment dose response. Photochem Photobiol, 2011. **87**(1): p. 223-34.

177. Mark, A.W. and S.P. Michael, *Monitoring oxygen concentration during photodynamic therapy using prompt photosensitizer fluorescence.* Physics in Medicine & Biology, 2013. **58**(20): p. 7039.
178. Zhu, T.C., et al., *Comparison of singlet oxygen threshold dose for PDT.* Proc SPIE Int Soc Opt Eng, 2014. **8931**.
179. Yuan, J., et al., *Predictions of mathematical models of tissue oxygenation and generation of singlet oxygen during photodynamic therapy.* Radiat Res, 1997. **148**(4): p. 386-94.
180. Wang, K.K., et al., *Explicit dosimetry for photodynamic therapy: macroscopic singlet oxygen modeling.* J Biophotonics, 2010. **3**(5-6): p. 304-18.
181. Liu, B., T.J. Farrell, and M.S. Patterson, *A dynamic model for ALA-PDT of skin: simulation of temporal and spatial distributions of ground-state oxygen, photosensitizer and singlet oxygen.* Phys Med Biol, 2010. **55**(19): p. 5913-32.
182. Liang, X., K.K. Wang, and T.C. Zhu, *Singlet oxygen dosimetry modeling for photodynamic therapy.* Proc SPIE Int Soc Opt Eng, 2012. **8210**.
183. Qiu, H., et al., *Macroscopic singlet oxygen modeling for dosimetry of Photofrin-mediated photodynamic therapy: an in-vivo study.* J Biomed Opt, 2016. **21**(8): p. 88002.
184. Lopez, N., R. Mulet, and R. Rodriguez, *Tumor reactive ringlet oxygen approach for Monte Carlo modeling of photodynamic therapy dosimetry.* J Photochem Photobiol B, 2016. **160**: p. 383-91.
185. Stummer, W., et al., *Predicting the "usefulness" of 5-ALA-derived tumor fluorescence for fluorescence-guided resections in pediatric brain tumors: a European survey.* Acta Neurochir (Wien), 2014.
186. Beez, T., et al., *Fluorescence-guided surgery with 5-aminolevulinic acid for resection of brain tumors in children—a technical report.* Acta Neurochirurgica, 2014. **156**(3): p. 597-604.
187. Stummer, W., et al., *Counterbalancing risks and gains from extended resections in malignant glioma surgery: a supplemental analysis from the randomized 5-aminolevulinic acid glioma resection study. Clinical article.* J Neurosurg, 2011. **114**(3): p. 613-23.

188. Johansson, A., et al. *ALA-mediated fluorescence-guided resection (FGR) and PDT of glioma*. in *Proc. of SPIE Photodynamic Therapy: Back to the Future*. 2009.
189. Stummer, W., et al., *Fluorescence-guided surgery with 5-aminolevulinic acid for resection of malignant glioma: a randomised controlled multicentre phase III trial.* Lancet Oncology, 2006. **7**(5): p. 392-401.
190. Braichotte, D.R., et al., *Optimizing light dosimetry in photodynamic therapy of early stage carcinomas of the esophagus using fluorescence spectroscopy.* Lasers Surg Med, 1996. **19**(3): p. 340-6.
191. Boere, I.A., et al., *Monitoring In Situ Dosimetry and Protoporphyrin IX Fluorescence Photobleaching in the Normal Rat Esophagus During 5-Aminolevulinic Acid Photodynamic Therapy* ¶. Photochemistry and Photobiology, 2003. **78**(3): p. 271-277.
192. Valentine, R.M., et al., *Modelling fluorescence in clinical photodynamic therapy.* Photochem Photobiol Sci, 2013. **12**(1): p. 203-13.
193. Mallidi, S., et al., *Photosensitizer fluorescence and singlet oxygen luminescence as dosimetric predictors of topical 5-aminolevulinic acid photodynamic therapy induced clinical erythema.* Journal of Biomedical Optics, 2014. **19**(2): p. 028001.
194. Georges, W., et al., *An optical phantom with tissue-like properties in the visible for use in PDT and fluorescence spectroscopy.* Physics in Medicine and Biology, 1997. **42**(7): p. 1415.
195. Maruyama, T., et al., *Intraoperative detection of malignant gliomas using 5-Aminolevulinic acid-induced protoporphyrin fluorescence, openMRI and real-time navigation system.* International Congress Series, 2001. **1230**: p. 281-286.
196. Baran, T.M., M.C. Fenn, and T.H. Foster, *Determination of optical properties by interstitial white light spectroscopy using a custom fiber optic probe.* J Biomed Opt, 2013. **18**(10): p. 107007.
197. Kanick, S.C., et al., *Dual-channel red/blue fluorescence dosimetry with broadband reflectance spectroscopic correction measures protoporphyrin IX production during photodynamic therapy of actinic keratosis.* Journal of Biomedical Optics, 2014. **19**(7): p. 075002.
198. de Visscher, S.A., et al., *In vivo quantification of photosensitizer concentration using fluorescence differential path-length spectroscopy: influence of photosensitizer formulation and tissue location.* J Biomed Opt, 2012. **17**(6): p. 067001.
199. Saager, R.B., et al., *Quantitative fluorescence imaging of protoporphyrin IX through determination of tissue optical properties in the spatial frequency domain.* Journal of

Biomedical Optics, 2011. **16**(12): p. 126013.

200. Sharwani, A. and F.A. Alharbi, *Monitoring of photobleaching in photodynamic therapy using fluorescence spectroscopy.* Gulf J Oncolog, 2014. **1**(16): p. 79-83.

201. Dochow, S., et al., *Combined fiber probe for fluorescence lifetime and Raman spectroscopy.* Anal Bioanal Chem, 2015. **407**(27): p. 8291-301.

202. Fischer, F., et al., *An affordable, portable fluorescence imaging device for skin lesion detection using a dual wavelength approach for image contrast enhancement and aminolaevulinic acid-induced protoporphyrin IX. Part I. Design, spectral and spatial characteristics.* Lasers Med Sci, 2001. **16**(3): p. 199-206.

203. Fischer, F., et al., *An affordable, portable fluorescence imaging device for skin lesion detection using a dual wavelength approach for image contrast enhancement and aminolaevulinic acid-induced protoporphyrin IX. Part II. In vivo testing.* Lasers Med Sci, 2001. **16**(3): p. 207-12.

204. Cubeddu, R., et al., *Fluorescence imaging during photodynamic therapy of experimental tumors in mice sensitized with disulfonated aluminum phthalocyanine.* Photochem Photobiol, 2000. **72**(5): p. 690-5.

205. Andrade, C.T., et al., *Identification of skin lesions through aminolaevulinic acid-mediated photodynamic detection.* Photodiagnosis Photodyn Ther, 2014. **11**(3): p. 409-15.

206. Tyrrell, J., S. Campbell, and A. Curnow, *Protoporphyrin IX photobleaching during the light irradiation phase of standard dermatological methyl-aminolevulinate photodynamic therapy.* Photodiagnosis Photodyn Ther, 2010. **7**(4): p. 232-8.

207. Flynn, B.P., et al., *White light-informed optical properties improve ultrasound-guided fluorescence tomography of photoactive protoporphyrin IX.* J Biomed Opt, 2013. **18**(4): p. 046008.

208. Rollakanti, K.R., et al., *Techniques for fluorescence detection of protoporphyrin IX in skin cancers associated with photodynamic therapy.* Photonics Lasers Med, 2013. **2**(4): p. 287-303.

209. Mo, W., D. Rohrbach, and U. Sunar, *Imaging a photodynamic therapy photosensitizer in vivo with a time-gated fluorescence tomography system.* J Biomed Opt, 2012. **17**(7): p. 071306.

210. Laubach, H.J., et al., *In-vivo singlet oxygen dosimetry of clinical 5-aminolevulinic acid photodynamic therapy.* J Biomed Opt, 2008. **13**(5): p. 050504.

211. Schlothauer, J., S. Hackbarth, and B. Röder, *A new benchmark for time-resolved*

detection of singlet oxygen luminescence – revealing the evolution of lifetime in living cells with low dose illumination. Laser Physics Letters, 2009. **6**(3): p. 216-221.

212. Jimenez-Banzo, A., et al., *Singlet oxygen photosensitization by EGFP and its chromophore HBDI.* Biophys J, 2008. **94**(1): p. 168-72.
213. Niedre, M., M.S. Patterson, and B.C. Wilson, *Direct near-infrared luminescence detection of singlet oxygen generated by photodynamic therapy in cells in vitro and tissues in vivo.* Photochem Photobiol, 2002. **75**(4): p. 382-91.
214. Gemmell, N.R., et al., *A compact fiber-optic probe-based singlet oxygen luminescence detection system.* Journal of Biophotonics, 2017. **10**(2): p. 320-326.
215. Boso, G., et al., *Time-resolved singlet-oxygen luminescence detection with an efficient and practical semiconductor single-photon detector.* Biomedical Optics Express, 2016. **7**(1): p. 211-224.
216. Rabbani, M.G., et al., *Zero-bias photocurrents in highly-disordered networks of Ge and Si nanowires.* Nanotechnology, 2016. **27**(4): p. 045201.
217. Tromberg, B.J., et al., *Tumor oxygen tension during photodynamic therapy.* J Photochem Photobiol B, 1990. **5**(1): p. 121-6.
218. Piffaretti, F., et al., *Real-time, in vivo measurement of tissular pO2 through the delayed fluorescence of endogenous protoporphyrin IX during photodynamic therapy.* J Biomed Opt, 2012. **17**(11): p. 115007.
219. Tromberg, B.J., et al., *In vivo tumor oxygen tension measurements for the evaluation of the efficiency of photodynamic therapy.* Photochem Photobiol, 1990. **52**(2): p. 375-85.
220. Bajgar, R., et al., *High oxygen partial pressure increases photodynamic effect on HeLa cell lines in the presence of chloraluminium phthalocyanine.* Anticancer Res, 2014. **34**(8): p. 4095-9.
221. Zhu, T.C. and J.C. Finlay, *The role of photodynamic therapy (PDT) physics.* Medical Physics, 2008. **35**(7): p. 3127-36.
222. Kienle, A. and M.S. Patterson, *Determination of the optical properties of turbid media from a single Monte Carlo simulation.* Phys Med Biol, 1996. **41**(10): p. 2221-7.
223. Pifferi, A., et al., *Real-time method for fitting time-resolved reflectance and transmittance measurements with a monte carlo model.* Appl Opt, 1998. **37**(13): p. 2774-80.
224. Alerstam, E., S. Andersson-Engels, and T. Svensson, *White Monte Carlo for time-resolved photon migration.* J Biomed Opt, 2008. **13**(4): p. 041304.

225. Liu, Q. and N. Ramanujam, *Scaling method for fast Monte Carlo simulation of diffuse reflectance spectra from multilayered turbid media.* J Opt Soc Am A Opt Image Sci Vis, 2007. **24**(4): p. 1011-25.
226. Graaff, R., et al., *Condensed Monte Carlo simulations for the description of light transport.* Appl Opt, 1993. **32**(4): p. 426-34.
227. Sassaroli, A., F. Martelli, and S. Fantini, *Perturbation theory for the diffusion equation by use of the moments of the generalized temporal point-spread function. II. Continuous-wave results.* Journal of the Optical Society of America A, 2006. **23**(9): p. 2119-2131.
228. Sassaroli, A., F. Martelli, and S. Fantini, *Perturbation theory for the diffusion equation by use of the moments of the generalized temporal point-spread function. I. Theory.* Journal of the Optical Society of America A, 2006. **23**(9): p. 2105-2118.
229. Sassaroli, A., F. Martelli, and S. Fantini, *Perturbation theory for the diffusion equation by use of the moments of the generalized temporal point-spread function. III. Frequency-domain and time-domain results.* Journal of the Optical Society of America. A, Optics, image science, and vision, 2010. **27**(7): p. 1723-1742.
230. Sassaroli, A., et al., *Monte carlo procedure for investigating light propagation and imaging of highly scattering media.* Appl Opt, 1998. **37**(31): p. 7392-400.
231. Nguyen, J., et al., *Development of perturbation Monte Carlo methods for polarized light transport in a discrete particle scattering model.* Biomedical Optics Express, 2016. **7**(5): p. 2051-2066.
232. Fabrizio, M., B. Samuele Del, and Z. Giovanni, *Perturbation model for light propagation through diffusive layered media.* Physics in Medicine & Biology, 2005. **50**(9): p. 2159.
233. Seo, I., et al., *Perturbation and differential Monte Carlo methods for measurement of optical properties in a layered epithelial tissue model.* Journal of Biomedical Optics, 2007. **12**(1): p. 014030-014030-15.
234. Zaccanti, G., F. Martelli, and S. Del Bianco, *Method to measure the optical properties of small volumes of diffusive media.* Applied Optics, 2002. **41**(34): p. 7317-7324.
235. Tseng, S.-H., et al., *Determination of Optical Properties of Superficial Volumes of Layered Tissue Phantoms.* IEEE transactions on bio-medical engineering, 2008. **55**(1): p. 335-339.
236. Kumar, Y.P. and R.M. Vasu, *Reconstruction of optical properties of low-scattering tissue using derivative estimated through perturbation Monte-Carlo method.* Journal

of Biomedical Optics, 2004. **9**(5): p. 1002-1012.

237. Nguyen, J., et al., *Perturbation Monte Carlo methods for tissue structure alterations.* Biomed Opt Express, 2013. **4**(10): p. 1946-63.
238. Sassaroli, A., *Fast perturbation Monte Carlo method for photon migration in heterogeneous turbid media.* Optics Letters, 2011. **36**(11): p. 2095-2097.
239. Zhu, C. and Q. Liu, *Hybrid method for fast Monte Carlo simulation of diffuse reflectance from a multilayered tissue model with tumor-like heterogeneities.* J Biomed Opt, 2012. **17**(1): p. 010501.
240. Hayakawa, C.K., et al., *Perturbation Monte Carlo methods to solve inverse photon migration problems in heterogeneous tissues*. 2001.
241. Flock, S.T., B.C. Wilson, and M.S. Patterson. *Hybrid Monte Carlo - Diffusion Theory Modelling Of Light Distributions In Tissue*. 1988.
242. Tinet, E., et al. *Fast and accurate new Monte Carlo simulation for light propagation through turbid media*. 1993.
243. Tinet, E., S. Avrillier, and J.M. Tualle, *Fast semianalytical Monte Carlo simulation for time-resolved light propagation in turbid media.* Journal of the Optical Society of America A, 1996. **13**(9): p. 1903-1915.
244. Wang, L. and S.L. Jacques, *Hybrid model of Monte Carlo simulation and diffusion theory for light reflectance by turbid media.* J Opt Soc Am A Opt Image Sci Vis, 1993. **10**(8): p. 1746-52.
245. Wang, L.V., *Rapid modeling of diffuse reflectance of light in turbid slabs.* Journal of the Optical Society of America A, 1998. **15**(4): p. 936-944.
246. Alexandrakis, G., et al., *Determination of the optical properties of two-layer turbid media by use of a frequency-domain hybrid monte carlo diffusion model.* Appl Opt, 2001. **40**(22): p. 3810-21.
247. Alexandrakis, G., T.J. Farrell, and M.S. Patterson, *Monte carlo diffusion hybrid model for photon migration in a two-layer turbid medium in the frequency domain.* Appl Opt, 2000. **39**(13): p. 2235-44.
248. Patterson, M.S., et al., *Frequency-domain reflectance for the determination of the scattering and absorption properties of tissue.* Appl Opt, 1991. **30**(31): p. 4474-6.
249. Kienle, A. and M.S. Patterson, *Determination of the optical properties of semi-infinite turbid media from frequency-domain reflectance close to the source.* Phys Med Biol, 1997. **42**(9): p. 1801-19.
250. Pogue, B.W. and M.S. Patterson, *Frequency-domain optical absorption spectroscopy*

of finite tissue volumes using diffusion theory. Phys Med Biol, 1994. **39**(7): p. 1157-80.

251. Chatigny, S., et al., *Hybrid Monte Carlo for photon transport through optically thick scattering media.* Appl Opt, 1999. **38**(28): p. 6075-86.
252. Hayashi, T., Y. Kashio, and E. Okada, *Hybrid Monte Carlo-diffusion method for light propagation in tissue with a low-scattering region.* Appl Opt, 2003. **42**(16): p. 2888-96.
253. Luo, B. and S. He, *An improved Monte Carlo diffusion hybrid model for light reflectance by turbid media.* Optics Express, 2007. **15**(10): p. 5905-5918.
254. Di Rocco, H.O., et al., *Acceleration of Monte Carlo modeling of light transport in turbid media; an approach based on hybrid, theoretical and numerical, calculations.* Journal of Quantitative Spectroscopy and Radiative Transfer, 2009. **110**(4): p. 307-314.
255. Kirkby, D.R. and D.T. Delpy, *Parallel operation of Monte Carlo simulations on a diverse network of computers.* Phys Med Biol, 1997. **42**(6): p. 1203-8.
256. Colasanti, A., et al., *Multiple processor version of a Monte Carlo code for photon transport in turbid media.* Computer Physics Communications, 2000. **132**(1): p. 84-93.
257. Gorshkov, A.V. and M.Y. Kirillin, *Acceleration of Monte Carlo simulation of photon migration in complex heterogeneous media using Intel many-integrated core architecture.* Journal of Biomedical Optics, 2015. **20**(8): p. 085002-085002.
258. Poole, C.M., et al., *Radiotherapy Monte Carlo simulation using cloud computing technology.* Australasian Physical & Engineering Sciences in Medicine, 2012. **35**(4): p. 497-502.
259. Miras, H., et al., *CloudMC: a cloud computing application for Monte Carlo simulation.* Physics in Medicine & Biology, 2013. **58**(8): p. N125.
260. Yong Hum, N., et al., *Toward a web-based real-time radiation treatment planning system in a cloud computing environment.* Physics in Medicine & Biology, 2013. **58**(18): p. 6525.
261. Peter, Z., et al., *Towards real-time photon Monte Carlo dose calculation in the cloud.* Physics in Medicine & Biology, 2017. **62**(11): p. 4375.
262. Pratx, G. and L. Xing, *Monte Carlo simulation of photon migration in a cloud computing environment with MapReduce.* Journal of Biomedical Optics, 2011. **16**(12): p. 125003.

263. Jacques, S.L., *Light Distributions from Point, Line and Plane Sources for Photochemical Reactions and Fluorescence in Turbid Biological Tissues.* Photochemistry and Photobiology, 1998. **67**(1): p. 23-32.
264. Doronin, A. and I. Meglinski, *Peer-to-peer Monte Carlo simulation of photon migration in topical applications of biomedical optics.* Journal of Biomedical Optics, 2012. **17**(9): p. 0905041-0905043.
265. Alerstam, E., T. Svensson, and S. Andersson-Engels, *Parallel computing with graphics processing units for high-speed Monte Carlo simulation of photon migration.* Journal of Biomedical Optics, 2008. **13**(6): p. 060504-060504-3.
266. Fang, Q. and D.A. Boas, *Monte Carlo simulation of photon migration in 3D turbid media accelerated by graphics processing units.* Optics Express, 2009. **17**(22): p. 20178-90.
267. Martinsen, P., et al., *Accelerating Monte Carlo simulations with an NVIDIA® graphics processor.* Computer Physics Communications, 2009. **180**(10): p. 1983-1989.
268. Ren, N., et al., *GPU-based Monte Carlo simulation for light propagation in complex heterogeneous tissues.* Optics Express, 2010. **18**(7): p. 6811-23.
269. Cai, F. and S. He, *Using graphics processing units to accelerate perturbation Monte Carlo simulation in a turbid medium.* Journal of Biomedical Optics, 2012. **17**(4): p. 0405021-0405023.
270. Glaser, A.K., et al., *A GAMOS plug-in for GEANT4 based Monte Carlo simulation of radiation-induced light transport in biological media.* Biomed Opt Express, 2013. **4**(5): p. 741-59.
271. Carbone, N., et al., *Solution of the direct problem in turbid media with inclusions using Monte Carlo simulations implemented in graphics processing units: new criterion for processing transmittance data.* Journal of Biomedical Optics, 2010. **15**(3): p. 035002-035002-9.
272. Leung, T.S. and S. Powell, *Fast Monte Carlo simulations of ultrasound-modulated light using a graphics processing unit.* Journal of Biomedical Optics, 2010. **15**(5): p. 055007-055007-7.
273. Powell, S. and T.S. Leung, *Highly parallel Monte-Carlo simulations of the acousto-optic effect in heterogeneous turbid media.* J Biomed Opt, 2012. **17**(4): p. 045002.
274. Yang, O. and B. Choi, *Accelerated rescaling of single Monte Carlo simulation runs with the Graphics Processing Unit (GPU).* Biomed Opt Express, 2013. **4**(11): p. 2667-

72.

275. Li, P., et al., *GPU acceleration of Monte Carlo simulations for polarized photon scattering in anisotropic turbid media.* Applied Optics, 2016. **55**(27): p. 7468-7476.

276. Amdahl, G.M., *Validity of the Single Processor Approach to Achieving Large Scale Computing Capabilities (Reprinted from the AFIPS Conference Proceedings, 1967).* IEEE Solid-State Circuits Society Newsletter, 2007. **12**(3): p. 19-20.

277. Hill, M.D. and M.R. Marty, *Amdahl's Law in the Multicore Era.* Computer, 2008. **41**(7): p. 33-38.

278. Jacques, S., T. Li, and S. Prahl. *mcxyz*. 2013 [cited 2017; Available from: http://omlc.org/software/mc/mcxyz/index.html.

279. Jacques, S.L., *Coupling 3D Monte Carlo light transport in optically heterogeneous tissues to photoacoustic signal generation.* Photoacoustics, 2014. **2**(4): p. 137-142.

280. Makoto Matsumoto, M.S., Hiroshi Haramoto, Takuji Nishimura, *Pseudorandom Number Generation: Impossibility and Compromise.* Journal of Universal Computer Science, 2006. **12**(6): p. 19.

281. Matsumoto, M. and T. Nishimura, *Mersenne Twister: A 623-dimensionally Equidistributed Uniform Pseudo-random Number Generator.* ACM Trans. Model. Comput. Simul., 1998. **8**(1): p. 3-30.

282. Rikitake, K., *TinyMT pseudo random number generator for Erlang*, in *Proceedings of the eleventh ACM SIGPLAN workshop on Erlang workshop*. 2012, ACM: Copenhagen, Denmark. p. 67-72.

283. L'Ecuyer, P. and R. Simard, *TestU01: A C library for empirical testing of random number generators.* ACM Trans. Math. Softw., 2007. **33**(4): p. 1-40.

284. Wrobel, M.S., et al., *Measurements of fundamental properties of homogeneous tissue phantoms.* J Biomed Opt, 2015. **20**(4): p. 045004.

285. Dong, E., et al., *Three-dimensional fuse deposition modeling of tissue-simulating phantom for biomedical optical imaging.* J Biomed Opt, 2015. **20**(12): p. 121311.

286. Luciana, C.C., et al., *Stable phantom materials for ultrasound and optical imaging.* Physics in Medicine and Biology, 2017. **62**(2): p. 432.

287. Ley, S., et al., *Phantom materials mimicking the optical properties in the near infrared range for non-invasive fetal pulse oximetry.* Conf Proc IEEE Eng Med Biol Soc, 2014. **2014**: p. 1432-5.

288. Ayers, F., et al. *Fabrication and characterization of silicone-based tissue phantoms with tunable optical properties in the visible and near infrared domain*. 2008.

289. Bays, R., et al., *Three-dimensional optical phantom and its application in photodynamic therapy.* Lasers in Surgery and Medicine, 1997. **21**(3): p. 227-234.
290. Lualdi, M., et al., *A phantom with tissue-like optical properties in the visible and near infrared for use in photomedicine.* Lasers Surg Med, 2001. **28**(3): p. 237-43.
291. Wang, J., et al. *Characterization and application of 3D-printed phantoms for biophotonic imaging*. 2013.
292. Wang, M., et al. *3D printing method for freeform fabrication of optical phantoms simulating heterogeneous biological tissue*. 2014.
293. Ninni, P.D., F. Martelli, and G. Zaccanti, *Intralipid: towards a diffusive reference standard for optical tissue phantoms.* Phys Med Biol, 2011. **56**(2): p. N21-8.
294. Aernouts, B., et al., *Dependent scattering in Intralipid® phantoms in the 600-1850 nm range.* Optics Express, 2014. **22**(5): p. 6086-6098.
295. Stringasci, M.D., et al., *Interstitial PDT using diffuser fiber-investigation in phantom and in vivo models.* Lasers Med Sci, 2017.
296. Spinelli, L., et al., *Determination of reference values for optical properties of liquid phantoms based on Intralipid and India ink.* Biomedical Optics Express, 2014. **5**(7): p. 2037-2053.
297. Johansson, A., et al., *Interstitial Photodynamic Therapy of Brain Tumors.* IEEE Journal of Selected Topics in Quantum Electronics, 2010. **16**(4): p. 841-853.
298. Rühm, A., et al. *5-ALA based photodynamic management of glioblastoma*. in *Proc. of SPIE Optical Techniques in Neurosurgery, Neurophotonics, and Optogenetics*. 2014.
299. Marijnissen, J.P. and W.M. Star, *Calibration of isotropic light dosimetry probes based on scattering bulbs in clear media.* Phys Med Biol, 1996. **41**(7): p. 1191-208.
300. Marijnissen, J.P. and W.M. Star, *Performance of isotropic light dosimetry probes based on scattering bulbs in turbid media.* Phys Med Biol, 2002. **47**(12): p. 2049-58.
301. Zhu, T. *AAPM recommendations for in-vivo light dosimetry for Photodynamic Therapy*. in *16th International Photodynamic Association World Congress* 2017. Comibra, Portugal.
302. Hetzel, F.W., et al., *AAPM REPORT NO. 88: PHOTODYNAMIC THERAPY DOSIMETRY*. 2005, American Association of Physicists in Medicine.
303. Baran, T.M., *Cylindrical diffuser axial detection profile is dependent on fiber design.* J Biomed Opt, 2015. **20**(4): p. 040502.
304. Farina, B., et al., *Monte Carlo simulation of light fluence in tissue in a cylindrical diffusing fibre geometry.* Phys Med Biol, 1999. **44**(1): p. 1-11.

305. Cheong, W.F., S.A. Prahl, and A.J. Welch, *A review of the optical properties of biological tissues.* IEEE Journal of Quantum Electronics, 1990. **26**(12): p. 2166-2185.
306. Vo-Dinh, T., *Biomedical photonics handbook*. 2003, Boca Raton, Fla.: CRC Press. 1787.
307. Alerstam, E., et al., *Next-generation acceleration and code optimization for light transport in turbid media using GPUs.* Biomedical Optics Express, 2010. **1**(2): p. 658-675.
308. Shafirstein, G., et al., *Interstitial Photodynamic Therapy-A Focused Review.* Cancers (Basel), 2017. **9**(2): p. 14.
309. Hennig, G., H. Stepp, and A. Johansson, *Photobleaching-based method to individualize irradiation time during interstitial 5-aminolevulinic acid photodynamic therapy.* Photodiagnosis Photodyn Ther, 2011. **8**(3): p. 275-81.
310. Rendon, A., J.C. Beck, and L. Lilge. *Linear feasibility algorithms for treatment planning in interstitial photodynamic therapy*. in *Proc. of SPIE Optical Methods for Tumor Treatment and Detection: Mechanisms and Techniques in Photodynamic Therapy XVII*. 2008.
311. Kharroubi Lakouas, D., et al., *Nuclear medicine for photodynamic therapy in cancer: planning, monitoring and nuclear PDT.* Photodiagnosis and Photodynamic Therapy, 2017. **18**: p. 17.
312. Dupont, C., et al., *5-ALA Photodynamic Therapy in Neurosurgery, Towards the Design of a Treatment Planning System: A Proof of Concept.* IRBM, 2017. **38**(1): p. 34-41.
313. Dewas, S., et al., *[Stereotactic body radiation therapy for liver primary and metastases: the Lille experience]*. Cancer Radiother, 2012. **16**(1): p. 58-69.
314. Taschner, C.A., et al., *Gamma Knife surgery for arteriovenous malformations in the brain: integration of time-resolved contrast-enhanced magnetic resonance angiography into dosimetry planning. Technical note.* J Neurosurg, 2007. **107**(4): p. 854-9.
315. Balossier, A., et al., *Role of radiosurgery in the management of pineal region tumours: indications, method, outcome.* Neurochirurgie, 2015. **61**(2-3): p. 216-22.
316. Zairi, F., et al., *Relevance of gamma knife radiosurgery alone for the treatment of non-small cell lung cancer brain metastases.* Clin Neurol Neurosurg, 2014. **125**: p. 87-93.
317. Tedford, C.E., et al., *Quantitative analysis of transcranial and intraparenchymal light penetration in human cadaver brain tissue.* Lasers in Surgery and Medicine, 2015.

47(4): p. 11.

318. Andrea Saltelli, M.R., Terry Andres, Francesca Campolongo, Jessica Cariboni, Debora Gatelli, Michaela Saisana and Stefano Tarantola, *Global Sensitivity Analysis*. 2008: John Wiley & Sons. 305.
319. Zhang, X.Y., et al., *Sobol Sensitivity Analysis: A Tool to Guide the Development and Evaluation of Systems Pharmacology Models.* CPT Pharmacometrics Syst Pharmacol, 2015. **4**(2): p. 69-79.
320. Alerstam, E., T. Svensson, and S. Andersson-Engels, *Parallel computing with graphics processing units for high-speed Monte Carlo simulation of photon migration.* J Biomed Opt, 2008. **13**(6): p. 060504.
321. Porz, N., et al., *Multi-modal glioblastoma segmentation: man versus machine.* PLoS One, 2014. **9**(5): p. e96873.
322. Dupont, C., et al., *On image segmentation methods applied to glioblastoma: State of art and new trends.* IRBM, 2016.
323. Dupont, C., et al., *On Image Segmentation Methods Applied to Glioblastoma: State of Art and New Trends.* IRBM, 2016. **37**(3): p. 131-143.
324. Yaroslavsky, A.N., et al., *Optical properties of selected native and coagulated human brain tissues in vitro in the visible and near infrared spectral range.* Physics in Medicine and Biology, 2002. **47**(12): p. 2059.
325. Gebhart, S.C., W.C. Lin, and A. Mahadevan-Jansen, *In vitro determination of normal and neoplastic human brain tissue optical properties using inverse adding-doubling.* Phys Med Biol, 2006. **51**(8): p. 2011-27.
326. Xie, J., et al., *Minimally invasive assessment of the effect of mannitol and hypertonic saline therapy on traumatic brain edema using measurements of reduced scattering coefficient (mus').* Appl Opt, 2010. **49**(28): p. 5407-14.
327. Eggert, H.R. and V. Blazek, *Optical Properties of Human Brain Tissue, Meninges, and Brain Tumors in the Spectral Range of 200 to 900 nm.* Neurosurgery, 1987. **21**(4): p. 459-464.
328. Genina, E.A., A.N. Bashkatov, and V.V. Tuchin, *Optical Clearing of Cranial Bone.* Advances in Optical Technologies, 2008. **2008**: p. 8.
329. Gordillo, N., E. Montseny, and P. Sobrevilla, *State of the art survey on MRI brain tumor segmentation.* Magn Reson Imaging, 2013. **31**(8): p. 1426-38.
330. Zelmann, R., et al., *Improving recorded volume in mesial temporal lobe by optimizing stereotactic intracranial electrode implantation planning.* Int J Comput Assist Radiol

Surg, 2015. **10**(10): p. 1599-615.

331. Sparks, R., et al., *Automated multiple trajectory planning algorithm for the placement of stereo-electroencephalography (SEEG) electrodes in epilepsy treatment.* Int J Comput Assist Radiol Surg, 2017. **12**(1): p. 123-136.
332. Vesselov, L.M., W. Whittington, and L. Lilge, *Performance evaluation of cylindrical fiber optic light diffusers for biomedical applications.* Lasers in Surgery and Medicine, 2004. **34**(4): p. 348-51.
333. Petrecca, K., et al., *Failure pattern following complete resection plus radiotherapy and temozolomide is at the resection margin in patients with glioblastoma.* J Neurooncol, 2013. **111**(1): p. 19-23.
334. Heon Yoo, et al., *Reduced local recurrence of a single brain metastasis through microscopic total resection.* Journal of Neurosurgery, 2009. **110**(4): p. 730-736.
335. Wilson, B.C., P.J. Muller, and J.C. Yanch, *Instrumentation and light dosimetry for intra-operative photodynamic therapy (PDT) of malignant brain tumours.* Physics in Medecine and Biology, 1986. **31**(2): p. 125-33.
336. Jacques, S.L., *Optical properties of biological tissues: a review.* Physics in Medecine and Biology, 2013. **58**(11): p. R37-61.
337. Kostron, H., et al., *CHAPTER 20 Photodynamic Medicine in Neurosurgery: Biochemical, Technical and Clinical Aspects*, in *Photodynamic Medicine: From Bench to Clinic*. 2016, The Royal Society of Chemistry. p. 353-403.
338. Vignion-Dewalle, A.S., et al., *Comparison of three light doses in the photodynamic treatment of actinic keratosis using mathematical modeling.* Journal of Biomedical Optics, 2015. **20**(5): p. 58001.
339. Natarajan, P. and C. Raja, *Studies on interpolymer self-organisation behaviour of protoporphyrin IX bound poly(carboxylic acid)s with complimentary polymers by means of fluorescence techniques.* European Polymer Journal, 2004. **40**(10): p. 2291-2303.
340. Miga, M.I., et al., *In vivo quantification of a homogeneous brain deformation model for updating preoperative images during surgery.* IEEE Trans Biomed Eng, 2000. **47**(2): p. 266-73.
341. Miller, K., et al., *Mechanical properties of brain tissue in-vivo: experiment and computer simulation.* J Biomech, 2000. **33**(11): p. 1369-76.
342. Ferrant, M., et al., *Registration of 3-D intraoperative MR images of the brain using a finite-element biomechanical model.* IEEE Trans Med Imaging, 2001. **20**(12): p. 1384-

97.

343. Soza, G., et al., *Determination of the elasticity parameters of brain tissue with combined simulation and registration.* Int J Med Robot, 2005. **1**(3): p. 87-95.

344. Budday, S., et al., *Mechanical properties of gray and white matter brain tissue by indentation.* Journal of the mechanical behavior of biomedical materials, 2015. **46**: p. 318-330.

345. Stewart, D.C., et al., *Mechanical characterization of human brain tumors from patients and comparison to potential surgical phantoms.* PLoS ONE, 2017. **12**(6): p. e0177561.

346. Yeoh, O.H., *Some Forms of the Strain Energy Function for Rubber.* Rubber Chemistry and Technology, 1993. **66**(5): p. 754-771.

347. Selvadurai, A.P.S., *Deflections of a rubber membrane.* Journal of the Mechanics and Physics of Solids, 2006. **54**(6): p. 1093-1119.

348. Hirschberg, H., et al., *Effects of ALA-mediated photodynamic therapy on the invasiveness of human glioma cells.* Lasers Surg Med, 2006. **38**(10): p. 939-45.

349. Kamoshima, Y., S. Terasaka, and Y. Iwasaki, *Photodynamic therapy mediated with 5-aminolevulinic acid for C6 glioma spheroids.* Hokkaido Igaku Zasshi, 2008. **83**(3): p. 167-73.

350. Zelenkov, P., et al., *Acute morphological sequelae of photodynamic therapy with 5-aminolevulinic acid in the C6 spheroid model.* J Neurooncol, 2007. **82**(1): p. 49-60.

351. Tirapelli, L.F., et al., *Apoptosis in glioma cells treated with PDT.* Photomed Laser Surg, 2011. **29**(5): p. 305-9.

352. Valdes, P.A., et al., *delta-aminolevulinic acid-induced protoporphyrin IX concentration correlates with histopathologic markers of malignancy in human gliomas: the need for quantitative fluorescence-guided resection to identify regions of increasing malignancy.* Neuro Oncology, 2011. **13**(8): p. 846-56.

353. Hetzel, F.W., et al., *Photodynamic Therapy Dosimetry*. 2005, American Association of Physicists in Medicine.

354. Juzeniene, A., Q. Peng, and J. Moan, *Milestones in the development of photodynamic therapy and fluorescence diagnosis.* Photochem Photobiol Sci, 2007. **6**(12): p. 1234-45.

355. Krammer, B. and K. Plaetzer, *ALA and its clinical impact, from bench to bedside.* Photochem Photobiol Sci, 2008. **7**(3): p. 283-9.

356. Vella, L.J., et al., *A rigorous method to enrich for exosomes from brain tissue.* J

Extracell Vesicles, 2017. **6**(1): p. 1348885.

357. Ho, C.J.H., et al., *Multifunctional Photosensitizer-Based Contrast Agents for Photoacoustic Imaging.* Scientific Reports, 2014. **4**: p. 5342.
358. Shao, P., et al., *Monitoring photodynamic therapy with photoacoustic microscopy.* J Biomed Opt, 2015. **20**(10): p. 106012.
359. Mallidi, S., et al., *Prediction of Tumor Recurrence and Therapy Monitoring Using Ultrasound-Guided Photoacoustic Imaging.* Theranostics, 2015. **5**(3): p. 289-301.
360. Thecua, E., et al. *Light emitting fabric for photodynamic treatment of actinic keratosis*. in *Proc. SPIE 10037, Photonics in Dermatology and Plastic Surgery*. 2017. San Francisco.
361. Mordon, S., et al., *Light emitting fabric technologies for photodynamic therapy.* Photodiagnosis Photodyn Ther, 2015. **12**(1): p. 1-8.
362. Liang, X., et al., *Maximizing fluence rate and field uniformity of light blanket for intraoperative PDT.* Proceedings of SPIE--the International Society for Optical Engineering, 2012. **8210**: p. 82100X.
363. Hu, Y., K. Wang, and T.C. Zhu, *Pre-clinic study of uniformity of light blanket for intraoperative photodynamic therapy.* Proc SPIE Int Soc Opt Eng, 2010. **7551**.
364. Hu, Y., K. Wang, and T.C. Zhu, *A light blanket for intraoperative photodynamic therapy.* Proc SPIE Int Soc Opt Eng, 2013. **7380**: p. 73801W.

List of figures

List of tables

Contributions

Articles

A novel device for intraoperative photodynamic therapy dedicated to glioblastoma treatment, C. Dupont, S. Mordon, P. Deleporte, N. Reyns, M. Vermandel, Future Oncology, 2017 [In press]

Photodynamic Therapy for glioblastoma: A preliminary approach for practical application of light propagation models, C. Dupont, A.-S. Vignion, S. Mordon, N. Reyns, M. Vermandel, Lasers in Surgery and Medicine, 2017 [In press]

5-ALA Photodynamic Therapy in Neurosurgery, Towards the Design of a Treatment Planning System: A Proof of Concept, C. Dupont, N. Betrouni, S. Mordon, N. Reyns, M. Vermandel, IRBM, 2017, Volume 38, issue 1, p. 34-41

Photodynamic therapy in neurosurgery: a proof of concept of treatment planning system, C. Dupont, N. Reyns, S. Mordon, M. Vermandel, Proc. SPIE 10047, Optical Methods for Tumor Treatment and Detection: Mechanisms and Techniques in Photodynamic Therapy XXVI, 1004714, February 8, 2017, SPIE BiOS 2017, San Francisco (USA)

Intraoperative photodynamic treatment for high-grade gliomas, C. Dupont, N. Reyns, P. Deleporte, S. Mordon, M. Vermandel, Proc. SPIE 10047, Optical Methods for Tumor Treatment and Detection: Mechanisms and Techniques in Photodynamic Therapy XXVI, 100470N (February 8, 2017), SPIE BiOS 2017, San Francisco (USA)

On image segmentation methods applied to glioblastoma: State of art and new trends, C. Dupont, N. Betrouni, N. Reyns, M. Vermandel, IRBM, 2016, Volume 37, issue 3, p. 131-143.

Patent

System for treatment by photodynamic therapy of a cavity of a patient's body and method for preparation of such system, M. Vermandel, S. Mordon, Dupont, P. Deleporte, N. Reyns, Inserm (ongoing)

Conferences

Characterization of a novel device for intraoperative photodynamic therapy in neurosurgery, C. Dupont, N. Reyns, P. Deleporte, S. Mordon, M. Vermandel, Lasers in Surgery and Medicine, 2017, Volume 49(28), p. 50.
ASLMS 2017, 37th annual conference of the American Society for Laser Medicine and Surgery, San Diego (USA)

Set-up of the first pilot study on intraoperative 5-ALA PDT: INDYGO trial, M. Vermandel, C. Dupont, M. Quidet, F. Lecomte, E. Lerhun, S. Mordon, N. Betrouni, N. Reyns, Photodiagnosis and Photodynamic Therapy, 2017, Volume 17, p. A21.
Photodynamic Therapy and Photodiagnosis update, Nancy (France)

A novel device for intraoperative photodynamic therapy dedicated to glioblastoma treatment, C. Dupont, N. Betrouni, J.-B. Tylcz, P. Deleporte, S. Mordon, N. Reyns, M. Vermandel, Lasers in Surgery and Medicine, 2016, Volume 48 (27), p. 54.
ASLMS 2016, 36th annual conference of the American Society for Laser Medicine and Surgery, Boston (USA)

Dosimetry dedicated to interstitial photodynamic treatment for glioblastoma, C. Dupont, S. Mordon, N. Betrouni, N. Reyns, M. Vermandel, Lasers in Surgery and Medicine, 2016, Volume 48 (27), p. 54.
ASLMS 2016, 36th annual conference of the American Society for Laser Medicine and Surgery, Boston (USA)

Dosimetry dedicated to photodynamic therapy planning, C. Dupont, N. Betrouni, N. Reyns, M. Vermandel, Physica Medica, 2015, Volume 31, supplement 2, p. e32
SFPM 2015, 54th annual conference of the French society of Medical Physics, Lille

French summary

Introduction

Ce travail de recherche a été réalisé au sein du laboratoire U1189 ONCO-THAI (Inserm, Université de Lille, Hôpital universitaire de Lille), lequel développe des thérapies minimalement invasives utilisant la lumière laser, en oncologie principalement. Une ligne de recherche interdisciplinaire est privilégiée afin d'atteindre l'évaluation clinique des technologies développées au laboratoire.

Parmi les cibles potentielles des thérapies par laser, le traitement de cancers cérébraux est en cours d'exploration. Bien qu'aucun facteur de risque environnemental n'a pu être identifié à l'exception des thérapies ionisantes [1, 2], l'augmentation et le vieillissement de la population, l'amélioration du diagnostic et la gravité du pronostic de ce type de cancers mettent la recherche au défi de trouver des réponses appropriées à cette urgence médicale [3].

Parmi les récentes alternatives, la thérapie photodynamique (PDT) apparaît comme un traitement prometteur en oncologie et plus précisément dans le traitement de certains types de

cancers cérébraux, dont le glioblastome (GBM). Néanmoins, cette thérapie n'est pas encore adaptée aux contraintes cliniques actuelles pour plusieurs raisons. Aucun consensus n'a été défini sur l'utilisation d'un agent médicamenteux et il existe une absence de systèmes de délivrance de la thérapie (dispositifs médicaux et logiciels de planification de traitement) fiables et reproductibles. Toutes ces disparités entraînent une absence d'essais cliniques multicentriques randomisés et contrôlés sur le traitement du GBM par PDT.

L'objectif principal de cette thèse est donc de développer des outils technologiques, aussi bien logiciels que matériels, dédiés au traitement du GBM par PDT. Plusieurs axes de recherche ont été poursuivis en ayant la dosimétrie comme fil conducteur : la planification de la PDT dans ses deux modalités d'illumination (interstitielle et peropératoire) et développer des dispositifs de délivrance du traitement.

I. Etat de l'art

1. La thérapie photodynamique

Avec l'évolution technologique du laser (miniaturisation, fiabilité et rendement), l'utilisation de ses propriétés physiques en médecine a permis de développer plusieurs thérapies utilisant les différents effets du laser sur les tissus biologiques. Parmi ces thérapies, la PDT définit un traitement local et sélectif consistant en l'illumination de tissus photosensibilisés dans le but de générer un effet cytotoxique sur les cellules ciblées. Cette thérapie est composée de trois éléments principaux : Le photosensibilisateur (PS), qui est une molécule se concentrant sélectivement dans les cellules cancéreuses ; L'oxygène, présent naturellement dans le métabolisme, et la lumière, délivrée par le biais d'un laser, qui apporte l'énergie nécessaire à la réaction chimique entre le PS et l'oxygène. Cette réaction de photo-oxydation aboutit à la production d'espèces cytotoxiques (principalement d'oxygène singulet) et de radicaux libres. Cette réaction chimique entraîne des effets directs (nécrose, apoptose) et indirects (réponses immunitaires) sur les cellules tumorales (voir figure 1.8).
Plusieurs sources lumineuses sont développées (fibres diffusantes, ballonnet diffusant, tissus lumineux) pour adapter l'illumination à la cible thérapeutique (voir figure 1.7).

2. Le glioblastome

Les gliomes sont les tumeurs du cerveau les plus fréquentes chez l'adulte. Elles sont classées en fonction de quatre grades par l'Organisation Mondiale de la Santé [4]. Le glioblastome (GBM) ou gliome de grade 4 est la tumeur la plus fréquente et la plus agressive

du système nerveux central (SNC) [5-7]. L'incidence annuelle se situe entre 3 à 5 cas par an pour 100 000 personnes [8-10]. Le pronostic de cette tumeur est dans la plupart des cas fortement péjoratif. Une médiane de survie variant entre 14 et 15 mois est mesurée en fonction de la qualité de la chirurgie. Actuellement, aucun traitement parmi l'éventail thérapeutique disponible ne permet une guérison.

Le GBM se distingue par une infiltration importante dans les méninges ainsi qu'une forte hétérogénéité tissulaire observées à l'imagerie et sur le profil histopathologique. Ces caractéristiques le rendent difficile à traiter efficacement.

Le protocole de traitement standard recommandé par la *European Society for Medical Oncology* (ESMO) décrit l'utilisation de trois différents types de thérapies dans le cadre du traitement du GBM.

L'élément principal et le plus déterminant de ce protocole est la résection chirurgicale. Le retrait du tissu tumoral impacte de façon significative le pronostic vital du/de la patient.e [11-13]. La complexité de cette opération réside dans le choix effectué lors de l'opération. Le.a neurochirurgien.ne doit distinguer au mieux les tissus tumoraux des tissus sains et conserver les organes à risques ainsi que les zones fonctionnelles. Des techniques de guidage par fluorescence (FGR) sont mises en place afin de mieux identifier les tissus tumoraux résiduels. Une augmentation de 2 mois de la survie sans progression est observée lors d'une chirurgie avec FGR [14, 15].

Des traitements adjuvants sont ensuite proposés en fonction du grade et du profil génétique de la tumeur (voir figure 1.10). Dans la plupart des cas, les radiothérapies et chimiothérapies servent de support à l'exérèse afin de détruire le reliquat de cellules tumorales présentes dans les berges du foyer opératoire et, ainsi, prolonger la survie sans progression du/de la patient.e.

De nombreuses thérapies alternatives sont actuellement en cours de développement et d'évaluation telles que l'immunothérapie [16, 17], les ultrasons focalisés de haute intensité (HIFU) [16, 18-21], la proton thérapie [22] et la PDT.

3. Traitements des gliomes de haut grade par thérapie photodynamique

Les premières études de traitement de tumeurs cérébrales ont débuté en 1972 [23]. Le premier essai clinique chez l'humain a été mené en 1980 par Perria et al. [24]. Depuis, un nombre grandissant d'études du traitement du GBM par la PDT est observé.

Deux modes d'administration de la thérapie sont étudiés. Lorsque la résection ne peut pas être réalisée du fait de contraintes chirurgicales (environ 15% des cas [25, 26]), la PDT

interstitielle (iPDT) peut être envisagée. Cette modalité de traitement consiste en l'insertion de fibres optiques (diffuseurs frontaux ou cylindriques) au sein même de la cible thérapeutique afin de délivrer la lumière directement *in situ*. Dans la plupart des cas de traitement de GBM par iPDT, les fibres optiques sont insérées dans un référentiel stéréotaxique qui permet de localiser leur insertion dans le cerveau du/de la patient.e. Les principaux essais cliniques de traitement de GBM par iPDT sont listés dans le tableau 1.1.

Dans le cas où la chirurgie peut avoir lieu, la PDT peropératoire (perPDT) peut être administrée en fin de résection. Un dispositif lumineux (ballon, fibre cylindrique, laser couplé au microscope chirurgical) est inséré dans la cavité afin de générer un effet cytotoxique dans les berges opératoires. Les principaux essais cliniques de traitement de GBM par perPDT sont listés dans le tableau 1.2.

4. Dosimétrie prédictive de la PDT

La dosimétrie prédictive utilisée pour planifier la délivrance d'un traitement PDT comprend la modélisation des trois composants principaux de la PDT (i.e., la propagation de la lumière, la distribution du PS et la concentration de l'oxygène dans les tissus).

Ainsi, la modélisation du transport de la lumière dans la matière est une composante essentielle afin d'obtenir une dosimétrie pertinente. Différents modèles ont été conçus pour prédire cette propagation dans les tissus biologiques. Le modèle mathématique, connu sous le nom de méthode analytique, provient de la solution à l'état stationnaire de l'équation de transport de Boltzmann (équation 2.19). Ce modèle permet la modélisation de différentes sources lumineuses (source ponctuelle (équation 2.25), cylindrique (équation 2.26), plane et sphérique (équations 2.28)). Sa simplicité de mise en œuvre le rend particulièrement intéressant pour une estimation rapide de la distribution de la lumière lors d'un traitement PDT via l'utilisation de système de planification de traitement (TPS). Cependant, ce calcul reste une estimation et n'est pas valide dans certaines conditions critiques, notamment près des sources lumineuses.

Un autre modèle de propagation de la lumière utilise une approche numérique pour résoudre l'équation différentielle partielle de Helmholtz (équation 2.23). L'espace de simulation est discrétisé afin de créer un maillage, tétraédrique dans la plupart des cas. Ce maillage fournit des valeurs limites pour résoudre les équations différentielles. Cependant, la mise en œuvre d'un tel modèle dans un TPS reste complexe car elle nécessite plusieurs étapes préliminaires (optimisation du maillage, résolution numérique des sources lumineuses).

Enfin, le modèle Monte-Carlo, considéré comme méthode de référence, permet une

grande flexibilité dans la modélisation de sources lumineuses. Cette approche consiste à suivre le parcours de chaque photon, depuis leur création jusqu'à leur absorption, en fonction de leur probabilité d'interactions avec les tissus. Ainsi, pour obtenir une simulation réaliste, des millions de photons doivent être générés, entraînant de longs temps de calcul.

5. La méthode de Monte-Carlo appliquée à la dosimétrie de la PDT

Puisque la méthode de Monte-Carlo permet une modélisation du déplacement des photons dans la matière, son algorithme est basé sur les lois physiques qui régissent leur propagation. D'un point de vue simplifié, un photon peut être absorbé ou non dans un milieu. S'il ne l'est pas, il est dévié de sa trajectoire initiale. Ces deux notions définissent les deux principales interactions fondamentales de la propagation des photons dans le domaine du visible et sont donc transposées dans l'algorithme de Monte-Carlo. Dans l'ensemble de l'algorithme de Monte-Carlo, des nombres aléatoires sont injectés lors des calculs des interactions. Ces nombres aléatoires permettent de ne pas reproduire le même parcours pour deux photons et ainsi obtenir une simulation pertinente.

Chaque photon est défini par plusieurs paramètres tels que sa position, sa direction et son « poids ». Ce poids peut être interprété comme une « barre de vie » où chaque collision diminue sa valeur jusqu'à atteindre la valeur nulle, i.e., l'absorption totale du photon. Comme la plupart des sources lumineuses ont une émission considérée idéalement comme isotropique (c.-à-d., qui émet la lumière de façon homogène, indépendamment de la direction d'émission), la direction initiale est calculée à l'aide d'un nombre aléatoire (équation 3.3). Une fois la direction calculée, une longueur de déplacement est prédite. Si le photon reste dans le même milieu, même après ce déplacement, ce dernier va se déplacer à la position suivante. Dans le cas où le photon change de milieu lors de son déplacement, celui-ci est modifié en fonction des coefficients optiques des deux milieux. Une transmission ou une réflexion du photon peut avoir lieu à l'interface entre les deux milieux. Une fois le photon déplacé, son poids va diminuer en fonction des coefficients optiques du milieu dans lequel il se trouve. Une nouvelle direction va ensuite être calculée. Ces trois parties (« *hop-drop-spin* » en anglais) vont être répétées jusqu'à ce que le poids du photon soit considéré comme négligeable. Ce n'est qu'alors que le parcours du photon est terminé. Un nouveau photon sera généré jusqu'à atteindre un nombre suffisant de photons simulés pour obtenir une estimation correcte de la quantité de poids déposée dans l'espace. Cette quantité sera ensuite convertie afin d'obtenir l'estimation du débit de fluence (*fluence rate* en anglais, [W/cm^2]) déposé par la source lumineuse.

6. Méthode d'accélération de la méthode de Monte-Carlo par l'utilisation du calcul parallèle sur processeurs graphiques

Bien que la méthode de Monte-Carlo reste la référence pour modéliser la propagation de la lumière, son utilisation en routine clinique est limitée par le temps de calcul nécessaire pour obtenir des résultats précis. Avec l'amélioration des capacités informatiques et des nouvelles technologies, différentes techniques ont été développées pour diminuer ce temps de calcul. Parmi elles, l'utilisation de processeurs graphiques (carte graphique permettant l'accélération de calculs numériques) est la meilleure option pour accélérer un calcul à un prix raisonnable. Cette technique est basée sur la parallélisation d'un algorithme. Les processeurs graphiques développés par le fabriquant NVIDIA possèdent de nombreuses unités de calcul (*thread* en anglais) permettant d'exécuter un même code en parallèle sur l'ensemble de ces unités de calcul. Dans le cas de l'algorithme de Monte-Carlo, le parcours d'un photon ne dépend pas des autres parcours. Chaque photon peut ainsi être généré indépendamment des autres. Plusieurs parcours de photons peuvent être calculés en parallèle ; un parcours de photon par unité de calcul. Le temps de calcul est alors drastiquement réduit [27, 28].

II. Contributions

Afin de couvrir l'ensemble des patient.es (admissibles en chirurgie ou non), les deux modalités de traitement photodynamiques (interstitielle et intracavitaire) ont été étudiées. Les contributions de ces travaux de thèse se situent dans la création d'un code informatique permettant la simulation de fibres cylindriques par méthode Monte-Carlo accélérée par processeur graphique et le développement d'un nouveau dispositif médical dédié à l'illumination de la cavité opératoire en fin de FGR.

1. Développement, validation et optimisation d'un code Monte-Carlo accéléré par processeurs graphiques

Afin d'utiliser la méthode Monte-Carlo pour planifier un traitement PDT en routine clinique, un code Monte-Carlo accéléré par processeur graphique a été développé. Il permet la modélisation d'une fibre cylindrique insérée dans un milieu hétérogène et le calcul du débit de fluence délivrée par celle-ci.

Les résultats du code informatique (c.-à-d., la matrice du débit de fluence) ont été comparés à des mesures expérimentales. Pour cela, un fantôme optique a été développé, composé d'eau, de liquide intralipidique et d'encre de chine. Ce type de mélange est l'un des

plus utilisés pour la création de fantômes optiques. Le liquide intralipidique influe uniquement sur le coefficient de diffusion. L'encre de chine affecte majoritairement le coefficient d'absorption. Grâce à ce mélange, il est possible de créer une solution ayant des propriétés optiques connues. Les masses de ces composants ont été calculées à partir d'une étude réalisée par Spinelli et al. [29] (voir équations 3.30) afin d'obtenir un coefficient d'absorption μ_a égal à 0.2 cm^{-1} et un coefficient de diffusion réduit μ'_s égal à 20 cm^{-1}. Ces deux coefficients correspondent aux valeurs moyennes d'un cerveau humain standard infiltré par des cellules de gliomes [14, 30-32].

La puissance [W] est l'unique grandeur pouvant être mesurée pour quantifier la quantité de photons en un point de l'espace. Cependant, pour pouvoir calculer une dose (ou fluence [J/cm²]), l'estimation du débit de fluence [W/cm²] est nécessaire. Un facteur de calibration permettant de convertir les mesures de puissance en débit de fluence a été calculé à partir des études de Star et Marijnissen [33, 34], recommandées par l'*American Association of Physicists in Medicine* (AAPM) [35, 36]. Ce facteur de calibration est le résultat de la multiplication de cinq facteurs permettant de corriger l'influence du capteur sur la mesure (inhomogénéité, dimensions du capteur, matériaux utilisés).

Une fois ce facteur correctif estimé, cinq fibres cylindriques ont été placées au centre d'une boite noire, remplie par le fantôme. Des mesures de puissance autour de chaque fibre ont été réalisées (voir figures 3.8 et 3.9). Ces mêmes fibres ont été modélisées à l'aide du code Monte-Carlo dans un milieu homogène et possédant les mêmes coefficients optiques que ceux du fantôme. L'erreur relative entre les mesures de puissance considérées comme références et les résultats obtenus par simulation Monte-Carlo a été calculée pour chaque mesure. Une erreur relative moyenne de l'ensemble des fibres égale à 14.97 (± 6.16) a été obtenue. Elle se situe dans l'intervalle d'acceptation recommandé par l'AAPM (erreur inférieure à 20%) et permet donc de valider la précision du code Monte-Carlo accéléré par processeur graphique.

Concernant les performances du code proposé, une optimisation de l'utilisation des mémoires liées au processeur graphique a été réalisée. Une accélération d'environ 660 a été obtenue en comparaison avec une version similaire exécutée séquentiellement sur processeur (CPU). Cette accélération est cohérente par rapport à celle reportée dans la littérature et permet également des temps de simulation permettant son utilisation en routine clinique.

2. Développement et évaluation d'une preuve de concept d'un système de planification de traitement dédié au traitement photodynamique du glioblastome par voie interstitielle et en conditions stéréotaxiques

Un traitement iPDT nécessite l'utilisation d'un TPS pour planifier l'insertion des fibres optiques ainsi que la dosimétrie associée (voir figure 4.1). L'objectif ici est d'établir la preuve de concept d'un système de modélisation et de planification de délivrance d'un traitement iPDT. L'intégration de cette technique au bloc opératoire pose de nombreuses contraintes technologiques. En outre, l'utilisation d'un référentiel stéréotaxique (référentiel de Leksell) doit être prise en compte afin de localiser les fibres optiques dans l'espace. Un TPS, nommé *iPDT-Plan,* a donc été développé. Ce logiciel permet l'importation de séquences d'imagerie (IRM, Scanner) dans le référentiel de Leksell, la définition d'une cible thérapeutique, l'insertion de différentes fibres cylindriques avec leurs caractéristiques associées (longueur de diffusion, puissance délivrée) et le calcul dosimétrique afin d'obtenir un temps de traitement.

La précision de l'algorithme de recalage dans le référentiel stéréotaxique de Leksell implémenté dans *iPDT-Plan* a été évaluée avec la création d'un fantôme (voir figure 4.6). Ce fantôme cubique composé de poly-méthacrylate de méthyle comporte 39 billes radio-opaques reparties sur différents niveaux. Il a ensuite été imagé par scanner (voir figure 4.7). Ces images ont été importées dans le logiciel GammaPlan® (Elekta, Stockholm, Suède) qui intègre un recalage stéréotaxique semi-automatique. Chaque bille a été localisée à la fois dans le GammaPlan® et l'*iPDT-Plan*. La distance entre ces deux localisations a été calculée. La moyenne de ces distances s'élève à 0.8mm ± 0.3 mm (maximum = 1.3 mm). Cette moyenne, inférieure à la résolution d'une l'IRM habituellement utilisée pendant la planification d'un traitement, permet de valider l'algorithme de recalage semi-automatique.

Concernant la dosimétrie, puisqu'aucun algorithme de segmentation ou de classification n'a été implémenté, le modèle Monte-Carlo présenté précédemment ne peut pas être exécuté dans le TPS actuel. Une méthode analytique a donc été implémentée afin d'estimer rapidement et facilement la lumière émise par l'ensemble des fibres cylindriques insérées dans le cerveau du/de la patient.e. Cette méthode analytique a été comparée aux résultats obtenus par méthode Monte-Carlo, considérée comme référence. Six fibres cylindriques de longueurs de diffusion différentes ont été modélisées à la fois par méthode Monte-Carlo et approche analytique. L'erreur relative moyenne entre ces deux méthodes s'élève à 2.53% (écart-type 2.09%). Cette méthode permet donc d'estimer correctement la propagation de la lumière dans un milieu homogène. Cependant, le GBM est connu pour sa grande hétérogénéité tissulaire, ce que le modèle analytique ne peut prendre en considération. La méthode analytique a ensuite été soumise à une étude de sensibilité avec pour objectif de déterminer l'influence des variations des paramètres d'entrée du modèle sur sa sortie. Cette

sensibilité a été évaluée à l'aide des indices de Sobol [37, 38]. Les résultats de cette étude montrent que l'absorption pondère plus la diffusion à une distance supérieure de 3 mm de la source lumineuse, et inversement pour la diffusion. Cette sensibilité de la variance de la méthode analytique souligne l'importance de remplacer le modèle analytique par le modèle Monte-Carlo.

3. Développement et évaluation d'un nouveau dispositif médical dédié au traitement photodynamique peropératoire du glioblastome

La seconde modalité de traitement du GBM, appelée perPDT (*intraoperative PDT* en anglais), est l'illumination de la cavité opératoire au cours de l'intervention chirurgicale. Cette modalité s'inscrit dans le processus standard de traitement du GBM. Avant l'intervention, le précurseur du PS (l'acide 5-aminolévulinique, 5-ALA) est administré au/à la patient.e dans le cadre de la FGR. En effet, le 5-ALA est actuellement approuvé comme agent de contraste pour la FGR dans le cadre du traitement du GBM chez l'humain en Europe, Asie, Australie et aux Etats-Unis. Une fois le PS (la protoporphyrine IX, PpIX) concentré dans les cellules tumorales (attente de quelques heures), la résection chirurgicale est réalisée, suivie par la FGR. Lorsque la cavité opératoire est illuminée par une lumière bleue (375 - 440 nm), le PS émet une fluorescence rougeâtre (635 nm). L'objectif de la FGR est de guider le geste chirurgical afin d'améliorer la qualité de résection. Cependant, bien que macroscopiquement aucun reliquat tumoral ne soit visible en fin de FGR, des cellules tumorales sont toujours présentes dans les berges de la cavité. Ce résidu de cellules est à l'origine de plus de 85% de récidive tumorale [15, 39, 40]. Un contrôle local pour diminuer ce risque de récidive est donc primordial. La PDT intervient donc en fin de FGR, profitant ainsi de l'administration du PS au/à la patient.e pour le fluoroguidage. Le PS est ainsi repositionné an tant qu'agent thérapeutique et non de contraste. Pour réaliser cette illumination, un dispositif dédié à la perPDT a été développé.

Ce dernier repose sur les études antérieures réalisées pour développer l'illumination peropératoire de la cavité opératoire [41-46]. Le dispositif présenté dans cette étude est composé de deux parties. La première, commercialisée par B-Braun® Aesculap® (Tuttlingen, Germany) sous le nom de Herloon© balloon, est à l'origine un ballon utilisé en chirurgie endoscopique (voir figure 5.3). Il s'agit d'un ballon gonflable et jetable inséré dans un trocart réutilisable. La seconde partie, développée au sein du laboratoire ONCO-THAI, est un guide de fibre lumineux s'insérant dans le trocart et permettant l'insertion et le placement d'une fibre cylindrique diffusante de 70 mm (RD-ML 70, Medlight, Ecublens, Suisse) au centre du

ballon (voir figure 5.4). Une fois assemblée, le ballon est gonflé à l'aide d'une solution diffusante (solution intralipidique diluée à 0.1%) permettant une meilleure homogénéisation de la distribution de la lumière autour du ballon (voir figure 5.5).

La caractérisation dosimétrique du dispositif a été réalisée sur banc optique afin de simplifier la procédure chirurgicale, notamment l'estimation du temps de traitement. Plus la taille de la cavité est importante, plus le temps d'illumination est important pour déposer la même fluence. Ainsi la durée d'illumination doit être déductible en fonction de la taille de la cavité, et donc de la quantité de solution diffusante injectée dans le ballon. Pour réaliser cette dosimétrie, des mesures expérimentales sur cerveaux de veaux ont été effectuées. Le dispositif était placé dans une boite noire et entouré de cerveaux de veau (voir figure 5.6). Des mesures de puissance ont été réalisées à 15 positions différentes autour du ballon et allant jusqu'à 10 mm de profondeur dans les tissus. Différents volumes de solution diffusante ont été injectés (de 40 mL à 500 mL) permettant de modéliser l'ensemble des volumes de cavité opératoire. Ainsi pour chaque volume, 150 points de mesures ont été effectués.

Pour convertir ces mesures de puissance [W] en débit de fluence [w/cm²], le même protocole utilisé pour la validation du modèle Monte-Carlo présenté précédemment a été utilisé. Un facteur de calibration a donc été calculé pour convertir les mesures de puissance dans les cerveaux de veau en débit de fluence. Une fois ces mesures réalisées, un temps de traitement a été calculé afin de déposer une fluence de 200 J/cm^2 correspondant à 25 J/cm^2 pour chaque volume de solution diffusante injecté. Ainsi, une fonction de transfert liant directement la quantité injectée dans le dispositif au temps d'illumination requis pour obtenir un effet PDT jusqu'à 5 mm dans les berges de la cavité a été obtenue. Cette fonction de transfert a également été modélisée via plusieurs modélisations Monte-Carlo. Une erreur moyenne de 9.998% entre les deux fonctions de transfert a été calculée.

Plusieurs autres études ont été réalisées pour la caractérisation du dispositif. La conformation du ballon aux bords de la cavité a été modélisée grâce à la création d'un fantôme mécanique. Une séquence IRM peropératoire d'une résection chirurgicale de GBM a été segmentée. Le crâne a été imprimé en polymère AM3300. Le cerveau comportant ainsi une cavité a été formé à partir d'un moule imprimé en 3D. Le gel constituant le cerveau a été étudié par extensométrie afin de reproduire les propriétés mécaniques de tissus cérébraux humains, notamment l'élasticité caractérisée par le module de Young. Une fois créé, le fantôme a été imaginé par scanner avec un dispositif inséré dans la cavité. Avec le volume optimal pour occuper au maximum la cavité opératoire, le dispositif n'est au contact que de 32% de la surface de la cavité. Malgré ce faible taux, l'impact sur le débit de fluence reste

modéré.

L’impact sur les coefficients optiques de la non-présence du photosensibilisateur (i.e., la PpIX) lors des mesures expérimentales a été évalué. De la même façon, l’homogénéité de la distribution de la lumière autour du ballon, l’étanchéité du dispositif, l’impact thermique du rayonnement laser et la quantité limite de solution diffusante injectable dans le ballon avant déchirure de la paroi ont été étudiés afin de démarrer les procédures pour mettre en place une étude clinique de phase I.

Cette étude pilote de faisabilité nommée INDYGO (i.e., *intraoperative 5-ALA mediated photodynamic therapy for treating glioblastoma*) est actuellement en cours de recrutement. Elle vise à évaluer la faisabilité de la réalisation de la PDT peropératoire au cours de la chirurgie d’exérèse du GBM, sans toxicité immédiate inacceptable. Un recrutement de 10 participants est envisagé. Actuellement, cinq patient.e.s ont été traités ; aucun incident technologique ou médical n’a été reporté.

Conclusion

L'objectif principal de ce travail de thèse a été de fournir les outils technologiques permettant la mise en œuvre du traitement du GBM par PDT. Afin d'inclure la totalité des patient.es atteint.es du GBM (cas résécables et non-résécables), les deux modalités de traitement (i.e., iPDT et perPDT) ont été étudiées. Bien que nombreuses améliorations des travaux présentés dans ce manuscrit sont d’ores et déjà prévues, ces premières activités de recherche ont permis le transfert des connaissances de la PDT vers la clinique avec les premiers traitements photodynamiques en neurochirurgie en France.

1. Thakkar, J.P., et al., *Epidemiologic and molecular prognostic review of glioblastoma.* Cancer Epidemiol Biomarkers Prev, 2014. **23**(10): p. 1985-96.
2. Omuro, A. and L.M. DeAngelis, *Glioblastoma and other malignant gliomas: A clinical review.* JAMA, 2013. **310**(17): p. 1842-1850.
3. Popat, K., K. McQueen, and T.W. Feeley, *The global burden of cancer.* Best Practice & Research Clinical Anaesthesiology, 2013. **27**(4): p. 399-408.
4. Louis, D.N., et al., *The 2016 World Health Organization Classification of Tumors of the Central Nervous System: a summary.* Acta Neuropathologica, 2016. **131**(6): p. 803-820.
5. Fisher, T., et al., *Mechanisms operative in the antitumor activity of temozolomide in glioblastoma multiforme.* Cancer J, 2007. **13**(5): p. 335-44.
6. Ostrom, Q.T., et al., *The epidemiology of glioma in adults: a "state of the science" review.* Neuro-Oncology, 2014.
7. Sathornsumetee, S., J.N. Rich, and D.A. Reardon, *Diagnosis and treatment of high-grade astrocytoma.* Neurol Clin, 2007. **25**(4): p. 1111-39, x.
8. Jordan, J.T., et al., *Glioblastoma care in the elderly.* Cancer, 2016. **122**(2): p. 189-97.
9. Ohgaki, H. and P. Kleihues, *Population-Based Studies on Incidence, Survival Rates, and Genetic Alterations in Astrocytic and Oligodendroglial Gliomas.* Journal of Neuropathology & Experimental Neurology, 2005. **64**(6): p. 479-489.
10. Ostrom, Q.T., et al., *Epidemiology of Gliomas*, in *Current Understanding and Treatment of Gliomas*, J. Raizer and A. Parsa, Editors. 2015, Springer International Publishing: Cham. p. 1-14.
11. Kuhnt, D., et al., *Correlation of the extent of tumor volume resection and patient survival in surgery of glioblastoma multiforme with high-field intraoperative MRI guidance.* Neuro-Oncology, 2011. **13**(12): p. 1339-1348.
12. Michel Lacroix, et al., *A multivariate analysis of 416 patients with glioblastoma multiforme: prognosis, extent of resection, and survival.* Journal of Neurosurgery, 2001. **95**(2): p. 190-198.
13. Stummer, W., et al., *Extent of resection and survival in glioblastoma multiforme: identification of and adjustment for bias.* Neurosurgery, 2008. **62**(3): p. 564-76; discussion 564-76.
14. Stepp, H., et al., *ALA and Malignant Glioma: Fluorescence-Guided Resection and Photodynamic Treatment.* Journal of Environmental Pathology, Toxicology and Oncology, 2007. **26**(2): p. 157-164.

15. Leroy, H.A., et al., *Fluorescence guided resection and glioblastoma in 2015: A review.* Lasers in Surgery and Medicine, 2015. **47**(5): p. 441-51.
16. Cohen-Inbar, O., Z. Xu, and J.P. Sheehan, *Focused ultrasound-aided immunomodulation in glioblastoma multiforme: a therapeutic concept.* Journal of Therapeutic Ultrasound, 2016. **4**: p. 2.
17. Hung, A.L., T. Garzon-Muvdi, and M. Lim, *Biomarkers and Immunotherapeutic Targets in Glioblastoma.* World Neurosurgery, 2017. **102**: p. 494-506.
18. Yang, F.Y. and S.C. Horng. *Chemotherapy of glioblastoma by targeted liposomal platinum compounds with focused ultrasound*. in *2013 35th Annual International Conference of the IEEE Engineering in Medicine and Biology Society (EMBC)*. 2013.
19. Phenix, C.P., et al., *High intensity focused ultrasound technology, its scope and applications in therapy and drug delivery.* J Pharm Pharm Sci, 2014. **17**(1): p. 136-53.
20. Yang, F.Y., et al., *Treating glioblastoma multiforme with selective high-dose liposomal doxorubicin chemotherapy induced by repeated focused ultrasound.* Int J Nanomedicine, 2012. **7**: p. 965-74.
21. Feng-Yi Yang, G.-L.L., Shih-Cheng Horng, Tien-Kuei Chang, Shih-Yen Wu, Tai-Tong Wong, and a.H.-E. Wang, *Pulsed High-Intensity Focused Ultrasound Enhances the Relative Permeability of the Blood–Tumor Barrier in a Glioma-Bearing Rat Model.* IEEE TRANSACTIONS ON ULTRASONICS, FERROELECTRICS, AND FREQUENCY CONTROL, 2011. **58**(5): p. 7.
22. von Neubeck, C., et al., *Glioblastoma multiforme: emerging treatments and stratification markers beyond new drugs.* The British Journal of Radiology, 2015. **88**(1053): p. 20150354.
23. Diamond, I., et al., *Photodynamic therapy of malignant tumours.* Lancet, 1972. **2**(7788): p. 1175-7.
24. Perria, C., et al., *First attempts at the photodynamic treatment of human gliomas.* J Neurosurg Sci, 1980. **24**(3-4): p. 119-29.
25. Paquette, B., et al., *Prognostic value of health-related quality of life for death risk stratification in patients with unresectable glioblastoma.* Cancer Med, 2016. **5**(8): p. 1753-64.
26. Fazeny-Dorner, B., et al., *Survival and prognostic factors of patients with unresectable glioblastoma multiforme.* Anticancer Drugs, 2003. **14**(4): p. 305-12.
27. Wang, L., S.L. Jacques, and L. Zheng, *MCML—Monte Carlo modeling of light transport in multi-layered tissues.* Computer Methods and Programs in Biomedicine,

1995. **47**(2): p. 131-146.

28. Fang, Q. and D.A. Boas, *Monte Carlo simulation of photon migration in 3D turbid media accelerated by graphics processing units.* Optics Express, 2009. **17**(22): p. 20178-90.
29. Spinelli, L., et al., *Determination of reference values for optical properties of liquid phantoms based on Intralipid and India ink.* Biomedical Optics Express, 2014. **5**(7): p. 2037-2053.
30. Beck, T.J., et al., *Interstitial photodynamic therapy of nonresectable malignant glioma recurrences using 5-aminolevulinic acid induced protoporphyrin IX*. Lasers in Surgery and Medicine, 2007. **39**(5): p. 386-93.
31. Johansson, A., et al., *Interstitial Photodynamic Therapy of Brain Tumors.* IEEE Journal of Selected Topics in Quantum Electronics, 2010. **16**(4): p. 841-853.
32. Rühm, A., et al. *5-ALA based photodynamic management of glioblastoma*. in *Proc. of SPIE Optical Techniques in Neurosurgery, Neurophotonics, and Optogenetics*. 2014.
33. Marijnissen, J.P. and W.M. Star, *Calibration of isotropic light dosimetry probes based on scattering bulbs in clear media.* Phys Med Biol, 1996. **41**(7): p. 1191-208.
34. Marijnissen, J.P. and W.M. Star, *Performance of isotropic light dosimetry probes based on scattering bulbs in turbid media.* Phys Med Biol, 2002. **47**(12): p. 2049-58.
35. Zhu, T. *AAPM recommendations for in-vivo light dosimetry for Photodynamic Therapy*. in *16th International Photodynamic Association World Congress* 2017. Comibra, Portugal.
36. Hetzel, F.W., et al., *AAPM REPORT NO. 88: PHOTODYNAMIC THERAPY DOSIMETRY*. 2005, American Association of Physicists in Medicine.
37. Andrea Saltelli, M.R., Terry Andres, Francesca Campolongo, Jessica Cariboni, Debora Gatelli, Michaela Saisana and Stefano Tarantola, *Global Sensitivity Analysis*. 2008: John Wiley & Sons. 305.
38. Zhang, X.Y., et al., *Sobol Sensitivity Analysis: A Tool to Guide the Development and Evaluation of Systems Pharmacology Models.* CPT Pharmacometrics Syst Pharmacol, 2015. **4**(2): p. 69-79.
39. Petrecca, K., et al., *Failure pattern following complete resection plus radiotherapy and temozolomide is at the resection margin in patients with glioblastoma.* J Neurooncol, 2013. **111**(1): p. 19-23.
40. Heon Yoo, et al., *Reduced local recurrence of a single brain metastasis through microscopic total resection.* Journal of Neurosurgery, 2009. **110**(4): p. 730-736.

41. Wilson, B.C., P.J. Muller, and J.C. Yanch, *Instrumentation and light dosimetry for intra-operative photodynamic therapy (PDT) of malignant brain tumours.* Physics in Medecine and Biology, 1986. **31**(2): p. 125-33.
42. Dwyer, P.J., et al., *Optical integrating balloon device for photodynamic therapy.* Lasers in Surgery and Medicine, 2000. **26**(1): p. 58-66.
43. Moseley, H., et al., *In vitro light distributions from intracranial PDT balloons.* Photodiagnosis Photodyn Ther, 2007. **4**(3): p. 213-20.
44. Eljamel, M.S., C. Goodman, and H. Moseley, *ALA and Photofrin fluorescence-guided resection and repetitive PDT in glioblastoma multiforme: a single centre Phase III randomised controlled trial.* Lasers Med Sci, 2008. **23**(4): p. 361-7.
45. Schmidt, M.H., et al., *Light-emitting diodes as a light source for intraoperative photodynamic therapy.* Neurosurgery, 1996. **38**(3): p. 552-6; discussion 556-7.
46. Akimoto, J., J. Haraoka, and K. Aizawa, *Preliminary clinical report on safety and efficacy of photodynamic therapy using talaporfin sodium for malignant gliomas.* Photodiagnosis Photodyn Ther, 2012. **9**(2): p. 91-9.